

FRAME SELECTION AND BISPECTRUM  
FOR SPECKLE IMAGING THROUGH  
ATMOSPHERIC TURBULENCE

THESIS  
Elizabeth A. Harpold  
Captain, USAF

AFIT/GAP/ENP/95D-07

**DISTRIBUTION STATEMENT H**

Approved for public release;  
Distribution Unlimited

DTIC QUALITY INSPECTED 1

DEPARTMENT OF THE AIR FORCE  
AIR UNIVERSITY  
**AIR FORCE INSTITUTE OF TECHNOLOGY**

Wright-Patterson Air Force Base, Ohio

AFIT/GAP/ENP/95D-07

FRAME SELECTION AND BISPECTRUM  
FOR SPECKLE IMAGING THROUGH  
ATMOSPHERIC TURBULENCE

THESIS  
Elizabeth A. Harpold  
Captain, USAF

AFIT/GAP/ENP/95D-07

19960207 030

Approved for public release; distribution unlimited

The views expressed in this thesis are those of the author and do not reflect the official policy or position of the Department of Defense or the U. S. Government.

AFIT/GAP/ENP/95D-07

THE ROLE OF FRAME SELECTION AND BISPECTRUM  
PHASE RECONSTRUCTION FOR SPECKLE IMAGING  
THROUGH ATMOSPHERIC TURBULENCE

THESIS

Presented to the Faculty of the School of Engineering  
of the Air Force Institute of Technology  
Air University  
In Partial Fulfillment of the  
Requirements for the Degree of  
Master of Science

Elizabeth A. Harpold, B.S.  
Captain, USAF

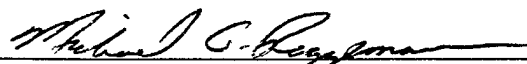
December, 1995

Approved for public release; distribution unlimited

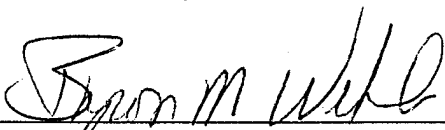
THE ROLE OF FRAME SELECTION AND BISPECTRUM  
PHASE RECONSTRUCTION FOR SPECKLE IMAGING  
THROUGH ATMOSPHERIC TURBULENCE

Elizabeth A. Harpold, B.S.  
Captain, USAF

Approved:

  
\_\_\_\_\_  
Michael C. Roggemann, Major, USAF  
Chairman, Advisory Committee

8 Nov 95

  
\_\_\_\_\_  
Byron M. Welsh  
Member, Advisory Committee

8 Nov 95

  
\_\_\_\_\_  
Theodore E. Luke  
Member, Advisory Committee

8 Nov 95

## *Acknowledgements*

I'd like to thank my faculty advisor, Major Michael C. Roggemann for his assistance and encouragement throughout this project. His enthusiasm and his keen interest in this subject area were constant sources of inspiration.

I'd also like to thank my thesis committee members, Dr. Byron M. Welsh, and Dr. Theodore E. Luke, for their many suggestions and comments, which greatly contributed to the quality of this thesis.

I'd like to thank my former organization, the Office of Aerospace Studies, for supporting my decision to pursue AFIT and particularly Lt Col Swehosky for his guidance and for giving me that initial nudge in the right direction.

I'd like to thank my fellow AFIT students. For always being there when I needed that extra insight, and for their sense of humor and *sillysophical* discussions which often brought things into perspective.

I'd like to thank my sister, Dana Byrd, PhD (candidate), for her humorous e-mail and late night talks which never failed to inspire and uplift me.

Finally, I'd like to thank my husband Brian Sholler for his unfaltering, loving support and encouragement throughout the many sacrifices in the name of AFIT, and my son Daniel for those warm hugs, kisses and smiles at the end of each day. Without their loving support, none of this would have been possible.

Elizabeth A. Harpold

## *Preface*

This thesis presents the results of an investigation into the feasibility of using frame selection and bispectrum phase reconstruction as a post-processing technique for Air Force speckle imaging systems. The key result is a frame selection and bispectrum phase reconstruction algorithm that can be immediately implemented at Air Force space surveillance sites to improve their mission effectiveness. I hope that this research effort will contribute to our nation's defense by enhancing the effectiveness of the Air Force's space surveillance capabilities. Furthermore, I hope that this thesis will inspire future AFIT students to pursue research in this challenging and vital area.

Elizabeth A. Harpold

## *Table of Contents*

	Page
Acknowledgements . . . . .	ii
Preface . . . . .	iii
List of Figures . . . . .	viii
List of Tables . . . . .	xiii
Abstract . . . . .	xiv
I. Introduction . . . . .	1-1
1.1 Motivation . . . . .	1-1
1.2 Problem Statement . . . . .	1-2
1.3 Approach . . . . .	1-3
1.4 Scope . . . . .	1-4
1.5 Chapter Outlines . . . . .	1-4
1.5.1 Chapter 2 . . . . .	1-4
1.5.2 Chapter 3 . . . . .	1-5
1.5.3 Chapter 4 . . . . .	1-5
1.5.4 Chapter 5 . . . . .	1-5
1.5.5 Appendix A . . . . .	1-5
1.5.6 Appendix B . . . . .	1-5
1.6 Summary of Key Results . . . . .	1-5
1.7 Conclusion . . . . .	1-5

	Page
II. Background . . . . .	2-1
2.1 Introduction . . . . .	2-1
2.2 Images and Objects . . . . .	2-1
2.3 Atmospheric Turbulence . . . . .	2-2
2.4 Speckle Interferometry . . . . .	2-2
2.4.1 Noise Bias Effects . . . . .	2-8
2.5 Bispectrum Calculations . . . . .	2-10
2.5.1 Bispectrum Definition . . . . .	2-10
2.5.2 Insensitivity to Tilt Error . . . . .	2-11
2.5.3 Noise Bias Effects . . . . .	2-12
2.5.4 Phase Error . . . . .	2-12
2.6 Frame Selection . . . . .	2-13
2.6.1 Frame Selection Rate (FSR) . . . . .	2-14
2.6.2 Signal-to-Noise Ratio (SNR) . . . . .	2-14
2.6.3 Quality Sharpness Metrics for Individual Frames	2-17
2.7 Independent Parameters . . . . .	2-20
2.7.1 Visual Magnitude . . . . .	2-20
2.7.2 Fried Seeing Parameter . . . . .	2-21
2.8 Recent Developments in Frame Selection . . . . .	2-22
2.9 Limits of Current Knowledge . . . . .	2-24
2.10 Summary . . . . .	2-24
III. Approach and Methodology . . . . .	3-1
3.1 Introduction . . . . .	3-1
3.2 Computer Simulation . . . . .	3-1
3.3 General Parameters . . . . .	3-2
3.3.1 Number of Short Exposure Images . . . . .	3-5
3.3.2 Quality Sharpness Metrics . . . . .	3-5

	Page
3.3.3	Frame Selection Rate (FSR) . . . . . 3-6
3.3.4	Visual Magnitude . . . . . 3-6
3.3.5	Fried Seeing Parameter . . . . . 3-6
3.4	Bispectrum Parameters . . . . . 3-7
3.4.1	Phase Spectrum Reconstruction . . . . . 3-7
3.5	Image Reconstruction . . . . . 3-8
3.6	Summary . . . . . 3-10
IV.	Results . . . . . 4-1
4.1	Introduction . . . . . 4-1
4.2	System Parameters . . . . . 4-1
4.3	Quality Metric Performance . . . . . 4-1
4.3.1	Point Source . . . . . 4-2
4.3.2	Extended source . . . . . 4-5
4.3.3	Conclusions . . . . . 4-5
4.4	Frame Selection Performance . . . . . 4-5
4.4.1	Point Source . . . . . 4-5
4.4.2	Extended source . . . . . 4-8
4.4.3	Conclusions . . . . . 4-8
4.5	Performance Under Various Seeing Conditions . . . . . 4-10
4.5.1	Point Source . . . . . 4-10
4.5.2	Extended Source . . . . . 4-11
4.5.3	Conclusions . . . . . 4-14
4.6	Performance Under Various Target Brightness Levels . . . . . 4-14
4.6.1	Point Source . . . . . 4-14
4.6.2	Extended Source . . . . . 4-14
4.6.3	Conclusions . . . . . 4-17
4.7	Image Reconstruction Results . . . . . 4-17

	Page
4.7.1 Conclusions . . . . .	4-17
4.8 Summary . . . . .	4-17
V. Conclusions and Recommendations . . . . .	5-1
5.1 Conclusions . . . . .	5-1
5.2 Recommendations for Further Research . . . . .	5-2
Appendix A. Simulation Results for Point Source . . . . .	A-1
A.1 Point Source Bispectrum Phase Error . . . . .	A-2
A.2 Point Source Power Spectrum SNR . . . . .	A-15
A.3 Point Source Power Spectrum Gain Plots . . . . .	A-28
A.4 Point Source Comparative Phase Error Difference Plots	A-41
Appendix B. Simulation Results for Extended Source . . . . .	B-1
B.1 Extended Source Bispectrum Phase Error . . . . .	B-2
B.2 Simulation Results for Extended Source . . . . .	B-15
B.3 Extended Source Power Spectrum Gain Plots . . . . .	B-28
B.4 Extended Source Comparative Phase Error Difference Plots . . . . .	B-41
Bibliography . . . . .	BIB-1
Vita . . . . .	VITA-1

## *List of Figures*

Figure	Page
2.1. Extended Source Images . . . . .	2-3
2.2. Block diagram of the speckle imaging technique . . . . .	2-5
2.3. Block diagram of the frame selection technique . . . . .	2-15
2.4. Example SNR plot illustrating the theoretical relationship of SNR to randomly selected data. $m_\nu = 1, r_0 = 12$ cm. . . . .	2-18
3.1. Block diagram of the speckle imaging computer simulation . . .	3-3
3.2. Reference star images at various Fried parameters . . . . .	3-9
4.1. Quality metric performance for a point source . . . . .	4-3
4.2. Quality metric performance for a point source . . . . .	4-4
4.3. Quality metric performance for an extended source . . . . .	4-6
4.4. Frame selection performance for a point source . . . . .	4-7
4.5. Frame selection performance for an extended source . . . . .	4-9
4.6. Seeing conditions for a point source . . . . .	4-12
4.7. Seeing conditions for an extended source . . . . .	4-13
4.8. Brightness levels for a point source . . . . .	4-15
4.9. Brightness levels for an extended source . . . . .	4-16
4.10. Reconstructed image of an extended source . . . . .	4-18
A.1. Bispectrum phase error, point source, $m_\nu = 1, r_0 = 7$ cm . . . .	A-3
A.2. Bispectrum phase error, point source, $m_\nu = 3, r_0 = 7$ cm . . . .	A-4
A.3. Bispectrum phase error, point source, $m_\nu = 5, r_0 = 7$ cm . . . .	A-5
A.4. Bispectrum phase error, point source, $m_\nu = 7, r_0 = 7$ cm . . . .	A-6
A.5. Bispectrum phase error, point source, $m_\nu = 1, r_0 = 12$ cm . . . .	A-7
A.6. Bispectrum phase error, point source, $m_\nu = 3, r_0 = 12$ cm . . . .	A-8

Figure	Page
A.7. Bispectrum phase error, point source, $m_\nu = 5, r_o = 12$ cm . . . .	A-9
A.8. Bispectrum phase error, point source, $m_\nu = 7, r_o = 12$ cm . . . .	A-10
A.9. Bispectrum phase error, point source, $m_\nu = 1, r_o = 17$ cm . . . .	A-11
A.10. Bispectrum phase error, point source, $m_\nu = 3, r_o = 17$ cm . . . .	A-12
A.11. Bispectrum phase error, point source, $m_\nu = 5, r_o = 17$ cm . . . .	A-13
A.12. Bispectrum phase error, point source, $m_\nu = 7, r_o = 17$ cm . . . .	A-14
A.13. Power spectrum SNR, point source, $m_\nu = 1, r_o = 7$ cm . . . . .	A-16
A.14. Power spectrum SNR, point source, $m_\nu = 3, r_o = 7$ cm . . . . .	A-17
A.15. Power spectrum SNR, point source, $m_\nu = 5, r_o = 7$ cm . . . . .	A-18
A.16. Power spectrum SNR, point source, $m_\nu = 7, r_o = 7$ cm . . . . .	A-19
A.17. Power spectrum SNR, point source, $m_\nu = 1, r_o = 12$ cm . . . . .	A-20
A.18. Power spectrum SNR, point source, $m_\nu = 3, r_o = 12$ cm . . . . .	A-21
A.19. Power spectrum SNR, point source, $m_\nu = 5, r_o = 12$ cm . . . . .	A-22
A.20. Power spectrum SNR, point source, $m_\nu = 7, r_o = 12$ cm . . . . .	A-23
A.21. Power spectrum SNR, point source, $m_\nu = 1, r_o = 17$ cm . . . . .	A-24
A.22. Power spectrum SNR, point source, $m_\nu = 3, r_o = 17$ cm . . . . .	A-25
A.23. Power spectrum SNR, point source, $m_\nu = 5, r_o = 17$ cm . . . . .	A-26
A.24. Power spectrum SNR, point source, $m_\nu = 7, r_o = 17$ cm . . . . .	A-27
A.25. Power spectrum gain, point source, $m_\nu = 1, r_o = 7$ cm . . . . .	A-29
A.26. Power spectrum gain, point source, $m_\nu = 3, r_o = 7$ cm . . . . .	A-30
A.27. Power spectrum gain, point source, $m_\nu = 5, r_o = 7$ cm . . . . .	A-31
A.28. Power spectrum gain, point source, $m_\nu = 7, r_o = 7$ cm . . . . .	A-32
A.29. Power spectrum gain, point source, $m_\nu = 1, r_o = 12$ cm . . . . .	A-33
A.30. Power spectrum gain, point source, $m_\nu = 3, r_o = 12$ cm . . . . .	A-34
A.31. Power spectrum gain, point source, $m_\nu = 5, r_o = 12$ cm . . . . .	A-35
A.32. Power spectrum gain, point source, $m_\nu = 7, r_o = 12$ cm . . . . .	A-36
A.33. Power spectrum gain, point source, $m_\nu = 1, r_o = 17$ cm . . . . .	A-37

Figure	Page
A.34. Power spectrum gain, point source, $m_\nu = 3$ , $r_o = 17$ cm . . . . .	A-38
A.35. Power spectrum gain, point source, $m_\nu = 5$ , $r_o = 17$ cm . . . . .	A-39
A.36. Power spectrum gain, point source, $m_\nu = 7$ , $r_o = 17$ cm . . . . .	A-40
A.37. Comparative phase error difference, point source, $m_\nu = 1$ , $r_o = 7$ cm . . . . .	A-42
A.38. Comparative phase error difference, point source, $m_\nu = 3$ , $r_o = 7$ cm . . . . .	A-43
A.39. Comparative phase error difference, point source, $m_\nu = 5$ , $r_o = 7$ cm . . . . .	A-44
A.40. Comparative phase error difference, point source, $m_\nu = 7$ , $r_o = 7$ cm . . . . .	A-45
A.41. Comparative phase error difference, point source, $m_\nu = 1$ , $r_o = 12$ cm . . . . .	A-46
A.42. Comparative phase error difference, point source, $m_\nu = 3$ , $r_o = 12$ cm . . . . .	A-47
A.43. Comparative phase error difference, point source, $m_\nu = 5$ , $r_o = 12$ cm . . . . .	A-48
A.44. Comparative phase error difference, point source, $m_\nu = 7$ , $r_o = 12$ cm . . . . .	A-49
A.45. Comparative phase error difference, point source, $m_\nu = 1$ , $r_o = 17$ cm . . . . .	A-50
A.46. Comparative phase error difference, point source, $m_\nu = 3$ , $r_o = 17$ cm . . . . .	A-51
A.47. Comparative phase error difference, point source, $m_\nu = 5$ , $r_o = 17$ cm . . . . .	A-52
A.48. Comparative phase error difference, point source, $m_\nu = 7$ , $r_o = 17$ cm . . . . .	A-53
B.1. Bispectrum phase error, extended source, $m_\nu = 1$ , $r_o = 7$ cm . .	B-3
B.2. Bispectrum phase error, extended source, $m_\nu = 3$ , $r_o = 7$ cm . .	B-4

Figure	Page
B.3. Bispectrum phase error, extended source, $m_\nu = 5, r_o = 7$ cm . .	B-5
B.4. Bispectrum phase error, extended source, $m_\nu = 7, r_o = 7$ cm . .	B-6
B.5. Bispectrum phase error, extended source, $m_\nu = 1, r_o = 12$ cm .	B-7
B.6. Bispectrum phase error, extended source, $m_\nu = 3, r_o = 12$ cm .	B-8
B.7. Bispectrum phase error, extended source, $m_\nu = 5, r_o = 12$ cm .	B-9
B.8. Bispectrum phase error, extended source, $m_\nu = 7, r_o = 12$ cm .	B-10
B.9. Bispectrum phase error, extended source, $m_\nu = 1, r_o = 17$ cm .	B-11
B.10. Bispectrum phase error, extended source, $m_\nu = 3, r_o = 17$ cm .	B-12
B.11. Bispectrum phase error, extended source, $m_\nu = 5, r_o = 17$ cm .	B-13
B.12. Bispectrum phase error, extended source, $m_\nu = 7, r_o = 17$ cm .	B-14
B.13. Power spectrum SNR, extended source, $m_\nu = 1, r_o = 7$ cm . . .	B-16
B.14. Power spectrum SNR, extended source, $m_\nu = 3, r_o = 7$ cm . . .	B-17
B.15. Power spectrum SNR, extended source, $m_\nu = 5, r_o = 7$ cm . . .	B-18
B.16. Power spectrum SNR, extended source, $m_\nu = 7, r_o = 7$ cm . . .	B-19
B.17. Power spectrum SNR, extended source, $m_\nu = 1, r_o = 12$ cm . .	B-20
B.18. Power spectrum SNR, extended source, $m_\nu = 3, r_o = 12$ cm . .	B-21
B.19. Power spectrum SNR, extended source, $m_\nu = 5, r_o = 12$ cm . .	B-22
B.20. Power spectrum SNR, extended source, $m_\nu = 7, r_o = 12$ cm . .	B-23
B.21. Power spectrum SNR, extended source, $m_\nu = 1, r_o = 17$ cm . .	B-24
B.22. Power spectrum SNR, extended source, $m_\nu = 3, r_o = 17$ cm . .	B-25
B.23. Power spectrum SNR, extended source, $m_\nu = 5, r_o = 17$ cm . .	B-26
B.24. Power spectrum SNR, extended source, $m_\nu = 7, r_o = 17$ cm . .	B-27
B.25. Power spectrum gain, extended source, $m_\nu = 1, r_o = 7$ cm . . .	B-29
B.26. Power spectrum gain, extended source, $m_\nu = 3, r_o = 7$ cm . . .	B-30
B.27. Power spectrum gain, extended source, $m_\nu = 5, r_o = 7$ cm . . .	B-31
B.28. Power spectrum gain, extended source, $m_\nu = 7, r_o = 7$ cm . . .	B-32
B.29. Power spectrum gain, extended source, $m_\nu = 1, r_o = 12$ cm . . .	B-33

Figure	Page
B.30. Power spectrum gain, extended source, $m_\nu = 3, r_0 = 12$ cm . . .	B-34
B.31. Power spectrum gain, extended source, $m_\nu = 5, r_0 = 12$ cm . . .	B-35
B.32. Power spectrum gain, extended source, $m_\nu = 7, r_0 = 12$ cm . . .	B-36
B.33. Power spectrum gain, extended source, $m_\nu = 1, r_0 = 17$ cm . . .	B-37
B.34. Power spectrum gain, extended source, $m_\nu = 3, r_0 = 17$ cm . . .	B-38
B.35. Power spectrum gain, extended source, $m_\nu = 5, r_0 = 17$ cm . . .	B-39
B.36. Power spectrum gain, extended source, $m_\nu = 7, r_0 = 17$ cm . . .	B-40
B.37. Comparative phase error difference, extended source, $m_\nu = 1, r_o = 7$ cm . . . . .	B-42
B.38. Comparative phase error difference, extended source, $m_\nu = 3, r_o = 7$ cm . . . . .	B-43
B.39. Comparative phase error difference, extended source, $m_\nu = 5, r_o = 7$ cm . . . . .	B-44
B.40. Comparative phase error difference, extended source, $m_\nu = 7, r_o = 7$ cm . . . . .	B-45
B.41. Comparative phase error difference, extended source, $m_\nu = 1, r_o = 12$ cm . . . . .	B-46
B.42. Comparative phase error difference, extended source, $m_\nu = 3, r_o = 12$ cm . . . . .	B-47
B.43. Comparative phase error difference, extended source, $m_\nu = 5, r_o = 12$ cm . . . . .	B-48
B.44. Comparative phase error difference, extended source, $m_\nu = 7, r_o = 12$ cm . . . . .	B-49
B.45. Comparative phase error difference, extended source, $m_\nu = 1, r_o = 17$ cm . . . . .	B-50
B.46. Comparative phase error difference, extended source, $m_\nu = 3, r_o = 17$ cm . . . . .	B-51
B.47. Comparative phase error difference, extended source, $m_\nu = 5, r_o = 17$ cm . . . . .	B-52
B.48. Comparative phase error difference, extended source, $m_\nu = 7, r_o = 17$ cm . . . . .	B-53

*List of Tables*

Table		Page
2.1.	Visual magnitude and photo events for common sky objects . .	2-21

*Abstract*

Frame selection using quality sharpness metrics have been shown in previous AFIT theses [25] [5], to be effective in improving the final product of images obtained using adaptive optics. This thesis extends this idea to *uncompensated* speckle image data. Speckle image reconstruction is simulated with and without frame selection. Speckle images require the processing of hundreds of data frames. Frame selection is a method of reducing the amount of data required to reconstruct the image without significant loss in quality. A collection of short exposure image data frames of a single object are obtained and sorted based on sharpness metrics. Only the highest quality frames are retained and processed to form the final image. The fraction of the frames that are retained for processing is user defined. The phase spectrum is reconstructed using the bispectrum technique. The benefits of frame selection for point (star) sources and extended (satellite) sources are examined by comparing composite image data with and without frame selection. The resulting power spectrum is evaluated through the SNR gain measurements, and the resulting phase spectrum is evaluated by measuring the phase error between the data from the composite image and the data from the true object. In both cases, the results show that frame selection does not improve the power or the phase spectrums. For point sources, results show frame selection causes slight decrease in performance. For extended sources, the change in performance is insignificant. However, frame selection does offer a means for data reduction without significantly reducing performance in a wide variety of target brightness levels and atmospheric turbulence conditions.

# THE ROLE OF FRAME SELECTION AND BISPECTRUM PHASE RECONSTRUCTION FOR SPECKLE IMAGING THROUGH ATMOSPHERIC TURBULENCE

## *I. Introduction*

### *1.1 Motivation*

The Air Force has a mission to monitor the status and orbit of all space objects. One means of accomplishing their mission is through the use of high resolution optical imagery obtained from ground-based observatories. All observations from ground based observatories are corrupted by atmospheric turbulence effects. The Air Force employs various methods for compensating for turbulence effects on imaging systems. Adaptive optics uses a wavefront sensor and a deformable mirror to help compensate for some of the atmospheric distortion. Conversely, speckle imaging is a post-processing technique which uses short exposure, *uncompensated* images. It is often observed that for any given set of short exposure images, there are some images that are simply better than others [4, 5, 7, 18, 22, 23, 25]. Frame selection is based on the characteristics of the individual short exposure image and its associated spectrum. It is a three-step process for choosing a subset of images for further processing.

1. Calculate a frame quality metric value for each frame in the data set.
2. Sort the images in the data set from highest to lowest based on the quality metric value.
3. Select the highest value images for processing.

Previous work at AFIT has shown that frame selection does indeed improve the quality of compensated space images [24]. During the summers of 1993 and 1994, Captains Craig Stoudt and Steve Ford demonstrated that frame-selection can improve the performance of adaptive optics imaging systems when turbulence conditions limit the image spectrum SNR, but not when measurement noise limits the image spectrum SNR [5, 25].

The primary goal of this research is to extend frame selection to speckle imaging. Bispectrum phase reconstruction is incorporated into a new atmospheric simulation technique developed at AFIT. The power spectrum SNR and phase spectrum error are analyzed to determine the effects of various target brightness levels and turbulence conditions on speckle imaging systems. The goal of frame selection research is to devise a method for sifting through large sets of image data frames and selecting the fewest number of the *best* frames that maintains or improves the quality of the final image. An effective implementation of frame selection depends on the size of the data base to be processed. For extremely large data bases, a computer frame selection algorithm containing a simple but effective quality metric, may be used to effectively reduce the amount of data. The selected subset may then be processed using a bispectrum phase reconstruction algorithm.

## 1.2 Problem Statement

This thesis examines the role of frame selection for *uncompensated* speckle images, and measures the performance of frame selection by using bispectrum phase reconstruction and phase error analysis.

For each case study, the following user parameters are varied:

- Sharpness metric
- Frame Selection Rate,

and the following environmental parameters are varied:

- $r_o$  (Fried seeing parameter [6])
- $m_\nu$  (Visual Magnitude, or brightness levels).

In comparing the cases, the results are in the form of

- SNR plots
- SNR Gain plots
- Phase Error Plots
- Comparative Phase Error Difference Plots
- Deconvolved Images

### *1.3 Approach*

This thesis addresses the problem by investigating frame selection performance under a variety of conditions. The power and phase spectrums of the reconstructed image are measured to determine relative performance with and without frame selection. To achieve these goals, the following steps are undertaken:

1. Modified existing code to account for photon shot and CCD read noise sources.
2. Modified code to include bispectrum phase reconstruction.
3. Developed a phase error metric for comparing performance.
4. Developed a matrix of computer runs to evaluate performance based on a set of key optical parameters.
5. Developed a computer program for analyzing the data.
6. Performed runs
7. Analyzed data
8. Drawn conclusions

This research effort relies on computer simulation. Michael C. Roggemann developed a simulation package known as HYBISPSIM which simulates imaging through turbulence and calculates statistical quantities used for speckle imaging [25]. Another Roggemann code, referred to as HYSIM, also simulates imaging through turbulence, but does not compute speckle imaging quantities. In a separate research effort, Captain Craig A. Stoudt modified HYSIM to incorporate statistical frame selection and a charge coupled device (CCD) camera model [25]. This modified code was renamed HYSIMS [25]. This thesis effort combines HYBISPSIM and HYSIMS and modifies HYSIMS to do speckle imaging. A second simulation program, called BIPHASE, is created from a series of FORTRAN routines, also provided by Roggemann, which reconstructs the phase from the bispectrum, measures the phase error, implements the pseudo-Weiner filter [21], and reconstructs the image.

#### *1.4 Scope*

The scope of this thesis is restricted to the following topics:

- Extend statistical frame selection work to speckle imaging
- Extend current AFIT simulation capabilities to include the bispectrum technique, which is insensitive to tilt error.
- Investigate alternate sharpness metrics for frame selection.

#### *1.5 Chapter Outlines*

The following is a brief synopsis of the information found in each chapter of the thesis.

*1.5.1 Chapter 2.* This chapter presents an overview of the problems associated with processing space image data, including atmospheric conditions and equipment limitations. It also introduces the concept of frame selection as a strategy for correcting for some of these adverse affects. Chapter 2 also details speckle

image processing, including the theory of speckle interferometry and bispectrum phase reconstruction.

*1.5.2 Chapter 3.* This chapter lays out the approach to simulating the frame selection process and the development of bispectrum experiments.

*1.5.3 Chapter 4.* This chapter presents the results of the series of frame selection case studies for point sources and extended sources.

*1.5.4 Chapter 5.* This chapter states the conclusions based upon the results presented in chapter 4. It also concludes with recommendations to the user concerning the implementation of frame selection as it applies to speckle image data and recommendations for further research.

*1.5.5 Appendix A.* This appendix contains plots of data obtained in the point source experiments.

*1.5.6 Appendix B.* This appendix contains plots of data obtained in the extended source experiments.

## *1.6 Summary of Key Results*

This investigation demonstrates that frame selection for point and extended sources, such as satellites, does not significantly improve nor degrade the power or phase spectrums of the reconstructed image. This thesis demonstrates that the primary benefit of frame selection to speckle imaging is data reduction. Data can be reduced by as much as 50% with no loss in image quality.

## *1.7 Conclusion*

Atmospheric turbulence is a major impediment to Air Force space surveillance. Frame selection, although incapable of fully compensating for these effects, offers

an effective strategy for reducing, at least by 50%, the data required in the post processing of speckle image data.

## II. Background

### 2.1 Introduction

This chapter provides the background necessary to understand some key elements of measuring and processing Air Force space surveillance and astronomical image data. The first section explains some of the terms associated with speckle imaging. Next, the problem of atmospheric turbulence and how it adversely affects the quality of these images is discussed. Then, a method for correcting for some of the turbulence effects is detailed in three parts. First, speckle interferometry, a method for obtaining the object power spectrum is explained. Then the bispectrum technique of phase reconstruction is discussed. Finally, frame selection, a method of selecting and discarding data from the detected image of the object is outlined. Together, all three elements provide an effective post-processing technique for improving the quality, speed, and efficiency of acquiring space surveillance and astronomical imagery. Finally, section 2.7 introduces the independent variables effecting target visibility.

### 2.2 Images and Objects

An image is the result of averaging multiple short exposures (frames) of the same object. The final product of averaging together short exposure images is referred to as a *long exposure* image. An object is the actual source being imaged, also referred to as the target. Two types of sources are point sources and extended sources. A point source is typically a very bright single star (or a laser glint off of an extended source), and is treated mathematically as a two-dimensional delta function. An extended source has structure beyond that of a delta function. Examples of extended sources are binary stars and satellites. Figure 2.1 show the extended object used in this thesis, along with the photon limited image before frame selection is

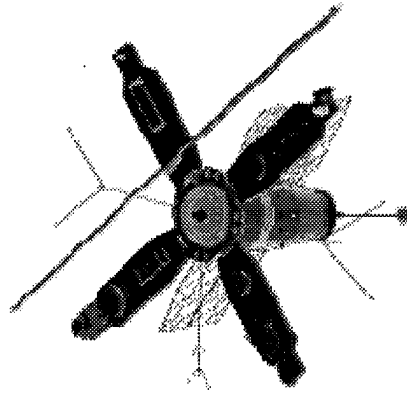
applied. Astronomical image data are essentially photographs of space objects such as stars and satellites. This thesis deals primarily with point sources and satellites.

### 2.3 Atmospheric Turbulence

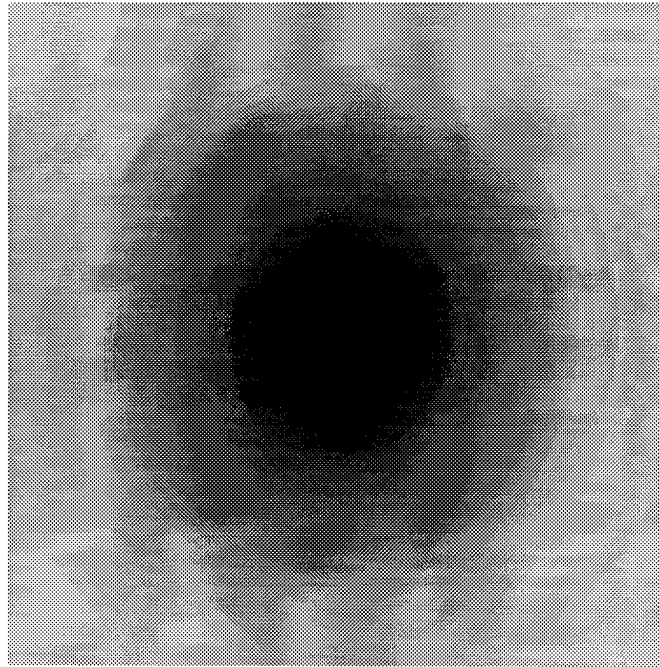
Atmospheric turbulence has been the greatest limiting factor for obtaining images of space objects since the invention of the telescope. Even Sir Isaac Newton (1730) complained of its effects [17]. With the invention of photographic film, one solution to the problem of seeing dim objects was to expose the film for a very long time and get a brighter picture than could otherwise be seen with the naked eye. But turbulence causes distortion in the images, as the image moves and changes shape during the long exposure. One solution to this would be to take a very short exposure and essentially *freeze* the turbulence and the motion of the object. The problem with short exposure images is that they are corrupted by high frequency modulation. Consequently, the image has a speckled appearance. This problem can be partially overcome by taking a series of many short exposure shots and averaging them together, thus smoothing out the speckles. These post processing techniques are now referred to as *speckle imaging*. Therefore, it would seem that more frames and less exposure time is the key to increasing the quality of the final image. However, exposure times are limited by detector sensitivity and brightness levels, typically several milliseconds. Therefore, further processing is required. Several post-processing techniques have been employed to further increase the final quality of the image. The technique investigated here is speckle interferometry using frame selection, combined with bispectrum phase reconstruction.

### 2.4 Speckle Interferometry

Speckle interferometry is a method of calculating the average power spectrum from a collection image data frames. It is a post-processing technique of combining a series of short exposure images and taking the average. Figure 2.2 illustrates the



(a)



(b)

Figure 2.1 Extended Source Images: a) original image before distortion. b) image as seen from a 1 meter telescope from 500 kilometers with seeing conditions of  $r_o=7$  cm and  $m_\nu=1$ , before frame selection.

flow process of converting detected speckle image data into the final estimate of the object [24]. First, image data from an unknown test object is collected along with reference data from a nearby bright star. A laser glint off of the object may function as the reference point source, if a suitably near and bright star is not available. The point source represents the point spread function (PSF) of the test object, and is characteristic only of the atmosphere and the optics. For this reason, it is used to calibrate for the effects of the optics and the atmospheric distortion. In the absence of the atmosphere and optics, the PSFs of point sources and an extended sources are pure delta functions. With an aberration free optical system, in the absence of atmosphere, the PSF is an Airy disc [24]. The size of the disk is inversely proportional to the size of the entrance pupil of the optics. By introducing the atmosphere, the PSF spreads even more. Aberrations associated with either the optical system, or the atmosphere, in the form of turbulence cause the PSF to become even more distorted. The first step in speckle interferometry is to compute the Fourier transform, or the *image spectrum*,  $I(\vec{f})$ , of each image,  $i(\vec{r})$ , in the data set. The spectrum has units of inverse length. The Fourier transform is a mathematical tool for converting an image to its spectrum, and is given by

$$I(\vec{f}) = \int i(\vec{r}) \exp\{-j2\pi\vec{f} \cdot \vec{r}\} d\vec{r}, \quad (2.1)$$

where  $\vec{r}$  is the spatial coordinate, and  $\vec{f}$  is the spatial frequency coordinate.

The inverse Fourier transform is a mathematical tool for converting an image spectrum back into an image. Its form is

$$i(\vec{r}) = \int I(\vec{f}) \exp\{j\pi\vec{f} \cdot \vec{r}\} d\vec{f}, \quad (2.2)$$

In their two dimensional formats,  $|\vec{r}(x, y)| = \sqrt{x^2 + y^2}$  and  $|\vec{f}(u, v)| = \sqrt{u^2 + v^2}$ . Capital letters, such as  $I(\vec{f})$  and  $O(\vec{f})$ , denote Fourier transforms of a function. These are referred to here as image and object *spectra*, respectively. The lower case

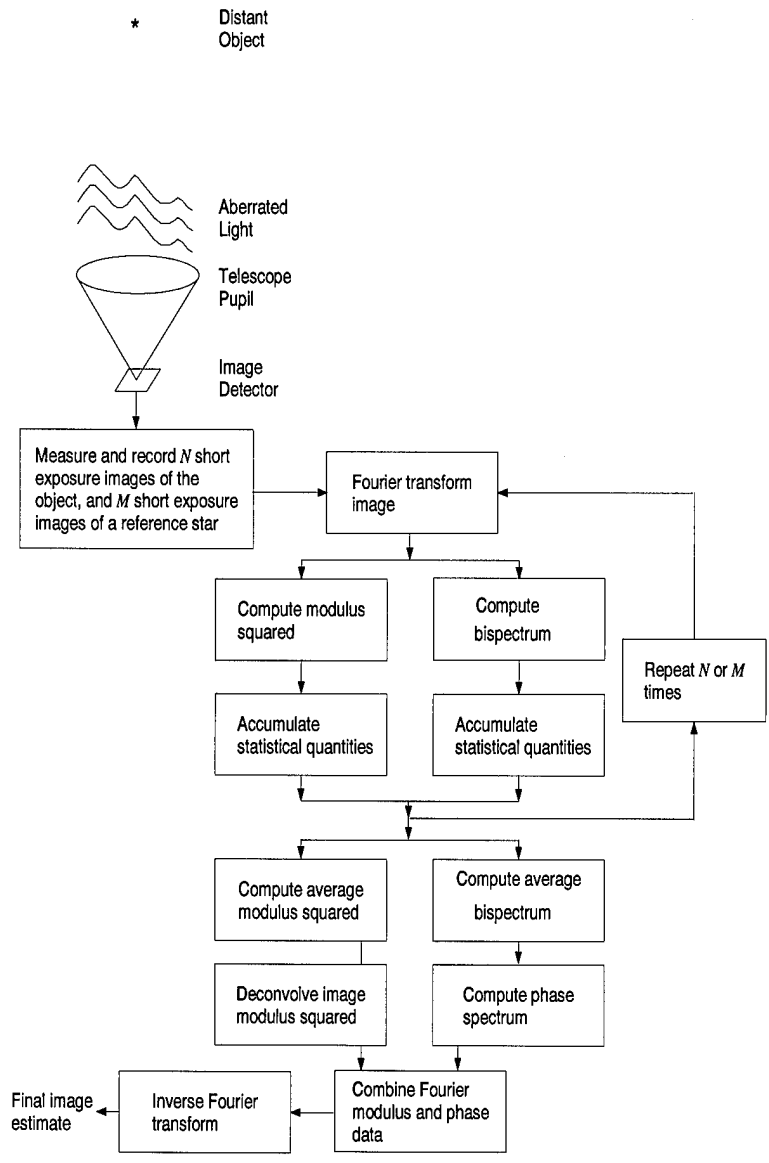


Figure 2.2 Block diagram of the speckle imaging technique

equivalents,  $i(\vec{r})$  and  $o(\vec{r})$ , refer to the image and object, respectively. The result of a Fourier transform is a complex-valued function:

$$I(\vec{f}) = |I(\vec{f})| \exp\{j\phi_i(\vec{f})\}. \quad (2.3)$$

The term,  $|I(\vec{f})|$ , in Eq. (2.3) is referred to as the *modulus* spectrum and  $\exp\{j\phi_i(\vec{f})\}$  is the *phase spectrum* of the image [24].

Next, the average modulus spectrum is estimated by computing the sample-based estimate of the average of the modulus squared of the spectra of the data frames. The notations used for the average modulus squared of the Fourier transform of the object and the reference star are, respectively,  $E\{|I(\vec{f})|^2\}$  and  $E\{|R(\vec{f})|^2\}$ , where  $E\{\cdot\}$  refers to the statistical *expectation* operator [24].

The image spectrum is related to the object spectrum,  $O(\vec{f})$  and the *optical transfer function* (OTF),  $\mathcal{H}(\vec{f})$  by

$$I(\vec{f}) = O(\vec{f})\mathcal{H}(\vec{f}), \quad (2.4)$$

where  $\mathcal{H}(\vec{f})$  is related to the pupil function by [9]

$$\mathcal{H}(\vec{f}) = \frac{\int \int_{-\infty}^{\infty} P(x + \frac{\lambda d_i f_x}{2}, y + \frac{\lambda d_i f_y}{2}) P(x - \frac{\lambda d_i f_x}{2}, y - \frac{\lambda d_i f_y}{2}) dx dy}{\int \int_{-\infty}^{\infty} P(x, y) dx dy}, \quad (2.5)$$

where  $d_i$  is the distance between the optic and the image plane, and  $f_x$  and  $f_y$  are the spatial frequencies in the  $x$  and  $y$  directions, respectively.

There is a limit to how much high frequency information from an object can be passed through an optical system. This limit is defined as the cutoff frequency,  $f_c$ .  $f_c$  is characteristic of equipment and atmospheric seeing conditions. Spatial frequency corresponds to the sharpness in detail of an image or object. For example, large flat surfaces exhibit low spatial frequencies, while ridges and sharp corners exhibit high

frequencies. The lower the  $f_c$ , the less detail an image will have.  $f_c$  defines the point in the spectrum where the OTF drops to zero. For this reason,  $f_c$  is also referred to as the OTF radius. The consequence of the frequency cutoff is that high spatial frequency information is lost. High spatial frequencies encode the fine details of an image. An image missing high frequency data of an object will appear whole but blurred. In other words, lower frequency cutoffs result in lower resolution.

The average modulus squared of the image spectrum,  $E\{|I(\vec{f})|^2\}$ , is computed in speckle imaging using

$$\begin{aligned} E\{|I(\vec{f})|^2\} &= E\{|O(\vec{f})\mathcal{H}(\vec{f})|^2\} \\ &= |O(\vec{f})|^2 E\{|\mathcal{H}(\vec{f})|^2\}. \end{aligned} \quad (2.6)$$

The term,  $|O(\vec{f})|^2$  can be pulled out of the expectation operator in Eq. (2.6), since the true object spectrum is assumed constant over the duration of the data collection. However, the OTF is random due to the random turbulence-induced fluctuations inherent in the OTF. Therefore the term,  $|\mathcal{H}(\vec{f})|^2$  must remain inside the expectation operator. A similar relationship holds for the reference star with one further simplification,  $|O(\vec{f})|^2 = C$ , a constant. For simplicity,  $C$  is set to unity in Eq. (2.7).

$$\begin{aligned} E\{|R(\vec{f})|^2\} &= E\{|O(\vec{f})\mathcal{H}(\vec{f})|^2\} \\ &= |O(\vec{f})|^2 E\{|\mathcal{H}(\vec{f})|^2\} \\ &= E\{|\mathcal{H}(\vec{f})|^2\} \end{aligned} \quad (2.7)$$

The next step is to remove the effects due to the average modulus squared of the OTF from the image power spectrum. This step is performed by using the

reference star data to obtain an estimate of  $|O(\vec{f})|^2$  using

$$\begin{aligned} \frac{E\{|I(\vec{f})|^2\}}{E\{|R(\vec{f})|^2\}} &= \frac{|O(\vec{f})|^2 E\{|\mathcal{H}(\vec{f})|^2\}}{E\{|\mathcal{H}(\vec{f})|^2\}} \\ &= |O(\vec{f})|^2. \end{aligned} \quad (2.8)$$

Eq. (2.8) provides the modulus of the object spectrum. This is the essence of Labeyrie's speckle interferometry technique [24]. In an operational setting, the power spectrum of the detected image is not proportional to  $|O(\vec{f})|^2$ , but rather has a bias associated with noise. The actual modulus can only be estimated from the detected image by accounting for these noise biases. Noise bias effects on the power spectrum are discussed in the next section.

*2.4.1 Noise Bias Effects.* Three sources of randomness are encountered in obtaining image data.

1. Turbulence
2. Photon noise
3. CCD read noise

Each of the above sources has a different statistical behavior and must be mathematically treated accordingly. Turbulence is governed by turbulence statistics, photon noise governed by Poisson statistics, and CCD read noise is governed by Gaussian statistics. Turbulence statistics are accounted for by using Labeyrie's technique described in the previous section. Photon noise, also referred to as shot noise, is associated with the random arrival times and locations of photo events on the image plan. When photon noise effects are included in Eq. (2.6) we find that  $E\{|I(\vec{f})|^2\}$  is not proportional to  $|O(\vec{f})|^2$ , but rather has a bias. The model for a detected image

corrupted with additive noise is given by [24]

$$d(\vec{r}) = \sum_{n=1}^K \delta(\vec{r} + \vec{r}_n) + \sum_{p=1}^P n_p \delta(\vec{r} + \vec{r}_p), \quad (2.9)$$

where the first term describes the photon-limited image, and the second term describes the additive noise. The location of the  $p^{th}$  pixel in the image is  $\vec{r}_p$ , and  $n_p$  is a random variable representing the amount of additive noise at the  $p^{th}$  pixel [24]. The bias associated with the additive noise is accounted for by simply subtracting the total number of photo events per image,  $K$  from the modulus squared of the spectrum of the detected image,  $|D(\vec{f})|^2$  resulting in [3].

$$Q(\vec{f}) = |D(\vec{f})|^2 - K, \quad (2.10)$$

where  $Q(\vec{f})$  is the unbiased estimation of the object spectrum.

CCD read noise is a source of noise which arises from the readout electronics in a CCD detector. The total number of pixels in the image is  $P$ . CCD noise is accounted for by subtracting  $P\sigma^2$  from the unbiased estimator, where  $\sigma^2$  is the standard deviation of the additive noise expressed in photo elections per pixel [25]. The equation for  $Q(\vec{f})$  becomes

$$Q(\vec{f}) = |D(\vec{f})|^2 - K - P\sigma^2. \quad (2.11)$$

The pseudo-Wiener Filter [24] is an additional step in the post-process of speckle image data which corrects for turbulence, equipment aberration, and filters out some of the high frequency noise. It is given by

$$|O(\vec{f})|^2 = \frac{Q_{obj}(\vec{f})}{Q_{ref}(\vec{f}) + \alpha/SNR_Q(\vec{f})}. \quad (2.12)$$

The term  $Q_{ref}(\vec{f})$  is data from a reference star and is representative of the PSF. The term,  $\alpha/SNR_Q(\vec{f})$  reduces high frequency noise. SNR is the signal-to-noise ratio, described later in section 2.6.2. The variable,  $\alpha$  can be adjusted until the desired filtering effect is achieved.

The limitations to this technique are that the phase of the Fourier transform is still required to create an estimate of the object. A phase estimator method such as the bispectrum technique, must be employed to estimate the phase of the Fourier transform of  $o(\vec{r})$ .

## 2.5 Bispectrum Calculations

Since speckle interferometry provides only the modulus of the object spectrum,  $|O(\vec{f})|$ , bispectrum phase reconstruction, reconstructs the phase spectrum of the object,  $\phi_o(\vec{f})$ , [24]. The bispectrum is a specialized moment of the image spectrum which contains high spatial frequency phase information.

*2.5.1 Bispectrum Definition.* The bispectrum of an image is defined as [13]

$$B(\vec{f}_1, \vec{f}_2) = I(\vec{f}_1)I(\vec{f}_2)I^*(\vec{f}_1 + \vec{f}_2), \quad (2.13)$$

where  $\vec{f}_1$  and  $\vec{f}_2$  are any two points in the image spectrum. The phase of the bispectrum encodes the phase of the object as point-to-point phase differences [24]. The object phase spectrum,  $\phi_o(\vec{f})$ , is obtained from sample based estimates of the bispectrum. Note, that since  $\vec{f}_1$  and  $\vec{f}_2$  are functions of spatial  $x$  and  $y$  coordinates, the bispectrum is a four dimensional data object. Hermite symmetry of the image spectrum results in an eight-fold bispectrum symmetry expressed by [13]

$$B(\vec{f}_1, \vec{f}_2) = B(\vec{f}_2, \vec{f}_1) = B(\vec{f}_1 - \vec{f}_2, \vec{f}_2) = B^*(-\vec{f}_1, -\vec{f}_2). \quad (2.14)$$

The object phase spectrum is encoded in the phases of the bispectrum according to the following relationship [24]:

$$\begin{aligned}
B(\vec{f}_1, \vec{f}_2) &= |O(\vec{f}_1)||O(\vec{f}_2)||O(\vec{f}_1 + \vec{f}_2)| \\
&\quad \times |\mathcal{H}(\vec{f}_1)||\mathcal{H}(\vec{f}_2)||\mathcal{H}(\vec{f}_1 + \vec{f}_2)| \\
&\quad \times \exp\{j[\phi_o(\vec{f}_1) + \phi_o(\vec{f}_2) - \phi_o(\vec{f}_1 + \vec{f}_2) + \phi_{\mathcal{H}}(\vec{f}_1) \\
&\quad + \phi_{\mathcal{H}}(\vec{f}_2) - \phi_{\mathcal{H}}(\vec{f}_1 + \vec{f}_2)]\}, \tag{2.15}
\end{aligned}$$

where the  $\exp\{j[\phi_o(\vec{f}_1) + \phi_o(\vec{f}_2) - \phi_o(\vec{f}_1 + \vec{f}_2)]\}$  terms contain the encoded object phase spectrum [24]. Any corruption in the phase spectrum by the random phase spectrum of the OTF is overcome by taking the average of several data points. The object spectrum is then related to the expected value of the bispectrum by [24]

$$E\{B(\vec{f}_1, \vec{f}_2)\} = O(\vec{f}_1)O(\vec{f}_2)O^*(\vec{f}_1 + \vec{f}_2)E\{\mathcal{H}(\vec{f}_1)\mathcal{H}(\vec{f}_2)\mathcal{H}^*(\vec{f}_1 + \vec{f}_2)\}, \tag{2.16}$$

where the phase of  $E\{\mathcal{H}(\vec{f}_1)\mathcal{H}(\vec{f}_2)\mathcal{H}^*(\vec{f}_1 + \vec{f}_2)\}$  is zero.

The symmetric nature of the bispectrum helps reduce the required number of calculations. Roggemann points out the importance of reducing the size of the bispectrum data object [24]. After considering all the possible combinations of  $\vec{f}_1$  and  $\vec{f}_2$  and the eight-fold symmetry of the bispectrum, a  $128 \times 128$  pixel image results in  $128^2 \times (128^2 - 1)/8 = 33,032,192$  calculations. One solution is to constrain the range of values  $(\vec{f}_1 + \vec{f}_2)$  are allowed to take [24]. This also argues a case for the benefits of frame selection as a means to data reduction.

*2.5.2 Insensitivity to Tilt Error.* The bispectrum technique has an advantage over an alternate phase estimation technique, known as the Knox-Thompson cross spectrum technique [26], in that the bispectrum is insensitive to random motion of the image centroid [24]. The necessity to correct for tilt by recentering all the images is eliminated. Any tilt errors, or linear shifts in the centroid appear as linear

phase shifts in the spectrum. For example, if a shift in the image is represented by  $i(\vec{r} + \Delta\vec{r})$ , the spectrum becomes  $\exp\{-j2\pi\vec{f} \cdot \Delta\vec{r}\}I(\vec{f})$ . The bispectrum of the shifted image is given by [24]

$$\begin{aligned} B_s(\vec{f}_1, \vec{f}_2) &= I(\vec{f}_1)I(\vec{f}_2)I^*(\vec{f}_1 + \vec{f}_2) \\ &\quad \times \exp\{-j2\pi[\vec{f}_1 \cdot \Delta\vec{r} + \vec{f}_2 \cdot \Delta\vec{r} - (\vec{f}_1 + \vec{f}_2) \cdot \Delta\vec{r}]\} \\ &= B(\vec{f}_1, \vec{f}_2). \end{aligned} \quad (2.17)$$

Therefore, the bispectrum of the shifted image is equivalent to the bispectrum of the unshifted image.

*2.5.3 Noise Bias Effects.* The unbiased estimator for the bispectrum is obtained from the spectrum of the detected image,  $D(\vec{f})$ , and is corrected for additive noise effects. Its equation is given by [24]

$$\begin{aligned} B_U(\vec{f}_1, \vec{f}_2) &= D(\vec{f}_1)D(\vec{f}_2)D^*(\vec{f}_1 + \vec{f}_2) - |D(\vec{f}_1)|^2 \\ &\quad - |D(\vec{f}_2)|^2 - |D(\vec{f}_1 + \vec{f}_2)|^2 + 2K + 3P\sigma^2, \end{aligned} \quad (2.18)$$

where  $K$ ,  $P$ , and  $\sigma$  are as defined in section 2.4.1.

*2.5.4 Phase Error.* The estimated phase spectrum,  $\phi_o(\vec{f})$ , is derived from the bispectrum. The specific method of reconstructing the phase spectrum of the object from the bispectrum is detailed in section 3.4.1. As a measure of performance,  $\phi_o(\vec{f})$  is compared to the actual phase spectrum,  $\phi_o(\vec{f})$ , of the true object in Fig. 2.1 by

$$\phi_e(\vec{f})^2 = (\phi_o(\vec{f}) - \phi_o(\vec{f}))^2, \quad (2.19)$$

where  $\phi_e(\vec{f})^2$  is the phase error in units of radians squared. The phase spectrum is then combined with the power spectrum and inverse Fourier transformed into the image.

The relative phase error performance of a case with frame selection is compared to that without by

$$\phi_{\Delta}(\vec{f}) = \phi_{\epsilon}(\vec{f})_{100\%}^2 - \phi_{\epsilon}(\vec{f})_{FS}^2, \quad (2.20)$$

where  $\phi_{\epsilon}(\vec{f})_{100\%}$  represents the phase error of the 100% case, and  $\phi_{\epsilon}(\vec{f})_{FS}$  represents a frame selected case. Areas in the spectrum where performance is improved as a result of frame selection, will have positive  $\phi_{\Delta}$  values. Conversely, where the performance declines as a result of frame selection,  $\phi_{\Delta}$  values are negative.

## 2.6 Frame Selection

This section discusses the frame selection process. It is often observed that for any given set of image data, there are some images that are simply better than others [4, 5, 7, 18, 22, 23, 25]. The goal of frame selection is to devise a method for sifting through large sets of image data frames and selecting the fewest number of the *best* frames that maintains or improves the quality of the final image. Frame selection is a three-step process for choosing a subset of images for further processing.

1. Calculate a frame quality metric value for each frame in the data set.
2. Sort the images in the data set from highest to lowest based on the quality metric value.
3. Select the highest value images for processing.

Captains Craig Stoudt and Steve Ford have done extensive research in the areas of frame selection combined with adaptive optics [5, 25]. They found that under favorable brightness levels, frame selection *improves* adaptive optic performance.

An effective implementation of frame selection depends on the size of the data base to be processed. For extremely large data bases, a computer frame selection algorithm containing a simple but effective quality metric, may be used to effectively reduce the amount of data. The selected subset may then be processed using a bispectrum phase reconstruction algorithm.

The basis of frame selection is to choose the best quality or highest resolution frames for averaging such that

$$I_S(\vec{f}) = \frac{1}{M} \sum_{i=1}^M I_i(\vec{f}), \quad (2.21)$$

where  $I_S(\vec{f})$  is the average image frequency spectrum due to frame selection,  $I_i(\vec{f})$  is the image frequency spectrum of an individual frame in the frame selection subset,  $M$  is the number of frames in the selected subset, and  $\vec{f}$  is a spatial frequency [5]. Figure 2.3 provides a block diagram of the process associated with Eq. (2.21) [23].  $N$  images are collected and Fourier transformed. The images are then sequentially rank-ordered from 0 to 1, according to a quality metric determination and the total number of frames. The best image is assigned the number 1, while the worst image receives 0. The images that are above a user defined cutoff (between 0 and 1) are maintained for further processing and those below are discarded. The user defines the cutoff through the frame selection rate (FSR). This is discussed in the next section.

*2.6.1 Frame Selection Rate (FSR).* The frame selection rate, FSR, is the ratio of the number of frames  $M$  in the selected subset to the number of frames  $N$  in the original ensemble. Therefore,

$$FSR = \frac{M}{N}, \quad M < N. \quad (2.22)$$

The FSR is a percentage value. An FSR of 70% means the selected subset consists of the *best* 70% of the frames from the original data set based on the frame quality metric values [5]. In the rank order system, all frames ranked below  $(1-FSR)$ —in the 70% case, 0.299 and below—are discarded.

*2.6.2 Signal-to-Noise Ratio (SNR).* As an aid to the user, a metric for judging the quality of the power spectrum estimate, the signal-to-noise ratio (SNR),

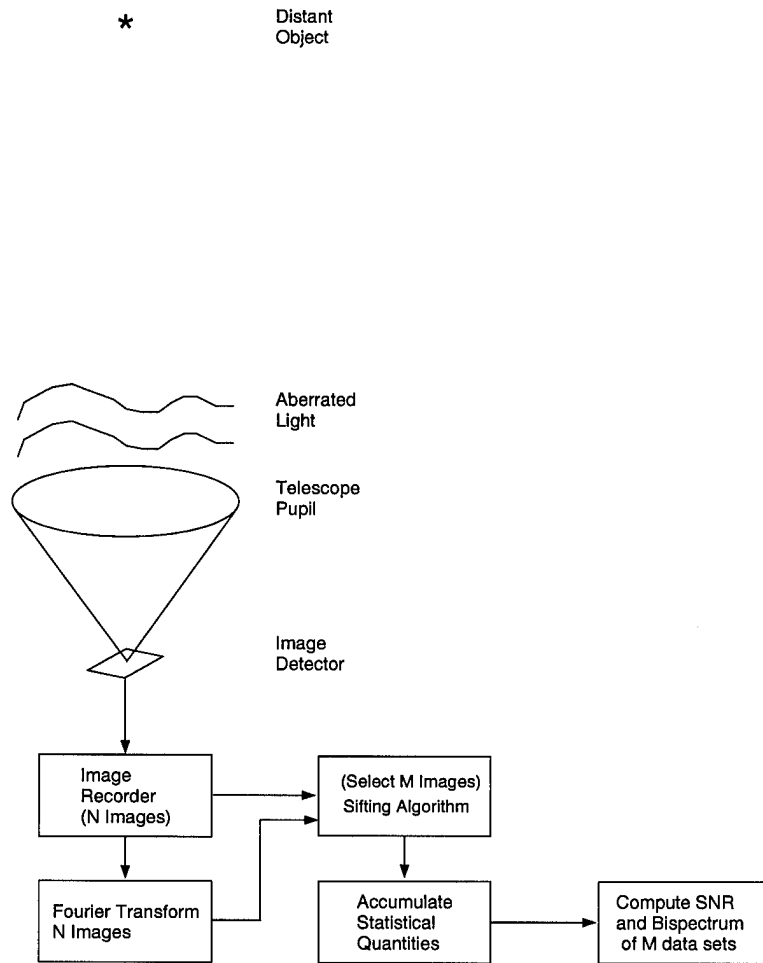


Figure 2.3 Block diagram of the frame selection technique

is calculated to compare the image quality of the total set versus the selected subset [5]. The SNR of the image spectrum is defined by

$$SNR_Q(\vec{f}) = \frac{E\{Q(\vec{f})\}}{\text{var}\{Q(\vec{f})\}^{1/2}} \quad (2.23)$$

The SNR of a frame selected case is compared to that of the 100% (without frame selection) case by

$$SNR_{gain} = \frac{SNR_{FS}}{SNR_{100\%}}, \quad (2.24)$$

where  $SNR_{gain}$  is the SNR gained as a result of frame selection,  $SNR_{FS}$  is the SNR resulting from frame selection, and  $SNR_{100\%}$  is the SNR resulting from not using frame selection. Areas in the spectrum where performance is improved as a result of frame selection, will have  $SNR_{gain}$  values greater than 1. Conversely, where the performance declines as a result of frame selection, the  $SNR_{gain}$  values less than 1.

One unavoidable consequence of frame selection is that it changes the statistics of the data set. Frame selection has been shown to increase the total SNR in some, but not all circumstances [5, 25]. This is because, although frame selection is designed to improve the data set by discarding the worst frames, there comes a point when throwing out more *bad* data means throwing out valuable information as well. This introduces an important limitation explained by the statistical nature of noise reduction through averaging [2]. The SNR of a set,  $SNR_{total}$ , containing  $N$  data points has been shown to increase by a factor  $\sqrt{N}$  over that of a single data point [2]. The average SNR of a data set,  $SNR_{avg(total)}$ , is representative of a single data point. This relationship is given by

$$SNR_{total} = \sqrt{N}SNR_{avg(total)} \quad (2.25)$$

In the case of frame selection, where  $M$  frames are retained,  $M < N$ , the SNR becomes

$$SNR_{subset} = \sqrt{M} SNR_{avg(subset)} \quad (2.26)$$

Therefore, in order for image quality to benefit from frame selection, the SNR of the subset must improve by at least a factor of  $\sqrt{\frac{N}{M}}$ . However, if the primary goal in frame selection is to reduce data, the total SNR may be allowed to decrease slightly. After all, the ultimate test of image quality is by visual inspection. Slight changes in SNR are often unnoticeable to the human eye. In this situation, the  $\sqrt{\frac{N}{M}}$  restriction may be relaxed to a user defined tolerance level.  $\sqrt{\frac{M}{N}}$  is the *minimum* SNR reduction, for frame selection to be more effective than selecting the frames at random, or just simply collecting a smaller set of image data in the first place. Fig. 2.4 is a typical SNR plot of a point source showing the resulting SNR plots of data that has been randomly selected without the benefit of a sharpness metric. It shows that the gradual reduction in the SNR as the number of randomly selected data is reduced.

The limitation to the SNR metric, is that it measures the composite image based only on the power spectrum. An additional metric is required to measure the composite image based on the phase spectrum. This is the phase error metric, discussed in section 2.5.4.

There are several methods available for sifting through large amounts of data for frame selection. One can computerize the process, after obtaining an effective quality metric. The next section discusses some specific quality metrics.

*2.6.3 Quality Sharpness Metrics for Individual Frames.* A quality metric is an algorithm which results in a single numerical value when applied to an image. The magnitude of a quality metric is directly related to a designated quality or feature of the image,  $i(\vec{r})$ , obtained in Eq. (2.2). These metrics are known to take their maximum value for a diffraction limited image. The quality metrics used in

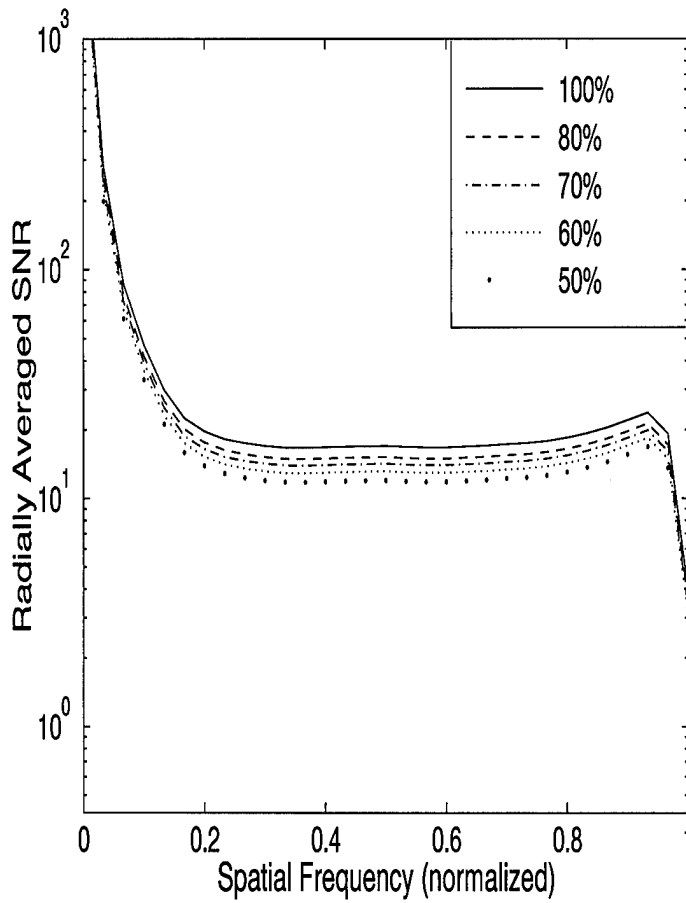


Figure 2.4 Example SNR plot illustrating the theoretical relationship of SNR to randomly selected data.  $m_\nu = 1$ ,  $r_0 = 12$  cm.

this thesis are derived from Muller and Buffington's eight sharpness functions. The complete list and a brief discussion is given below:

$$S_1 = \int \int i^2(\vec{r}) d\vec{r} \quad (2.27)$$

$$S_2 = i(0, 0) \quad (2.28)$$

$$S_3 = \int \int m(\vec{r})i(\vec{r}) d\vec{r} \quad (2.29)$$

$$S_4 = \int \int \left| \frac{\partial^{m+n} i(\vec{r})}{\partial x^m \partial y^n} \right|^2 d\vec{r} \quad (2.30)$$

$$S_5 = \int \int i^n(\vec{r}) d\vec{r} \quad (2.31)$$

$$S_6 = - \int \int i(\vec{r})r^2 d\vec{r}, \quad (2.32)$$

$$S_7 = - \int \int \ln[i(\vec{r})]i(\vec{r}) d\vec{r} \quad (2.33)$$

$$S_8 = - \int \int |i(\vec{r}) - o(\vec{r})|^2 d\vec{r}. \quad (2.34)$$

$S_1$  is the maximum structural content metric.  $m(\vec{r})$  is known as the mask function. If  $m(\vec{r})$  is a good replica of the undistorted image,  $S_3$ , Eq. (2.29), is a good sharpness definition which reduces to  $S_1$ , Eq. (2.27) when distortion is removed [16].  $S_2$  works well only for bright objects.  $S_4$  is the total differential metric.  $S_7$  is known as the maximum entropy metric.  $S_8$  is the fidelity defect function, which requires prior

knowledge of the object,  $o(\vec{r})$ .  $S_8$  is only useful in an experimental setting as a comparison check for judging the performance of other metrics. These metrics reach maximum values for unaberrated images [16]. In the form of computer algorithms, along with the associated maximum values, these metrics are tools for comparing the results of test data and assigning numerical values for determining the *relative* quality of an image within a given set of image frames. The actual metrics used in this thesis are discussed in section 3.3.2. The next section discusses parameters that may vary the overall quality of speckle images.

## 2.7 Independent Parameters

In this section, two key independent parameters in speckle imaging, target brightness levels and turbulence are discussed. These are referred to as visual magnitude and Fried's parameter of seeing conditions, respectively.

*2.7.1 Visual Magnitude.* Visual magnitude,  $m_v$ , is a system employed by astronomers to describe the relative brightness of objects in a night sky [25]. The average number of photons,  $K$ , is calculated based on this number, which is dependent on the rate of incident photons per unit area, or photon flux,  $P$ ; the total area, or the telescope pupil size,  $A_{pup}$ ; and the integration time of the processor,  $\tau$ .

Terry Gray of the Phillips Laboratory, Kirtland AFB, NM, wrote a program called VMAG for producing values for  $P$  based on a given target wavelength, bandwidth, and telescope transmission factor [10]. These values are for a standard atmospheric transmission factor,  $\kappa$  of 1. Therefore, the simulation must account for less than perfect atmospheric conditions, by including  $\kappa$  in the equation as follows:

$$K = (A_{pup})(P)(\tau)(\kappa) \quad (2.35)$$

Table 2.1 lists visual magnitudes and corresponding photon intensities of typical night time objects for a 1 meter aperture,  $\tau$  of 1.8 ms, and a wavelength of 500 nm

Table 2.1 Visual magnitude and photo events for common sky objects

OBJECT	$m_v$	$K$
Sun	-26.7	1.3 $10^{10}$
Full Moon	-12.5	4.7 $10^8$
Venus	-4.4	2.35 $10^7$
Jupiter	-2.5	4.11 $10^6$
Sirius	-1.5	1.59 $10^6$
Artificial Satellite ( <i>typical</i> )	-0.96	1.00 $10^6$
Polaris	+2.2	5.54 $10^4$

with a 10% bandwidth [5]. Note that the objects get brighter as  $m_v$  decreases in value.

*2.7.2 Fried Seeing Parameter.* As ground-based astronomical telescopes become increasingly larger and the optics become more powerful and less flawed, the ability to resolve distant images, such as satellites, stars, and neighboring galaxies, becomes limited not by diffraction nor aberration due to the optics, but by atmospheric distortion, due to turbulence [16]. The Fried's seeing parameter  $r_o$ , is a mathematical measure of this limit. For a given atmospheric condition,  $r_o$ , the atmospheric coherence diameter, is a figure of merit for the ability to resolve images through it. For large telescopes this limits the resolution to that obtainable by a telescope of diameter  $r_o$  [22]. The probability of obtaining diffraction limited images is exponentially dependent on the ratio squared of the pupil diameter,  $D$ , divided by  $r_o$ , as shown by

$$P_r \simeq 5.6e^{-0.1557(D/r_o)^2}. \quad (2.36)$$

As the diameter of the optic becomes much greater than the seeing parameter then the image is said to be limited by atmospheric distortion. If  $D \ll r_o$ ,  $f_c = D/\lambda d_i$ , If  $D \gg r_o$ ,  $f_c = r_o/\lambda d_i$ , where  $D$  is the telescope diameter,  $f_c$  is the OTF radius, discussed in section 2.4,  $\lambda$  is the mean wavelength of the detected image, and  $d_i$  is the distance between the aperture and the image plane. Typical values of  $r_o$  at good

observatories is approximately 10-30 cm [24], at visible wavelengths. The current state-of-the-art technology far surpasses this in the ability to create optical systems. But the Air Force's desire to have close up views of every satellite in orbit would require far more resources than is currently feasible. Therefore, an alternate solution to this problem is to compensate for turbulent distortion through adaptive optics or to deconvolve the images through the use of Fourier optics, in particular, speckle interferometry, combined with a systematic process of frame-selection. The next section discusses some recent AFIT accomplishments in the application of frame selection to adaptive optics.

### *2.8 Recent Developments in Frame Selection*

In 1993, Craig Stoudt, an AFIT graduate student, investigated the performance of frame selection by simulating a 1 meter fully compensated adaptive optics telescope [25]. He evaluated three of Muller and Buffington's original quality metrics,  $S_1$ ,  $S_4$ , and  $S_8$ , as well as a new metric  $S_{S1}$  defined as

$$S_{S1} = \int \int S_{OTF}(\vec{f}) |I(\vec{f})|^2 d\vec{f} \quad (2.37)$$

where  $S_{OTF}(\vec{f})$  is the support of the OTF. Since anything out side of the OTF radius is pure noise, this term defines limits to the integration so that everything outside the radius is ignored. Stoudt's use of computer simulation allowed a much broader examination of the effects of key independent parameters than those conducted by earlier researchers. Image spectrum SNR was used as the primary performance measure. He showed that

1. Frame selection rates of 60-70% improves the image spectrum SNR by ten to fifteen percent at mid spatial frequencies for both point and extended sources.
2. Lower selection rates (10-20%) result in sharper but noisier images.

3. For equivalent seeing conditions and light levels, frame selection is of greater benefit to point sources than extended objects.
4. Frame selection effectively corrects for poor seeing conditions, but is not as effective in correcting for photon noise and CCD camera noise.
5. The  $S_{S1}$  quality metric produced the highest overall image spectrum SNR gain compared to the other metrics.

In 1994, Steve Ford, also an AFIT graduate student, demonstrated frame selection on actual Air Force Maui Optical Site (AMOS) imagery. He has shown that:

1. Frame selection provides improved image spectrum SNR by discarding the worst manifestations of atmospheric turbulence. This results in reduced image spectrum variance and higher SNR.
2. For point source objects, the minimum visual magnitude for SNR gain due to frame selection was  $m_\nu = +7 - 8$  depending on the adaptive optics (AO) system modeled. An example extended object, a satellite model, required a much brighter minimum visual magnitude of  $m_\nu = +4$ . In general, average seeing conditions, represented by  $r_0 = 10$  centimeters, benefited the most from frame selection processing. This increased SNR gain is due, in part, to larger OTF variance for average seeing conditions when compared to poor or very good conditions.
3. CCD camera noise effects play a significant role in establishing frame selection performance limits.
4. When objects are sufficiently dim, photon and CCD camera noise effects dominate the single frame SNR expression. All available frames in the data set are needed to reduce this effect through averaging. Therefore, frame selection cannot provide image improvement.
5. Point spread functions (PSFs) are nearly identical for point source and extended objects after frame selection processing. This fact allows the optimal

use of deconvolution techniques, such as inverse and Weiner filters, to sharpen images after frame selection.

6. Short exposure times are necessary to get the full, predictable benefits of frame selection processing on real imagery. Improvements in SNR gain were demonstrated for reference star and satellite objects collected by the AMOS facility. Experiments using this data were not readily repeatable due to the 60-99 millisecond exposure times used for image collection.

### *2.9 Limits of Current Knowledge*

The Air Force uses adaptive optics (AO), to compensate for the random phase aberrations due to atmospheric turbulence. Unfortunately, AO cannot completely compensate for all phase fluctuations due to the atmosphere [27]. Therefore, some form of post-detection processing is needed. Recent research at the Air Force Institute of Technology (AFIT) has shown that images from AO systems can be improved using frame selection [25, 5]. However, in many situations adaptive optics are cost prohibitive. Therefore, an effective speckle imaging technique using frame selection is desirable. In the past, researchers have improved images from passive optics systems using frame selection [4, 7, 18]. However, so far, nothing is known about frame selection as it applies to speckle imaging.

### *2.10 Summary*

This chapter laid the foundation for understanding the problem of processing Air Force space surveillance and astronomical image data. Atmospheric turbulence imposes a fundamental limit on optical system performance. Speckle imaging techniques enhance image quality to some degree, but requires the post-detection processing of several hundred image data frames to create a single object. Frame selection is a promising post-detection processing technique that offers dramatic reduction in data without significant loss in image spectrum SNR, or increase in bispectrum

phase error. A complete investigation of frame selection performance over a substantial range of performance conditions and object brightness levels is presented in this thesis. This effort includes demonstrating the quality of images after frame selection and sharpening with deconvolution techniques. This chapter provided the basic terminology used in frame selection, speckle imaging and the bispectrum technique. It outlined the performance metrics, SNR and bispectrum phase error, used to evaluate the quality of composite images, and defined the independent parameters that are varied in the experiments. The methodology for conducting this investigation is developed in the next chapter.

### III. Approach and Methodology

#### 3.1 Introduction

Chapter two provided a brief overview of the atmospheric imaging problem and several possible solutions. A methodology for studying the performance of frame selection and bispectrum phase reconstruction, as they pertain to *uncompensated* speckle images, is developed in this chapter. Section 3.2 outlines the steps in the computer simulation for both frame selection and bispectrum phase reconstruction. Section 3.3 identifies the independent variables used in these experiments, including the various metrics employed and the justification for the use of the  $S_{S1}$  frame quality metric.

#### 3.2 Computer Simulation

Computer simulation is a critical tool for simulating speckle imaging, studying the performance of frame selection, and investigating the bispectrum technique. The user input data file allows convenient manipulation of key independent parameters. The simulation provides useful image spectrum statistics, such as the image spectrum SNR, and bispectrum phase error, which are measures of performance. The imaging and frame selection code used in this thesis was developed by Michael Roggemann [20] and further modified by Craig Stoudt [25]. The bispectrum code was also developed by Michael Roggemann [20].

Fig 3.1 is a block diagram of the computer simulation of the speckle imaging process. First, the parameters are read into the program by a user generated data file. Next, the object,  $o(\vec{r})$ , is created, scaled, and Fourier transformed into the spectrum,  $O(\vec{f})$ . For purposes of this investigation—simulating speckle imaging, under ideal equipment conditions—adaptive optics was turned off and the CCD read noise was set to zero. A series of short exposure images are created by a five step process:

- A random phase screen modeling atmospheric turbulence is created.
- The pupil is imposed to create the diffraction effects.
- The OTF, or  $\mathcal{H}(\vec{f})$  is calculated.
- The image spectrum,  $I(\vec{f})$ , is computed by multiplying the OTF with the object spectrum, and a photon-limited image,  $i(\vec{r})$ , corresponding to  $I(\vec{f})$  is created.
- The image,  $i(\vec{r})$ , is Fourier transformed to obtain the detected image spectrum,  $D(\vec{f})$ , and the total number of photo events in the image,  $K$ , is calculated.

Once  $N$  images are created, the frame selection algorithm sorts the images based on quality and selects  $M$  images to be retained for further processing. Each of the  $M$  images are sent through a two step process:

- The unbiased power spectrum,  $Q(\vec{f})$ , and bispectrum,  $B_U(\vec{f}_1, \vec{f}_2)$ , are computed.
- The statistics of  $Q(\vec{f})$  and  $B_U(\vec{f}_1, \vec{f}_2)$  are accumulated.

Finally, the average unbiased power spectrum and bispectrum are calculated based on the subset. From here the phase spectrum is calculated, compared to the phase spectrum of the original object,  $O(\vec{f})$ , for error analysis, and then the image is reconstructed.

### 3.3 General Parameters

For comparison, image data statistics and the bispectrum are accumulated in two stages: once before and once after frame selection. This data is used to determine SNR, SNR gain, phase error, and comparative phase error difference results of the composite image both with and without the benefits of frame selection. SNR is discussed in section 2.6.2, and phase error is discussed in section 2.5.4. Initially, the program creates the image composed of a series of data frames, then accumulates

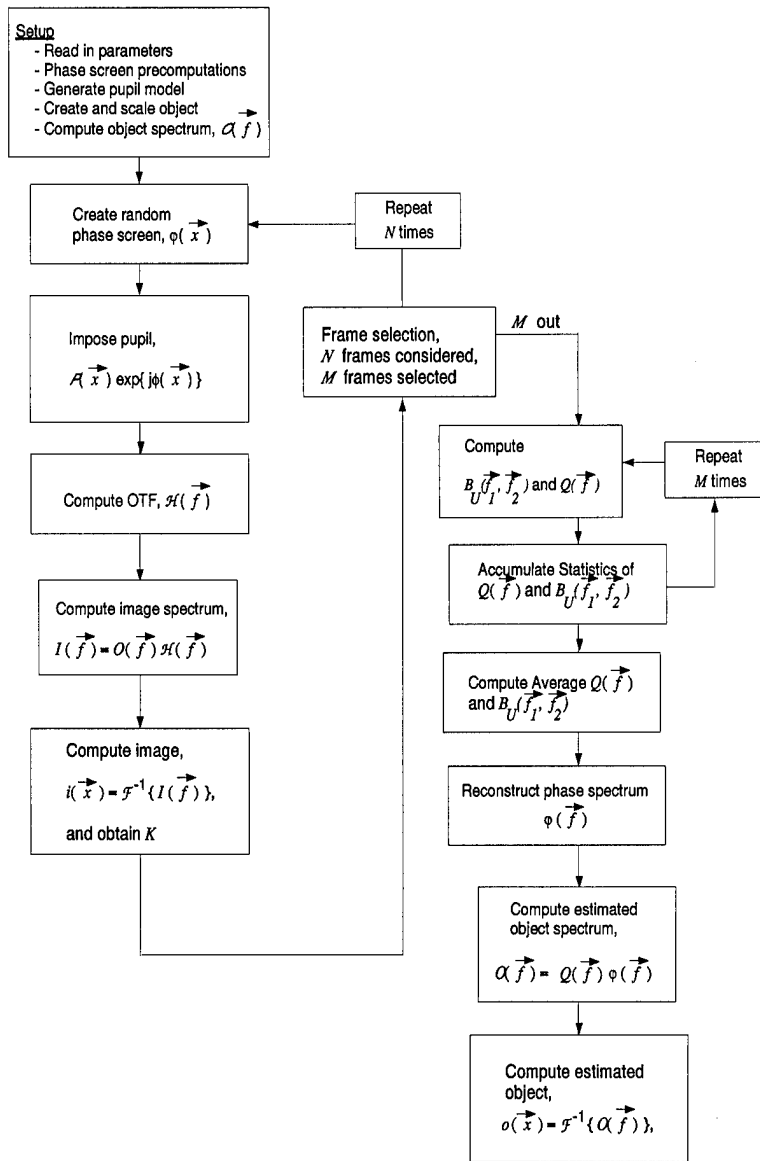


Figure 3.1 Block diagram of the speckle imaging computer simulation

statistics, calculates the bispectrum, and computes the quality metric values for each short exposure. These quality metric values are stored in a file. Next, the program reads the quality metric file and sorts these values from highest to lowest. The frame selection routines continue by calculating a minimum quality metric value based on the FSR indicated by the user. Then, the program recreates only the short exposure images with quality metric value greater than or equal to the minimum value. Next, the program accumulates a new set of statistics and a new mean bispectrum based on the selected subset. Finally, the results of the simulation are deconvolved and measured against the original, unaberrated, scaled object in terms of phase error. The phase errors are radially averaged as a function of spatial frequency, normalized to the OTF radius defined by the  $f_c$  as was discussed in section 2.4.

Four different parameters were examined to determine the behavior of frame selection for speckle imaging. Two of these are user defined: the effectiveness of various frame selection rates; and five different quality metrics. The other two are independent variables describing brightness levels, and seeing conditions. Other parameters remained fixed throughout the investigation. These include the following:

- number of short exposure images = 300
- optic diameter = 1 m
- CCD noise level = 0
- target range = 500 km
- target size = 10 square meters
- mean wavelength = 700 nm
- bandwidth = 10%
- integration time = 10 ms
- atmospheric transmittance = 10%
- telescope transmission factor = 10%

*3.3.1 Number of Short Exposure Images.* The total number of frames used for each simulation run was 300. This number is sufficiently high enough to provide an adequate sample base from which statistical data can be drawn. The importance of having a large data base is emphasized in section 2.6.2. Yet, it is small enough to permit the rapid completion of a series of computer runs within reasonable time. Another point to consider is that the number of images in a data set is limited by the motion of the object as it moves across the sky. A satellite may pass through the field-of-regard of a ground-based telescope in a matter of minutes, limiting the number of frames collected to a few hundred [5].

*3.3.2 Quality Sharpness Metrics.* Frames were selected using the image sharpness metrics developed by Muller and Buffington [16]. Refer to section 2.6.3 for a complete list and a mathematical description. Recall,  $S_{S1}$  from Eq. (2.37) is the modified version of one of the original eight, created at AFIT by Capt Craig Stoudt in 1993 [25]. This thesis examines the following sharpness metrics:

- Structural Content ( $S_1$ )
- Partial Differential ( $S_4$ )
- Maximum Entropy ( $S_7$ )
- Maximum Spectrum( $S_{S1}$ ) (a modified  $S_1$ )
- Fidelity Defect ( $S_8$ )

The  $S_{S1}$  metric is introduced in section 2.8. Its equation is repeated here:

$$S_{S1} = \int \int S_{OTF}(\vec{f}) |I(\vec{f})|^2 d\vec{f} \quad (3.1)$$

This is equivalent to the  $S_1$  metric, except the  $S_{OTF}$  term limits the integration to within the OTF radius. Stoudt concluded that  $S_{S1}$  was superior in the widest set of circumstances when combined with adaptive optics [25]. Ford's investigation was

narrowed to the performance limitations of this specific metric [5]. However, this investigation examines the other metrics to compare their performance on speckle images.

*3.3.3 Frame Selection Rate (FSR).* Five different FSRs were tested: 100%, 80%, 70%, 60%, and 50% FSR. The FSR can be selected by entering the desired rate in the input data file. The 100% case represents the baseline against which all other FSRs are compared. Previous works have shown that frame selection combined with adaptive optics has optimal values dependent upon the selected values of the independent variables. Optimal FSRs ranged from 60–80% [5, 25]. Therefore, it was the initial intent of this thesis effort to narrow the investigation down to the 60%, 70% and 80% cases. However, results from the speckle imaging data has indicated very little change in performance in any of the FSRs tested. Therefore, the investigation was extended to include the 50% FSR as well.

*3.3.4 Visual Magnitude.* This investigation explores objects with  $m_v$  values of +1, +3, +5, and +7, which are all dimmer than most items listed in table 2.1. The visual magnitude of an object can be selected in the simulation by changing the value of  $D$  and providing a value of  $P$  obtained from a table of flux values [10]. Both Ford and Stoudt conclude that out of all the independent parameters,  $m_v$  has the greatest effect on frame selection performance [5, 25].

*3.3.5 Fried Seeing Parameter.* The primary independent variable related to the mean and the variance of the OTF, is the relative seeing conditions, characterized by the parameter  $r_o$  [25]. The three  $r_o$  values tested in this thesis represent a wide range of operating conditions:

- 7 cm (poor seeing conditions)
- 12 cm (average seeing conditions)
- 17 cm (excellent seeing conditions).

The poor seeing conditions cause the greatest variance in the data for frame selection, while excellent seeing conditions put frame selection to the test of sorting frames that are very similar.

### 3.4 Bispectrum Parameters

*3.4.1 Phase Spectrum Reconstruction.* Section 2.5 discusses the process of obtaining the bispectrum estimate,  $B_V(\vec{f}_1, \vec{f}_2)$ , from the detected image and correcting for noise effects. The sample-based mean bispectrum is an accumulation of data from each of the frames in the selection. The phase spectrum of the object can be derived from the bispectrum. There are two methods available in the computer simulation: the *recursive* method and the *iterative weighted least squares method*. The recursive method for reconstruction is the easiest and most widely used [1, 12, 14, 15, 19, 24]. This method uses the fact that the object phase spectrum at  $(\vec{f}_1 + \vec{f}_2)$  can be expressed as a unit amplitude phaser, [24]

$$\exp\{j\phi_o(\vec{f}_1 + \vec{f}_2)\} = \exp\{j\phi_o(\vec{f}_1)\} + \exp\{j\phi_o(\vec{f}_2)\} - \exp\{j\phi_B(\vec{f}_1, \vec{f}_2)\}, \quad (3.2)$$

where  $\phi_B(\vec{f}_1, \vec{f}_2)$  is the phase of the mean bispectrum. The three starting points for the recursive process are set equal to zero:

$$\begin{aligned} \phi_o(\vec{f} = 0) &= 0 \\ \phi_o(\pm\Delta f, 0) &= 0 \\ \phi_o(0, \pm\Delta f) &= 0 \end{aligned} \quad (3.3)$$

While  $\phi_o(\vec{f} = 0)$  is known to be zero, zero is an arbitrary choice for the other two terms in Eq. (3.3). The consequence of choosing an arbitrary zero, versus a known value in Eq. (3.3) is a linear shift of the image in space [24], also known as tilt error. It is shown by Eq. (2.17) that the bispectrum is insensitive to tilt error. Once the estimated phase,  $\phi_o(\vec{f})$ , is reconstructed, it is then combined with the estimated

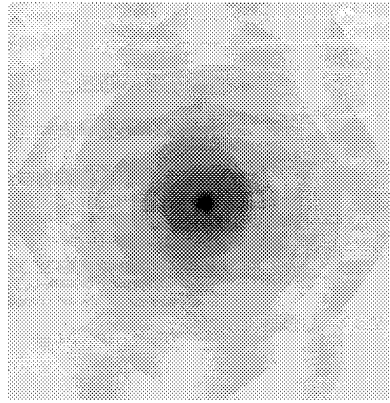
modulus of the object,  $Q(\vec{f})$ , to reconstruct the image of the object. As a measure of performance, the phase error and comparative phase error (discussed in section 2.5.4) are calculated and plotted.

### 3.5 Image Reconstruction

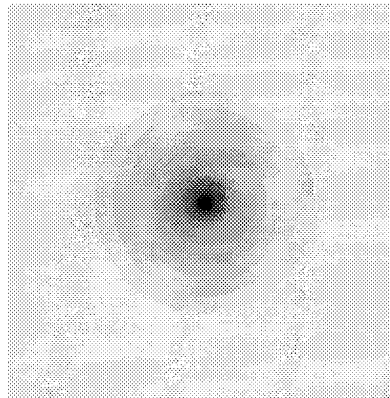
The final image is composed using the pseudo-Wiener filter described in section 2.4.1 in conjunction with the modulation transfer function (MTF) filter discussed in this section. The MTF is the modulus of the OTF [8, 11]. The  $\alpha/SNR_Q(\vec{f})$  term in Eq. (refeq:wiener) reduces the effects of high spatial frequency noise in the reconstructed image [24]. The results in this thesis were generated by using an  $\alpha$  value of 0.01. The  $f_c$  used in Eq. (3.4) for the MTF filter in the computer simulation is same as the calculated OTF radius of 30 pixels.

Fig. 3.2 shows the three reference star images used in the deconvolution process. In each case, a bright star was simulated regardless of the visual magnitude of the satellite, although the three different images correspond to different seeing conditions. The reference star for the poor seeing conditions,  $r_0 = 7$  cm, is noticeably more blurred around the edges of the image.

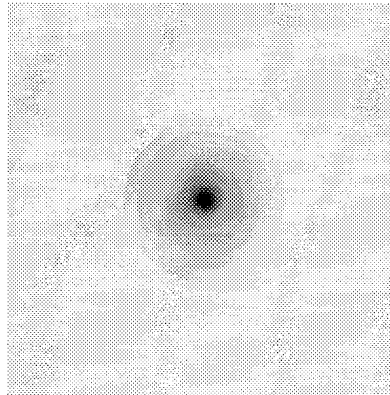
Once the modulus is obtained from the pseudo-Wiener filter calculation, and the phase has been obtained from the bispectrum calculations, the next step is image reconstruction. Before the final step of inverse Fourier transforming the spectrum back into the image, another filter is applied to correct for additional high frequency noise effects. There are two filters to choose from, the pill box, and the MTF, or conical filter. The MTF filter was chosen for this thesis effort, because it is less noisy and tapers off the high frequency noise better than the pill box filter. The filter is applied to the estimated modulus of the object spectrum,  $\tilde{O}(\vec{f})$ , obtained from the



(a)



(b)



(c)

Figure 3.2 Reference star images used in the pseudo-Wiener filter at three different Fried seeing levels: a)  $r_o = 7$  cm b)  $r_o = 12$  cm c)  $r_o = 17$  cm

square root of  $|O(\vec{f})|^2$ , from Eq. (2.12). It is defined by [24]

$$\begin{aligned} H(\vec{f}) &= 1 - \frac{|\vec{f}|}{f_c}, & |\vec{f}| \leq f_c \\ &= 0, & |\vec{f}| > f_c, \end{aligned} \quad (3.4)$$

where,  $f_c$  is the OTF radius. The object spectrum is obtained by multiplying the modulus, the phase, and the filter of Eq. (3.4):

$$O(\vec{f}) = \tilde{O}(\vec{f})H(\vec{f})\exp\{\phi_o(\vec{f})\}. \quad (3.5)$$

Finally, the image is obtained by taking the inverse Fourier transform of  $O(\vec{f})$ :

$$o(\vec{r}) = \int O(\vec{f})\exp\{j\pi\vec{f} \cdot \vec{r}\}d\vec{f}. \quad (3.6)$$

### 3.6 Summary

This chapter provided the methodology for conducting the computer simulation of creating speckle images, applying frame selection, using the bispectrum calculations for estimating the phase for image reconstruction, and applying filters in the image reconstruction process. This chapter also identified specific parameters used in conducting this research. The final quality of the composite image is determined by the power spectrum SNR and the bispectrum phase error. These metrics are the tools used in the analysis of two experiments: the point source and the extended source. The results of this analysis are presented in the next chapter.

## *IV. Results*

### *4.1 Introduction*

Chapter three developed the methodology and introduced the independent parameters and performance metrics for conducting this investigation. This chapter consists of the results of two frame selection experiments: point source and extended source. The point source is typically a single bright star. Point source data is of interest to astronomers, and is used in most deconvolution techniques for sharpening images. Satellites are the extended objects of primary interest to the Air Force. Figure 2.1 shows the computer rendering of a satellite used as the extended object in this study. The results are in the form of power spectrum SNR, bispectrum phase error analysis. The reconstructed images are also presented.

### *4.2 System Parameters*

In both experiments two independent parameters are varied: the Fried seeing parameter and the visual magnitude. The Fried seeing parameters are defined in section 2.7.2. The three  $r_o$  values tested in this thesis are: 7 cm; 12 cm; and 17 cm. Visual magnitude,  $m_v$ , is defined in 2.7.1. This investigation explores objects with  $m_v$  values of +1, +3, +5, and +7.

### *4.3 Quality Metric Performance*

This section presents a comparison of the performance of the five sharpness metrics tested in both the point source and extended source experiments. Results are given in terms of power spectrum SNR and bispectrum phase error. For illustration purposes, the vertical scale for the point source phase error diagrams is expanded much more than the extended source.

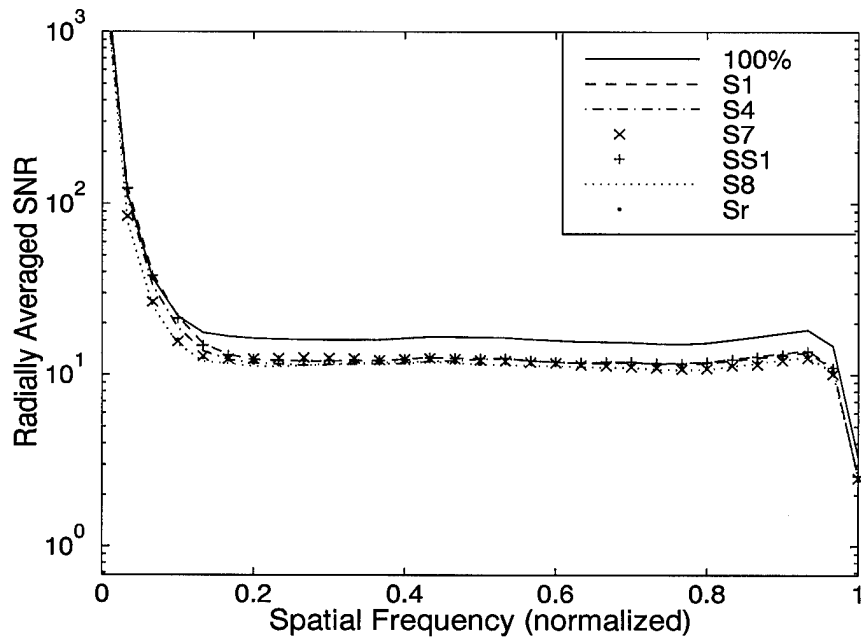
4.3.1 *Point Source.* Figure 4.1 shows the radially averaged power spectrum SNR and the Fourier phase error of the composite point source simulated with an  $r_o$  of 7 cm and a  $m_v$  of 1. These are the parameters for a bright target in poor seeing conditions. This figure plots the results for all of the sharpness metrics discussed in section 2.6.3. The frame selection rate, FSR, is 50%. Figures A.13–A.24 in the appendix are SNR plots, and figures A.1–A.12 are phase error plots of point source images simulated with other parameters.

When there are very poor seeing conditions, the  $S_7$  metric proves superior. This is because the  $S_7$  metric measures maximum entropy. Recall from section 2.6.3 the  $S_7$  metric is

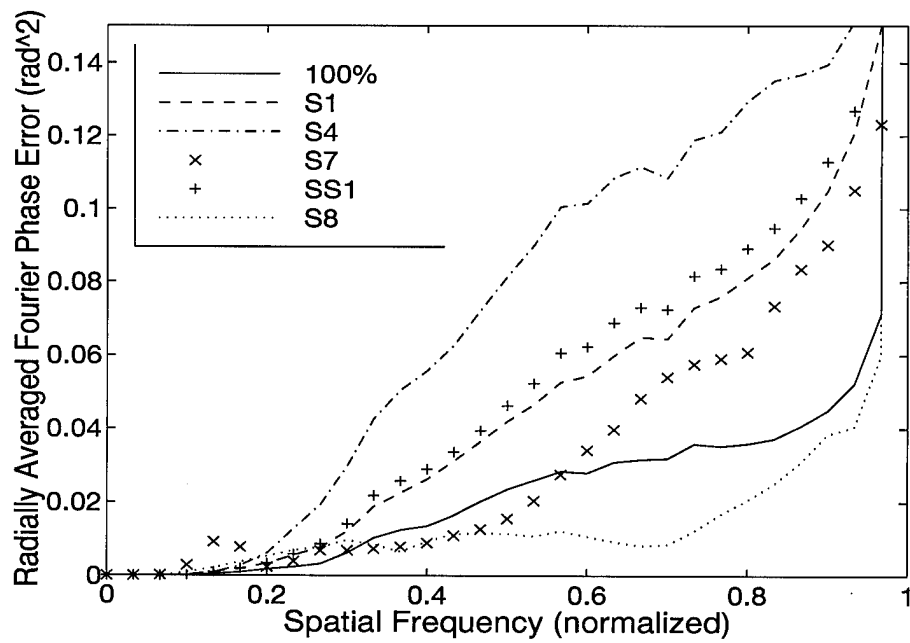
$$S_7 = - \int \int \ln[i(\vec{r})]i(\vec{r}) d\vec{r} \quad (4.1)$$

As seeing conditions worsen, the increased randomness results in increased errors in the image plane, resulting in poor quality images. Bright sources in poor seeing conditions are the conditions the  $S_7$  metric seems to work best in. The increased variance due to the poor seeing conditions combined with a high contrast due to the bright source is a favorable condition for the  $S_7$  metric to differentiate between frames. However, improving the seeing conditions by simply changing the  $r_o$  value from 7 to 12 cm results in a dramatically different performance as can be observed in Fig. 4.2. In fact, the results of the  $S_7$  metric were every inconsistent beyond the  $r_o = 7$ cm point. This inconsistency can be observed by comparing figures A.3–A.6. Therefore, to produce reliable results, a more consistent metric is desired.

The metrics that performed the most consistently were  $S_1$  and  $S_{S1}$ . Fig. 4.2 is typical of the relative performance of the  $S_{S1}$  and the  $S_1$  metrics. Here, they result in the highest SNR and the lowest phase error. However, considering the vertical scale in this example, and in most of the cases tested, all of the metrics performed about the same. The loss in SNR and the resulting error achieved by frame selection for a point source, even in the worst case, is insignificant. The worst phase error is less than  $0.15 \text{ rad}^2$ .

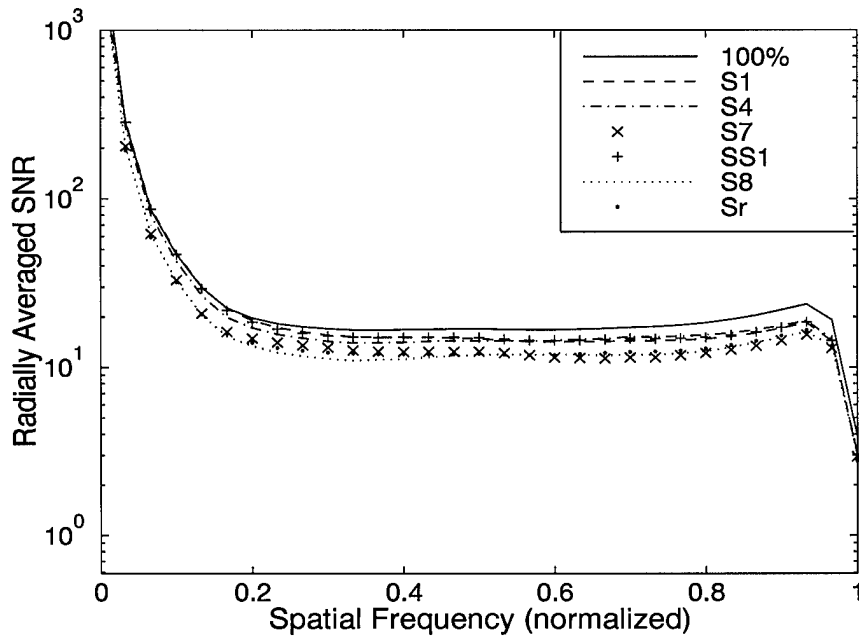


(a)

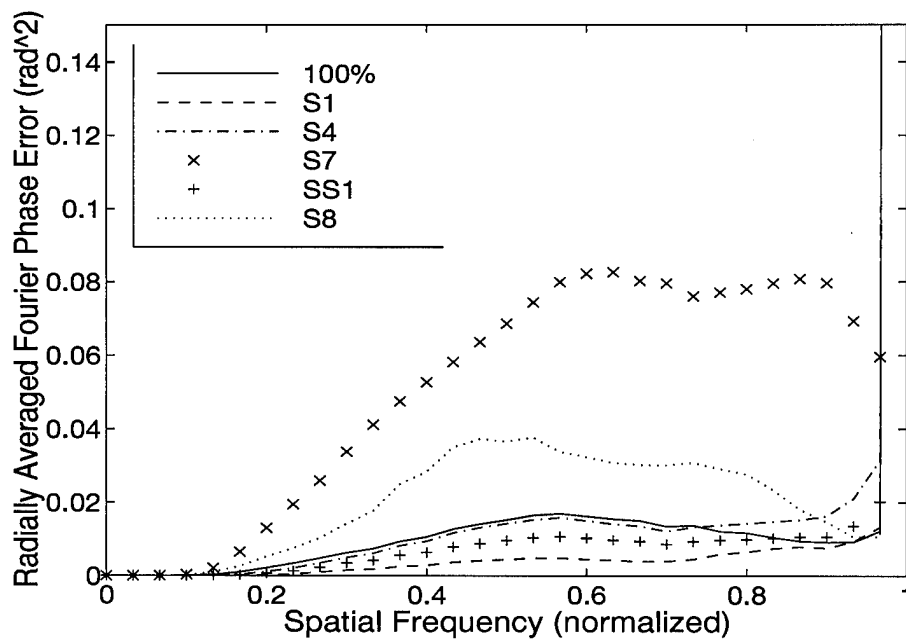


(b)

Figure 4.1 Quality metric performance for a point source : a) SNR and b) Phase error. Both cases indicate frame selection strategies for the 50% FSR. Visual parameters are  $r_o = 7$  cm,  $m_\nu = 1$



(a)



(b)

Figure 4.2 Quality metric performance for a point source : a) SNR and b) Phase error. Both cases indicate frame selection strategies for the 50% FSR. Visual parameters are  $r_o=12$  cm,  $m_\nu=1$

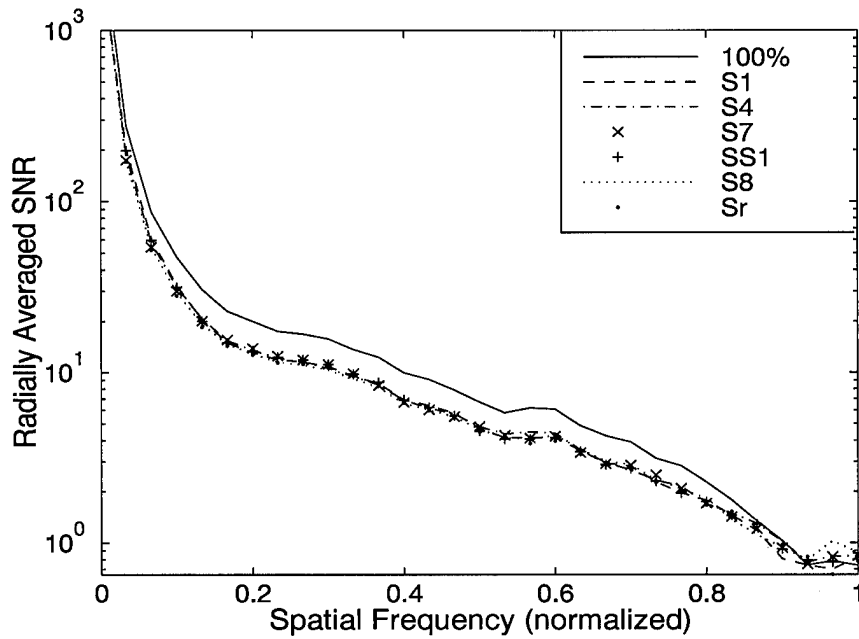
Contrary to expectations, in most of the cases tested, the fidelity defect metric,  $S_8$ , generally resulted in the lowest SNR. Additionally,  $S_8$  resulted in increased phase error over the other metrics in many of the scenarios. See also, figures A.2, A.5, and A.6. Since the fidelity defect also requires a known source, it is only practical as a basis for comparison in an adaptive optics simulation.

*4.3.2 Extended source.* Fig. 4.3 is representative of a bright extended source,  $m_v = 1$ , under average seeing conditions,  $r_o = 12$  cm. While there was some loss in the SNR due to frame selection, the metrics all performed about the same for an extended source. There was a slight increase in the phase error in the mid-spatial frequency regions. The data tended to fluctuate as the frequency increased. Figures B.1–B.12 in the appendix show that this result was consistent for all parameters.

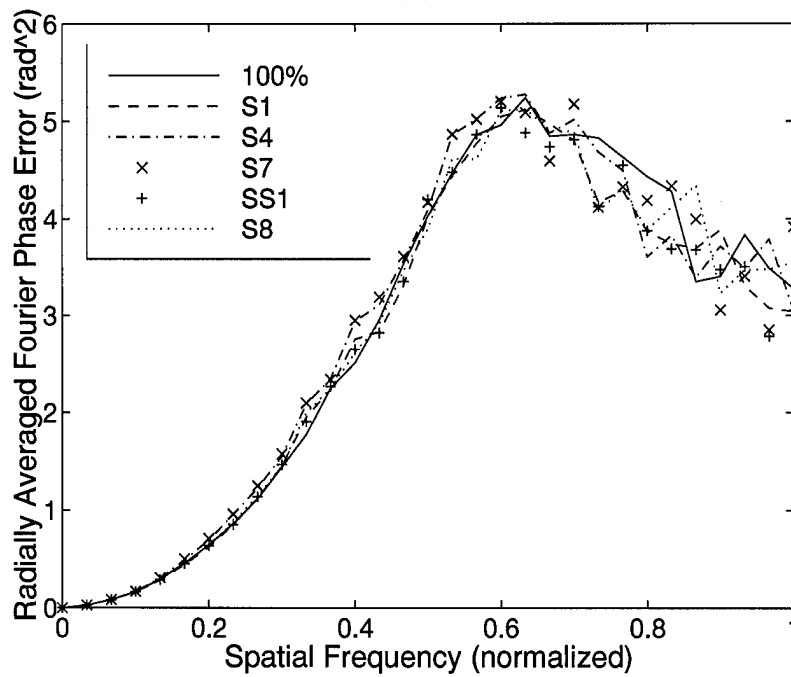
*4.3.3 Conclusions.* The  $S_7$  metric performed the best in poor seeing conditions for a bright point source, but performed the worst under improved seeing conditions. The  $S_1$  and the  $S_{S1}$  metrics performed most consistently, and performed well. There was very little difference in metric performance for an extended source. Since  $S_{S1}$  performed consistently well, and has been proven superior in previous works [5, 25], it will be used to represent the general performance of frame selection through out the remainder of this chapter.

#### *4.4 Frame Selection Performance*

*4.4.1 Point Source.* Fig. 4.4 shows the results for a bright point source,  $m_v = 1$ , under average seeing conditions,  $r_o = 12$  cm. Here, the only metric used is  $S_{S1}$ , but the frame selection rates are varied from 100% to 50%. Fig 4.4 a) shows a gradual decline in the SNR performance of frame selection for a point source as the FSR drops from 100% to 50%. The total drop in SNR is about 20%, overall. Figure 2.4, is a graph of the same 100% data as in figure 4.4, except the data is rep-

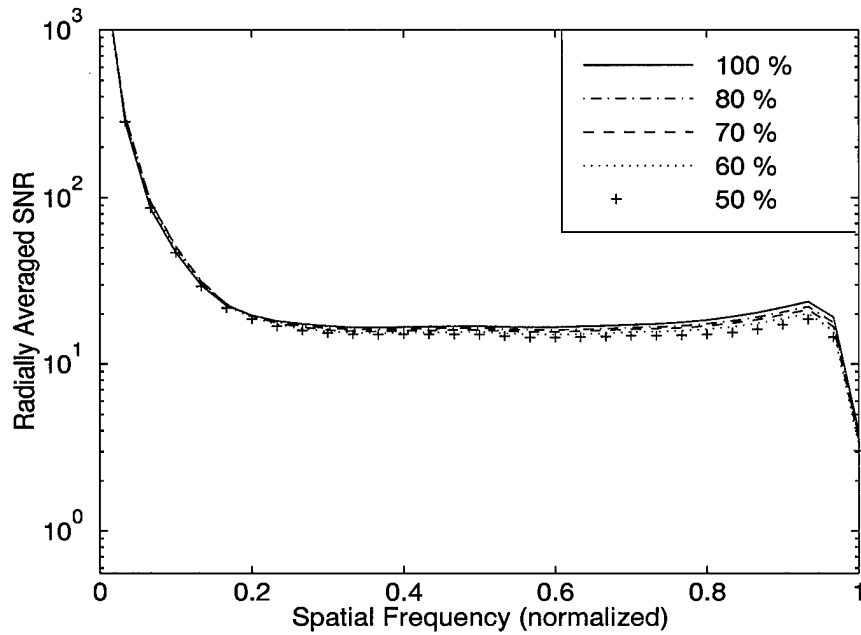


(a)

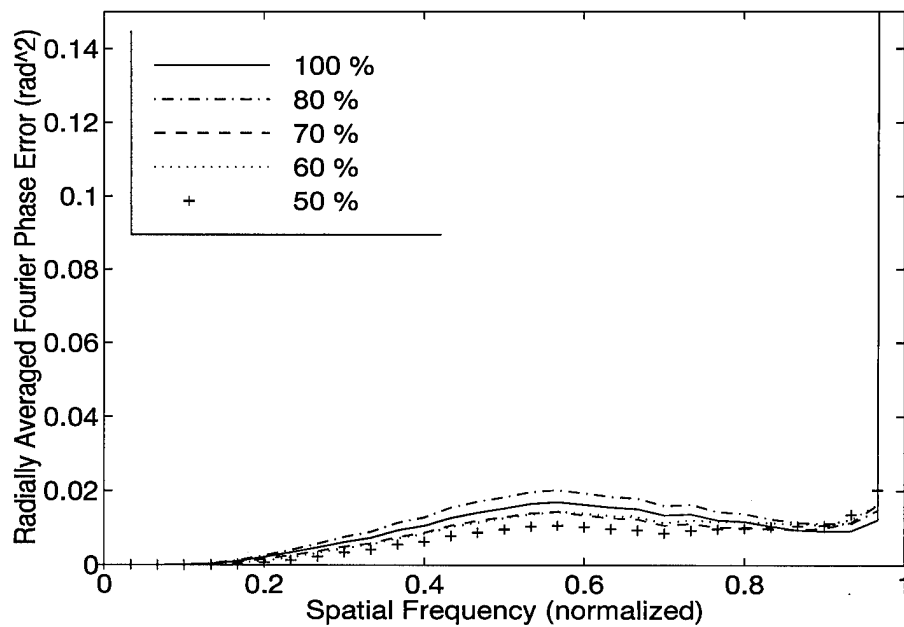


(b)

Figure 4.3 Quality metric performance for an extended source: a) SNR and b) Phase error. Both cases indicate frame selection strategies for the 50% FSR. Visual parameters are  $r_o=12$  cm,  $m_\nu=1$



(a)



(b)

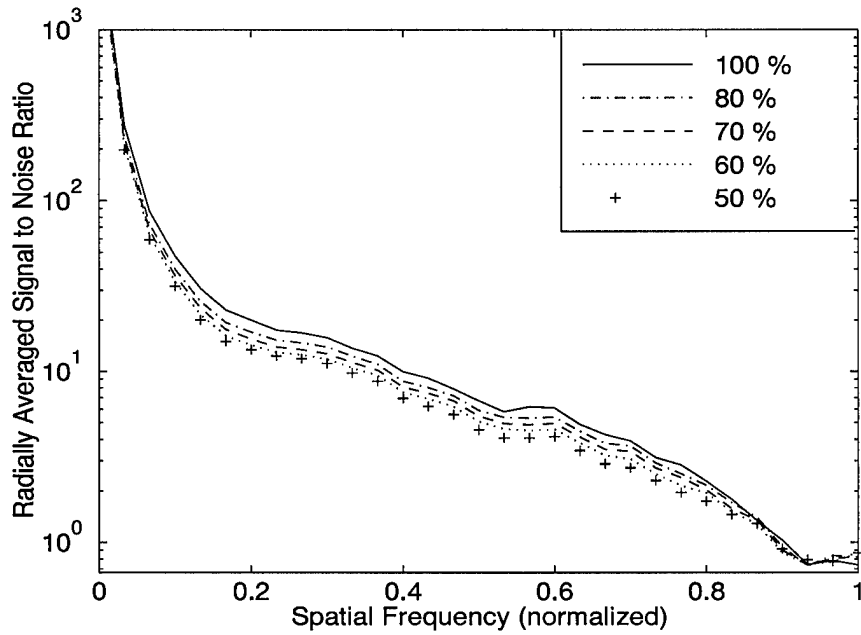
Figure 4.4 Frame selection performance for a point source: a) SNR and b) Phase error. Both cases indicate frame selection strategies using the  $S_{S1}$  performance metric. Visual parameters are  $r_o=12$  cm,  $m_\nu=1$

resents the theoretical reduction in SNR due to randomly selected data, as opposed to using any sharpness metric. Comparing figure 4.4 a) to figure 2.4 shows that reducing data using frame selection results in improved SNR over random selection.

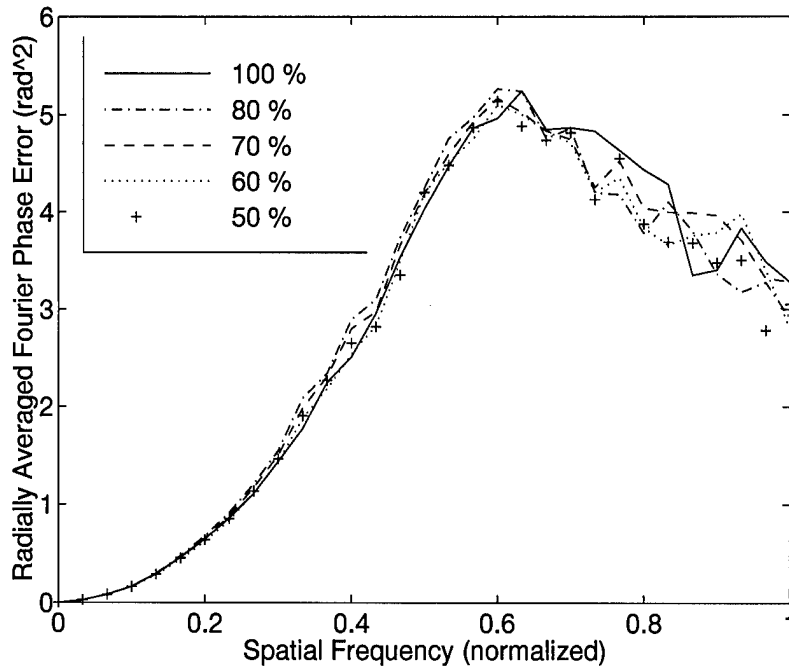
Figure 4.4 b) shows a slight improvement in phase error. According to the vertical scale in b), the improvement in phase error at the mid-spatial frequency region is less than one quarter of a graduation,  $0.005 \text{ rad}^2$ . Typically, however, the 50% FSR case is only as good or slightly worse than the other FSRs. This trend can be observed by comparing the  $S_{S1}$  curves in figures A.2–A.3, in the appendices. These figures are all results of poor seeing conditions,  $r_o = 7 \text{ cm}$ . These figures indicate that the 60% FSR performs best. Figure A.4 indicates that the 80% FSR performs best. In the succeeding figures, it becomes difficult to compare relative performance, since for improved seeing conditions, there is little variance in FSR performance. The results identified here are consistent when other parameters are used. Other parameters can be observed by referring to figures A.1–A.12. Each figure has four plots: one for each FSR. The different FSRs can be compared by selecting a specific metric curve from each plot and observing the trend as the FSR changes.

*4.4.2 Extended source.* The extended source SNR results are consistent with the point source SNR results. Fig. 4.5 a) indicates about a 20% drop in SNR for the 50% FSR case. Fig. 4.5 b) shows that the phase error performance of all FSRs tested are about the same, and the data tended to fluctuate in the high spatial frequency regions. This result is consistent with those using other parameters, and can be observed by referring to figures B.13–B.24.

*4.4.3 Conclusions.* Figures 4.4 and 4.5 indicate that there is a gradual worsening in the SNR performance of frame selection, for both point and extended sources, as the FSR decreases. This is consistent with the statistical nature of reducing data, discussed in section 2.6.2. Although, the SNR achieved using the  $S_{S1}$



(a)



(b)

Figure 4.5 Frame selection performance for an extended source: a) SNR and b) Phase error. Both cases indicate frame selection strategies using the  $S_{S1}$  performance metric. Visual parameters are  $r_o=12$  cm,  $m_v=1$

metric is improved over that of randomly selected data. The phase error performance did not change significantly as a function of FSR in either the point or extended source experiments. In general, frame selection performance decreased as the FSR was decreased. However, this degradation was slight enough that the 50% FSR was sufficient to illustrate the overall frame selection performance. For this reason, the 50% FSR will be used throughout the remainder of this chapter. The results obtained by using the other FSRs are included in the appendices.

#### 4.5 Performance Under Various Seeing Conditions

The seeing conditions tested are

- 7 cm (poor seeing conditions)
- 12 cm (average seeing conditions)
- 17 cm (excellent seeing conditions).

SNR gain and comparative phase error difference plots are used in this section to show relative frame selection performance between cases where seeing conditions are varied. The SNR gain is discussed in section 2.6.2, and phase error difference is discussed in section 2.5.4. Each data set in the graphs represents relative performance based on the 50% FSR.

*4.5.1 Point Source.* To create figure 4.6, a bright point source in varying seeing conditions is simulated. Here, the FSR is fixed to 50%, and the sharpness metric used is  $S_{S1}$ . Each of the three  $r_o$  values are compared. The complete set of SNR gain plots are in figures A.25–A.36. These figures include all the quality metrics and all of the FSRs. To determine the relative performance of different seeing conditions, three figures of different  $r_o$  values, but the same  $m_v$  values must be compared. For example, figure 4.6 a) displays the SNR gain data from the  $S_{S1}$  curve in the a) plots from figures A.25, A.29, and A.33. The SNR gain in Fig. 4.6 a)

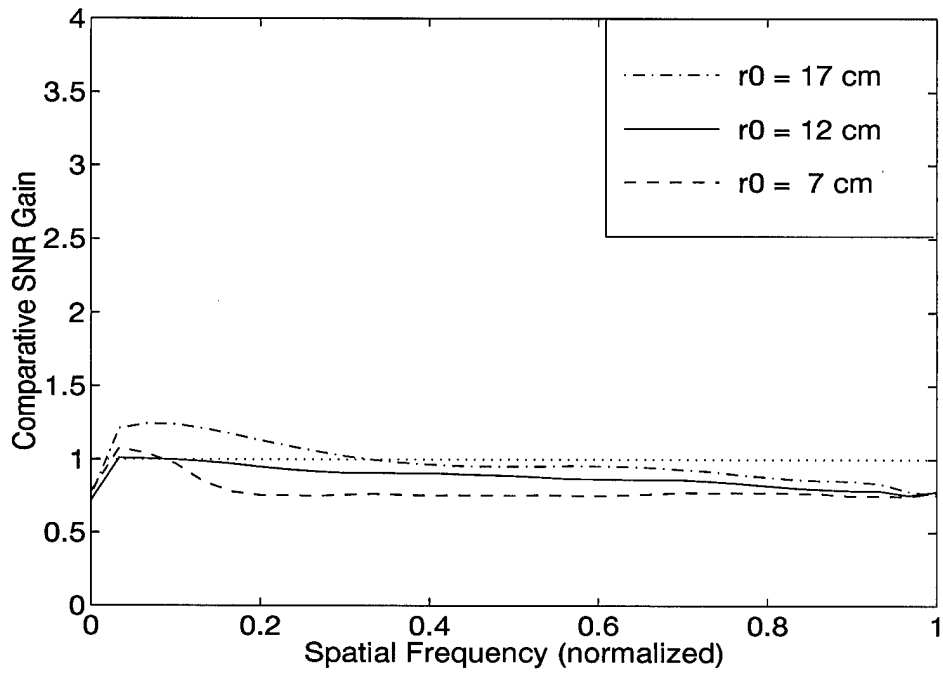
shows a slight decline in frame selection performance as seeing conditions get worse. In nearly every case studied, the SNR gain curves showed a slight improvement only in regions of low frequency, and a slight decline elsewhere.

The complete set of comparative phase error plots are in figures A.37–A.48. The comparative phase error is introduced in section 2.5.4. Figure 4.6 b) displays the comparative phase error data from the  $S_{S1}$  curve in the a) plots from figures A.37, A.41, and A.45. The comparative phase error plot in b) also shows that performance declines when the seeing conditions drop below  $r_o = 12$  cm. Although the plot in b) has such a small scale that there is really very little significant difference in performance. The lowest point in the curve is about  $0.1 \text{ rad}^2$ .

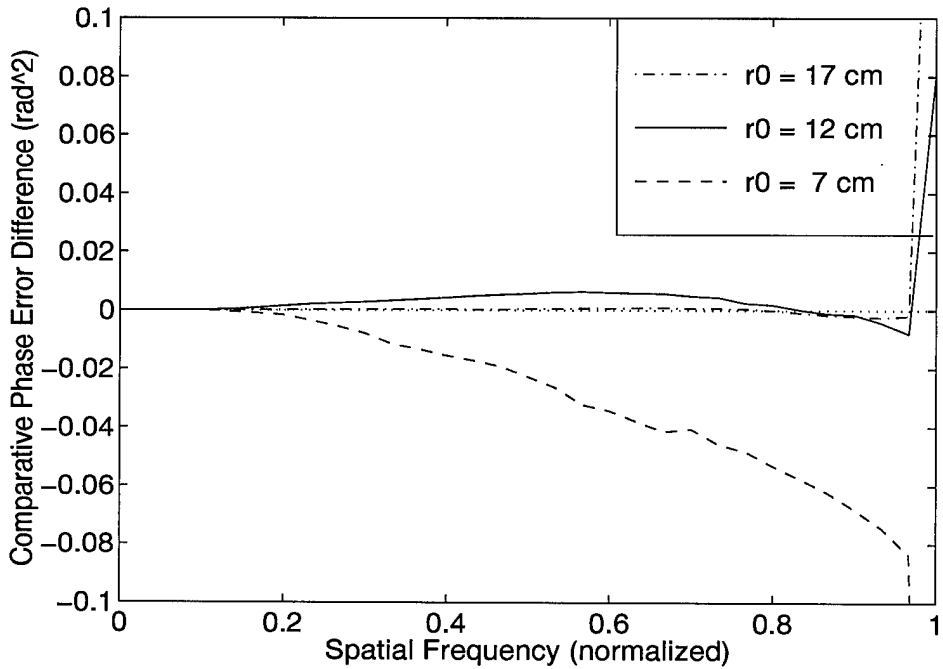
*4.5.2 Extended Source.* In figure 4.7, a bright extended source in varying seeing conditions is simulated. Here, the FSR is fixed to 50%, and the sharpness metric used is  $S_{S1}$ . Each of the three  $r_o$  values are compared. The complete set of SNR gain plots are in figures B.25–B.36. Figure 4.7 a) displays the SNR gain data from the  $S_{S1}$  curve in the a) plots from figures B.25, B.29, and B.33.

The SNR gain plot in Fig. 4.7 a) indicates a 20% drop in performance for the 50% frame selected case. It also shows that the performance is about the same for all seeing conditions. The complete set of comparative phase error plots are in figures B.37–B.48.

Figure 4.7 b) displays the comparative phase error data from the  $S_{S1}$  curve in the a) plots from figures B.37, B.41, and B.45. The phase error differences in Fig. 4.7 b) show there is no significant change in performance whether or not frame selection is used, at any of the  $r_o$  values tested. In nearly every case studied, the low spatial frequency region of the spectrum has almost zero phase error difference between the frame selected case and the non-frame selected case. As the frequency increases, the phase error difference oscillates about the zero axis.

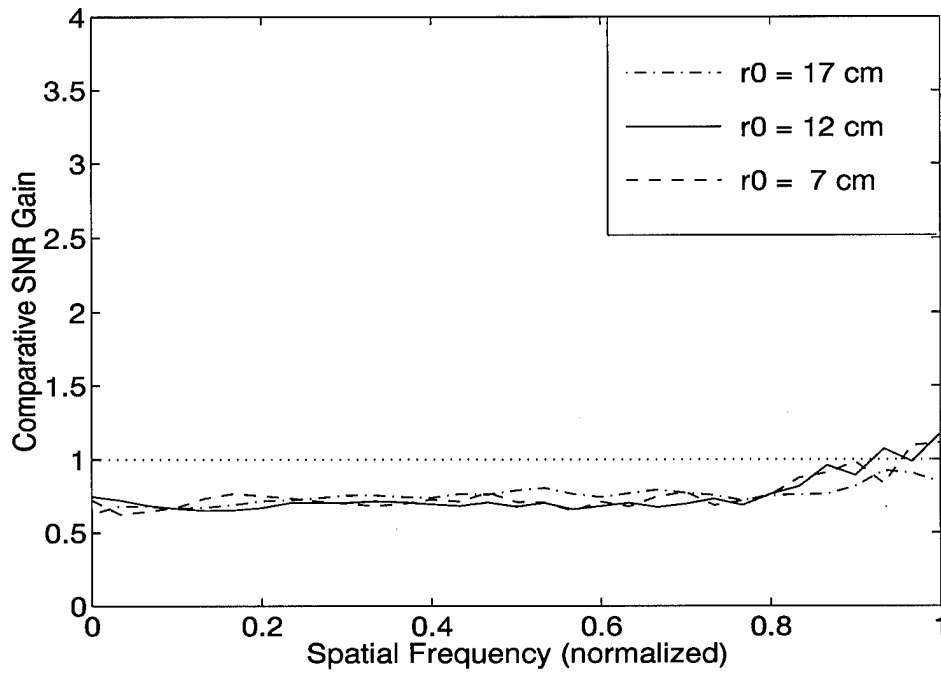


(a)

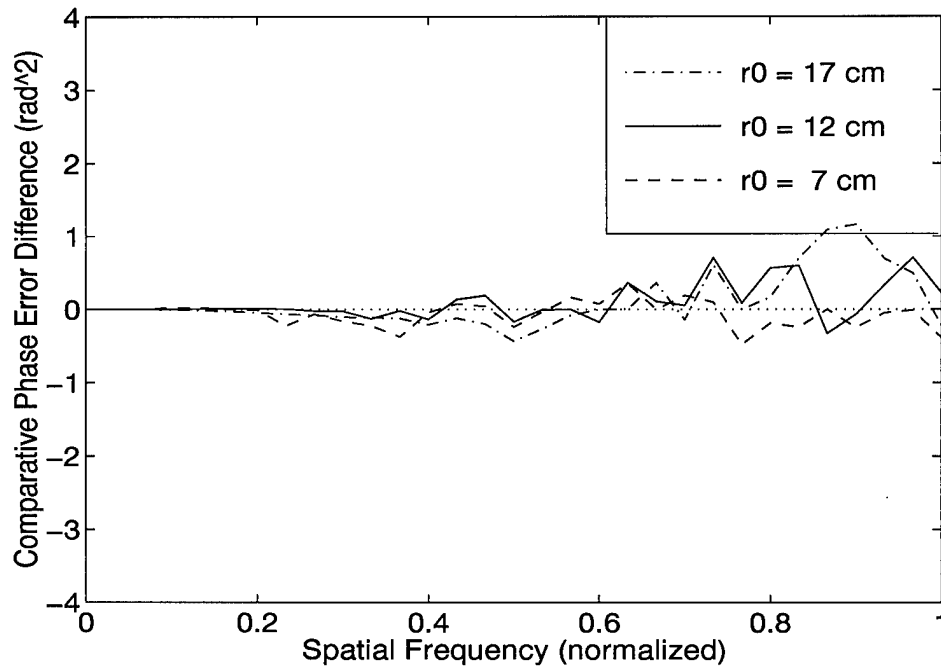


(b)

Figure 4.6 Seeing conditions for a point source: a) SNR gain curves and b) Phase error difference curves. Both cases indicate frame selection strategies for the 50% FSR, using the  $S_{S1}$  performance metric.  $m_\nu=1$



(a)



(b)

Figure 4.7 Seeing conditions for an extended source: a) SNR gain curves and b) Phase error difference curves. Both cases indicate frame selection strategies for the 50% FSR, using the  $S_{S1}$  performance metric.  $m_\nu=1$

*4.5.3 Conclusions.* The  $r_o$  values tested only affect frame selection performance for point sources. As seeing conditions improve, so does performance. In the case of extended sources, the effect of changing  $r_o$  is insignificant. These results are consistent with the results using the other  $m_\nu$  parameters tested.

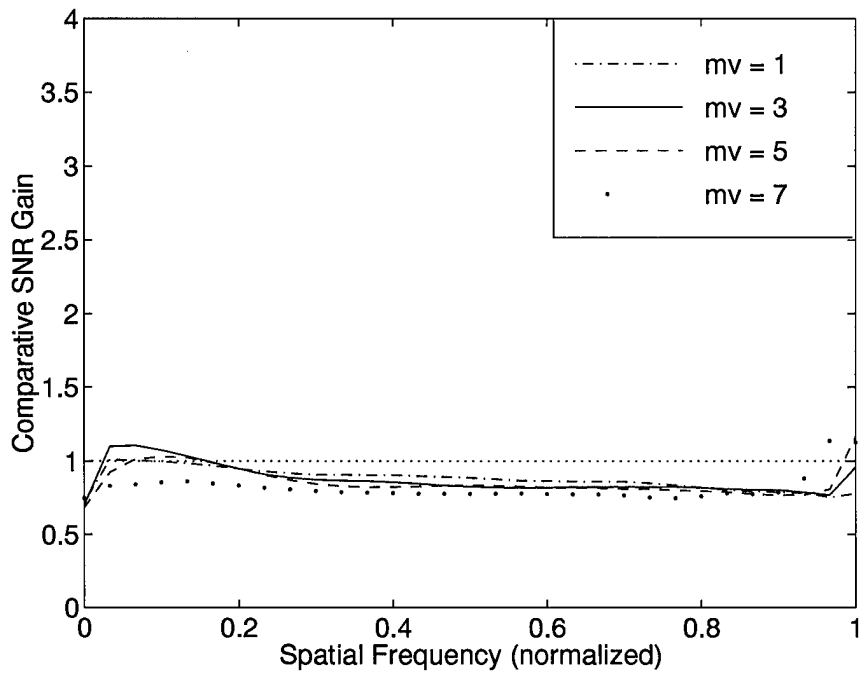
#### *4.6 Performance Under Various Target Brightness Levels*

The brightness levels tested are  $m_\nu$  values of +1, +3, +5, and +7.

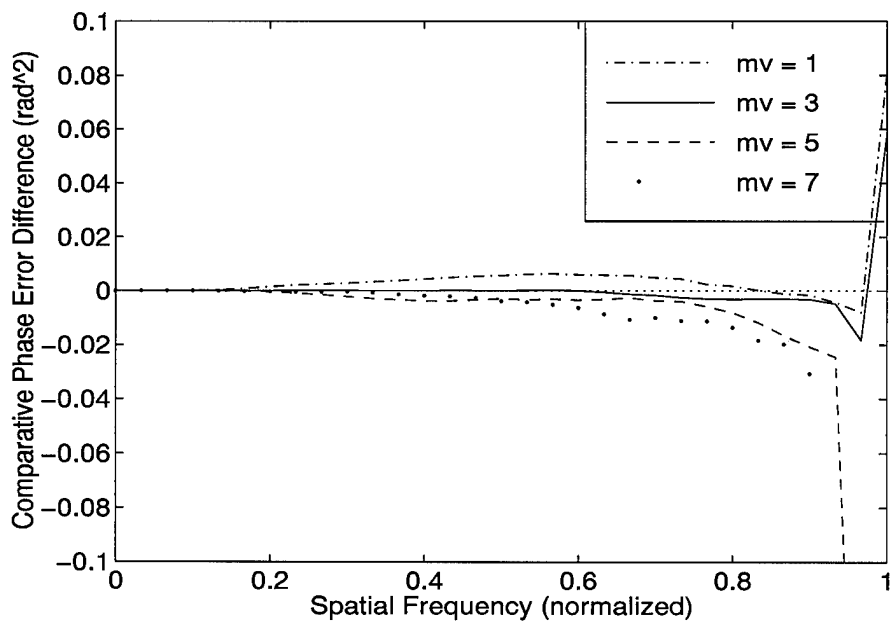
*4.6.1 Point Source.* In figure 4.8, a varying brightness point source in average seeing conditions is simulated. To determine the relative performance of varying brightness levels, four figures from the appendix containing the same  $r_o$  value but different  $m_\nu$  values may be compared. Figure 4.8 a) displays the SNR gain data from the  $S_{S1}$  curve in the a) plots from figures A.29, A.30, A.31, and A.32. Fig. 4.8 a) shows there is a very slight drop in frame selection SNR performance as the target brightness level decreases. The worst case tested was  $m_\nu = +7$ , which had about a 20% reduction in SNR performance.

Figure 4.8 b) displays the comparative phase error difference data from the  $S_{S1}$  curve in the a) plots from figures A.41, A.42, A.43, and A.44. Figure 4.8 b) also indicates a drop in phase error performance as target brightness decreases.

*4.6.2 Extended Source.* In figure 4.9, a varying brightness extended source in average seeing conditions is simulated. Figure 4.9 a) displays the SNR gain data from the  $S_{S1}$  curve in the a) plots from figures B.29, B.30, B.31, and B.32. Fig. 4.9 shows there is a very slight drop in frame selection SNR performance for all target brightness levels, especially at the low frequencies. There is no significant reduction in performance in the phase error for any of the brightness levels. Once again, performance begins to oscillate as the frequency increases, however, staying very close to the performance levels of the non-frame selected case.

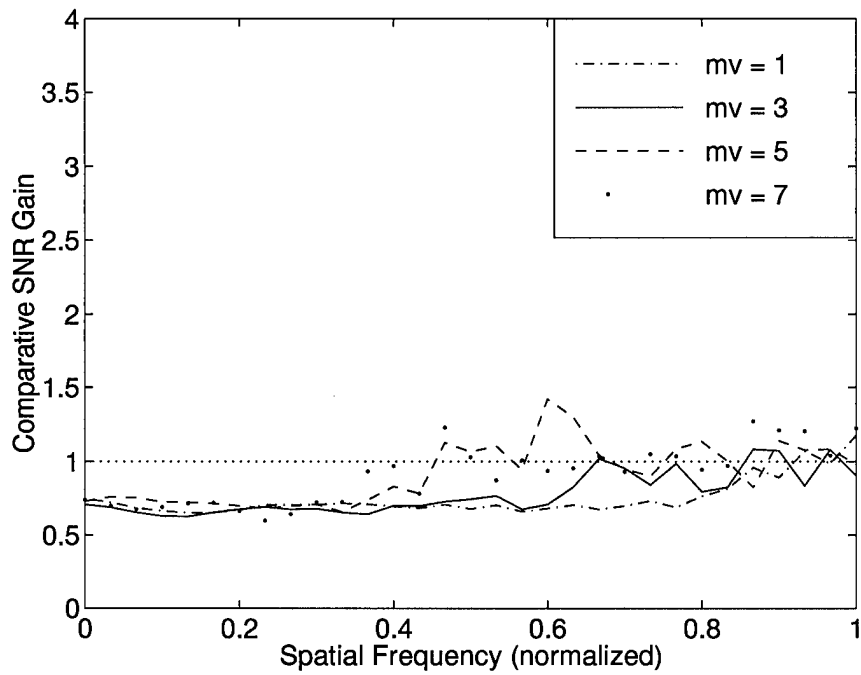


(a)

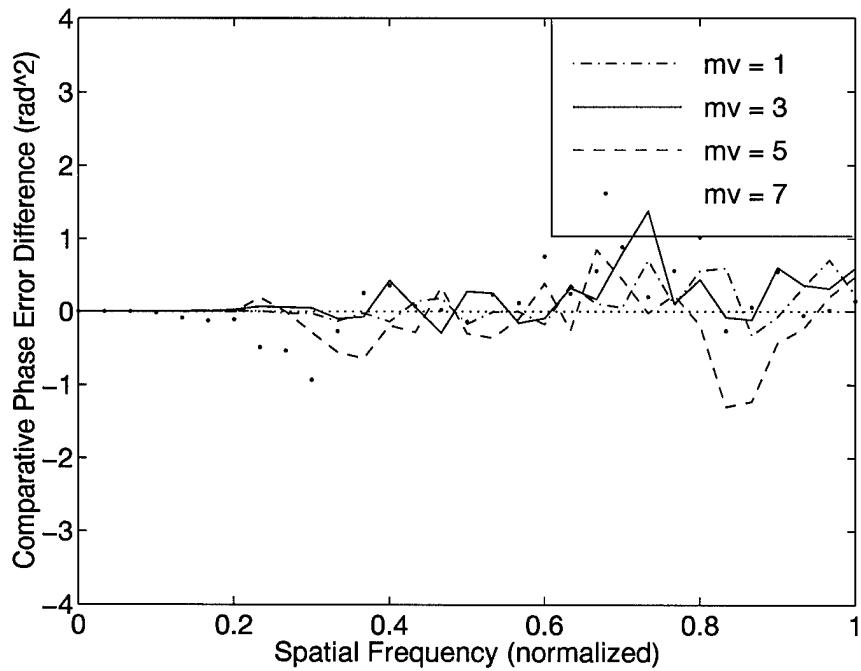


(b)

Figure 4.8 Brightness levels for a point source: a) SNR gain curves and b) Phase error difference curves. Both cases indicate frame selection strategies for the 50% FSR, using the  $S_{S1}$  performance metric.  $r_o=12$  cm



(a)



(b)

Figure 4.9 Brightness levels for an extended source: a) SNR gain curves and b) Phase error difference curves. Both cases indicate frame selection strategies for the 50% FSR, using the  $S_{S1}$  performance metric.  $r_o=12$  cm

4.6.3 *Conclusions.* Lower visual magnitude values tend to reduce performance for point sources. The visual magnitude values tested have no significant effect on the performance of frame selection for the extended sources. These results are consistent with other  $r_o$  parameters tested.

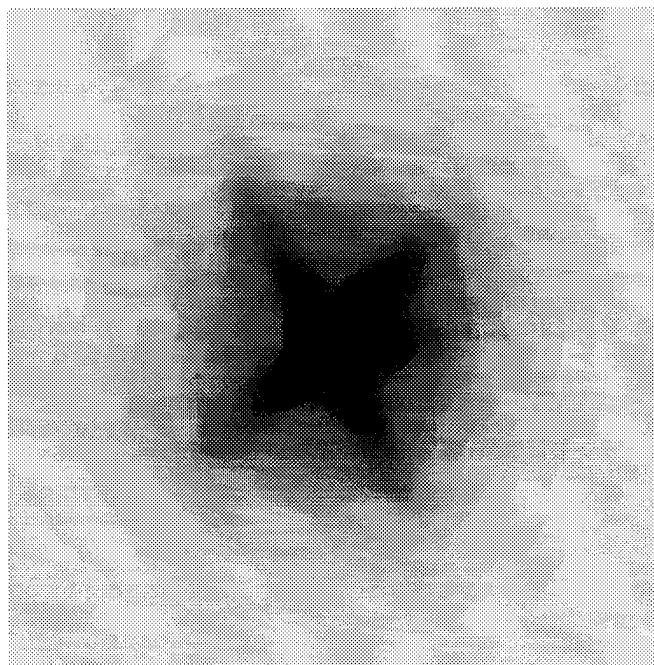
#### 4.7 *Image Reconstruction Results*

Figure 4.10 shows the reconstructed image of an extended source a) before frame selection and b) after a 50% FSR frame selection was imposed. There is no noticeable difference in final image quality whether 100% or 50% of the frames are retained for post processing.

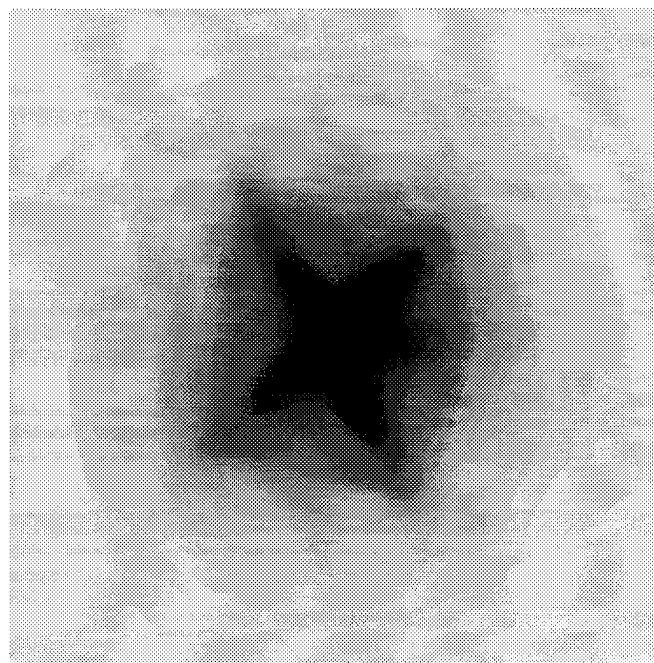
4.7.1 *Conclusions.* A 50% FSR frame selection, using the  $S_{S1}$  metric does not reduce the visual quality of speckle images.

#### 4.8 *Summary*

Frame selection is an effective way to reduce data by as much as 50%, thus reducing the expense and time of post-processing speckle image data, by nearly a factor of two. The quality sharpness metrics varied little in performance. In situations where the seeing conditions are very poor,  $r_o < 12$  cm, the maximum differential sharpness metric ( $S_7$ ) is superior. The spectral maximization metric ( $S_{S1}$ ) was chosen to represent frame selection performance because of its consistency to perform well over a wide variety of conditions. Although, frame selection SNR performance was reduced by about 20% for point sources, the phase error did not increase significantly. The benefit gained by a 50% data reduction outweighs the 20% drop in performance. Furthermore, when it comes to extended sources, the primary Air Force interest, frame selection, using the  $S_{S1}$  metric with a 50% FSR performed as well as the 100% case over all  $r_o$  and  $m_v$  values tested.



(a)



(b)

Figure 4.10 Typical extended source, reconstructed using a) 100% of the frames b) 50% frame selection, using the spectral maximization ( $S_{S1}$ ) metric, via a 1 meter telescope at 500 kilometers, with seeing conditions of  $r_o=07$  cm and  $m_\nu=1$ .

## *V. Conclusions and Recommendations*

This investigation began due to the need to devise an effective post-processing technique that does not rely on expensive adaptive optics. Frame selection needed to be extended to uncompensated speckle imaging. A complete understanding of the capability of this technique is critical to its application to U. S. Air Force imaging problems. This thesis determines whether or not frame selection processing enhances the speed and efficiency of data management for image processing, without significant loss in quality. This quality is measured in terms of power spectrum SNR and bispectrum phase error. This chapter presents a summary of the accomplishments documented in this thesis and provides recommendations for further research in this area.

### *5.1 Conclusions*

This thesis makes the following conclusions:

1. The five quality sharpness metrics all performed about the same for both point and extended sources.
2. Frame selection using the  $S_{S1}$  metric performed well in all circumstances for both point and extended sources. The 50% FSR resulted in a 20% reduction in SNR performance for the point source, but no significant change in phase error. For extended sources, there was no significant change in SNR or phase error performance.
3. Increasing the Fried seeing parameter,  $r_o$ , improves image quality, but has little effect on frame selection performance. Decreasing  $r_o$  had the effect of decreasing frame selection SNR performance for point sources, but no effect on phase error. Decreasing  $r_o$  had no effect on frame selection performance for extended sources.

4. Increased target brightness, in the form of decreased visual magnitude,  $m_v$ , improves image quality, but has little effect on frame selection performance. Increasing  $m_v$  had the effect of decreasing frame selection SNR performance for point sources, but no effect on phase error. Increasing  $m_v$  had no effect on frame selection performance for extended sources.
5. A 50% frame selection using the  $S_{S1}$  sharpness metric, for the extended source, results in a composite image that has the same visual quality as the 100% case. Satellites are the extended sources are of primary interest to the U. S. Air Force. The benefit gained from frame selection is a factor of two reduction in data required to produce the composite satellite image. A 50% reduction in data translates to nearly double the processing speed.

## 5.2 *Recommendations for Further Research*

1. Frame selection should be fully demonstrated on real data collected with adequately short exposure times. This data could be obtained from an Air Force facility such as the Starfire Optical Range (SOR) 3.5 meter telescope, or the Air Force Maui Optical Site (AMOS) 1.6 meter telescope.
2. The effects of exposure time on image quality should be fully demonstrated on speckle image processing. The simulation package used in this thesis does not take into account the effect of increasing the integration or exposure times,  $\tau$ , of each image data frame. In an operating environment, there exists an optimum value for  $\tau$ . This optical parameter has both positive and negative effects. This thesis has only taken into account the positive effect of increasing  $\tau$ , that is, increasing the total number of photons per image. This by itself translates into increased target brightness, which is a measure of image quality. However, this single assumption neglects the fact that increasing  $\tau$  has the negative effect of increasing the blurring caused by turbulence and target motion, thus decreasing the image quality.

3. Other metrics, involving the unbiased image, or the power and phase spectrums should be explored. Since each metric studied so far only examines a single characteristic of image features, a new metric might contain aspects of more than one of the metrics studied in this thesis.
4. Since speckle imaging has not been shown to improve as a result of frame selection, closer attention needs to be paid to how far the performance is reduced. A comparison of frame selected data to randomly selected data deserves further consideration.

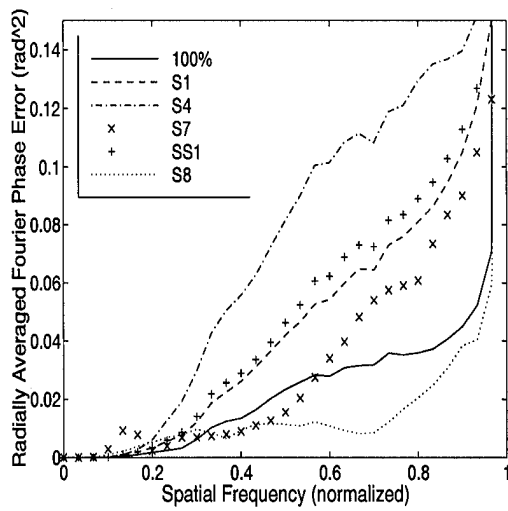
## *Appendix A. Simulation Results for Point Source*

The appendices include the complete collection of data results for all the quality sharpness metrics discussed in section 3.3.2. FSR's of 100, 80, 70, 60, and 50 % are all included. These are the results of two experiments: the point source, and the extended source. In each experiment, two visual parameters were varied: seeing conditions,  $r_o$ , and visual magnitude,  $m_v$ . The results of these experiments are presented in four parts: 1) the bispectrum phase error; 2) the power spectrum SNR; 3) the power spectrum SNR gain (with vs. without frame selection); and 4) the 4) comparative phase error plots.

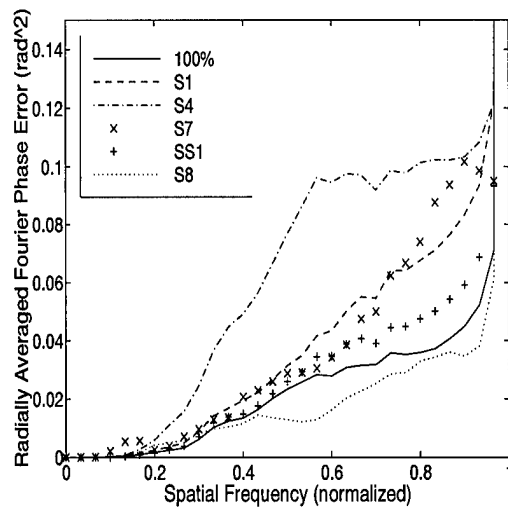
This appendix contains the results of the point source experiment.

### *A.1 Point Source Bispectrum Phase Error*

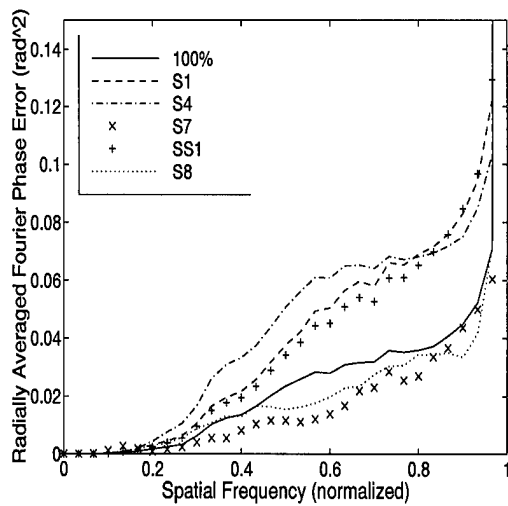
This section contains the phase error results for the point source experiment. On each page, the four FSR strategies are presented, containing the results of the five metrics tested. A given set of visual parameters,  $r_o$  and  $m_\nu$ , are identified below.



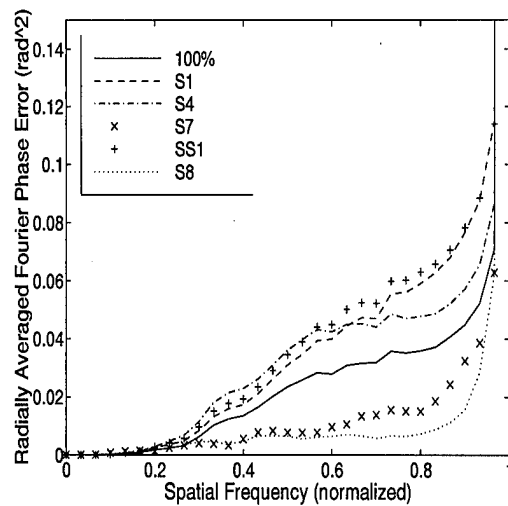
(a)



(b)



(c)



(d)

Figure A.1 Bispectrum phase error, point source,  $m_\nu = 1$ ,  $r_o = 7$  cm. FSR = a) 50% b) 60% c) 70% d) 80%

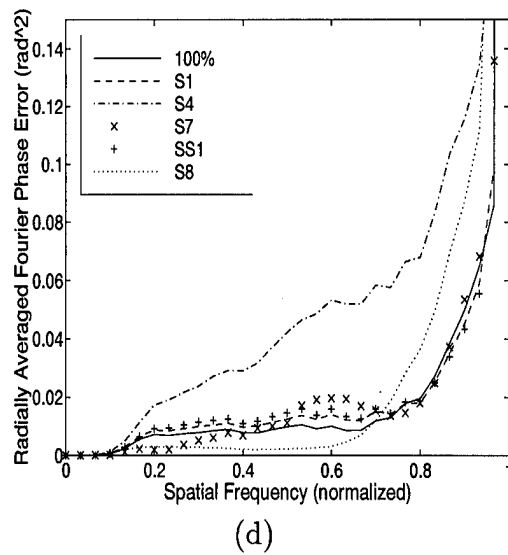
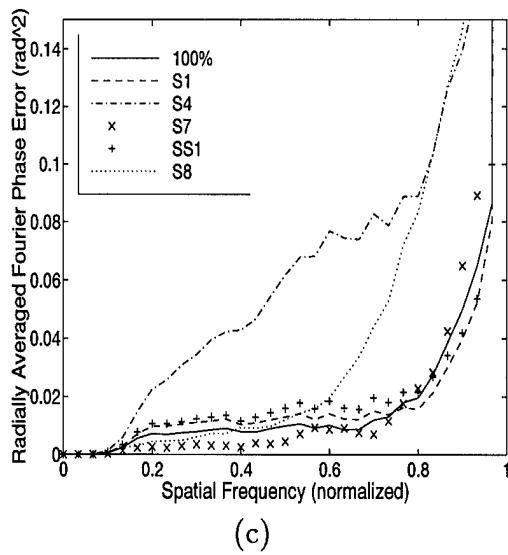
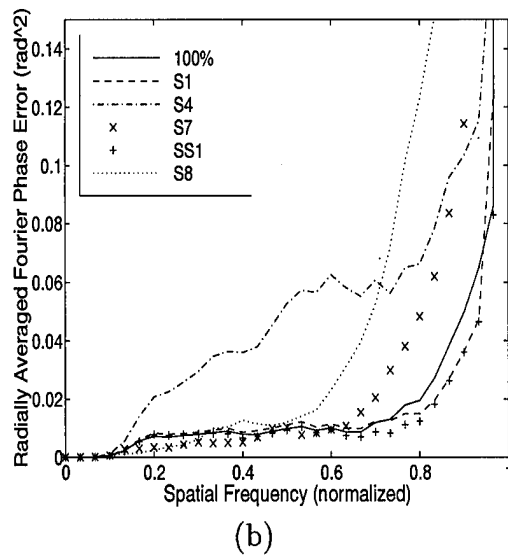
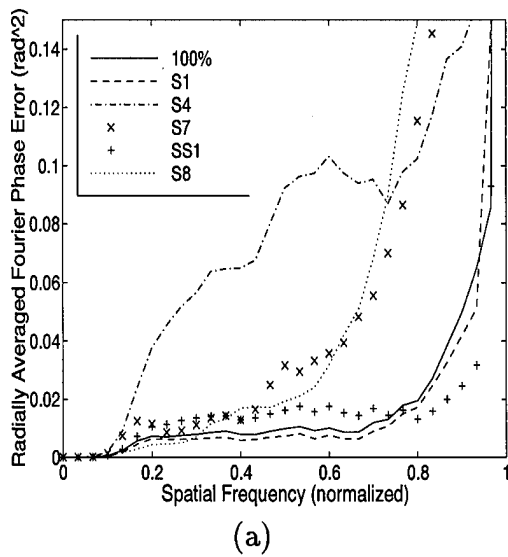
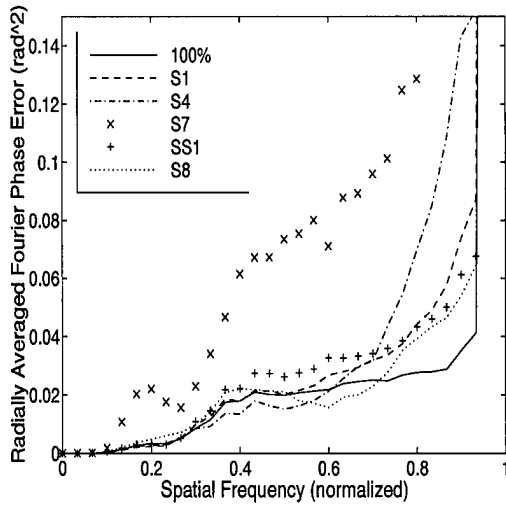
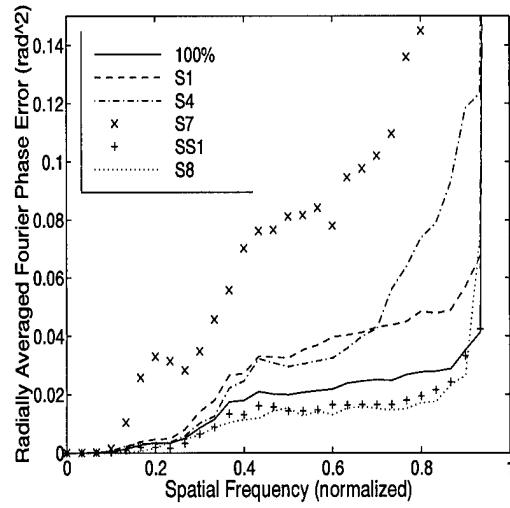


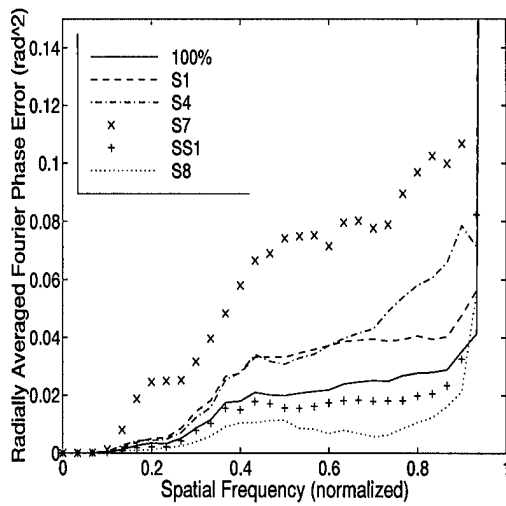
Figure A.2 Bispectrum phase error, point source,  $m_\nu = 3$ ,  $r_o = 7$  cm. FSR = a) 50% b) 60% c) 70% d) 80%



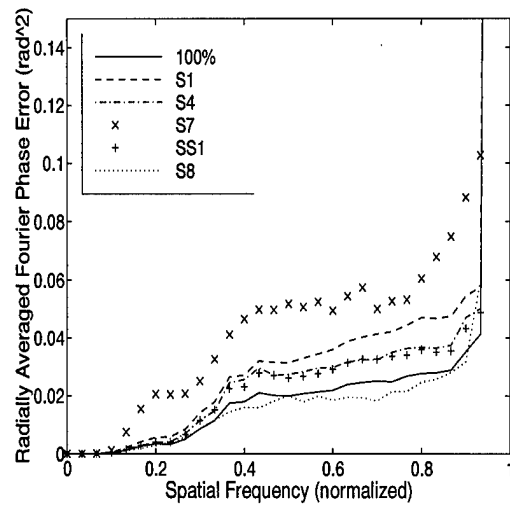
(a)



(b)



(c)



(d)

Figure A.3 Bispectrum phase error, point source,  $m_\nu = 5$ ,  $r_o = 7$  cm. FSR = a) 50% b) 60% c) 70% d) 80%

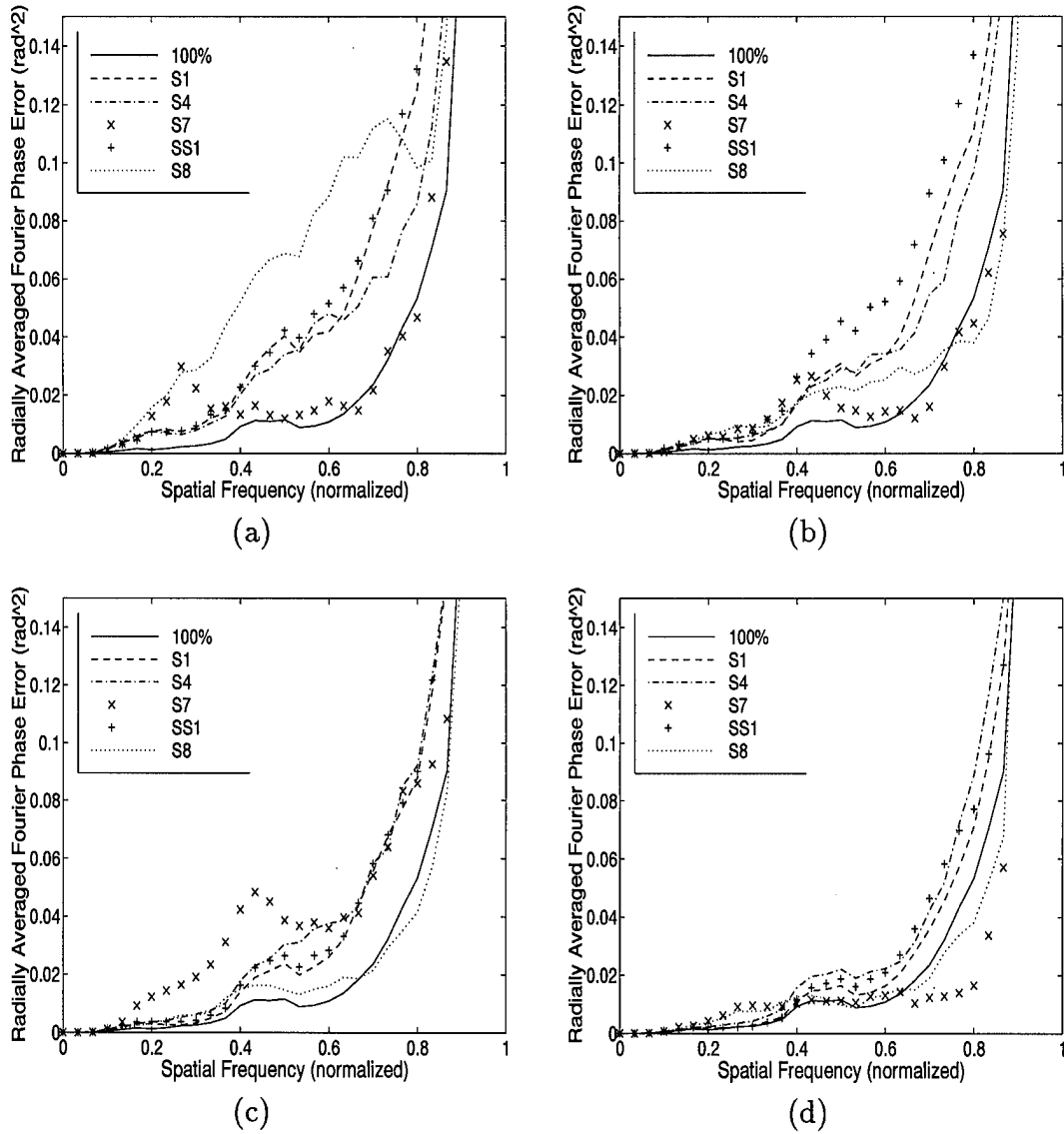


Figure A.4 Bispectrum phase error, point source,  $m_\nu = 7$ ,  $r_o = 7$  cm. FSR = a) 50% b) 60% c) 70% d) 80%

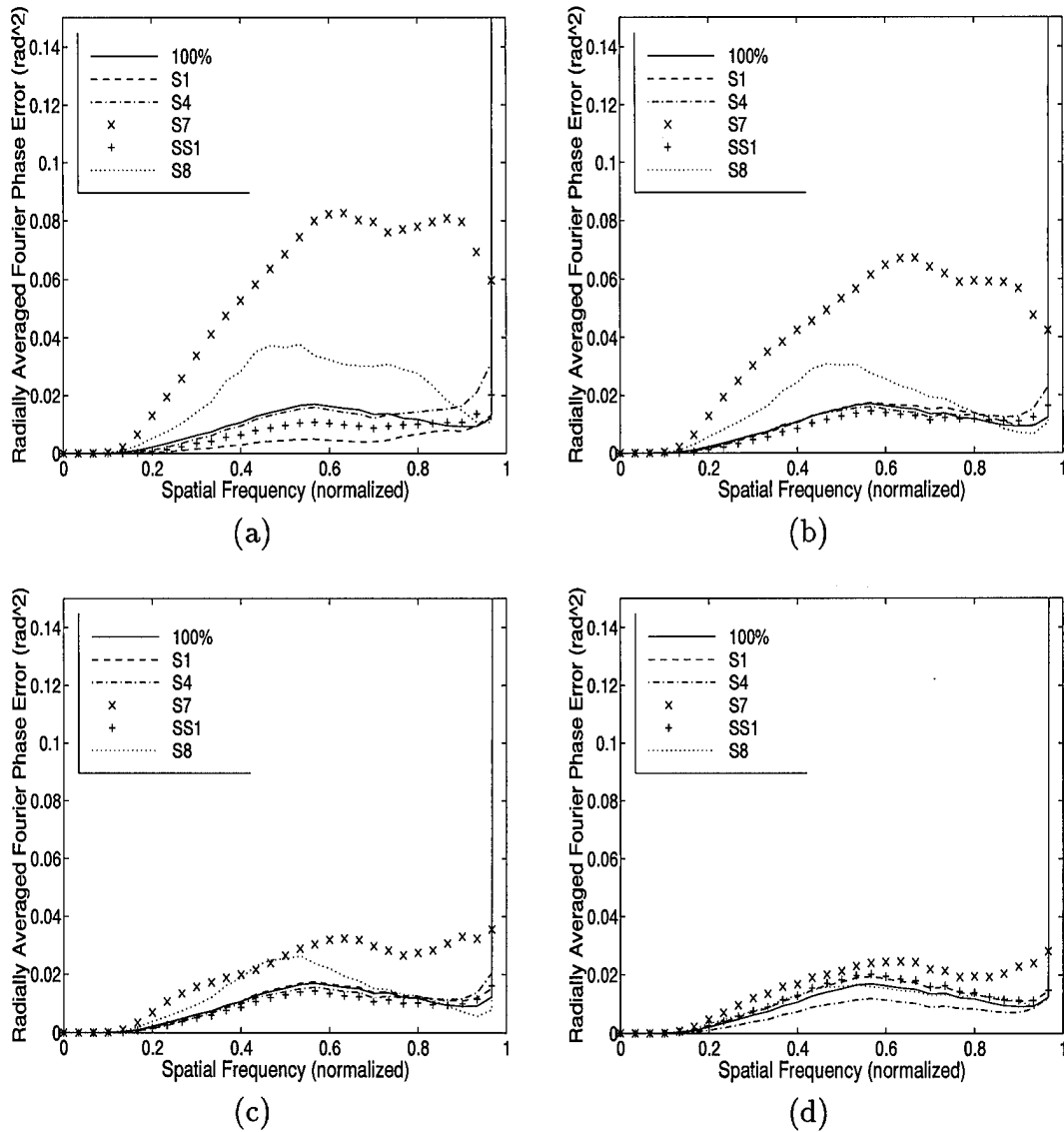


Figure A.5 Bispectrum phase error, point source,  $m_\nu = 1$ ,  $r_o = 12$  cm. FSR = a) 50% b) 60% c) 70% d) 80%

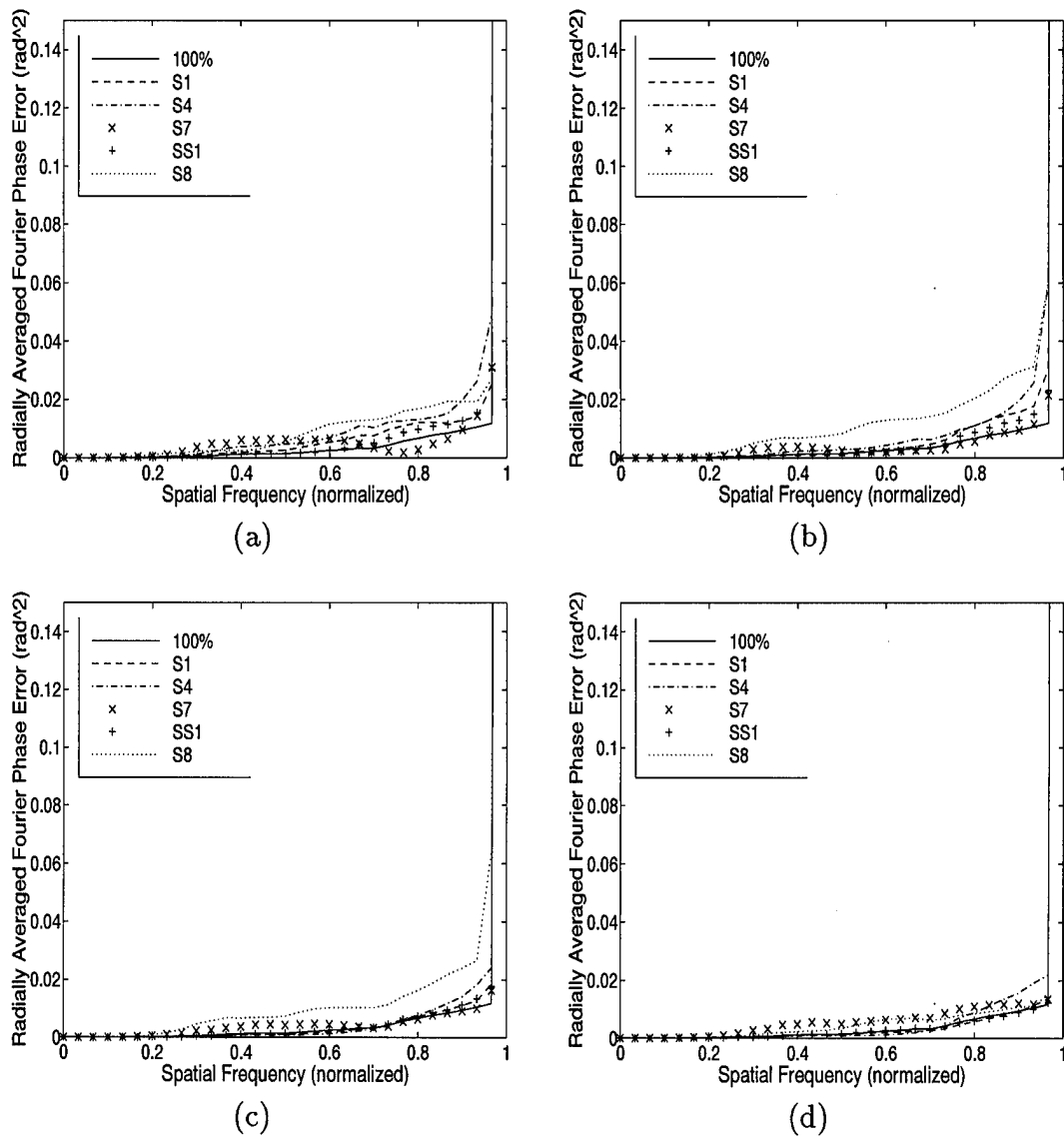
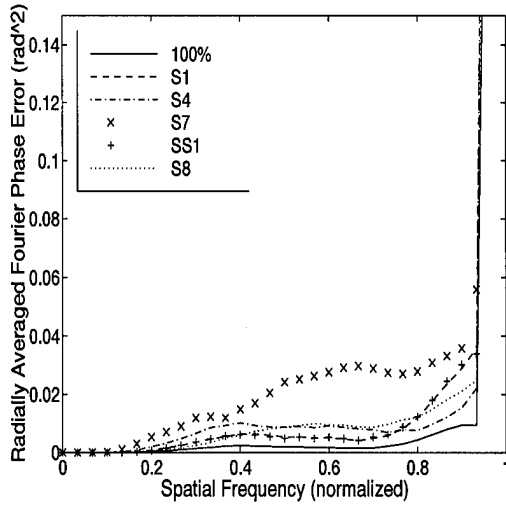
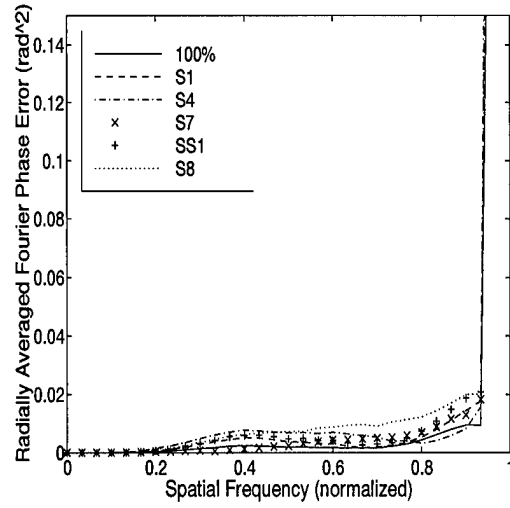


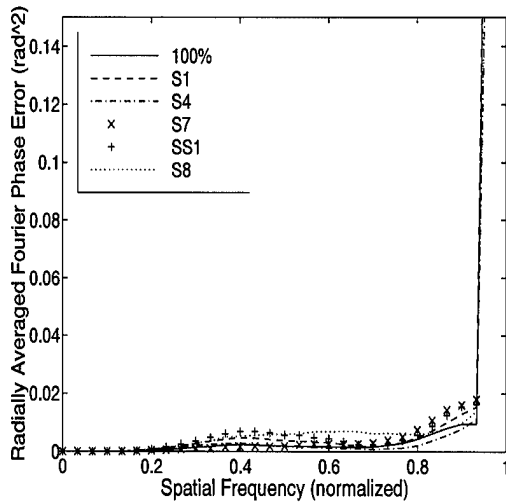
Figure A.6 Bispectrum phase error, point source,  $m_\nu = 3$ ,  $r_o = 12$  cm. FSR = a) 50% b) 60% c) 70% d) 80%



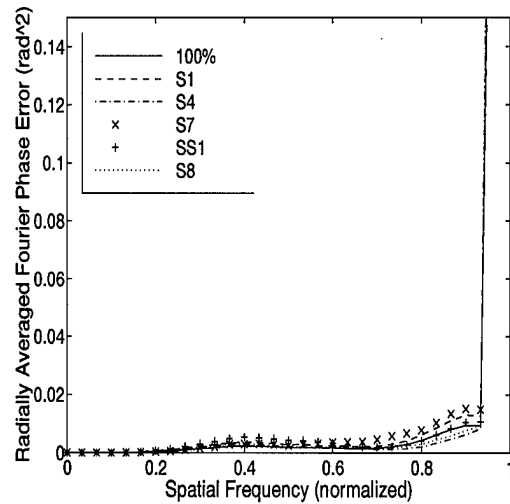
(a)



(b)

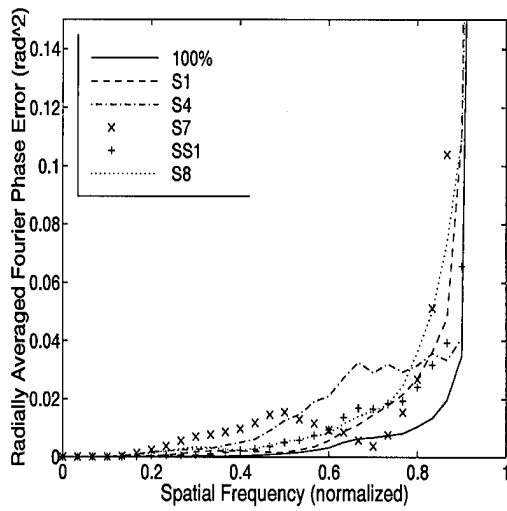


(c)

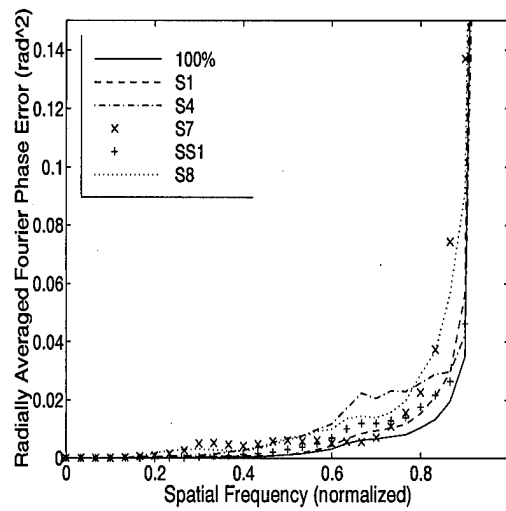


(d)

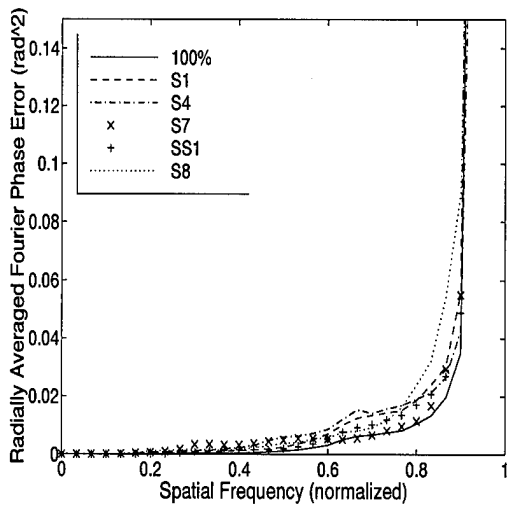
Figure A.7 Bispectrum phase error, point source,  $m_\nu = 5$ ,  $r_o = 12$  cm. FSR = a) 50% b) 60% c) 70% d) 80%



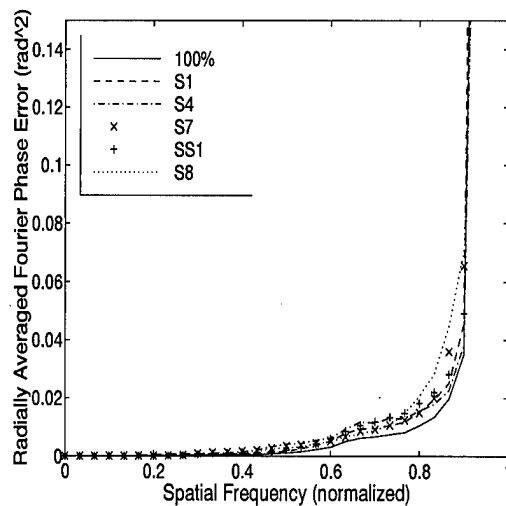
(a)



(b)

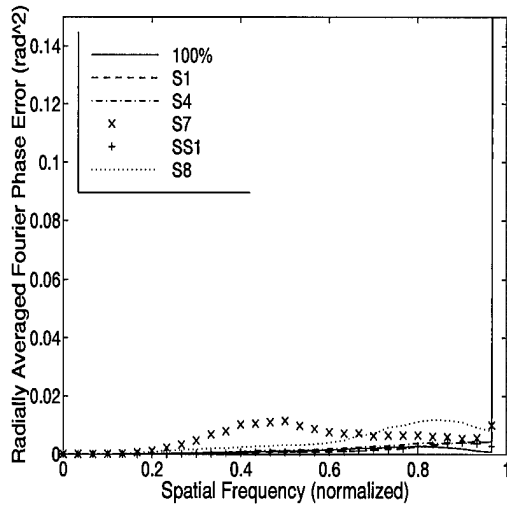


(c)

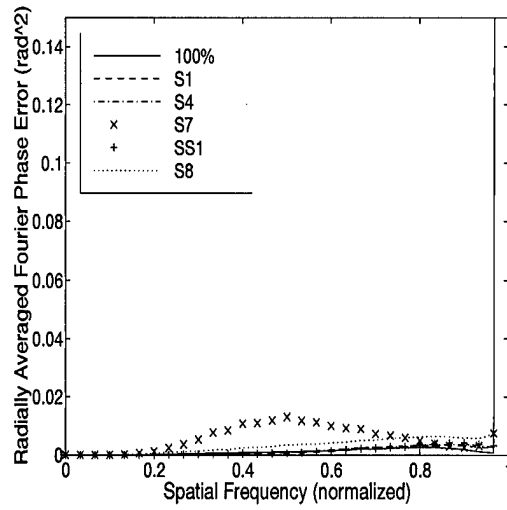


(d)

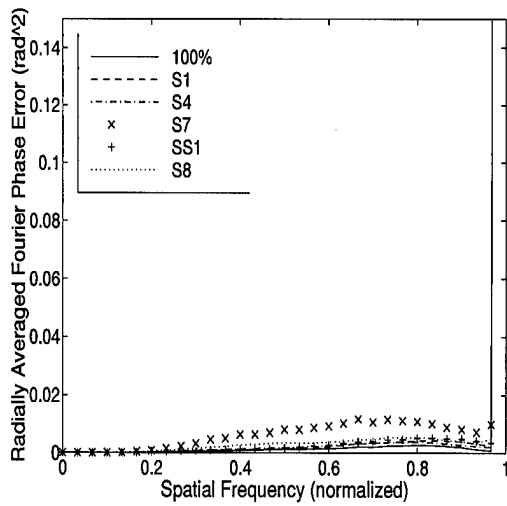
Figure A.8 Bispectrum phase error, point source,  $m_\nu = 7$ ,  $r_o = 12$  cm. FSR = a) 50% b) 60% c) 70% d) 80%



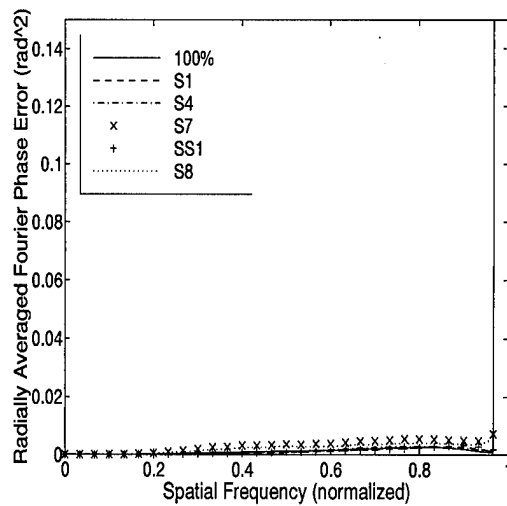
(a)



(b)

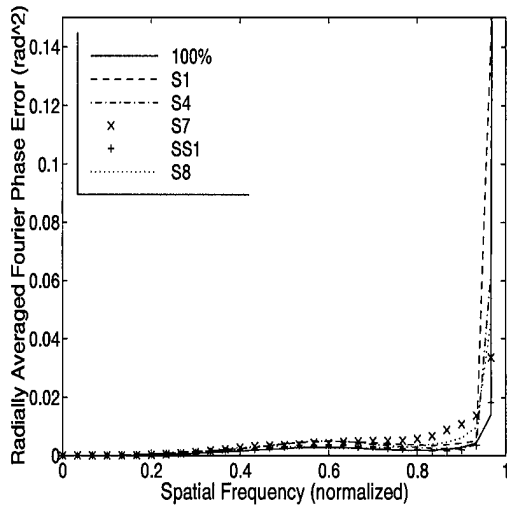


(c)

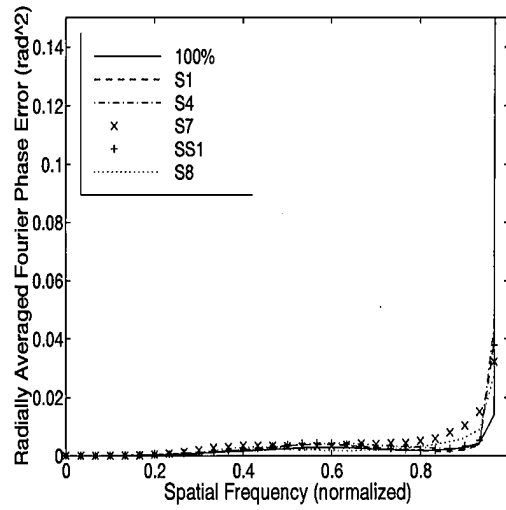


(d)

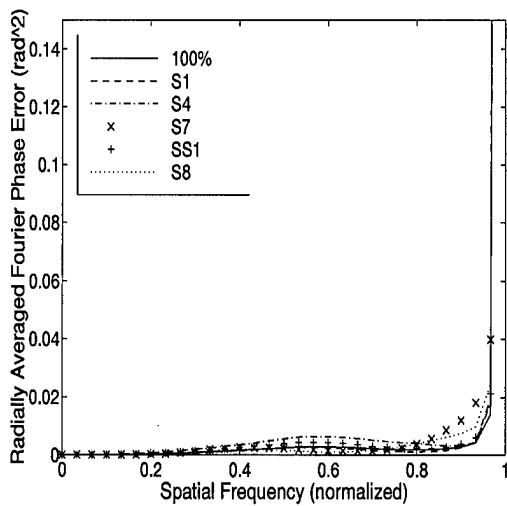
Figure A.9 Bispectrum phase error, point source,  $m_\nu = 1$ ,  $r_o = 17$  cm. FSR = a) 50% b) 60% c) 70% d) 80%



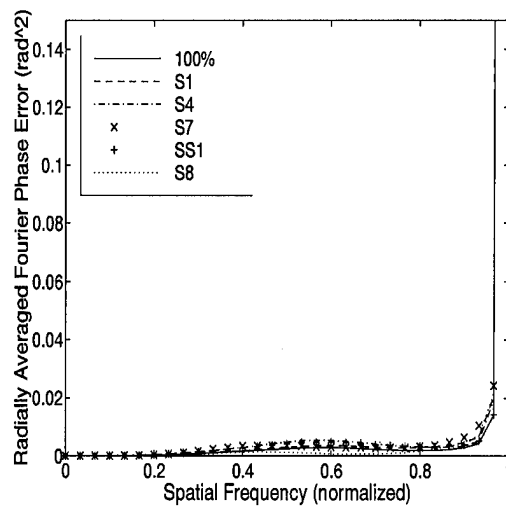
(a)



(b)

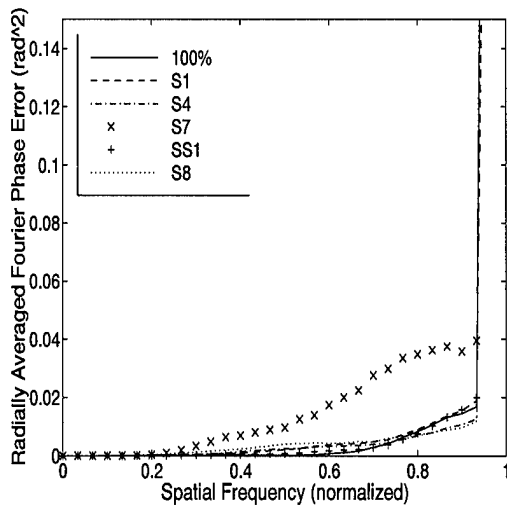


(c)

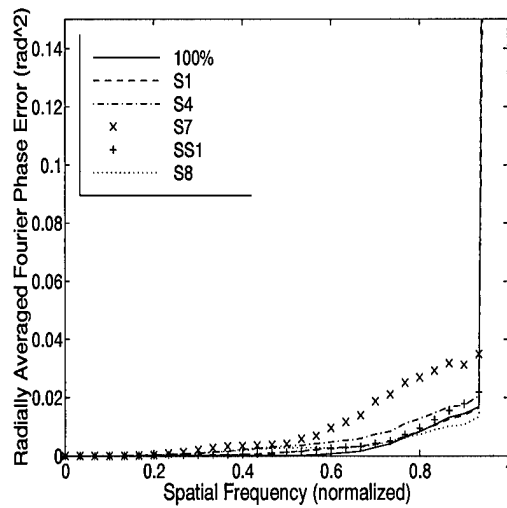


(d)

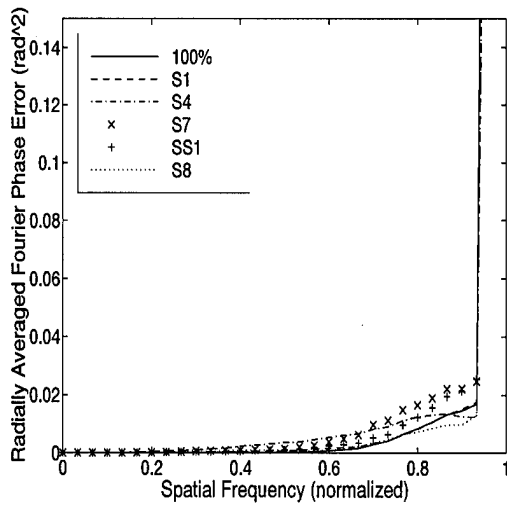
Figure A.10 Bispectrum phase error, point source,  $m_\nu = 3$ ,  $r_o = 17$  cm. FSR = a) 50% b) 60% c) 70% d) 80%



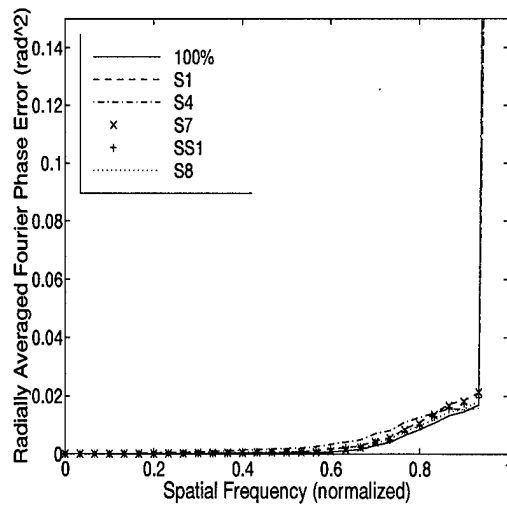
(a)



(b)

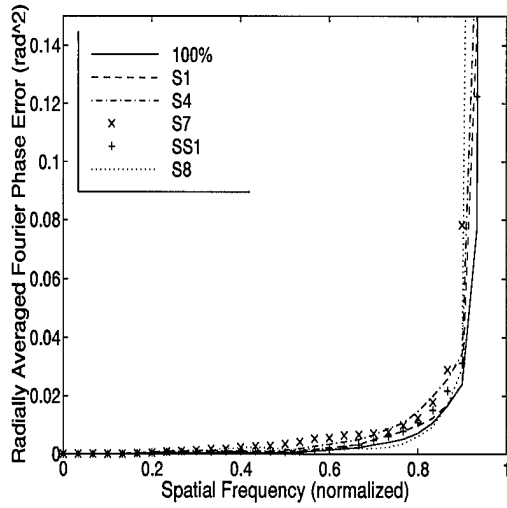


(c)

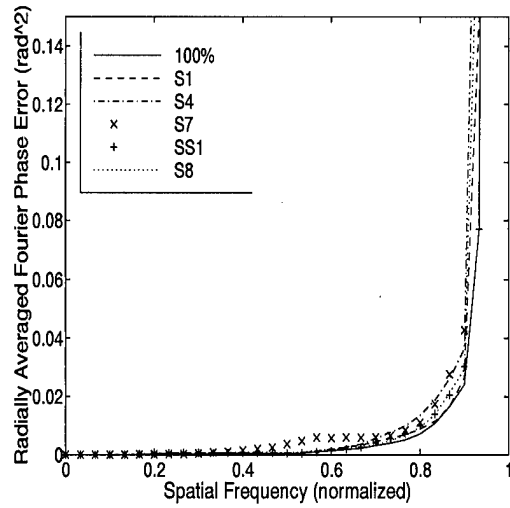


(d)

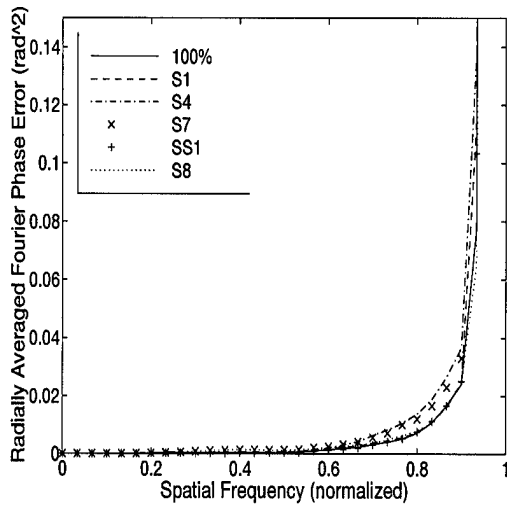
Figure A.11 Bispectrum phase error, point source,  $m_\nu = 5$ ,  $r_o = 17$  cm. FSR = a) 50% b) 60% c) 70% d) 80%



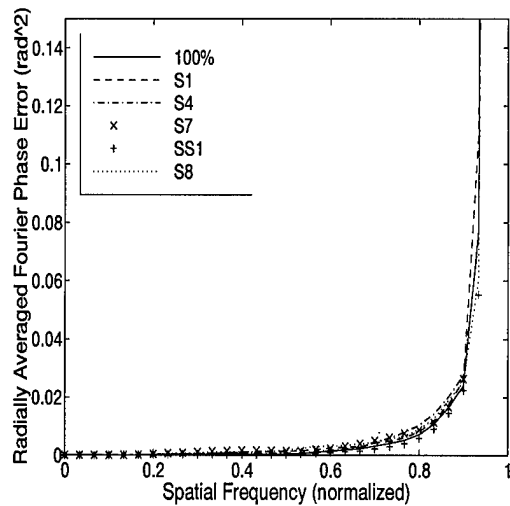
(a)



(b)



(c)

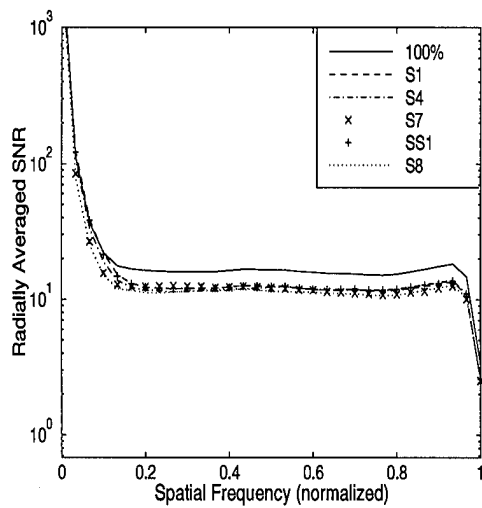


(d)

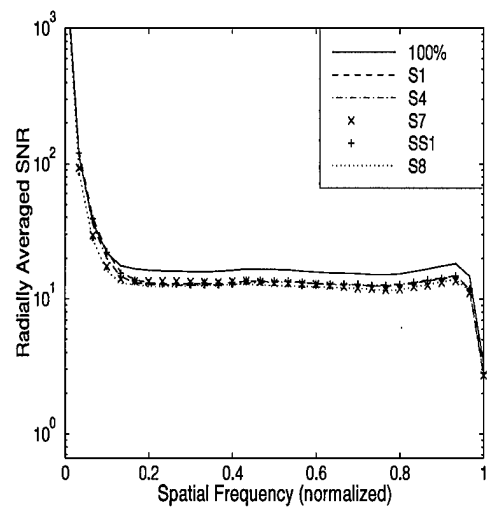
Figure A.12 Bispectrum phase error, point source,  $m_\nu = 7$ ,  $r_o = 17$  cm. FSR = a) 50% b) 60% c) 70% d) 80%

## *A.2 Point Source Power Spectrum SNR*

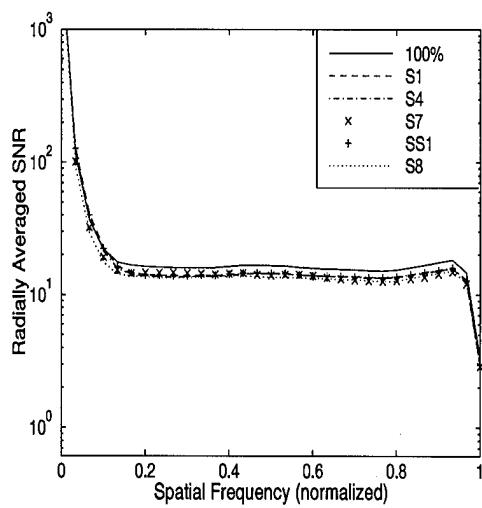
This section contains the power spectrum SNR results for the point source experiment. On each page, the four FSR strategies are presented, containing the results of the five metrics tested. A given set of visual parameters,  $r_o$  and  $m_\nu$ , are identified below.



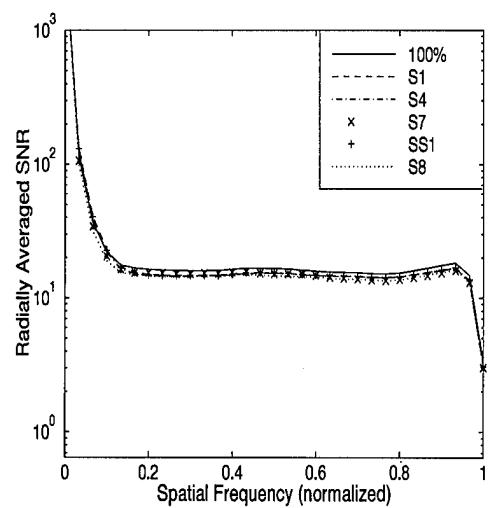
(a)



(b)

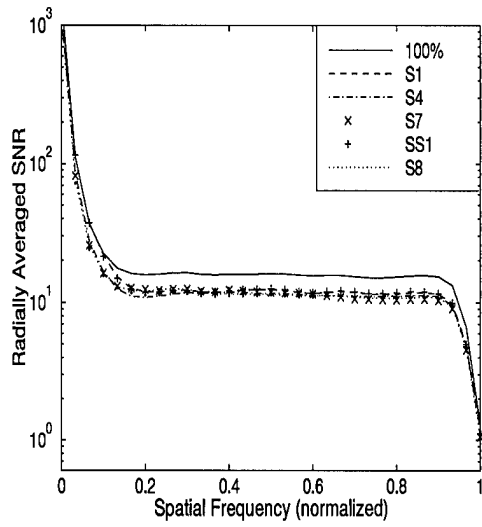


(c)

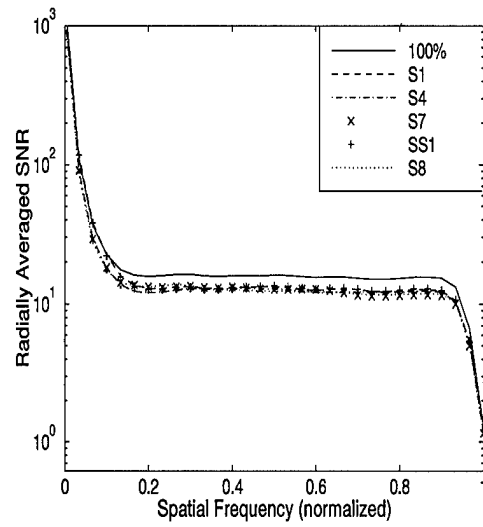


(d)

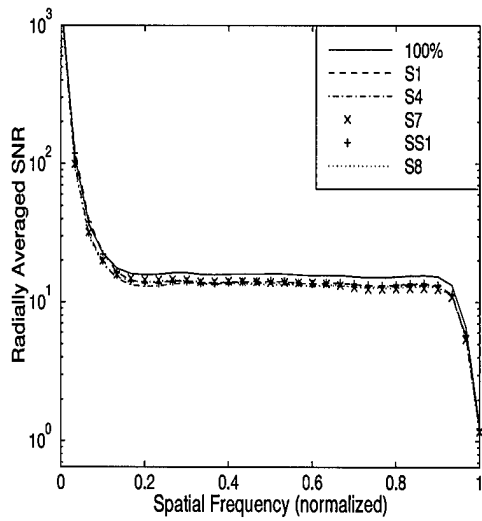
Figure A.13 Power spectrum SNR, point source,  $m_\nu = 1$ ,  $r_o = 7$  cm. FSR = a) 50% b) 60% c) 70% d) 80%



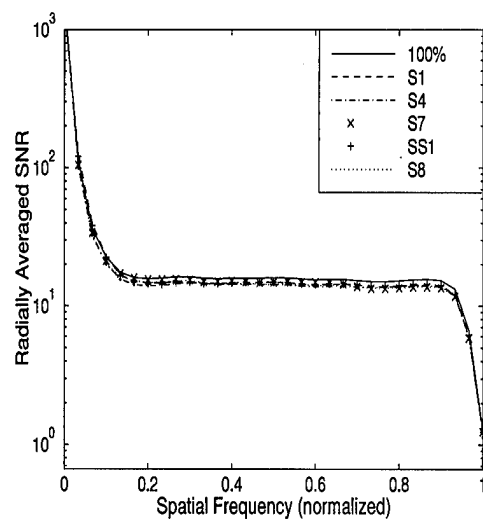
(a)



(b)

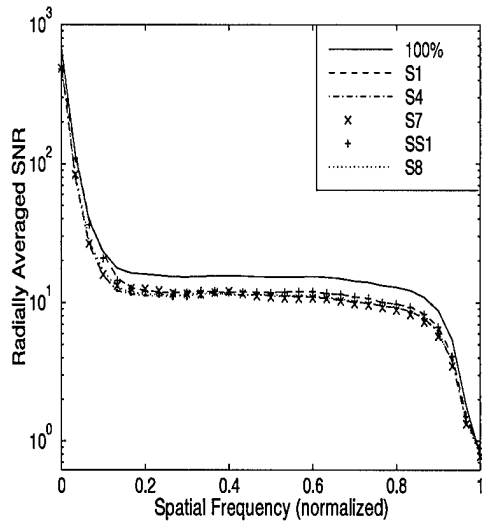


(c)

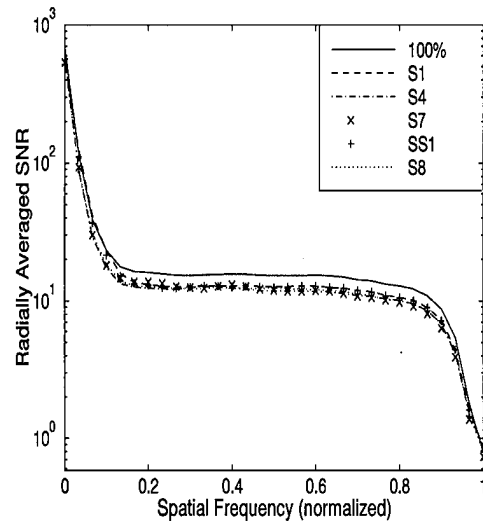


(d)

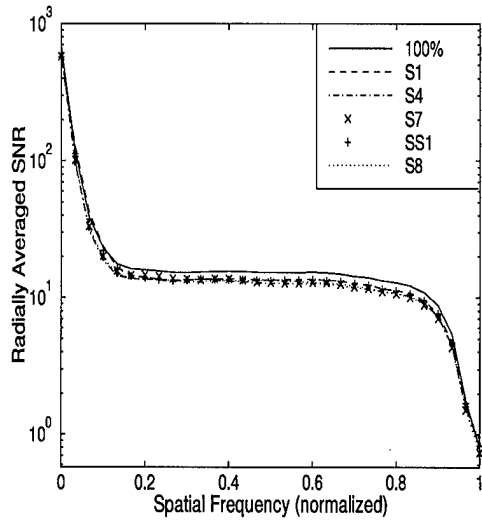
Figure A.14 Power spectrum SNR, point source,  $m_\nu = 3$ ,  $r_o = 7$  cm. FSR = a) 50% b) 60% c) 70% d) 80%



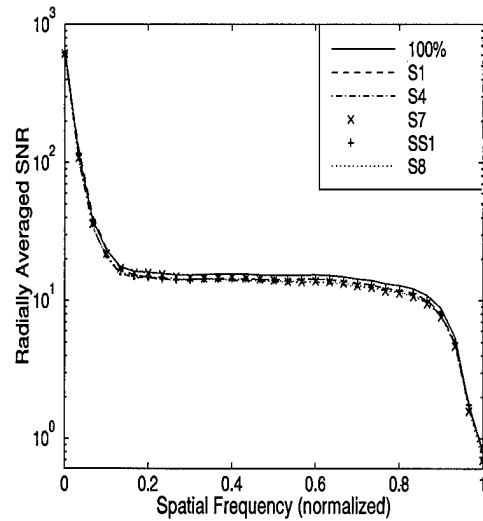
(a)



(b)

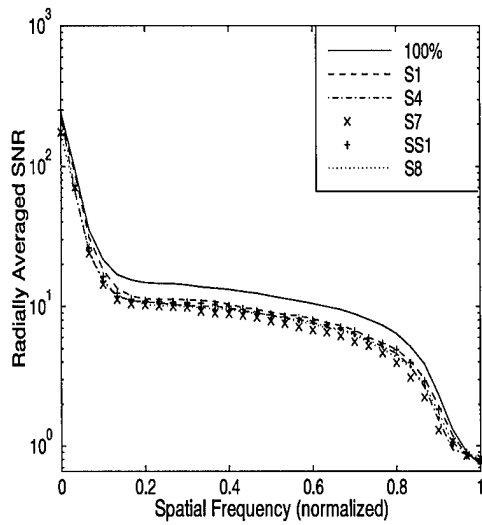


(c)

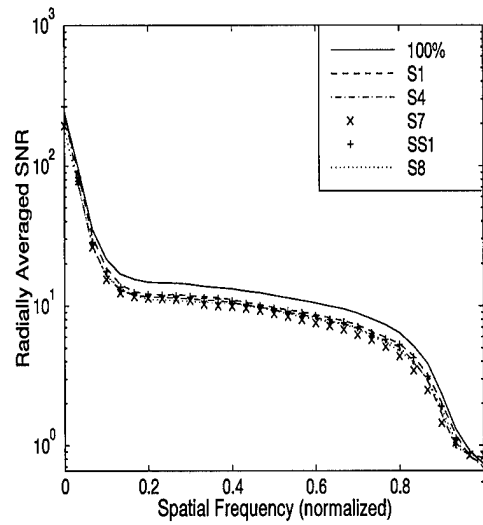


(d)

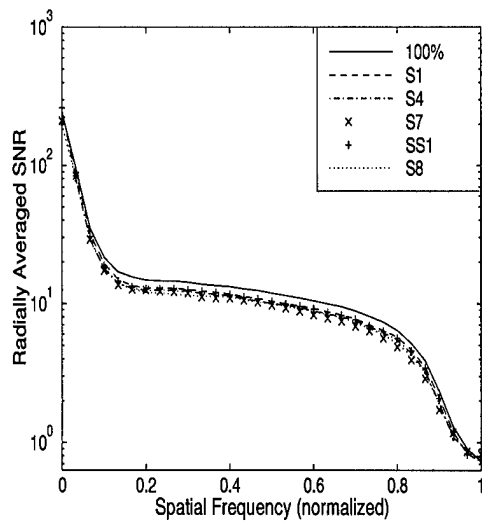
Figure A.15 Power spectrum SNR, point source,  $m_\nu = 5$ ,  $r_o = 7$  cm. FSR = a) 50% b) 60% c) 70% d) 80%



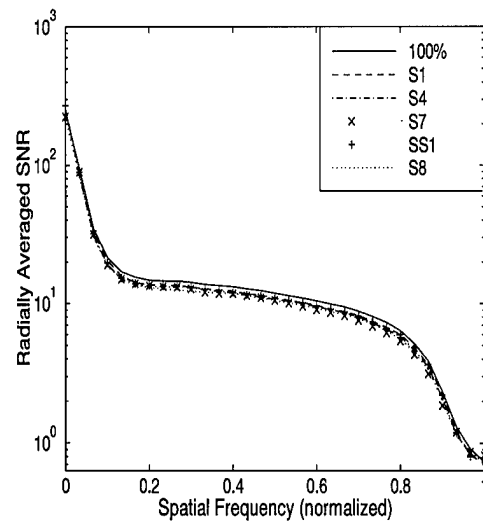
(a)



(b)

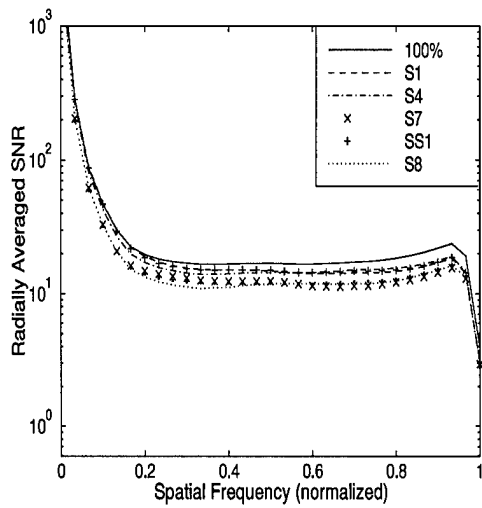


(c)

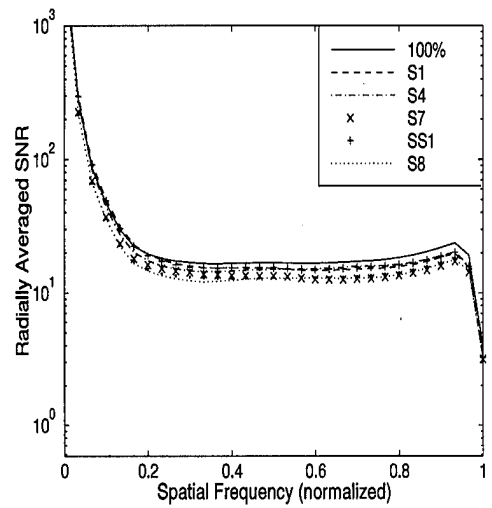


(d)

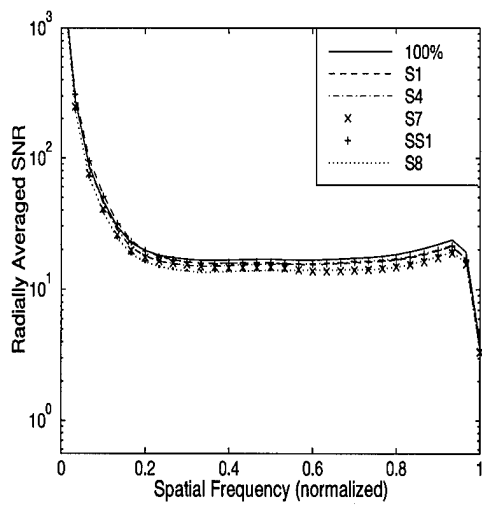
Figure A.16 Power spectrum SNR, point source,  $m_\nu = 7$ ,  $r_o = 7$  cm. FSR = a) 50% b) 60% c) 70% d) 80%



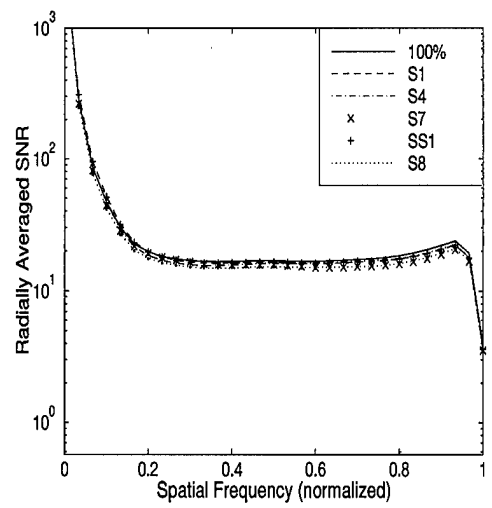
(a)



(b)

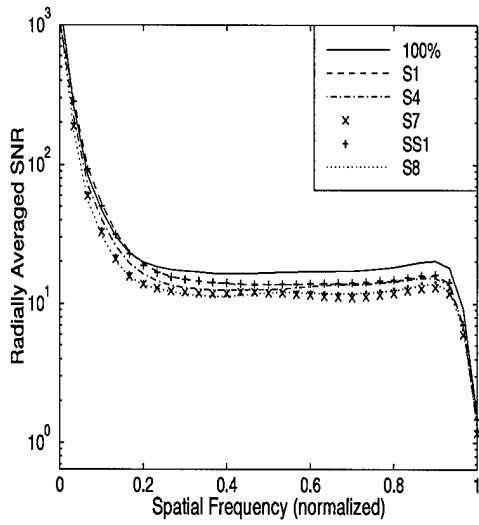


(c)

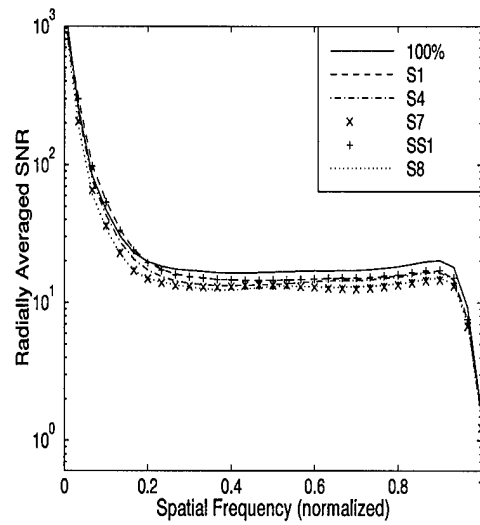


(d)

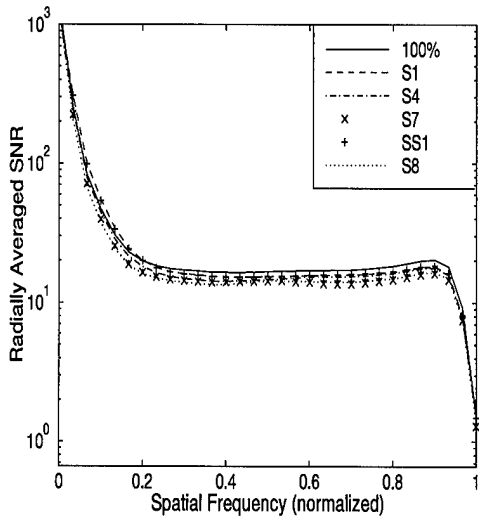
Figure A.17 Power spectrum SNR, point source,  $m_\nu = 1$ ,  $r_o = 12$  cm. FSR = a) 50% b) 60% c) 70% d) 80%



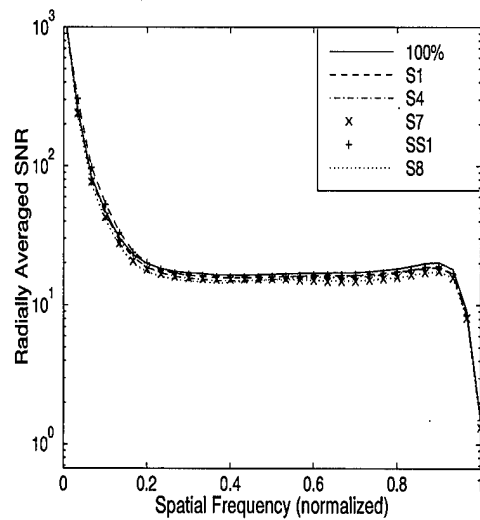
(a)



(b)

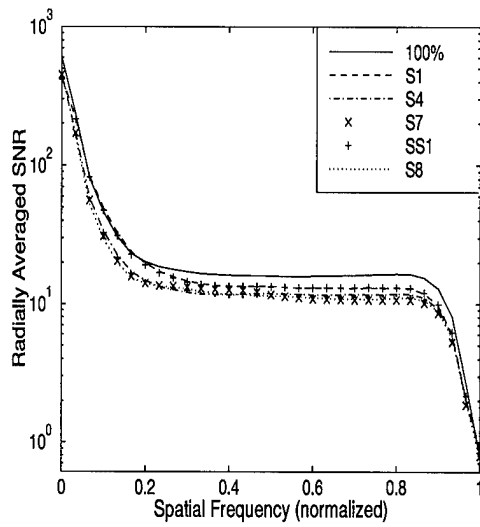


(c)

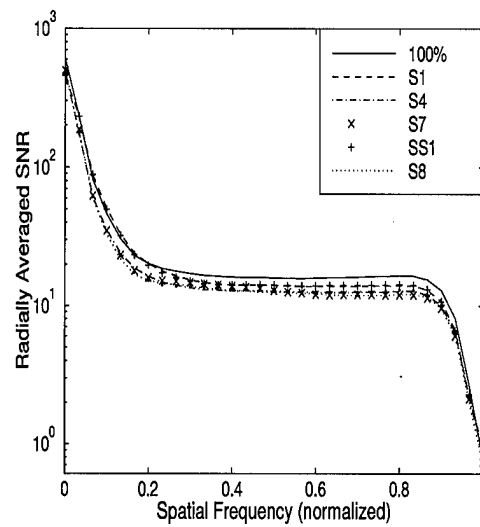


(d)

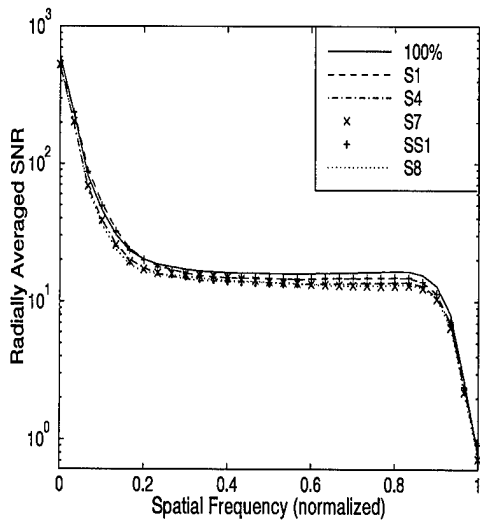
Figure A.18 Power spectrum SNR, point source,  $m_\nu = 3$ ,  $r_o = 12$  cm. FSR = a) 50% b) 60% c) 70% d) 80%



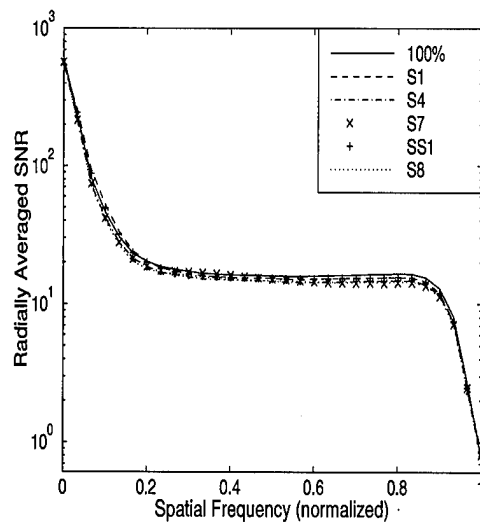
(a)



(b)

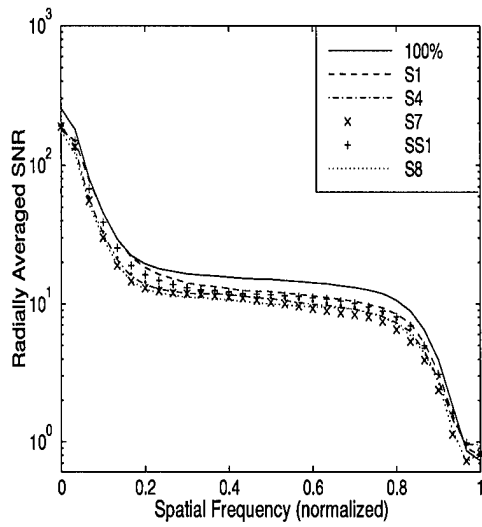


(c)

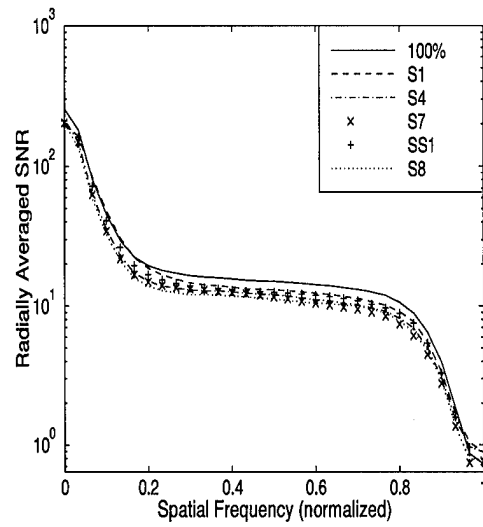


(d)

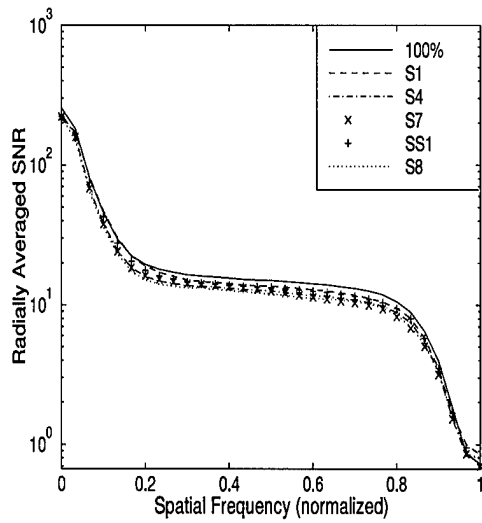
Figure A.19 Power spectrum SNR, point source,  $m_\nu = 5$ ,  $r_o = 12$  cm. FSR = a) 50% b) 60% c) 70% d) 80%



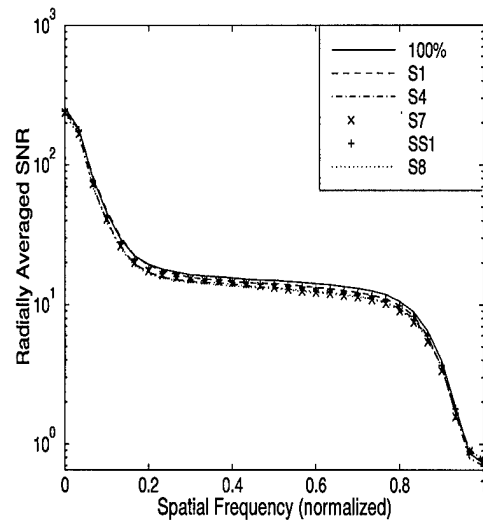
(a)



(b)

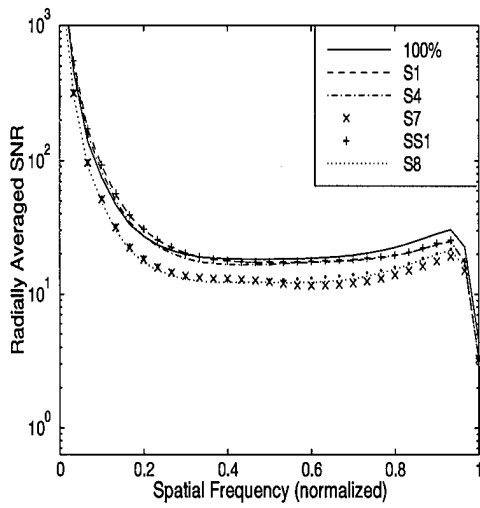


(c)

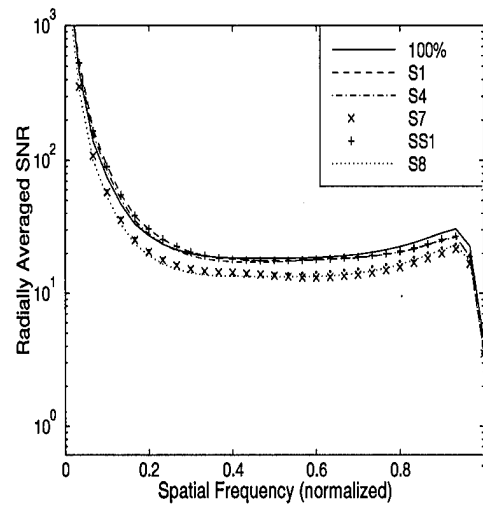


(d)

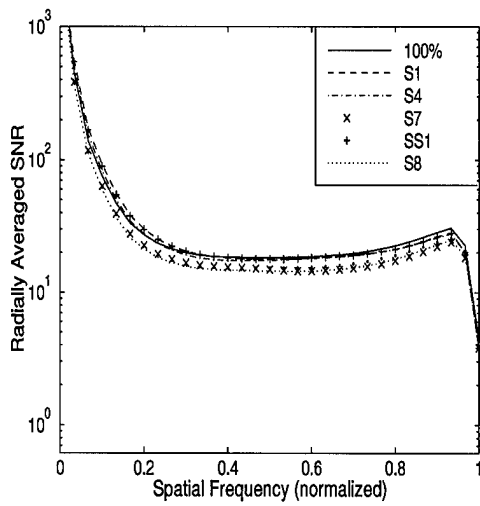
Figure A.20 Power spectrum SNR, point source,  $m_\nu = 7$ ,  $r_o = 12$  cm. FSR = a) 50% b) 60% c) 70% d) 80%



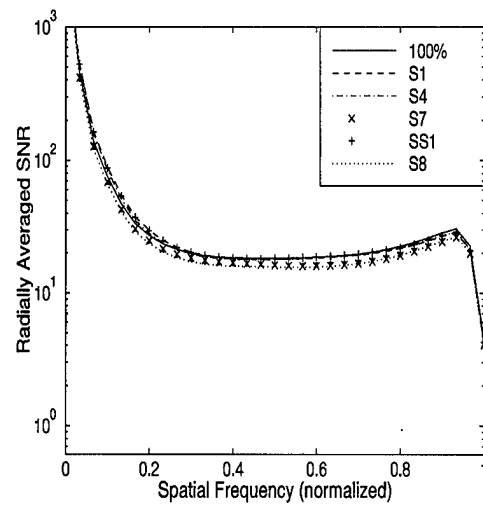
(a)



(b)

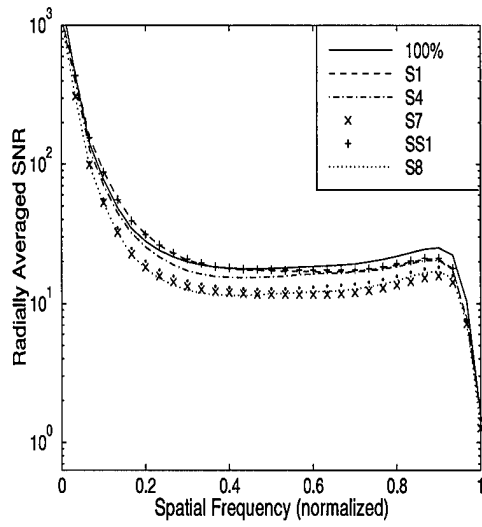


(c)

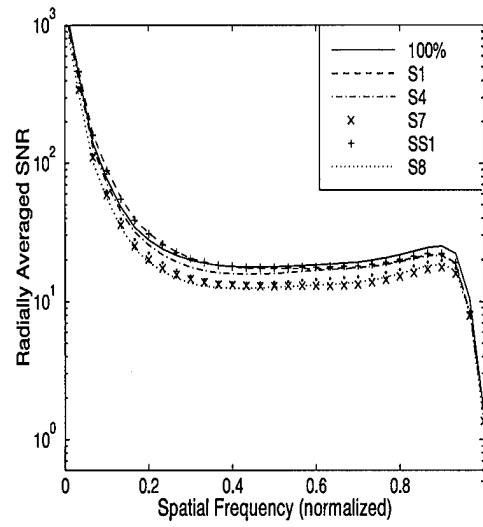


(d)

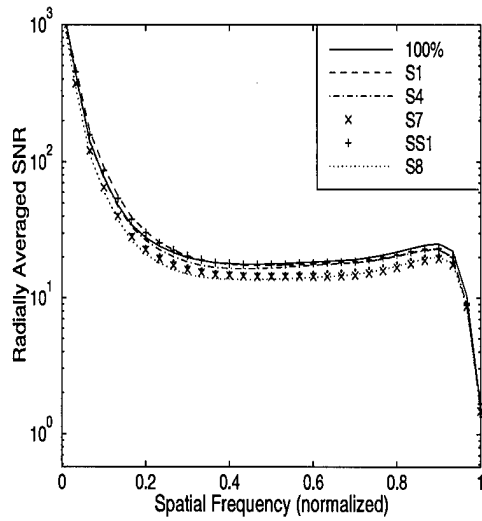
Figure A.21 Power spectrum SNR, point source,  $m_\nu = 1$ ,  $r_o = 17$  cm. FSR = a) 50% b) 60% c) 70% d) 80%



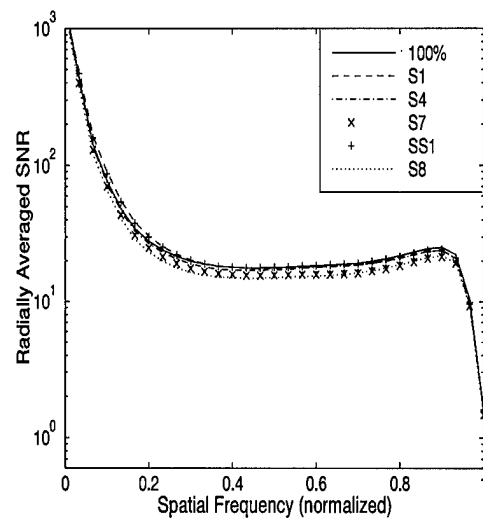
(a)



(b)

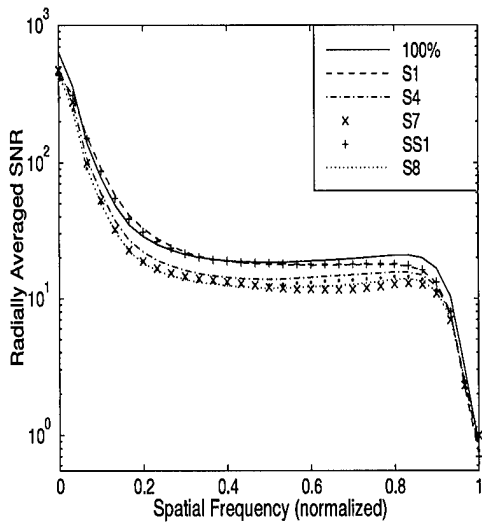


(c)

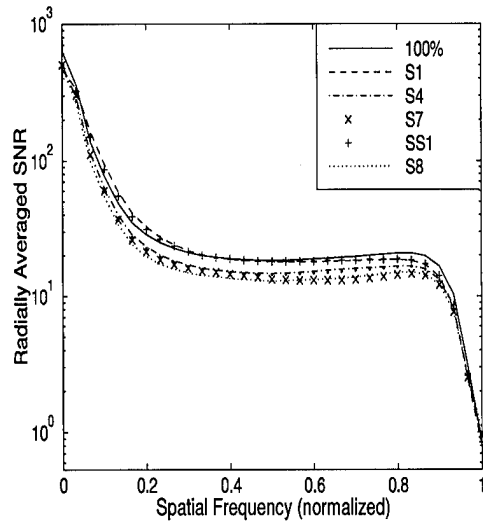


(d)

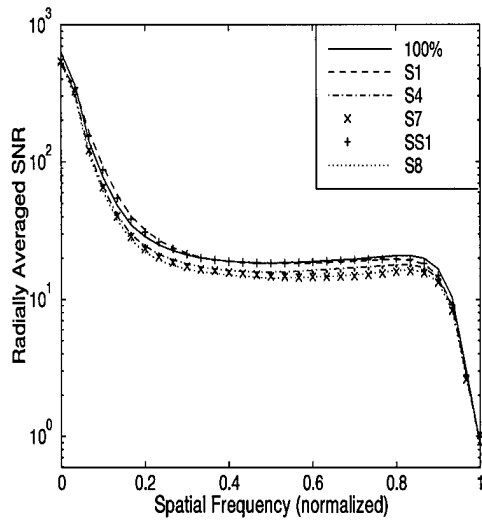
Figure A.22 Power spectrum SNR, point source,  $m_\nu = 3$ ,  $r_o = 17$  cm. FSR = a) 50% b) 60% c) 70% d) 80%



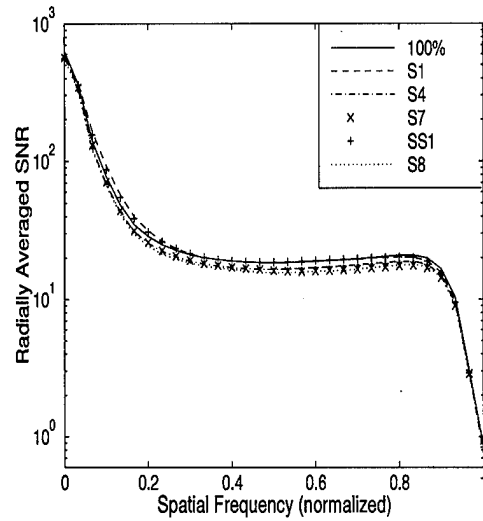
(a)



(b)

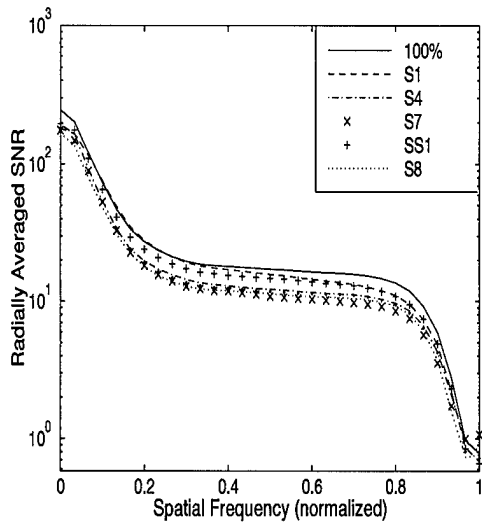


(c)

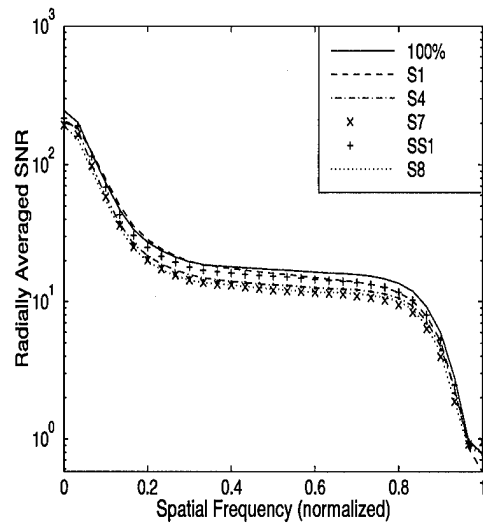


(d)

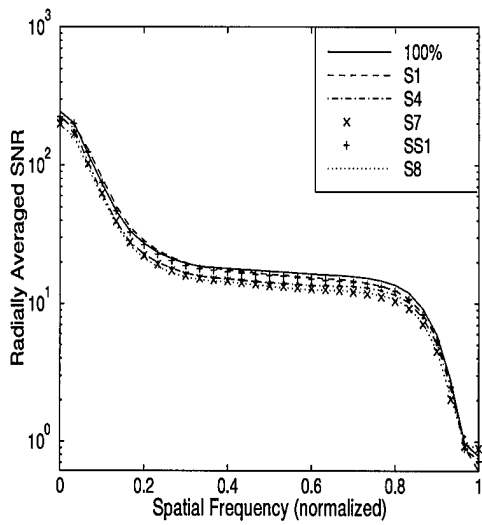
Figure A.23 Power spectrum SNR, point source,  $m_\nu = 5$ ,  $r_o = 17$  cm. FSR = a) 50% b) 60% c) 70% d) 80%



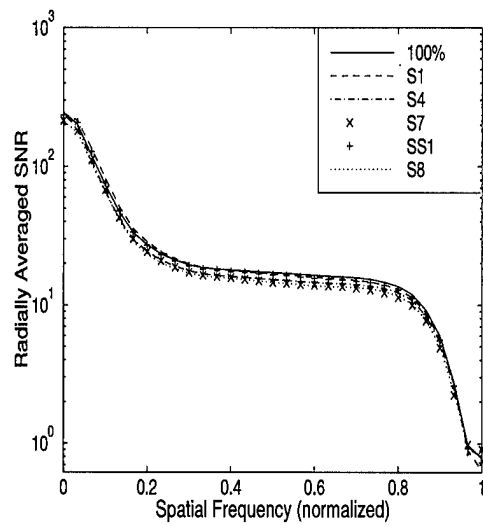
(a)



(b)



(c)

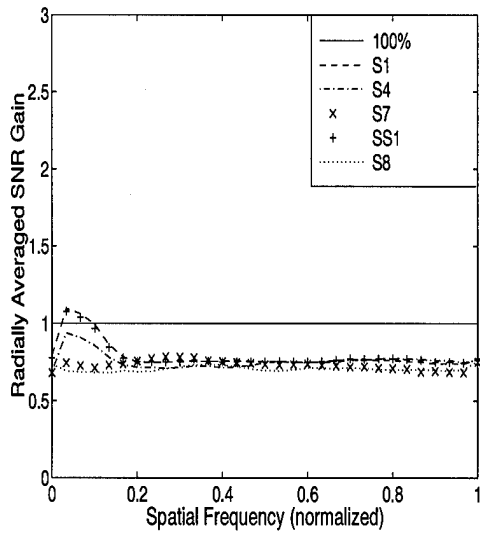


(d)

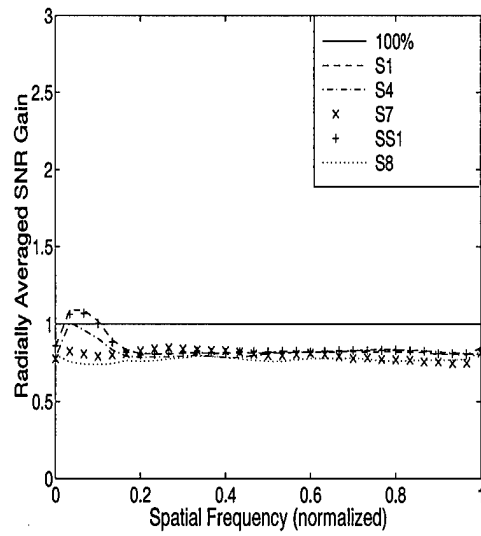
Figure A.24 Power spectrum SNR, point source,  $m_\nu = 7$ ,  $r_o = 17$  cm. FSR = a) 50% b) 60% c) 70% d) 80%

### *A.3 Point Source Power Spectrum Gain Plots*

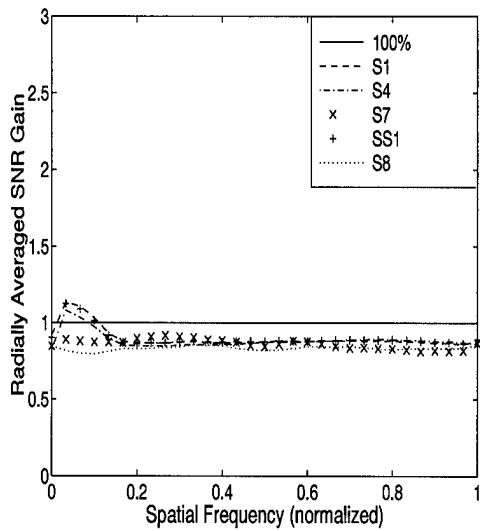
This section contains the power spectrum SNR gain plots for the extended source experiment. Gain is defined as the ratio of the power spectrum achieved by using frame selection to that without frame selection. On each page, the four FSR strategies are presented, containing the results of the five metrics tested. A given set of visual parameters,  $r_o$  and  $m_\nu$ , are identified below.



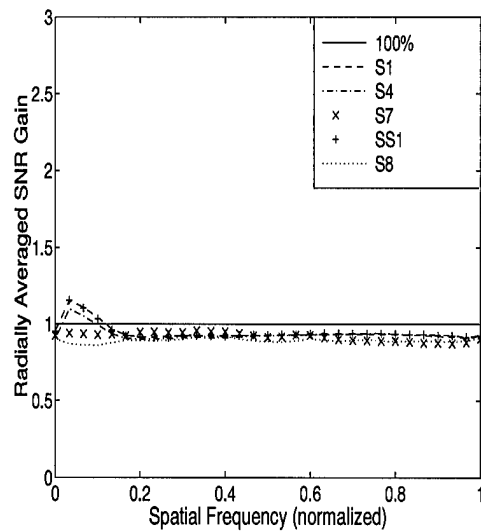
(a)



(b)

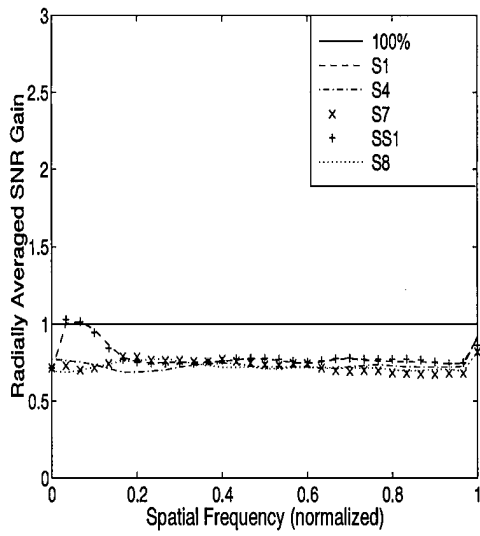


(c)

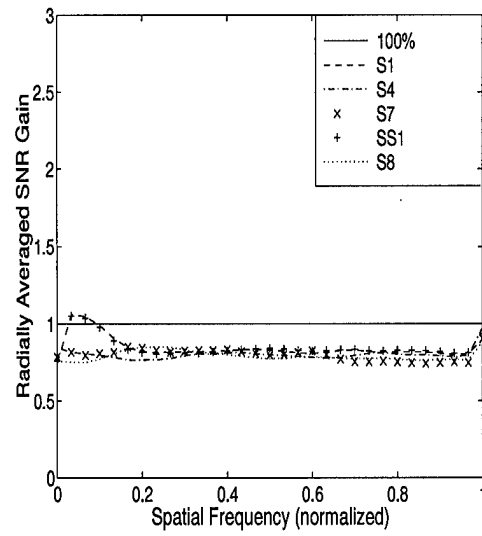


(d)

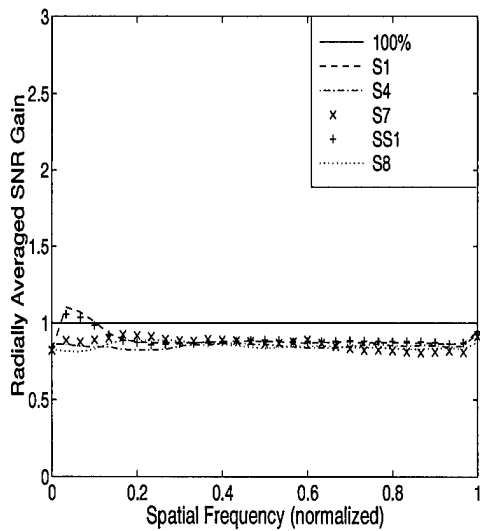
Figure A.25 Power spectrum gain, point source,  $m_\nu = 1$ ,  $r_o = 7$  cm. FSR = a) 50% b) 60% c) 70% d) 80%



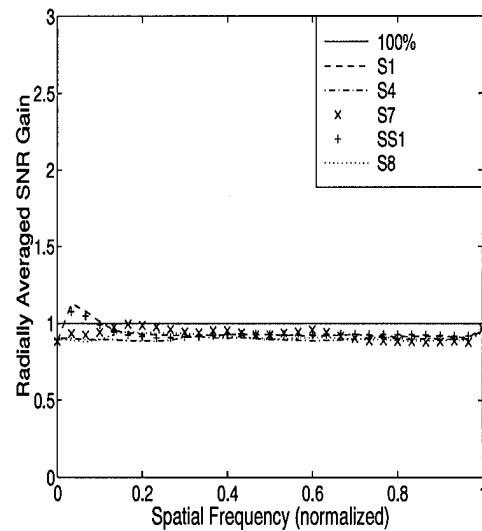
(a)



(b)

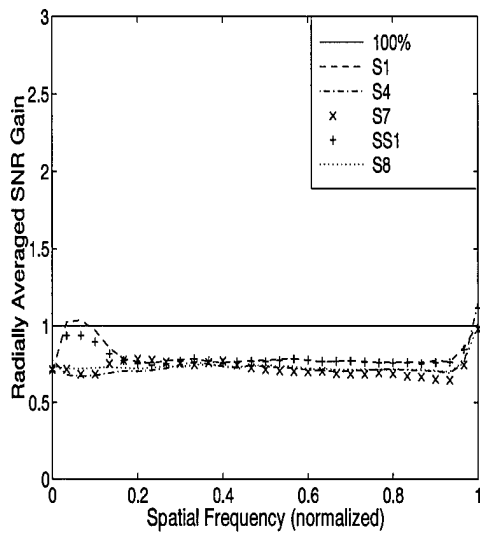


(c)

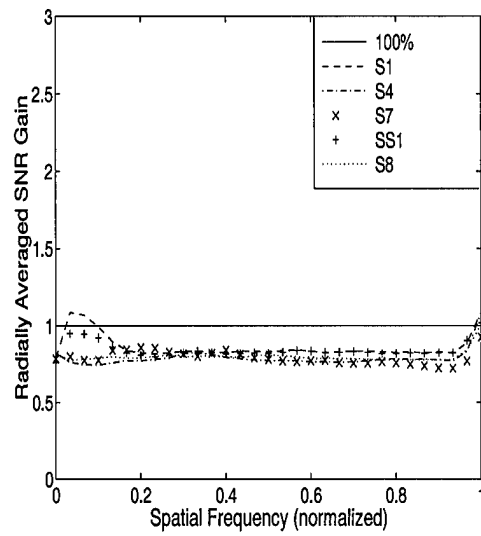


(d)

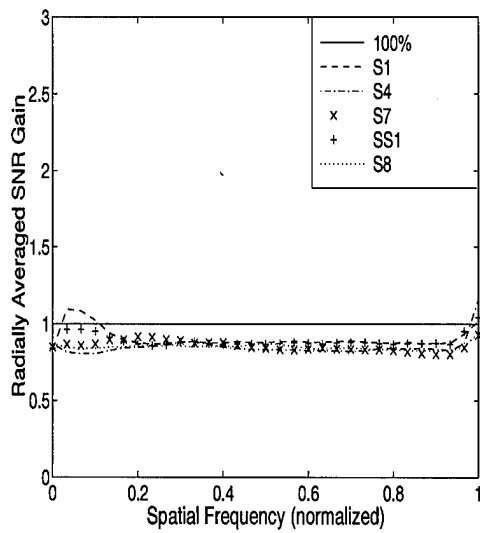
Figure A.26 Power spectrum gain, point source,  $m_\nu = 3$ ,  $r_o = 7$  cm. FSR = a) 50% b) 60% c) 70% d) 80%



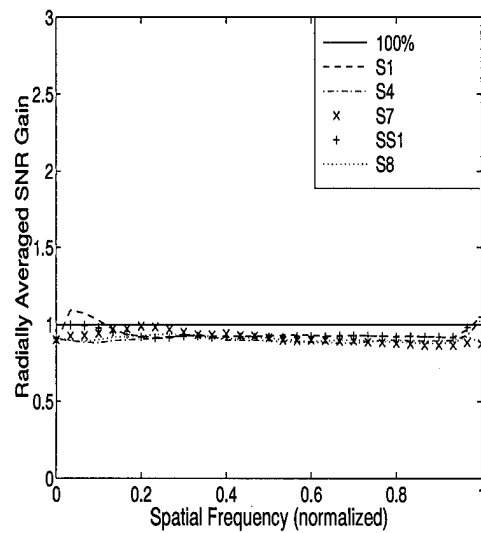
(a)



(b)

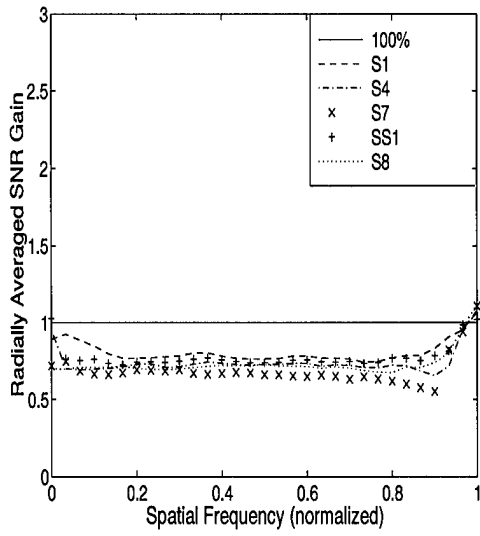


(c)

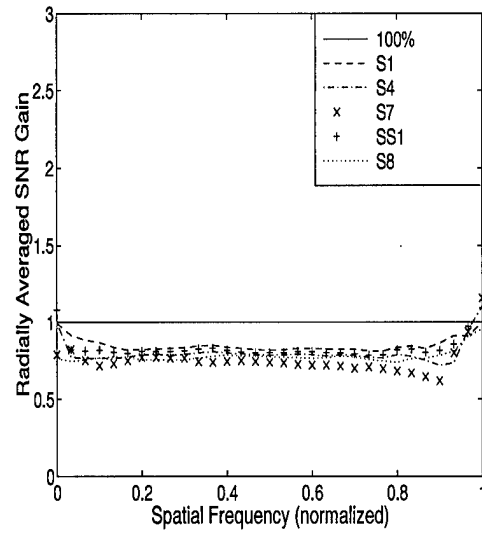


(d)

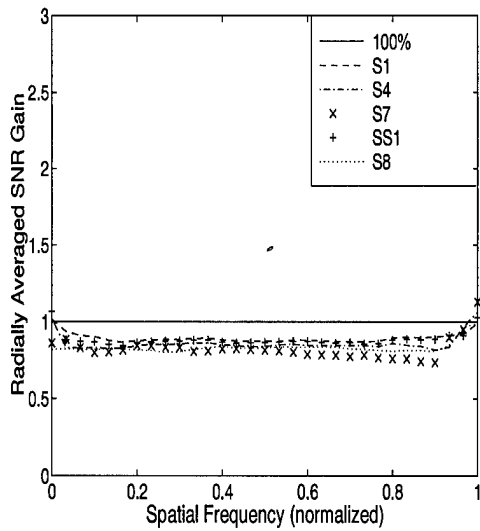
Figure A.27 Power spectrum gain, point source,  $m_\nu = 5$ ,  $r_o = 7$  cm. FSR = a) 50% b) 60% c) 70% d) 80%



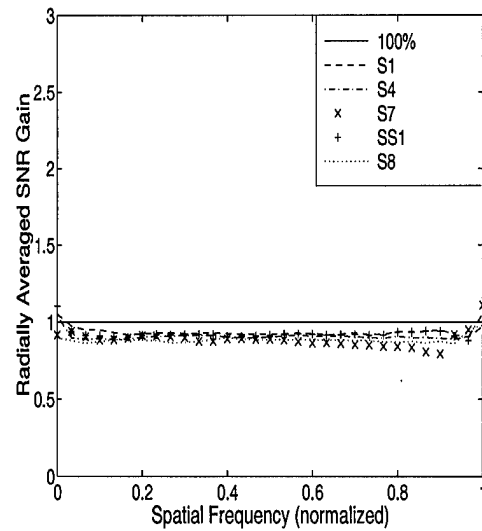
(a)



(b)

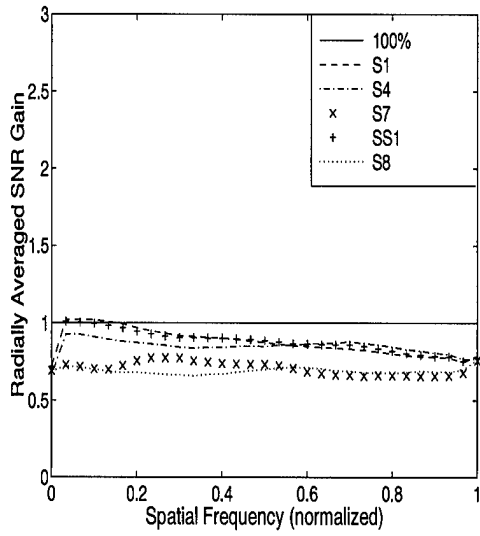


(c)

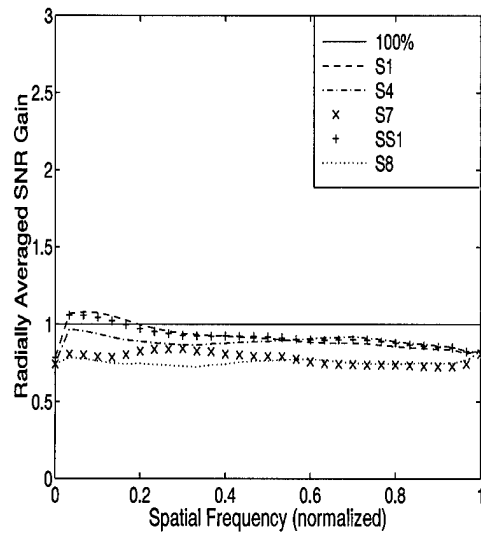


(d)

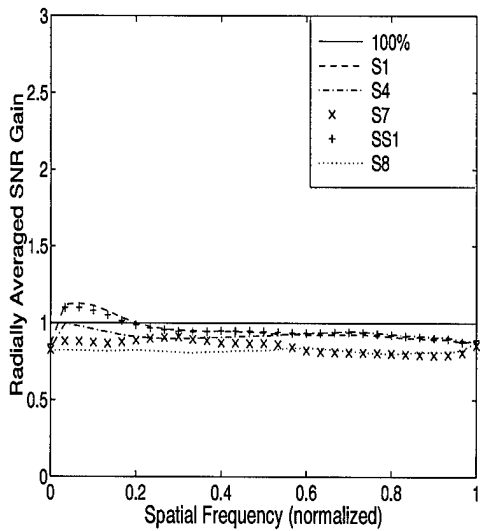
Figure A.28 Power spectrum gain, point source,  $m_\nu = 7$ ,  $r_o = 7$  cm. FSR = a) 50% b) 60% c) 70% d) 80%



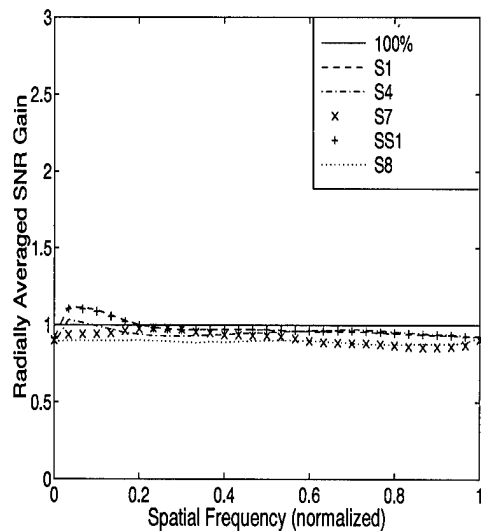
(a)



(b)

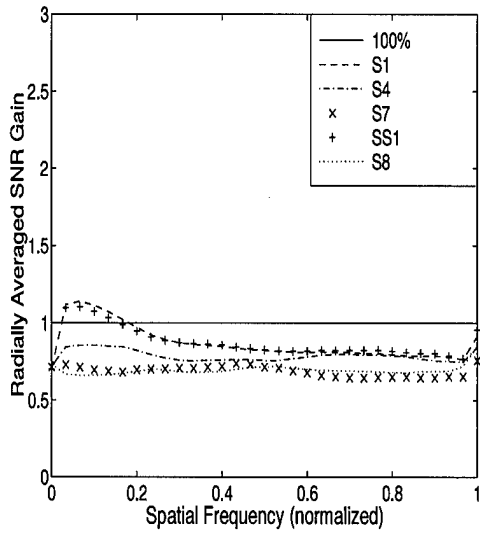


(c)

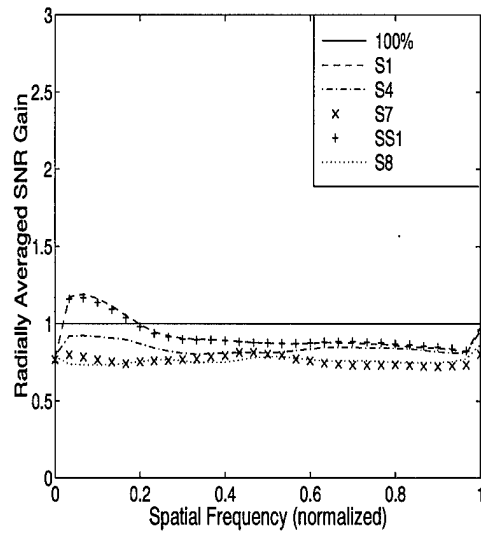


(d)

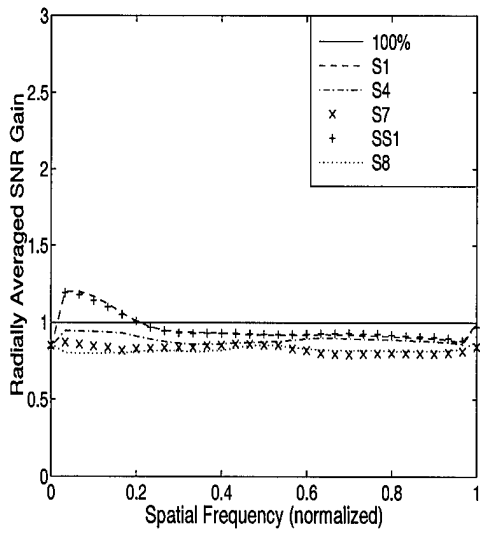
Figure A.29 Power spectrum gain, point source,  $m_\nu = 1$ ,  $r_o = 12$  cm. FSR = a) 50% b) 60% c) 70% d) 80%



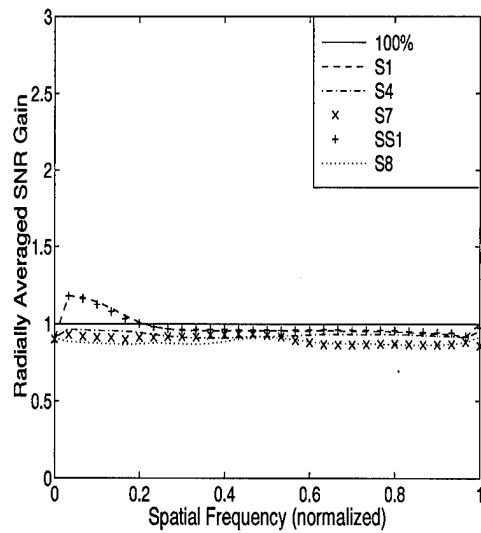
(a)



(b)

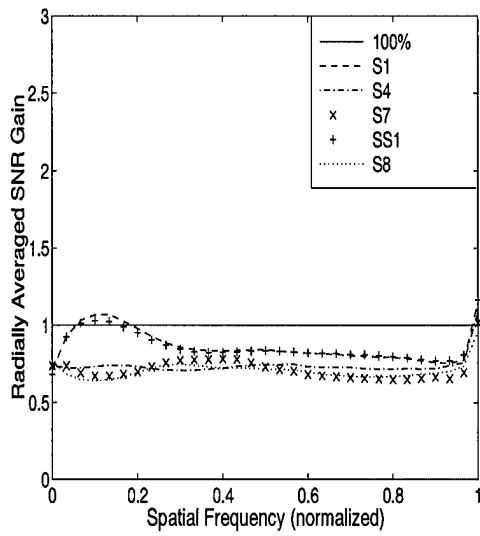


(c)

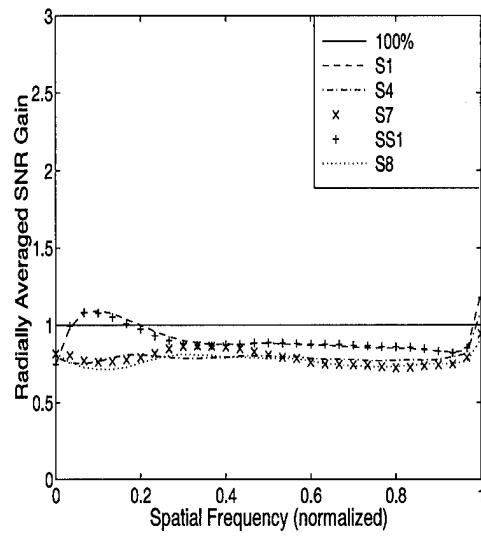


(d)

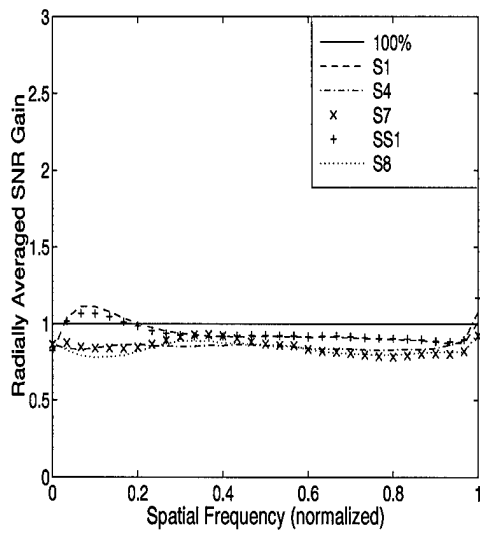
Figure A.30 Power spectrum gain, point source,  $m_\nu = 3$ ,  $r_o = 12$  cm. FSR = a) 50% b) 60% c) 70% d) 80%



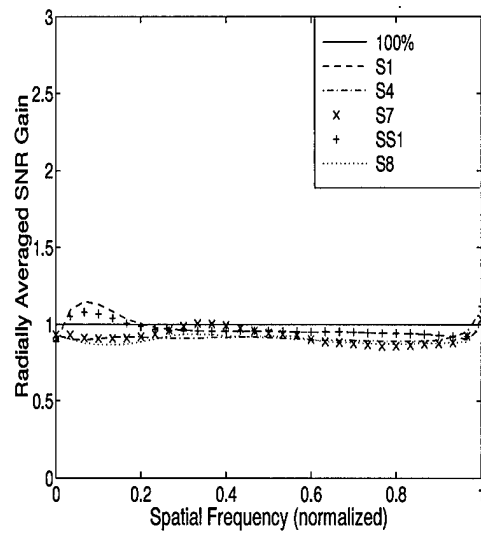
(a)



(b)

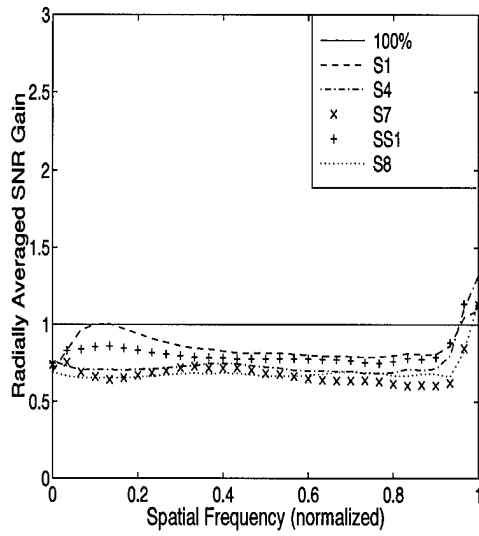


(c)

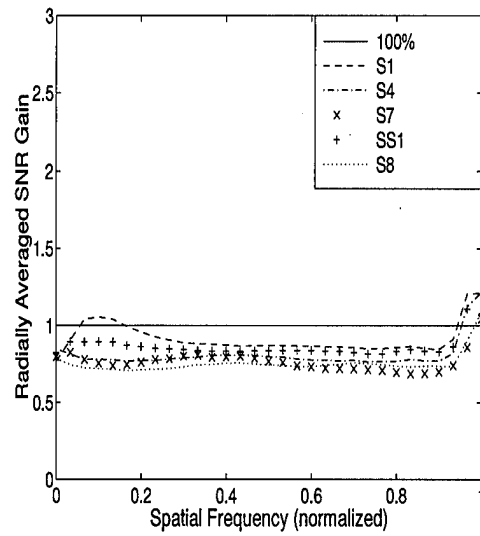


(d)

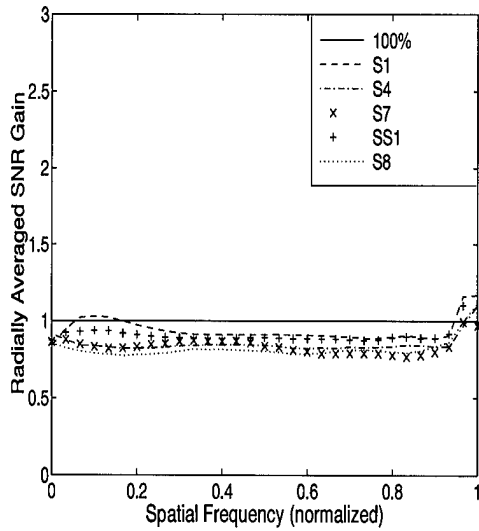
Figure A.31 Power spectrum gain, point source,  $m_\nu = 5$ ,  $r_o = 12$  cm. FSR = a) 50% b) 60% c) 70% d) 80%



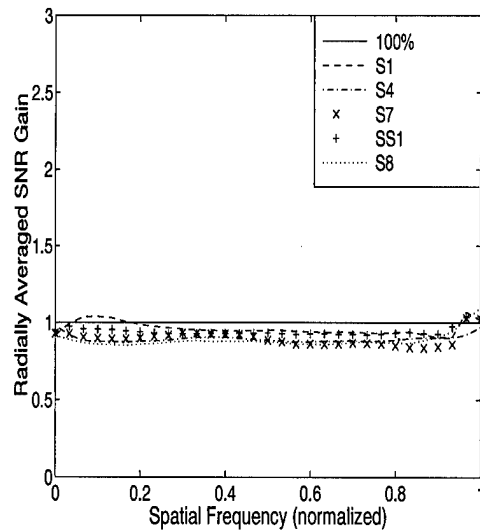
(a)



(b)

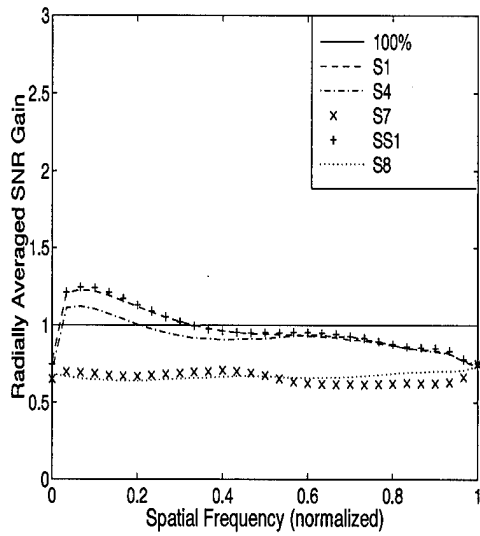


(c)

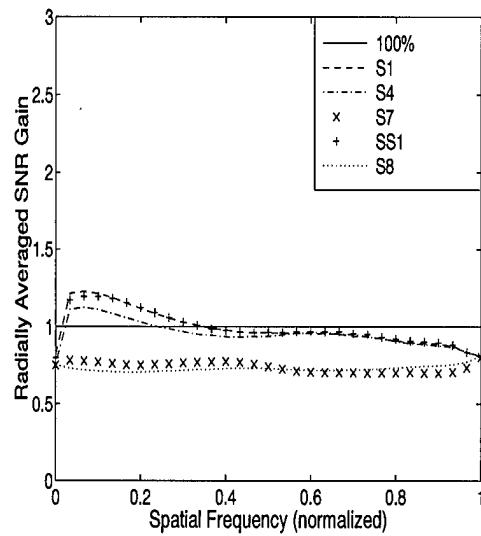


(d)

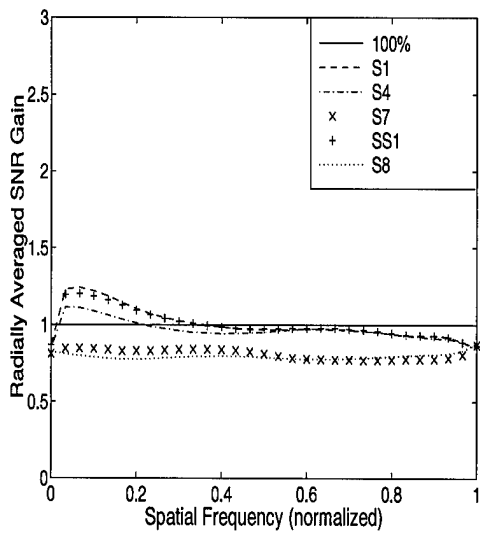
Figure A.32 Power spectrum gain, point source,  $m_\nu = 7$ ,  $r_o = 12$  cm. FSR = a) 50% b) 60% c) 70% d) 80%



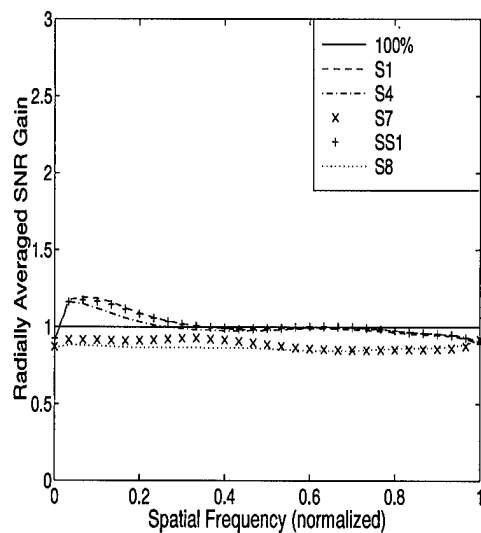
(a)



(b)

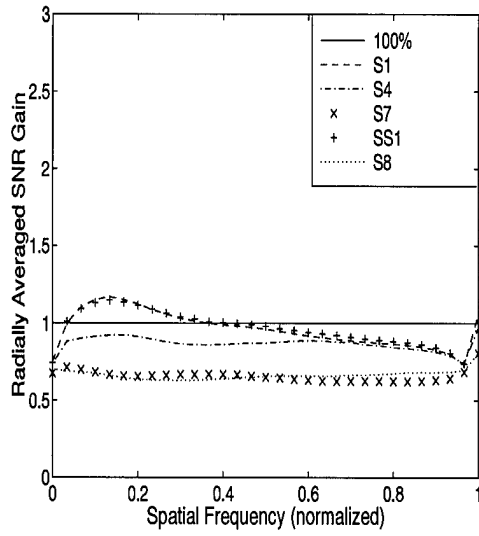


(c)

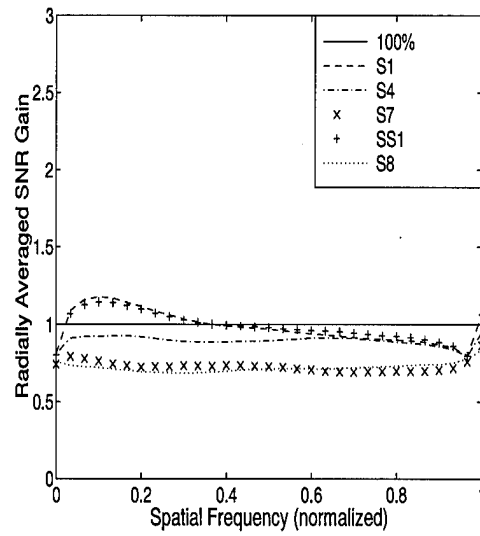


(d)

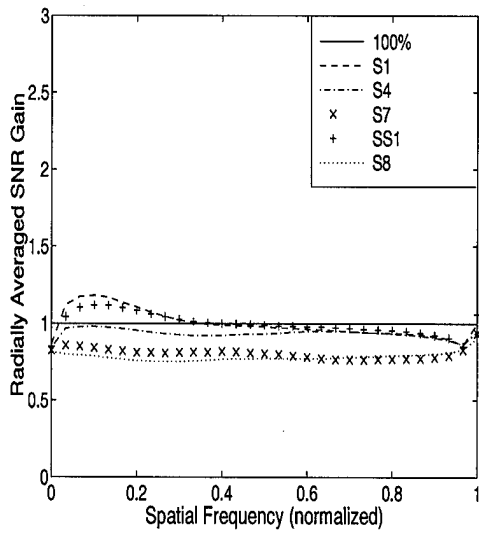
Figure A.33 Power spectrum gain, point source,  $m_\nu = 1$ ,  $r_o = 17$  cm. FSR = a) 50% b) 60% c) 70% d) 80%



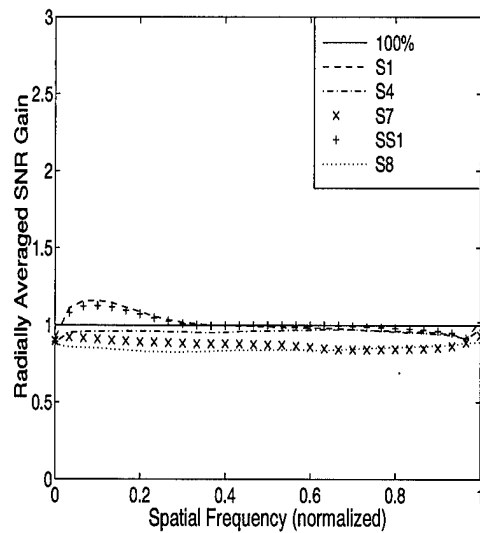
(a)



(b)

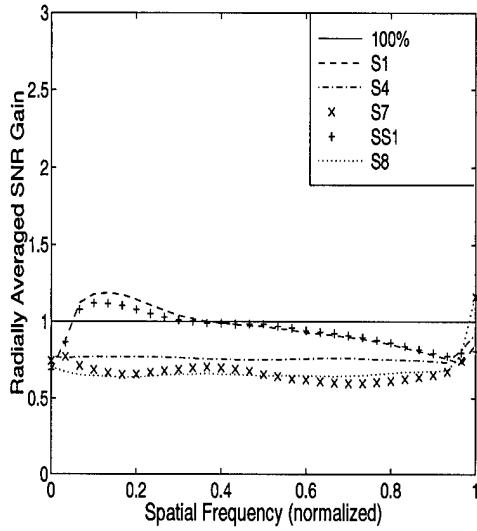


(c)

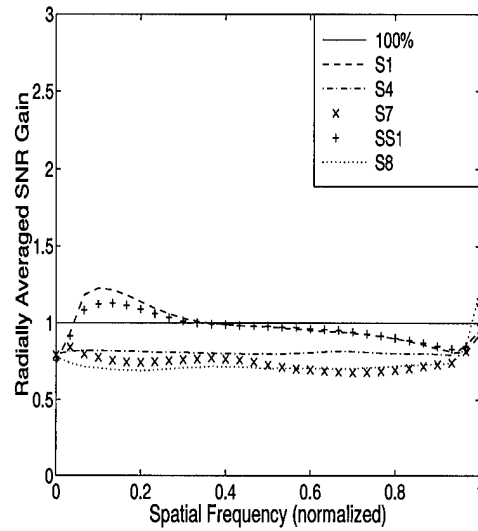


(d)

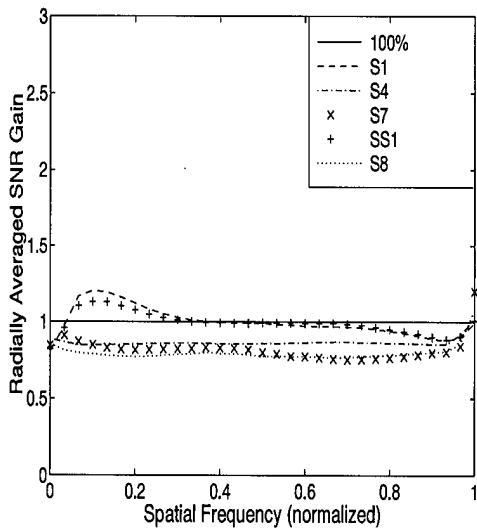
Figure A.34 Power spectrum gain, point source,  $m_\nu = 3$ ,  $r_o = 17$  cm. FSR = a) 50% b) 60% c) 70% d) 80%



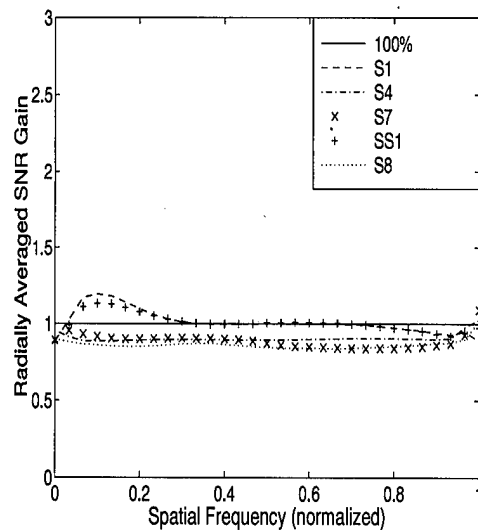
(a)



(b)

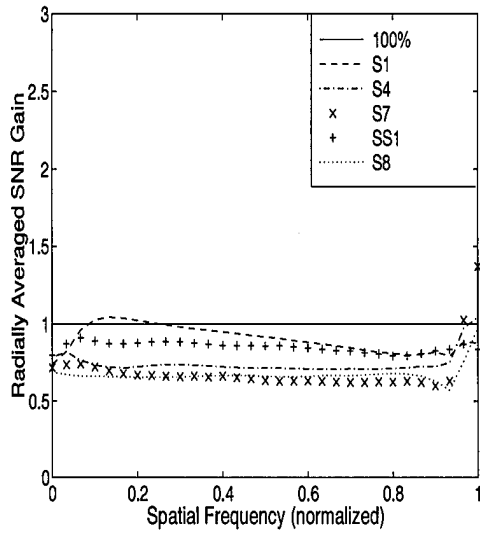


(c)

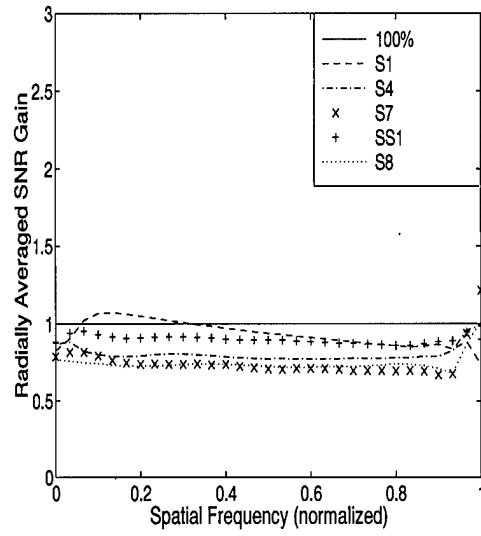


(d)

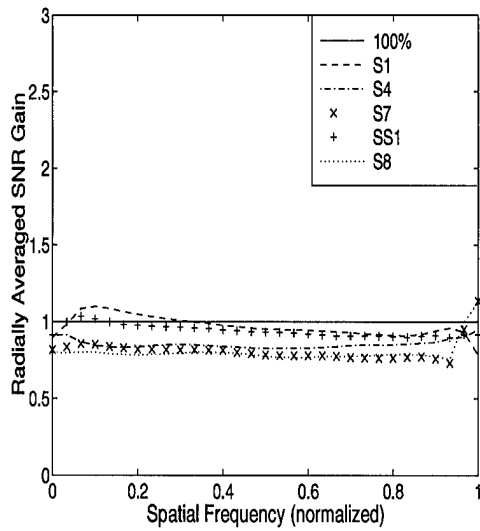
Figure A.35 Power spectrum gain, point source,  $m_v = 5$ ,  $r_o = 17$  cm. FSR = a) 50% b) 60% c) 70% d) 80%



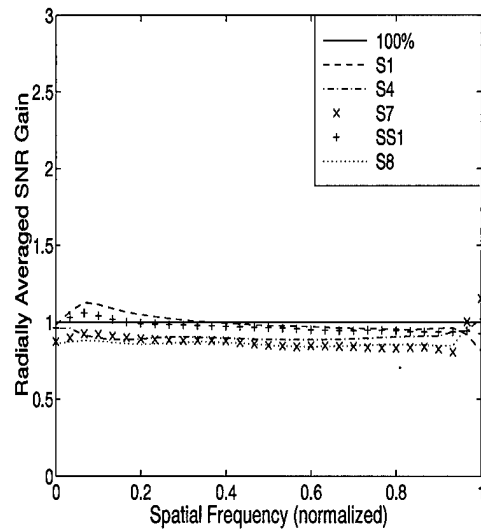
(a)



(b)



(c)



(d)

Figure A.36 Power spectrum gain, point source,  $m_\nu = 7$ ,  $r_o = 17$  cm. FSR = a) 50% b) 60% c) 70% d) 80%

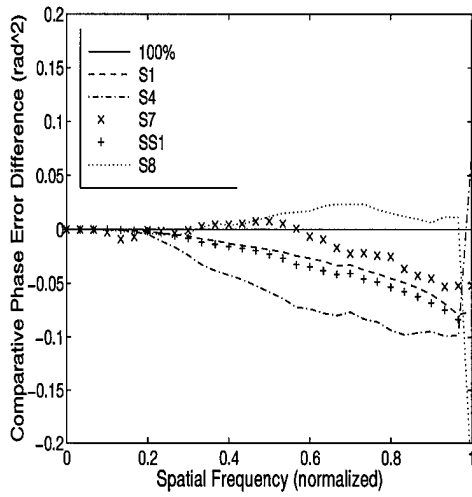
#### A.4 Point Source Comparative Phase Error Difference Plots

This section contains the phase error difference plots for the point source experiment. Phase error difference is defined as the difference in the phase errors between the cases using frame selection to that without frame selection.

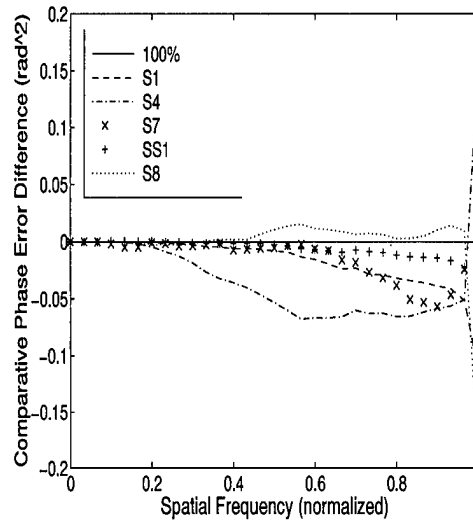
The relative phase error performance of a case with frame selection is compared to that without by

$$\phi_{\Delta}(\vec{f}) = \phi_{\epsilon}(\vec{f})_{100\%}^2 - \phi_{\epsilon}(\vec{f})_{FS}^2, \quad (\text{A.1})$$

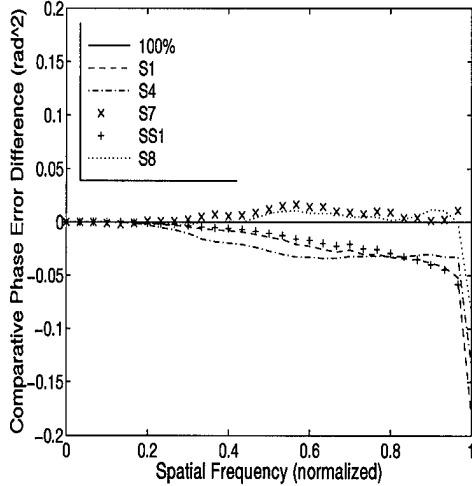
where  $\phi_{\epsilon}(\vec{f})_{100\%}$  represents the phase error of the 100% case, and  $\phi_{\epsilon}(\vec{f})_{FS}$  represents a frame selected case. Areas in the spectrum where performance is improved as a result of frame selection, will have positive  $\phi_{\Delta}$  values. Conversely, where the performance declines as a result of frame selection,  $\phi_{\Delta}$  values are negative.



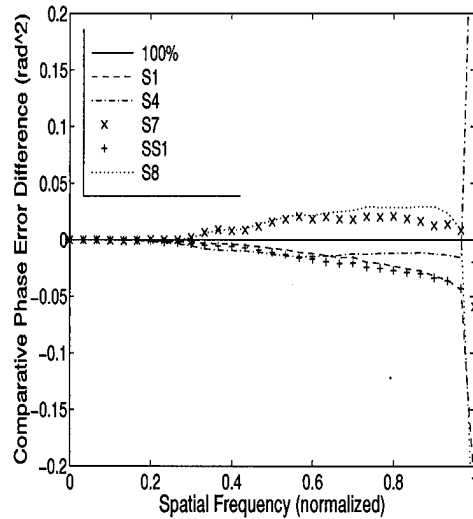
(a)



(b)

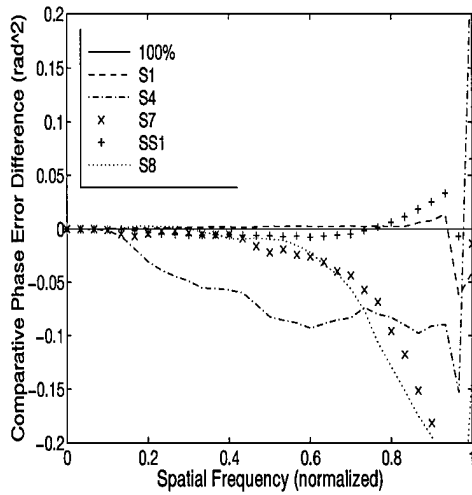


(c)

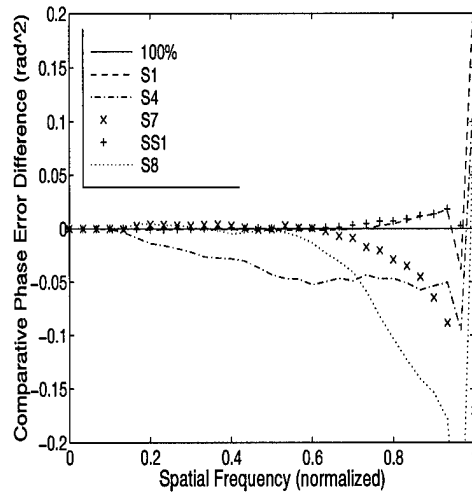


(d)

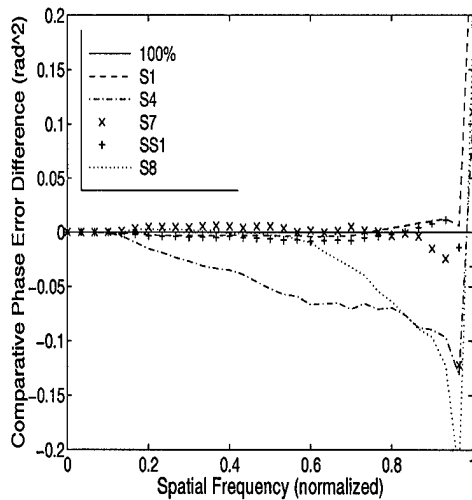
Figure A.37 Comparative phase error difference, point source,  $m_\nu = 1$ ,  $r_o = 7$  cm.  
FSR = a) 50% b) 60% c) 70% d) 80%



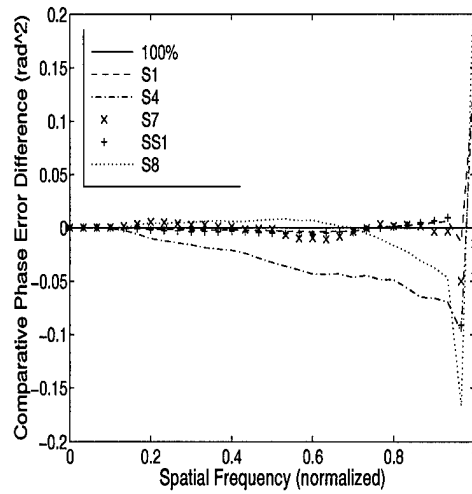
(a)



(b)

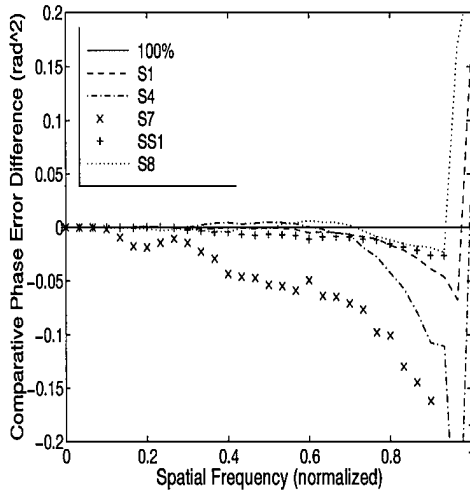


(c)

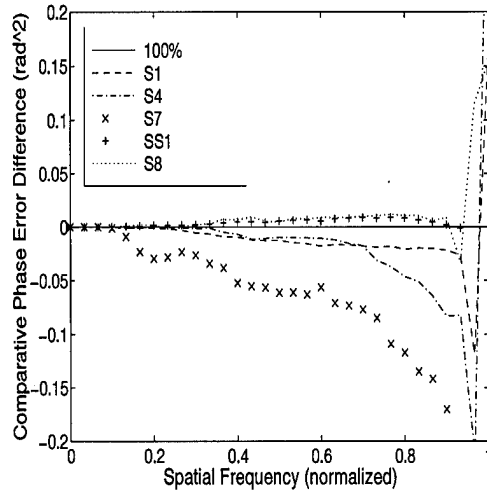


(d)

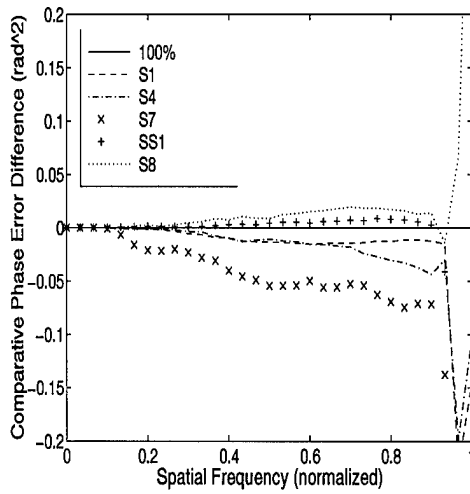
Figure A.38 Comparative phase error difference, point source,  $m_\nu = 3$ ,  $r_o = 7$  cm.  
FSR = a) 50% b) 60% c) 70% d) 80%



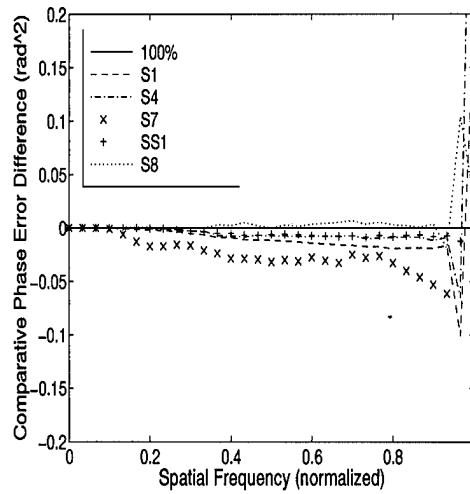
(a)



(b)

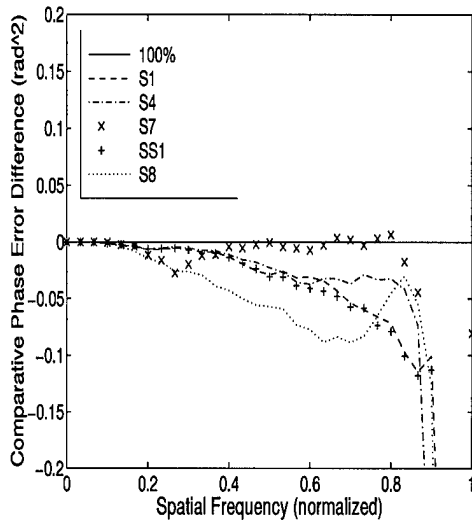


(c)

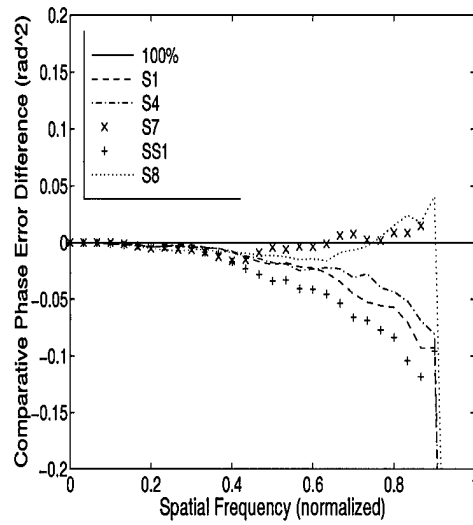


(d)

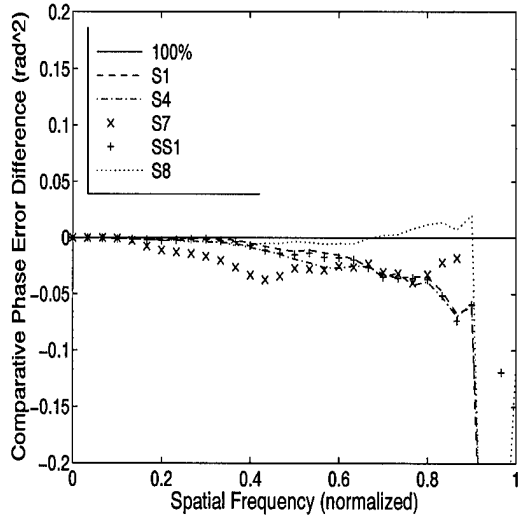
Figure A.39 Comparative phase error difference, point source,  $m_\nu = 5$ ,  $r_o = 7$  cm.  
FSR = a) 50% b) 60% c) 70% d) 80%



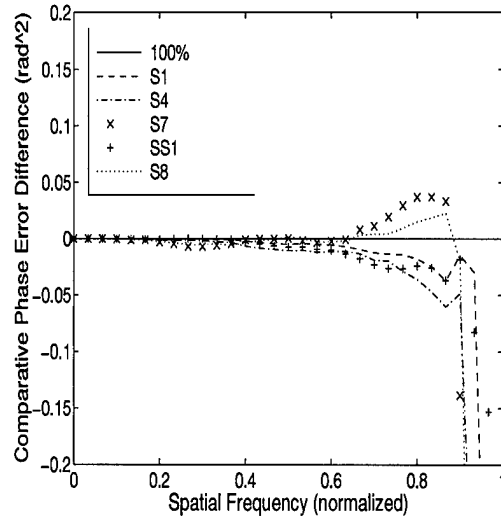
(a)



(b)

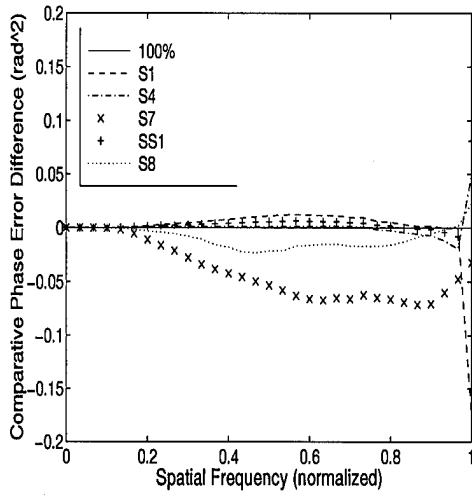


(c)

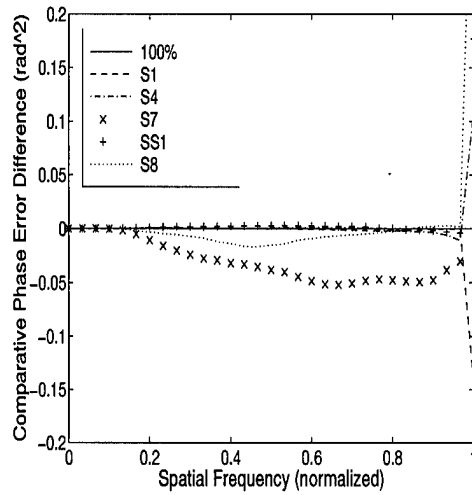


(d)

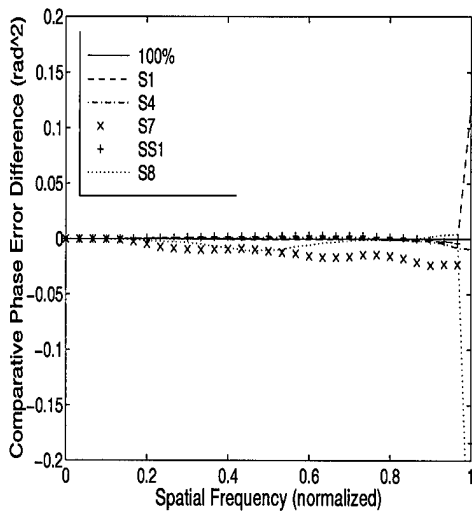
Figure A.40 Comparative phase error difference, point source,  $m_\nu = 7$ ,  $r_o = 7$  cm.  
FSR = a) 50% b) 60% c) 70% d) 80%



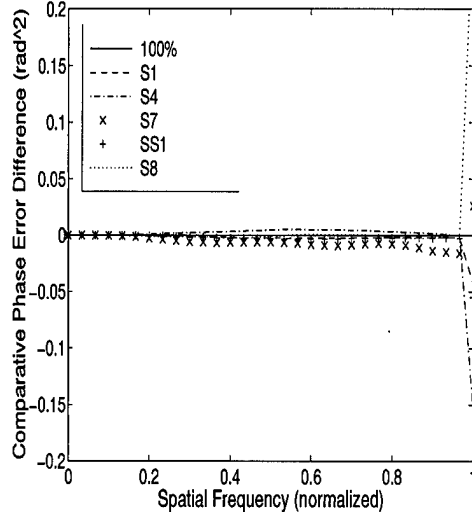
(a)



(b)

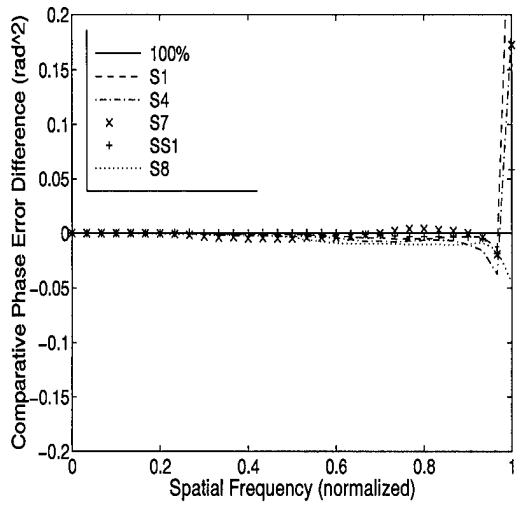


(c)

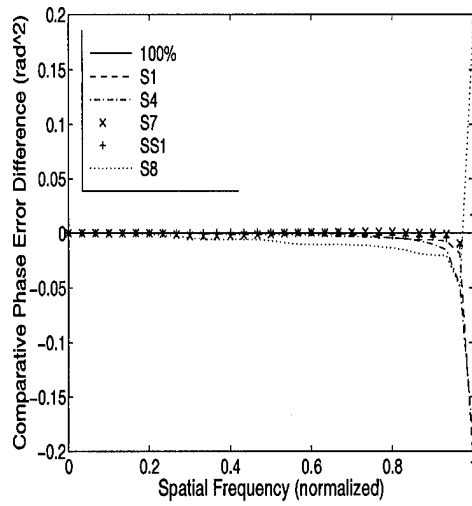


(d)

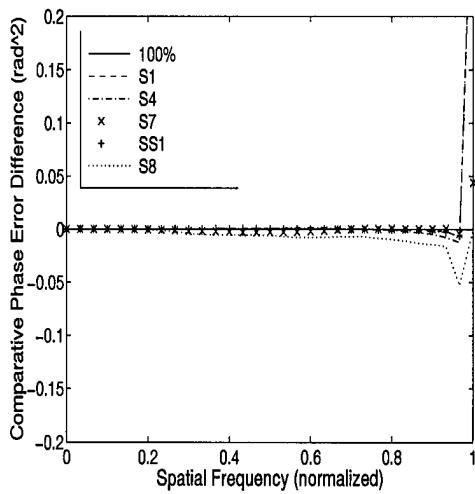
Figure A.41 Comparative phase error difference, point source,  $m_\nu = 1$ ,  $r_o = 12$  cm.  
FSR = a) 50% b) 60% c) 70% d) 80%



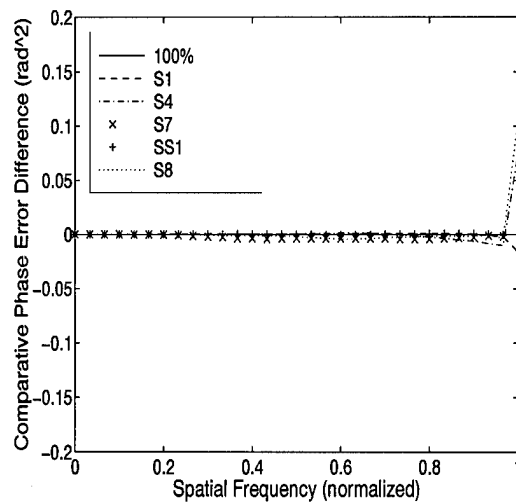
(a)



(b)

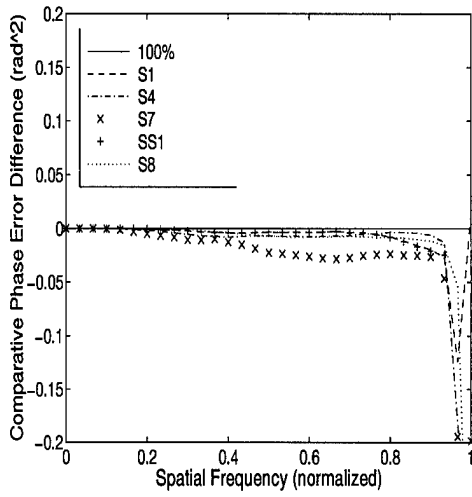


(c)

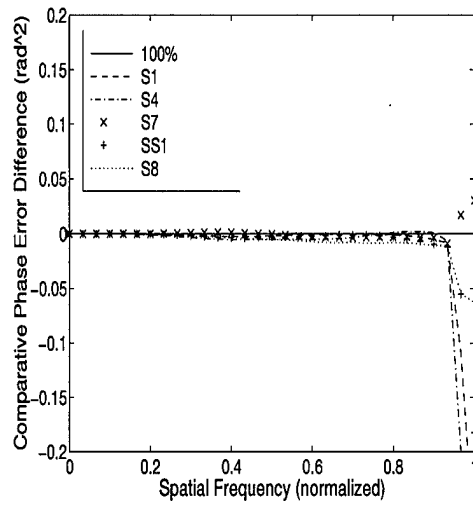


(d)

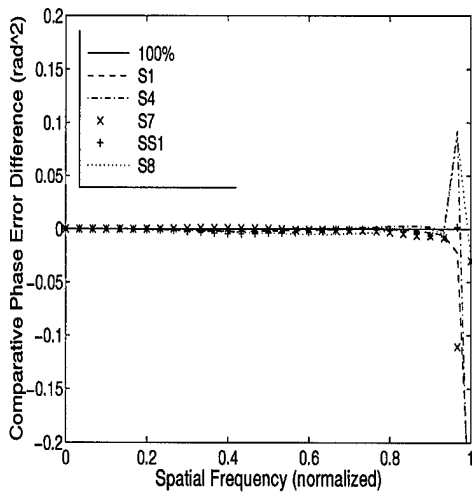
Figure A.42 Comparative phase error difference, point source,  $m_\nu = 3$ ,  $r_o = 12$  cm.  
FSR = a) 50% b) 60% c) 70% d) 80%



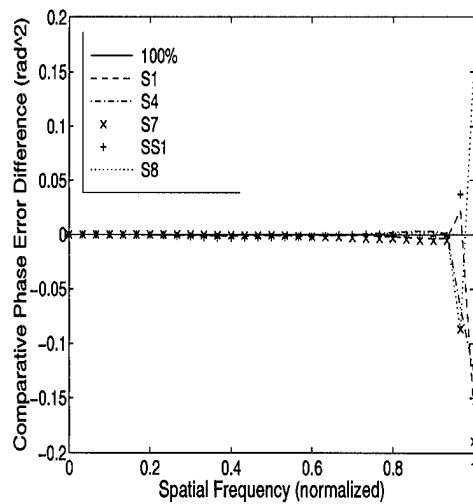
(a)



(b)

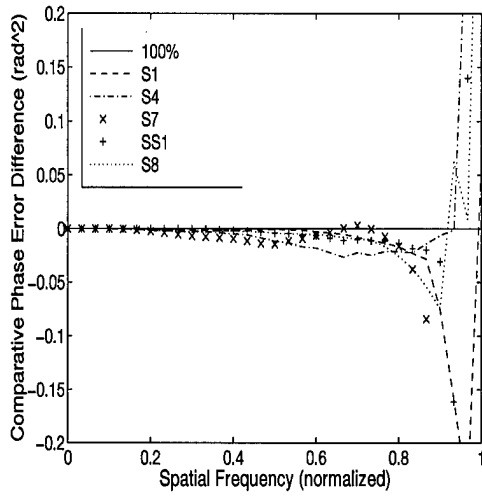


(c)

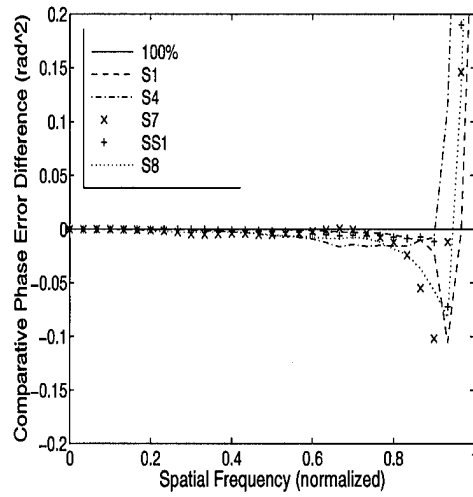


(d)

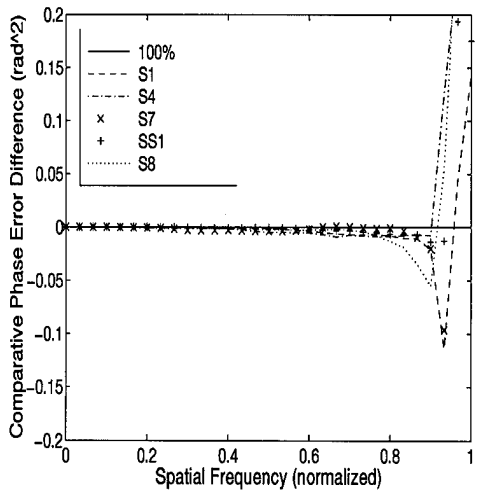
Figure A.43 Comparative phase error difference, point source,  $m_\nu = 5$ ,  $r_o = 12$  cm.  
FSR = a) 50% b) 60% c) 70% d) 80%



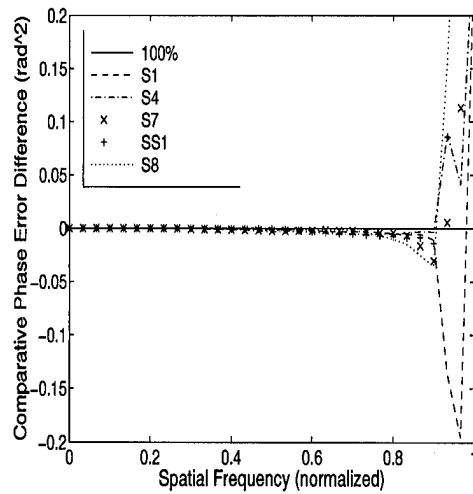
(a)



(b)

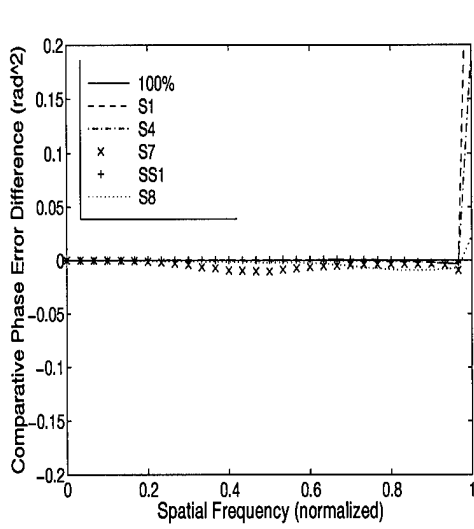


(c)

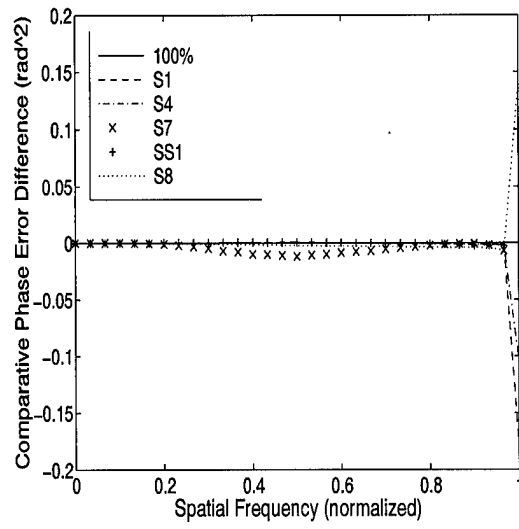


(d)

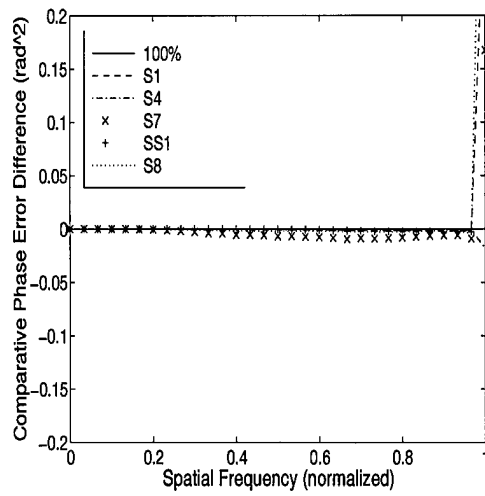
Figure A.44 Comparative phase error difference, point source,  $m_\nu = 7$ ,  $r_o = 12$  cm.  
FSR = a) 50% b) 60% c) 70% d) 80%



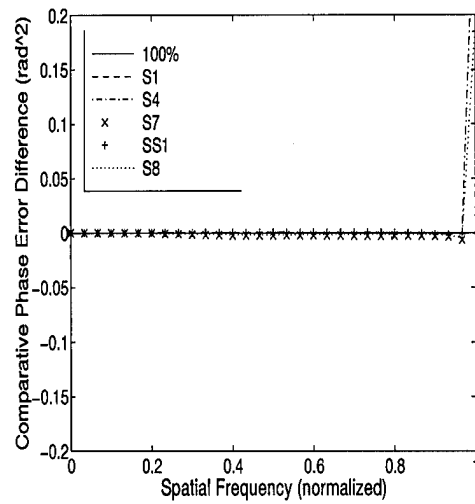
(a)



(b)

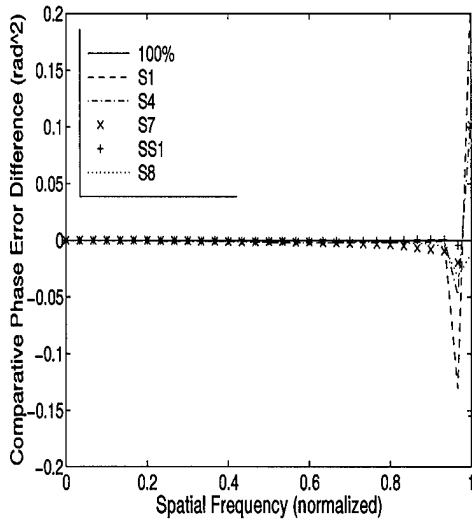


(c)

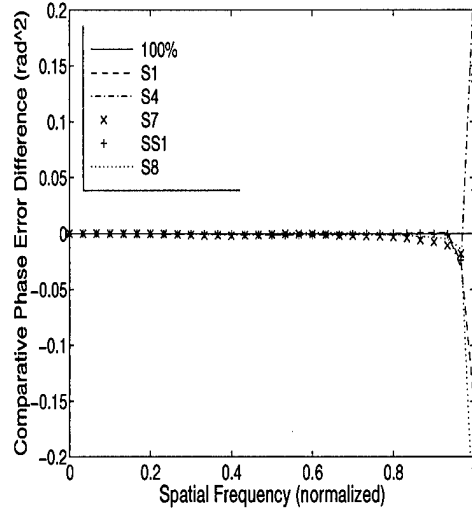


(d)

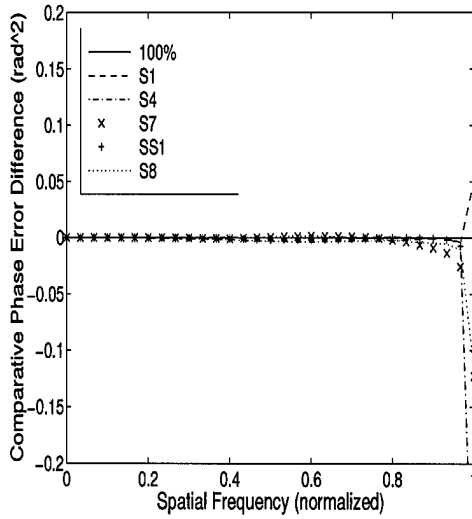
Figure A.45 Comparative phase error difference, point source,  $m_v = 1$ ,  $r_o = 17$  cm.  
FSR = a) 50% b) 60% c) 70% d) 80%



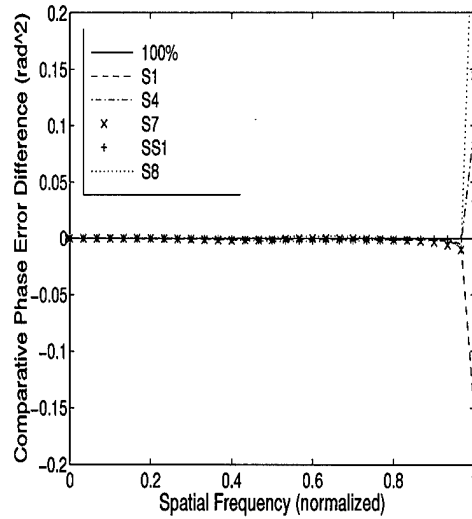
(a)



(b)

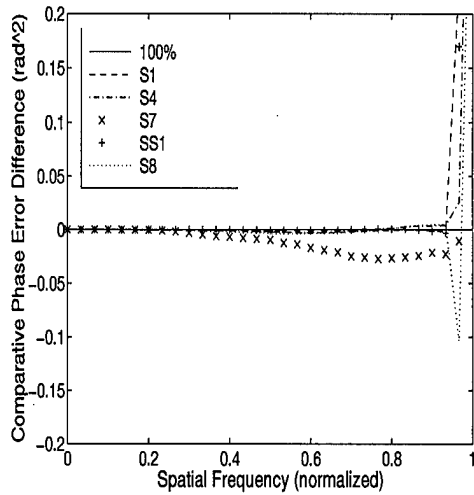


(c)

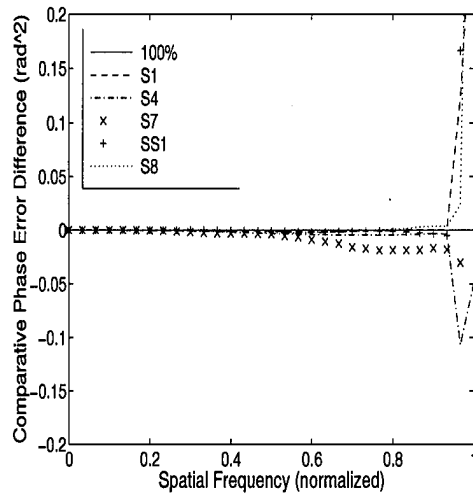


(d)

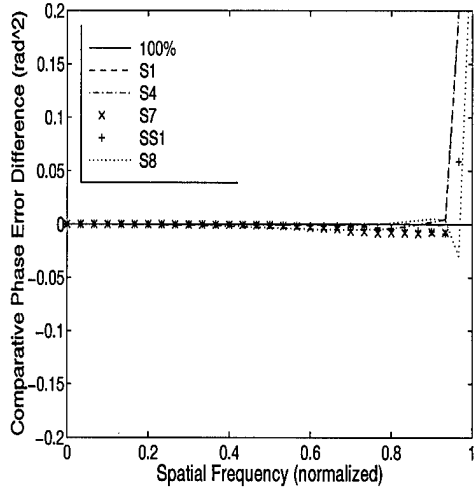
Figure A.46 Comparative phase error difference, point source,  $m_\nu = 3$ ,  $r_o = 17$  cm.  
FSR = a) 50% b) 60% c) 70% d) 80%



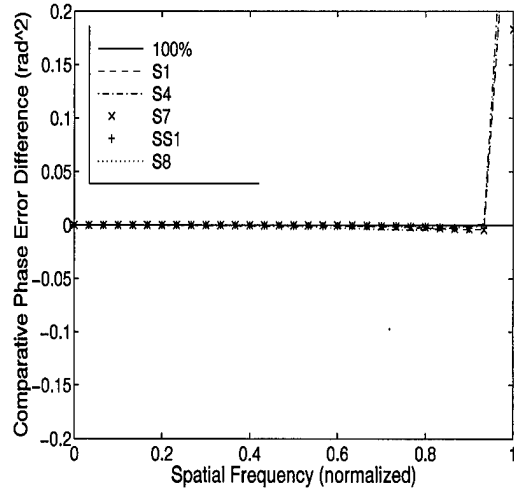
(a)



(b)

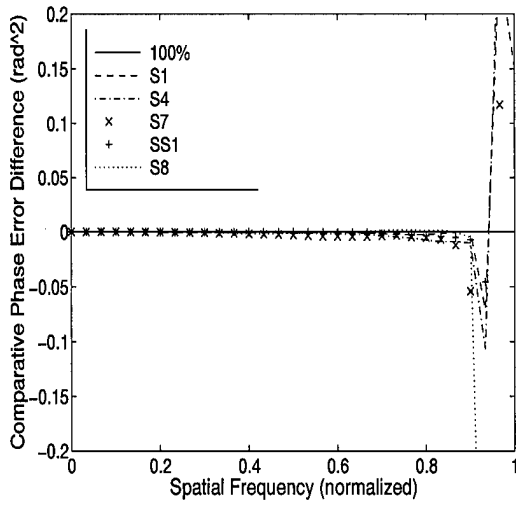


(c)

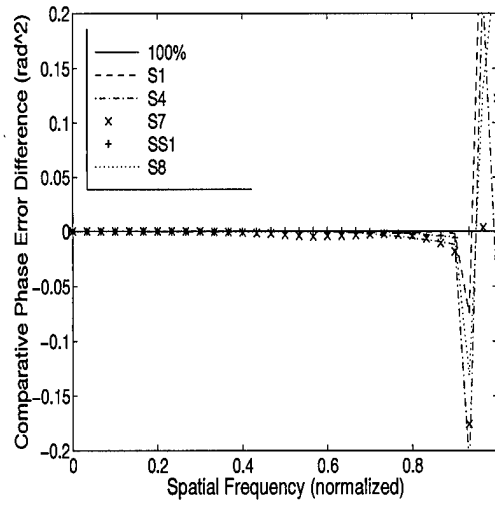


(d)

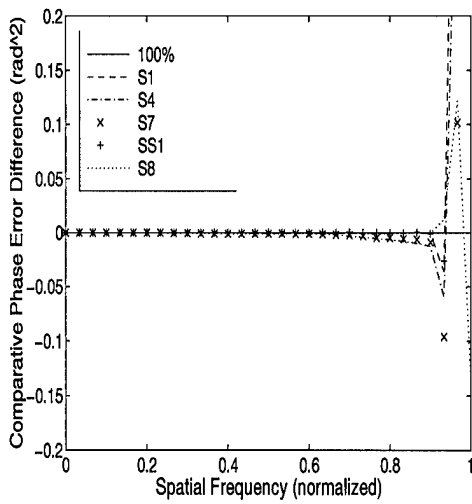
Figure A.47 Comparative phase error difference, point source,  $m_\nu = 5$ ,  $r_o = 17$  cm.  
FSR = a) 50% b) 60% c) 70% d) 80%



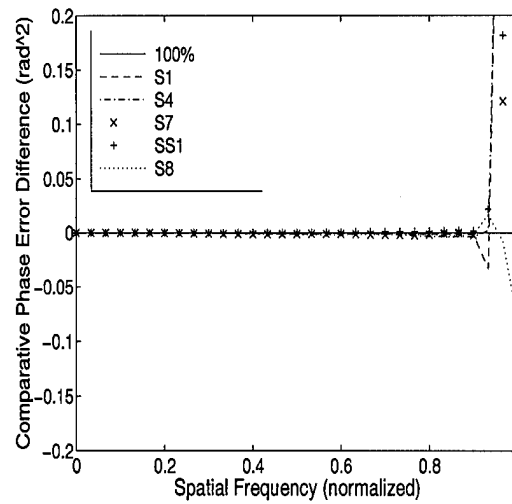
(a)



(b)



(c)



(d)

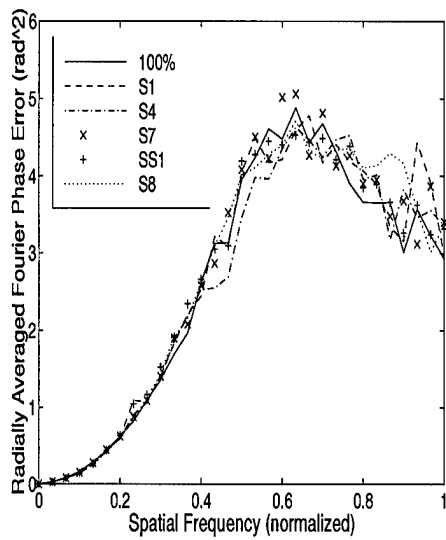
Figure A.48 Comparative phase error difference, point source,  $m_v = 7$ ,  $r_o = 17$  cm.  
FSR = a) 50% b) 60% c) 70% d) 80%

## *Appendix B. Simulation Results for Extended Source*

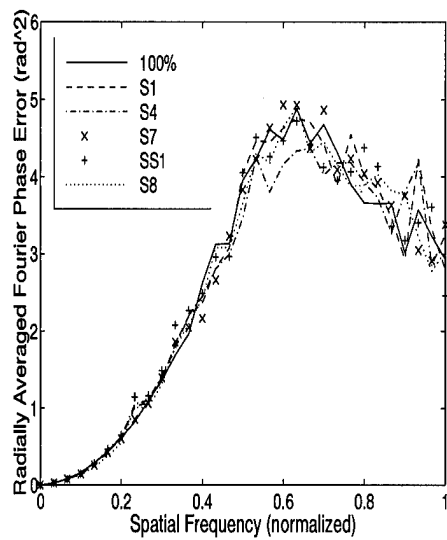
This section contains the results of the extended source experiment. The results of this experiment is presented in four parts: 1) the bispectrum phase error; 2) the power spectrum SNR; 3) the power spectrum SNR gain (with vs. without frame selection); and the comparative phase error plots.

### *B.1 Extended Source Bispectrum Phase Error*

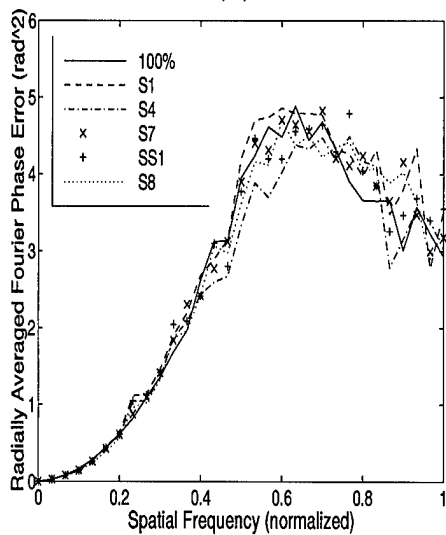
This section contains the phase error results for the extended source experiment. On each page, the four FSR strategies are presented, containing the results of the five metrics tested. A given set of visual parameters,  $r_o$  and  $m_\nu$ , are identified below.



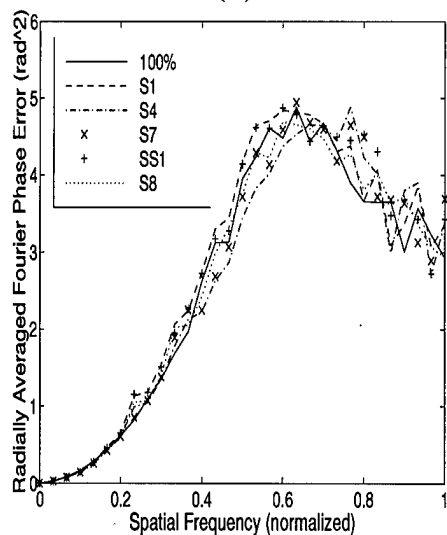
(a)



(b)

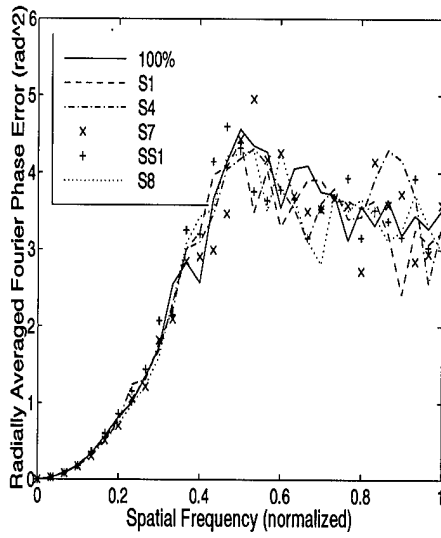


(c)

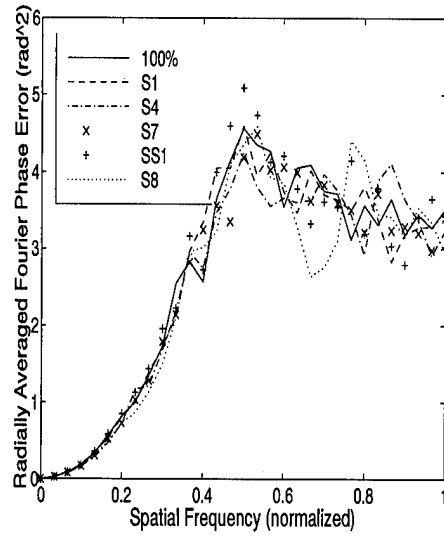


(d)

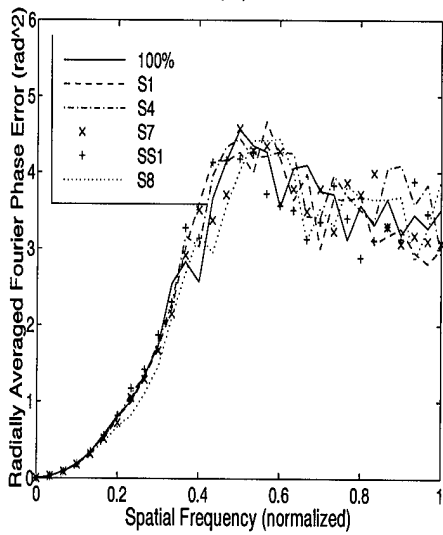
Figure B.1 Bispectrum phase error, extended source,  $m_\nu = 1$ ,  $r_o = 7$  cm. FSR = a) 50% b) 60% c) 70% d) 80%



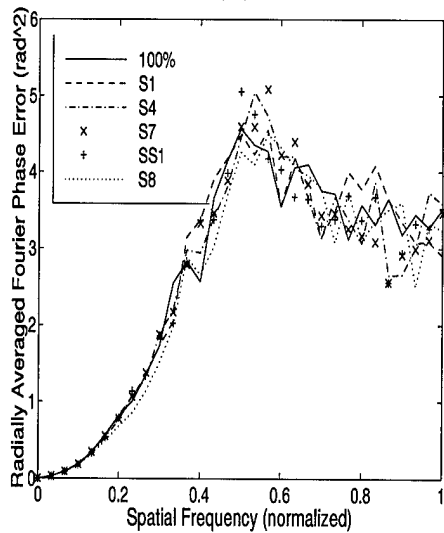
(a)



(b)

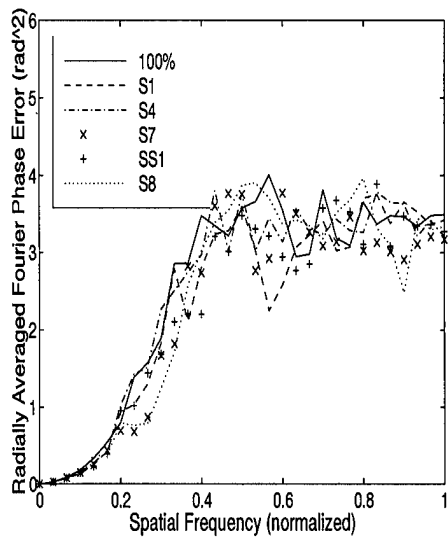


(c)

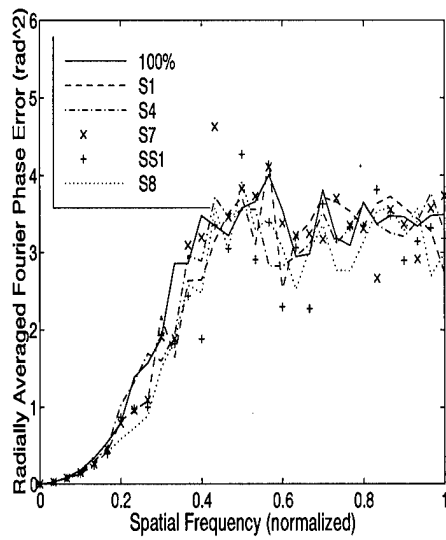


(d)

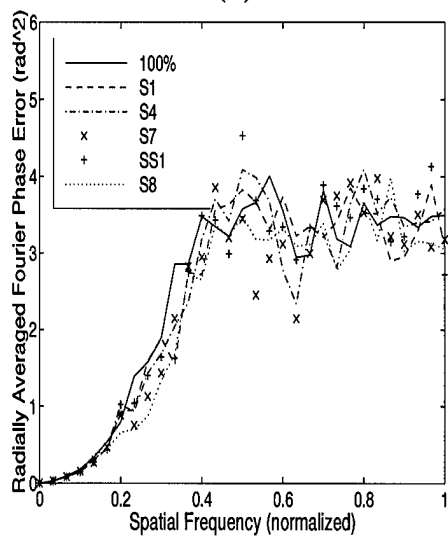
Figure B.2 Bispectrum phase error, extended source,  $m_\nu = 3$ ,  $r_o = 7$  cm. FSR =  
a) 50% b) 60% c) 70% d) 80%



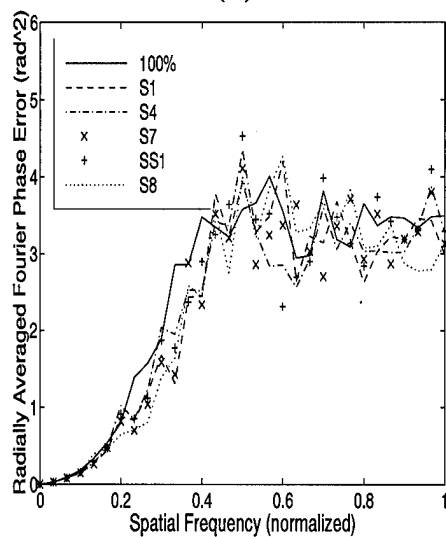
(a)



(b)

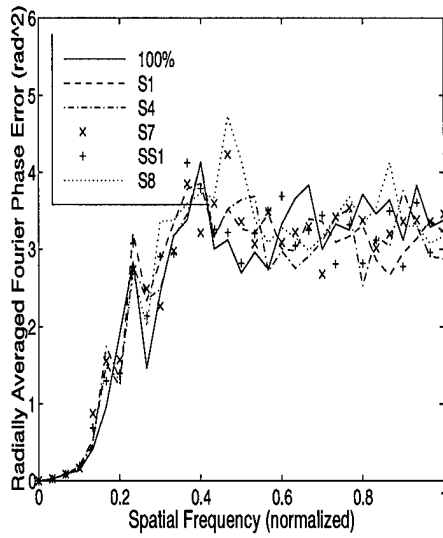


(c)

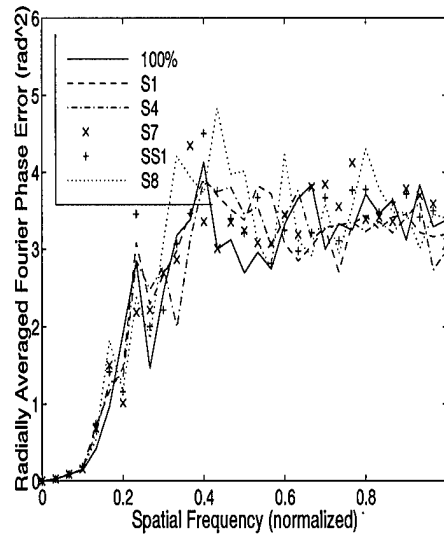


(d)

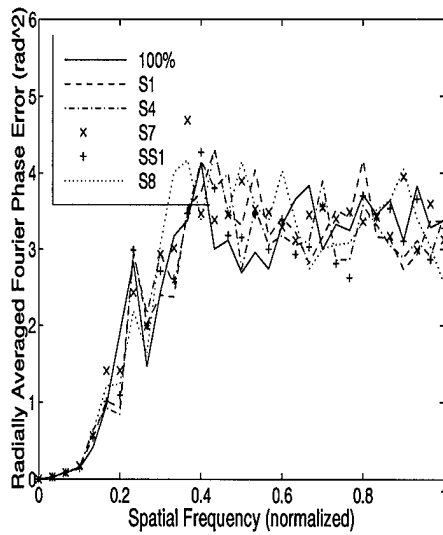
Figure B.3 Bispectrum phase error, extended source,  $m_\nu = 5$ ,  $r_o = 7$  cm. FSR = a) 50% b) 60% c) 70% d) 80%



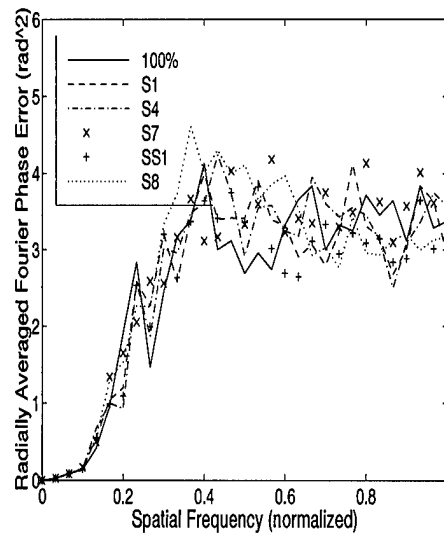
(a)



(b)

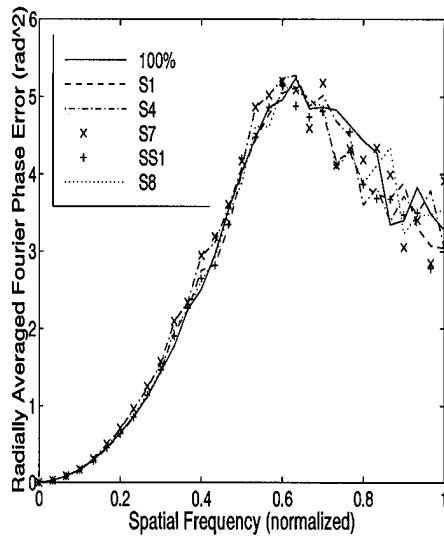


(c)

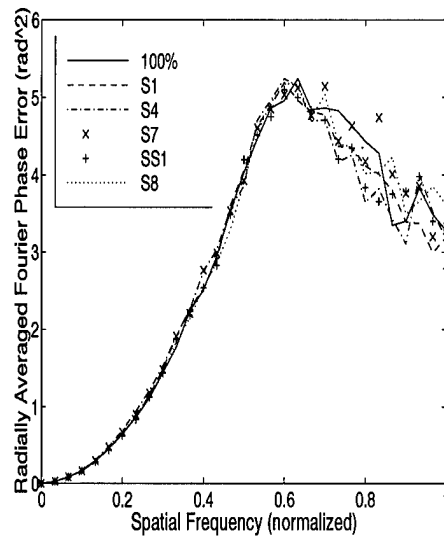


(d)

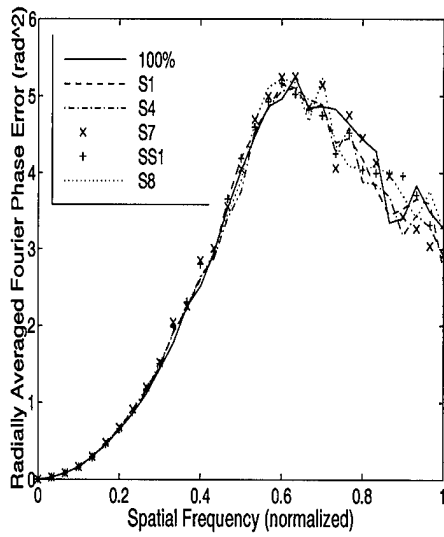
Figure B.4 Bispectrum phase error, extended source,  $m_v = 7$ ,  $r_o = 7$  cm. FSR = a) 50% b) 60% c) 70% d) 80%



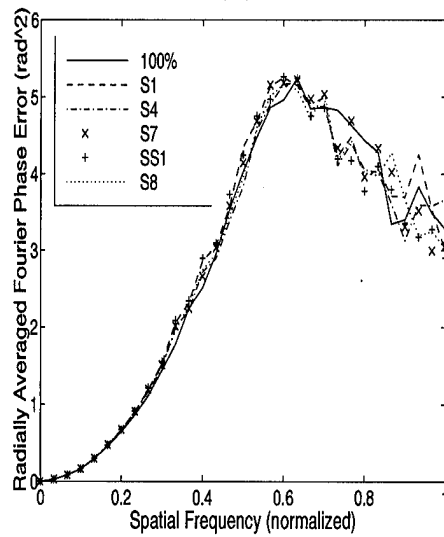
(a)



(b)

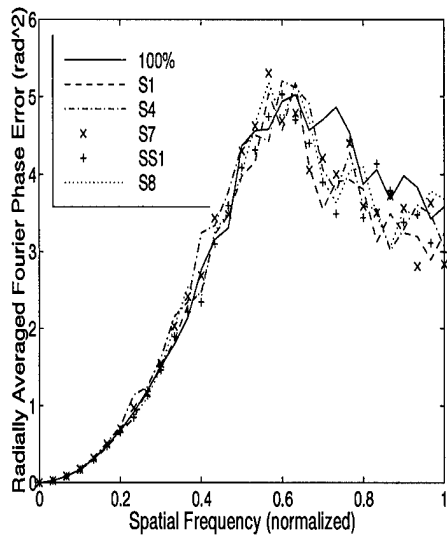


(c)

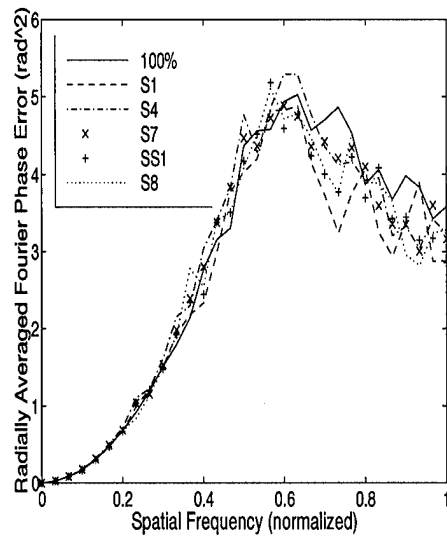


(d)

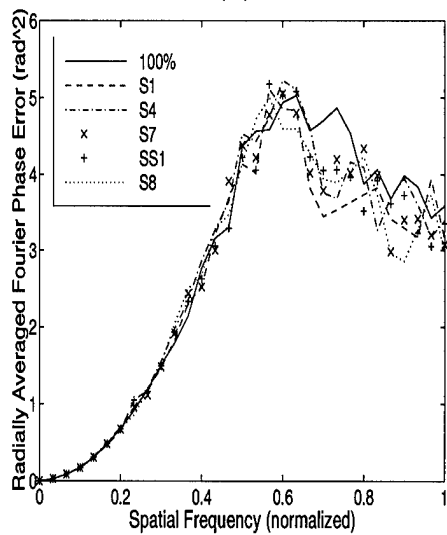
Figure B.5 Bispectrum phase error, extended source,  $m_\nu = 1$ ,  $r_o = 12$  cm. FSR = a) 50% b) 60% c) 70% d) 80%



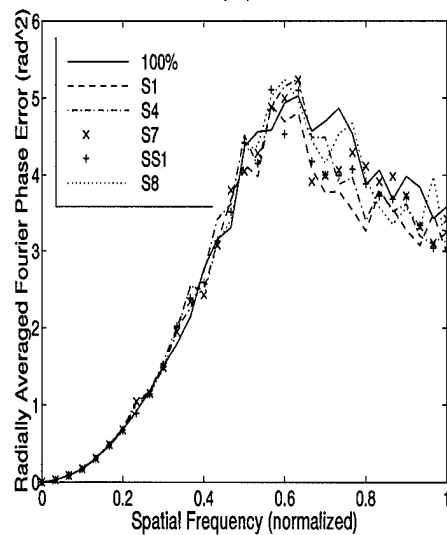
(a)



(b)

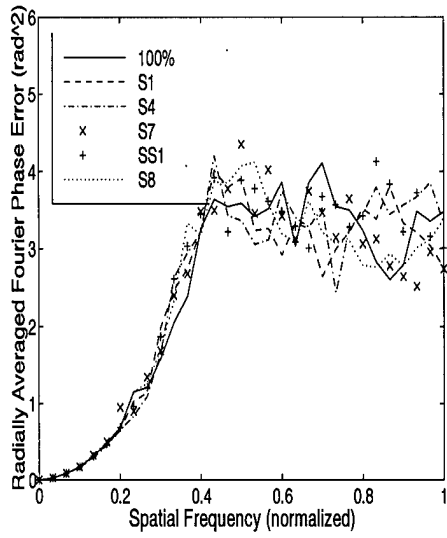


(c)

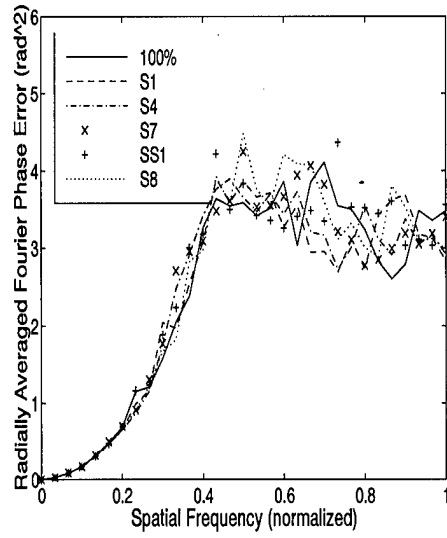


(d)

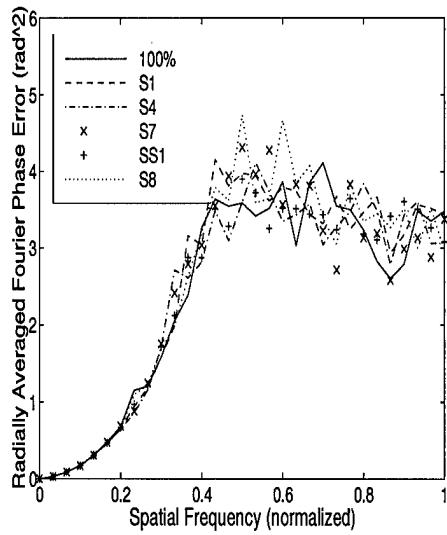
Figure B.6 Bispectrum phase error, extended source,  $m_\nu = 3$ ,  $r_o = 12$  cm. FSR = a) 50% b) 60% c) 70% d) 80%



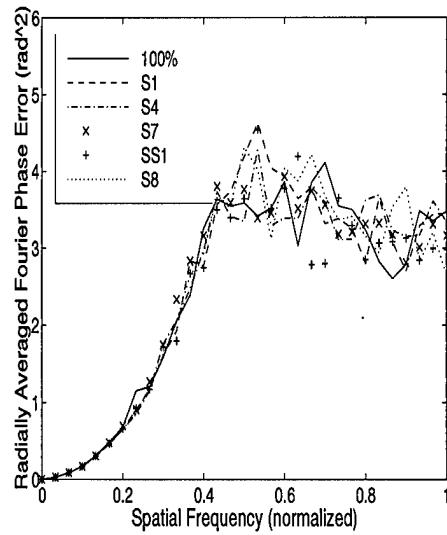
(a)



(b)

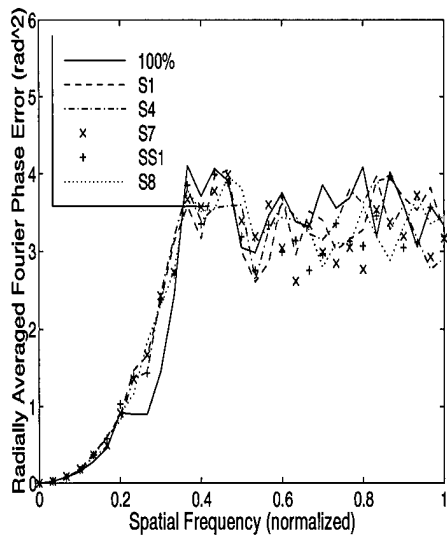


(c)

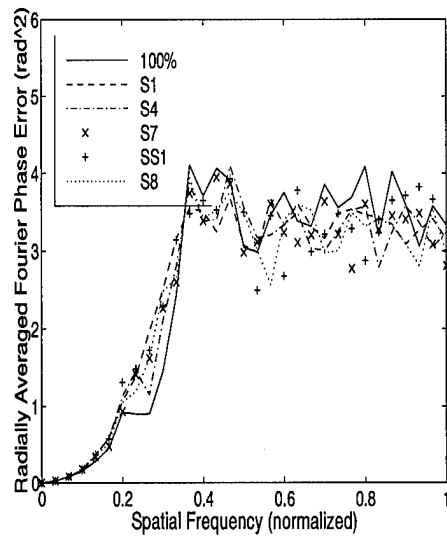


(d)

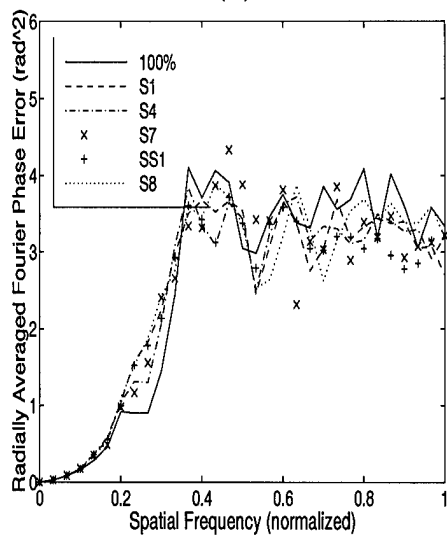
Figure B.7 Bispectrum phase error, extended source,  $m_\nu = 5$ ,  $r_o = 12$  cm. FSR = a) 50% b) 60% c) 70% d) 80%



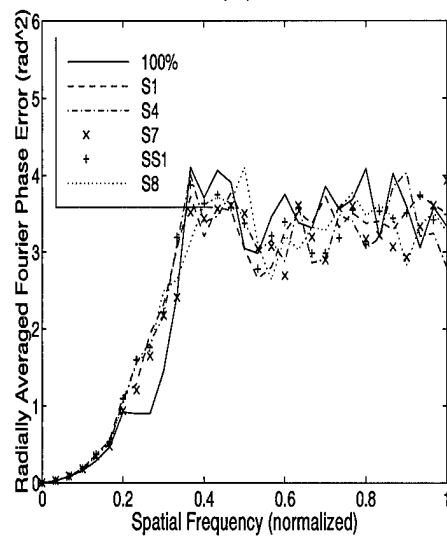
(a)



(b)

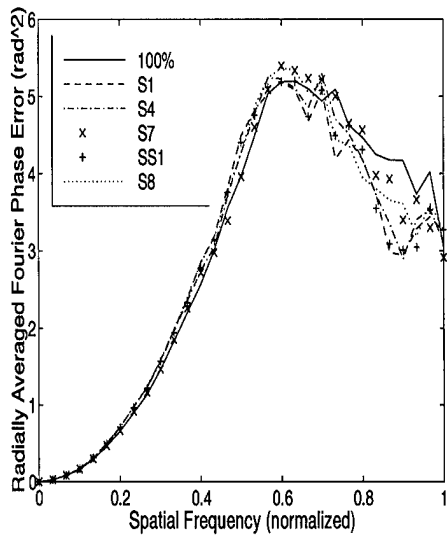


(c)

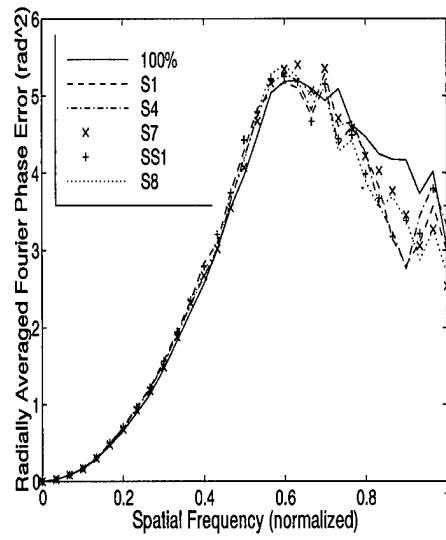


(d)

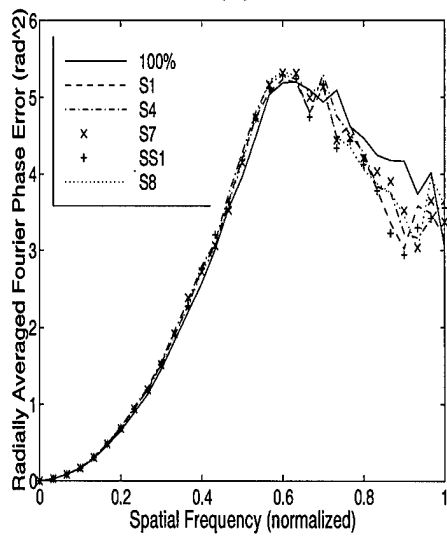
Figure B.8 Bispectrum phase error, extended source,  $m_\nu = 7$ ,  $r_o = 12$  cm. FSR = a) 50% b) 60% c) 70% d) 80%



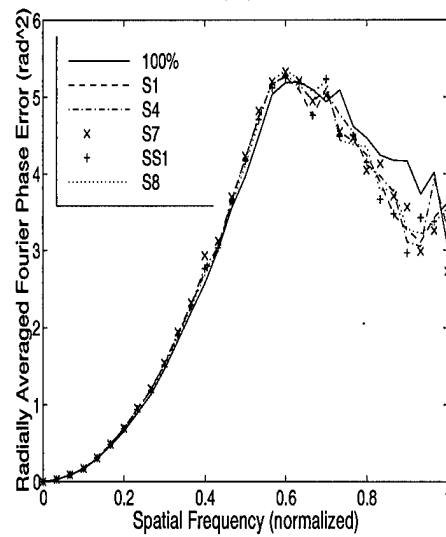
(a)



(b)

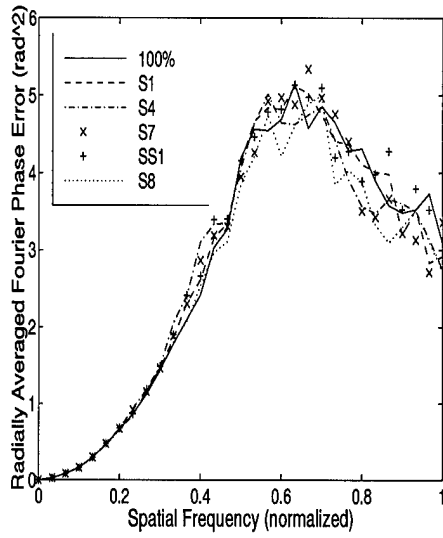


(c)

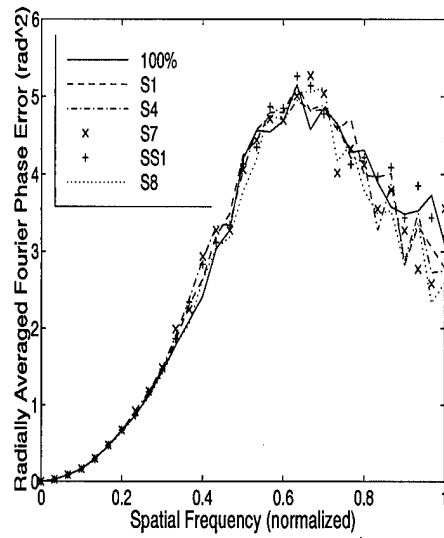


(d)

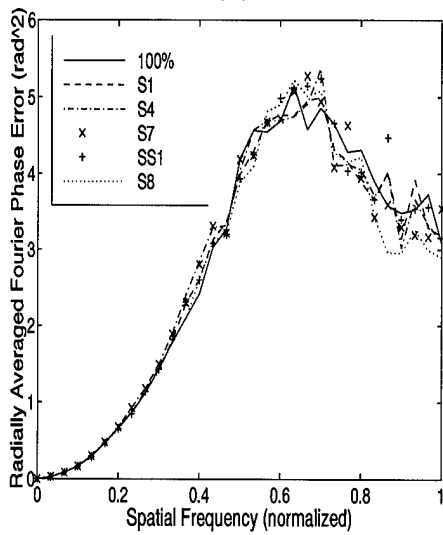
Figure B.9 Bispectrum phase error, extended source,  $m_\nu = 1$ ,  $r_o = 17$  cm. FSR = a) 50% b) 60% c) 70% d) 80%



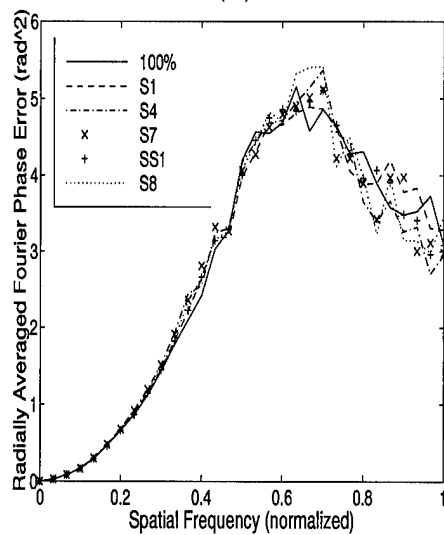
(a)



(b)

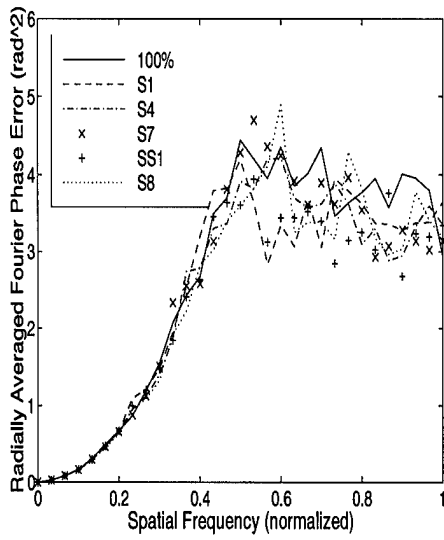


(c)

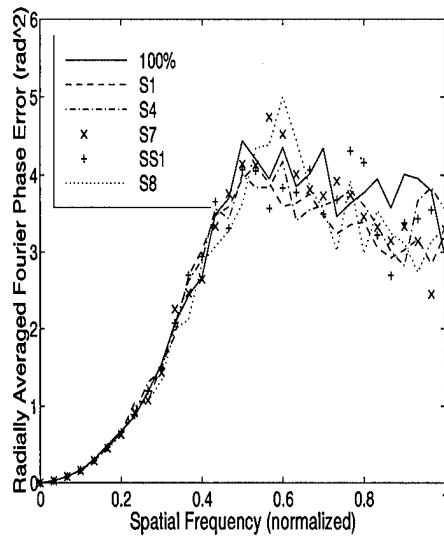


(d)

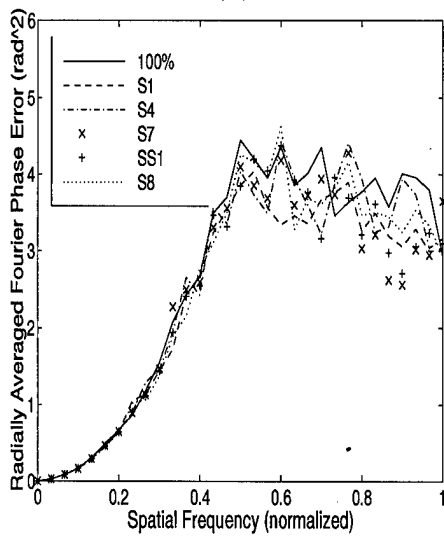
Figure B.10 Bispectrum phase error, extended source,  $m_\nu = 3$ ,  $r_o = 17$  cm. FSR = a) 50% b) 60% c) 70% d) 80%



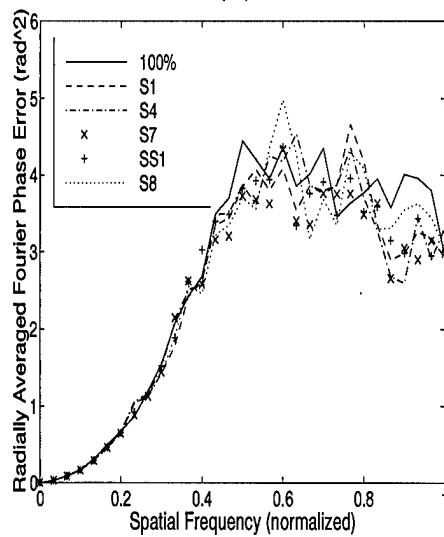
(a)



(b)

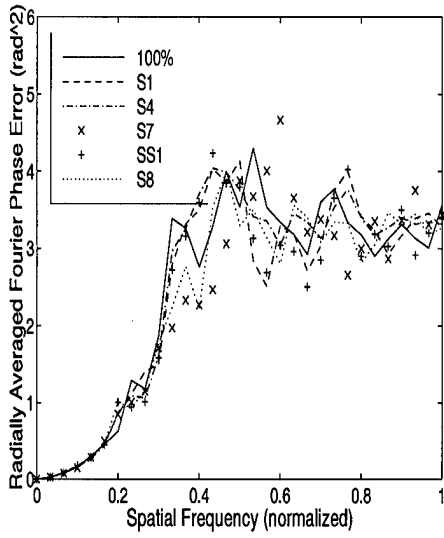


(c)

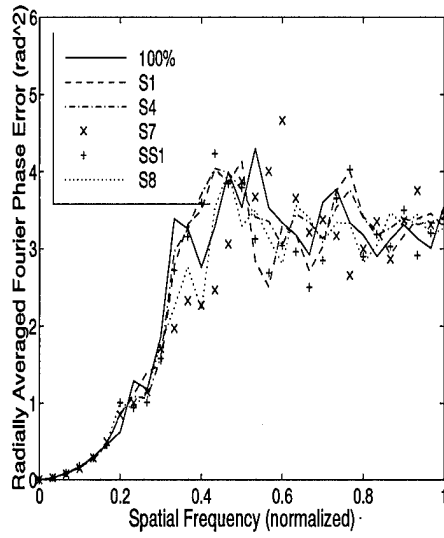


(d)

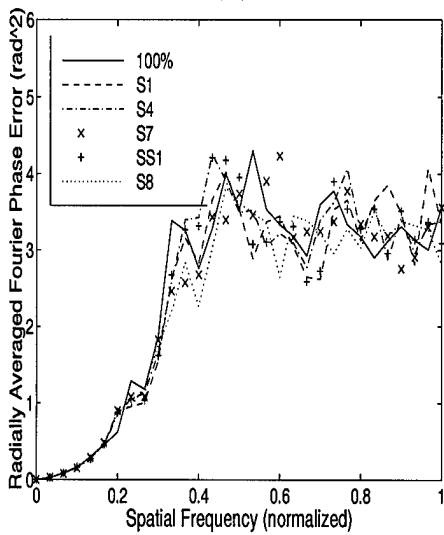
Figure B.11 Bispectrum phase error, extended source,  $m_\nu = 5$ ,  $r_o = 17$  cm. FSR = a) 50% b) 60% c) 70% d) 80%



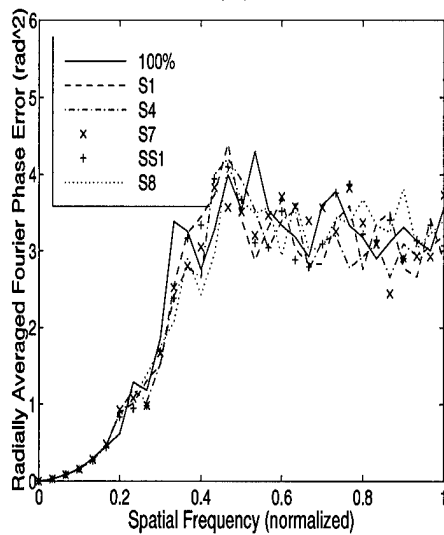
(a)



(b)



(c)

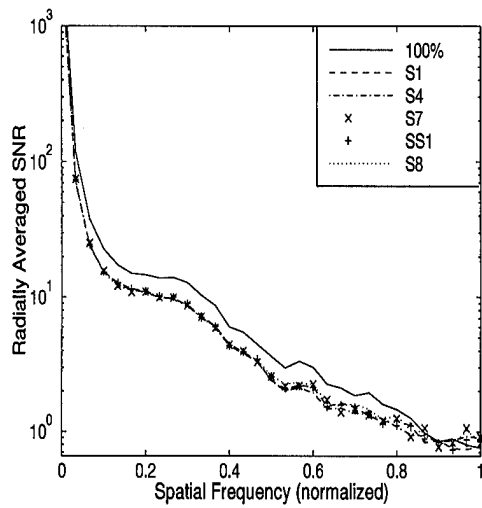


(d)

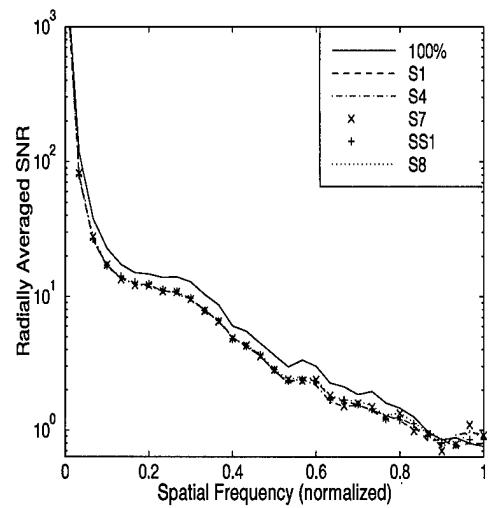
Figure B.12 Bispectrum phase error, extended source,  $m_\nu = 7$ ,  $r_o = 17$  cm. FSR = a) 50% b) 60% c) 70% d) 80%

## *B.2 Simulation Results for Extended Source*

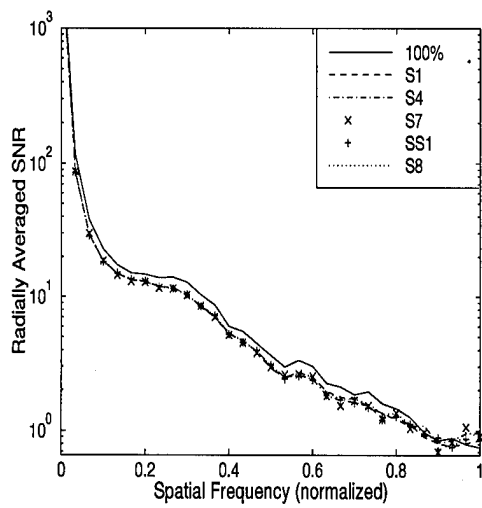
This section contains the power spectrum SNR results for the extended source experiment. On each page, the four FSR strategies are presented, containing the results of the five metrics tested. A given set of visual parameters,  $r_o$  and  $m_v$ , are identified below.



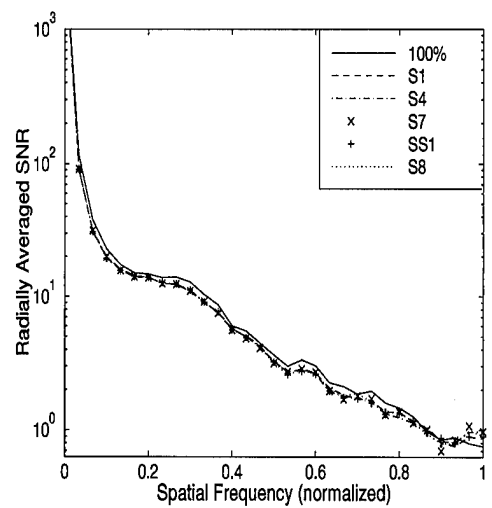
(a)



(b)

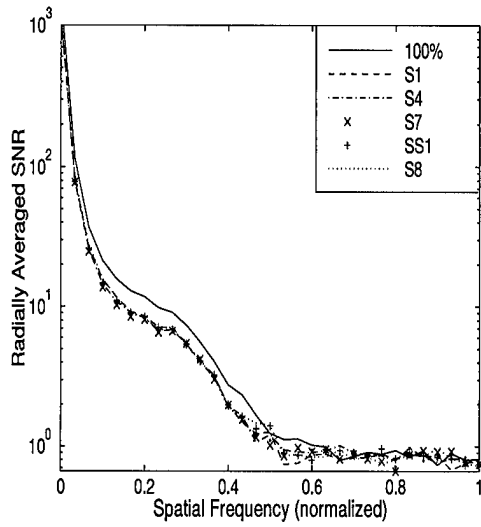


(c)

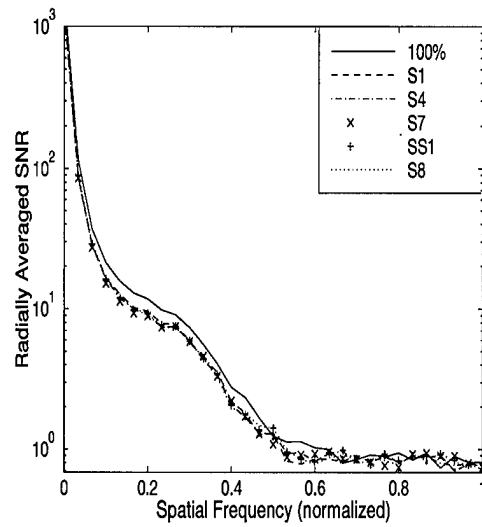


(d)

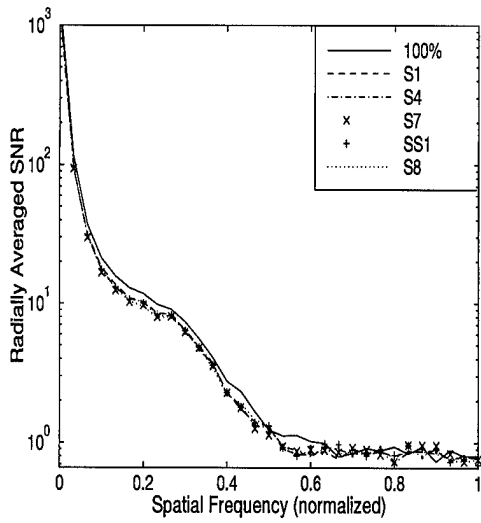
Figure B.13 Power spectrum SNR, extended source,  $m_\nu = 1$ ,  $r_o = 7$  cm. FSR = a) 50% b) 60% c) 70% d) 80%



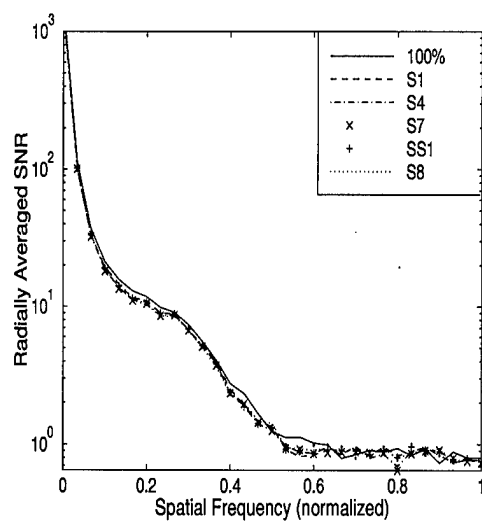
(a)



(b)

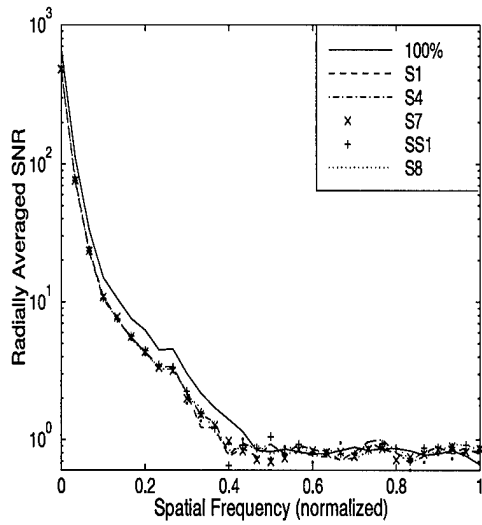


(c)

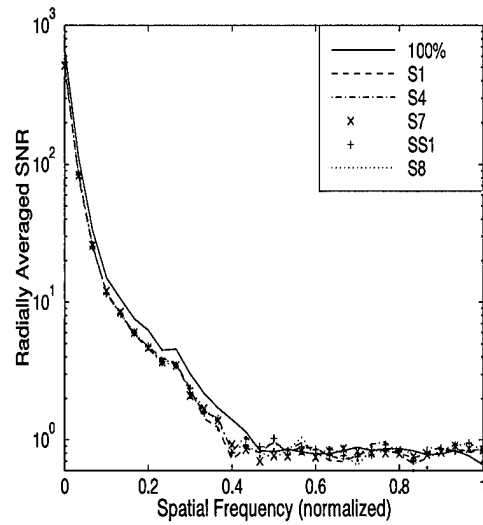


(d)

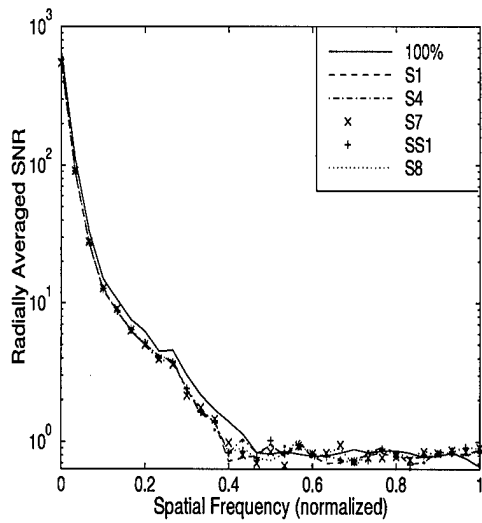
Figure B.14 Power spectrum SNR, extended source,  $m_\nu = 3$ ,  $r_o = 7$  cm. FSR = a) 50% b) 60% c) 70% d) 80%



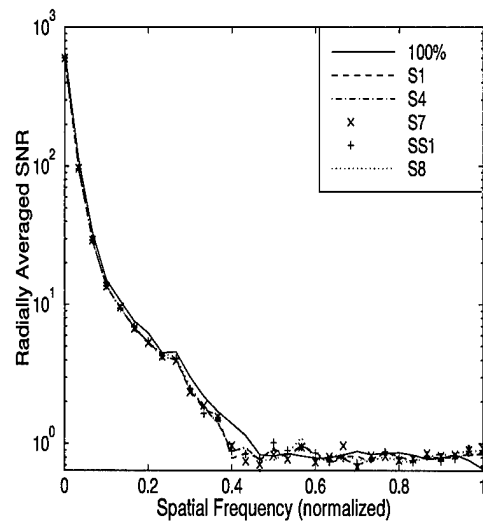
(a)



(b)

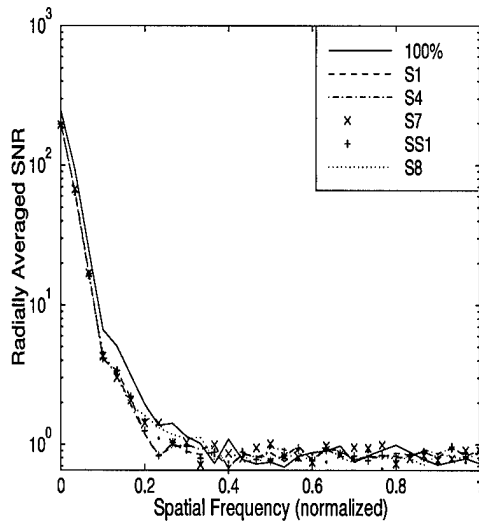


(c)

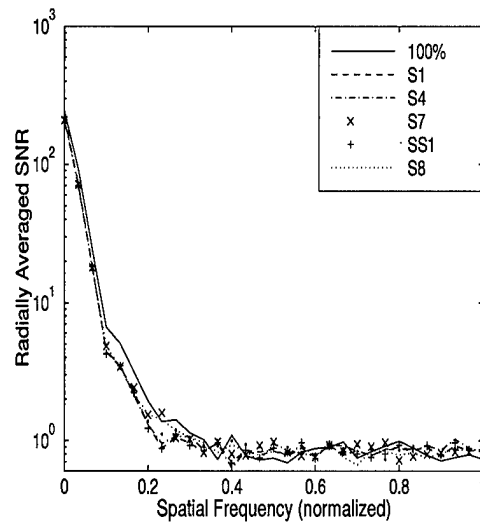


(d)

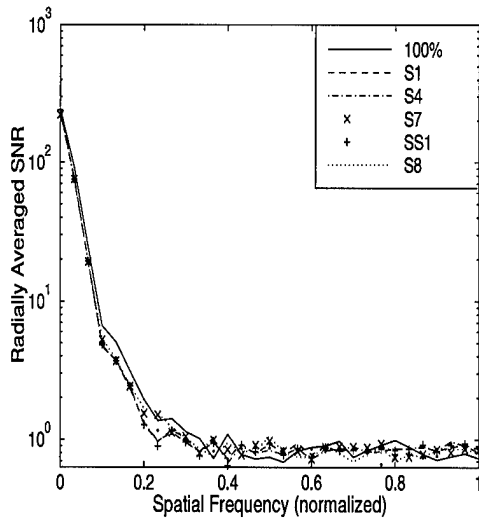
Figure B.15 Power spectrum SNR, extended source,  $m_\nu = 5$ ,  $r_o = 7$  cm. FSR = a) 50% b) 60% c) 70% d) 80%



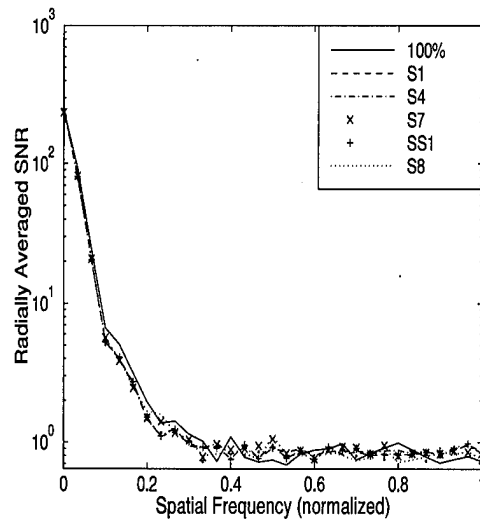
(a)



(b)

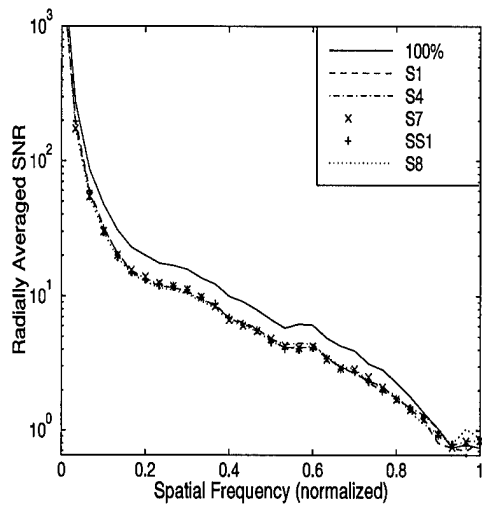


(c)

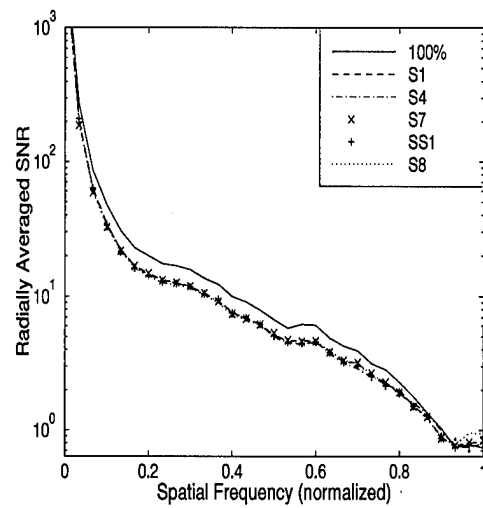


(d)

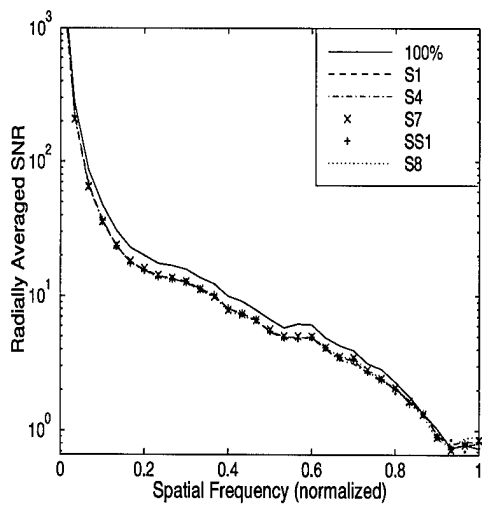
Figure B.16 Power spectrum SNR, extended source,  $m_\nu = 7$ ,  $r_o = 7$  cm. FSR = a) 50% b) 60% c) 70% d) 80%



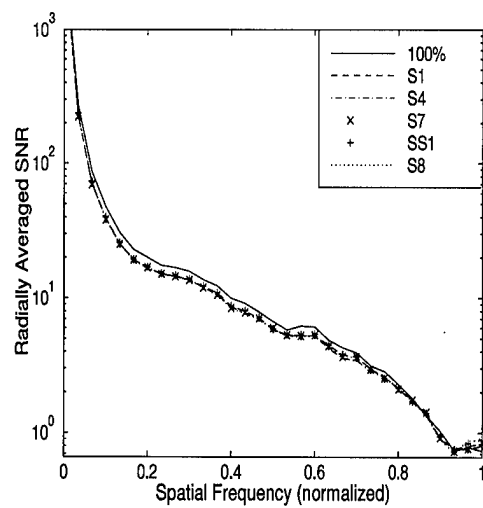
(a)



(b)

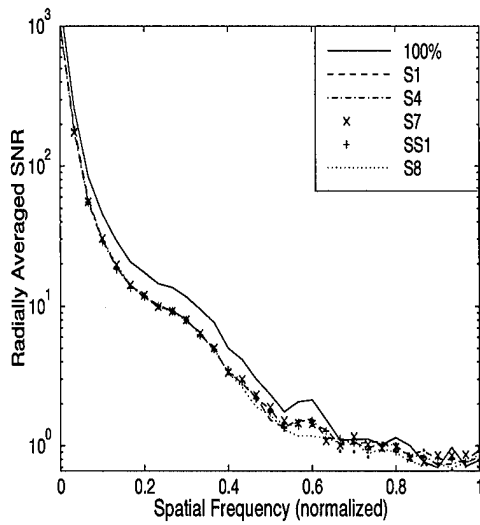


(c)

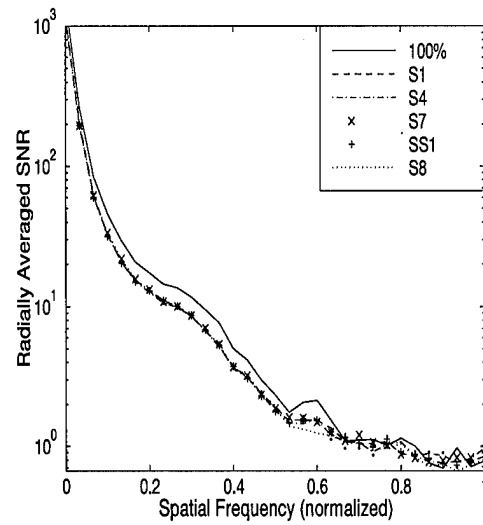


(d)

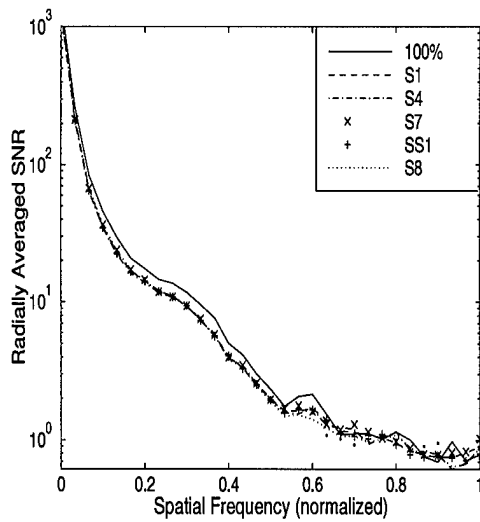
Figure B.17 Power spectrum SNR, extended source,  $m_\nu = 1$ ,  $r_o = 12$  cm. FSR = a) 50% b) 60% c) 70% d) 80%



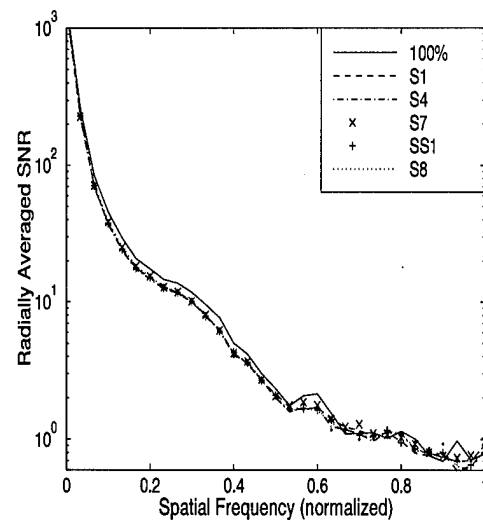
(a)



(b)

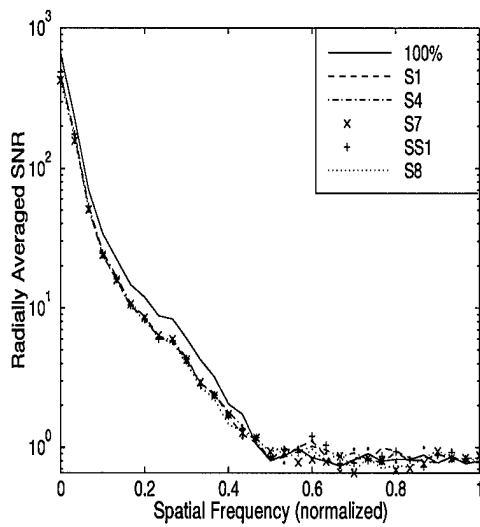


(c)

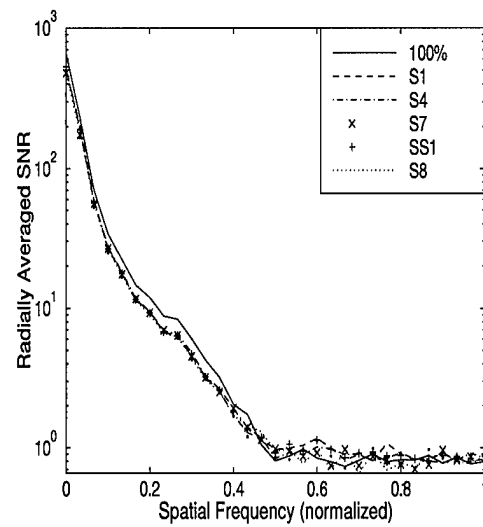


(d)

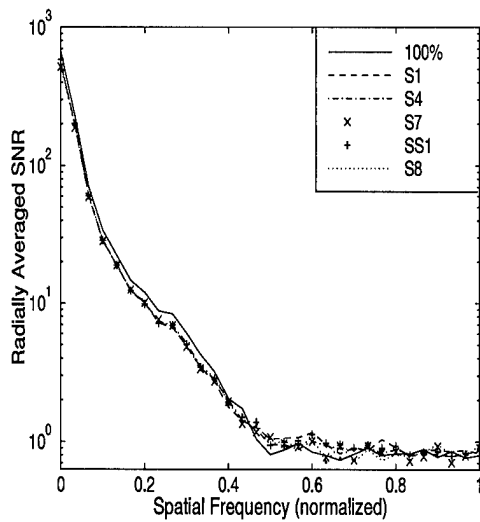
Figure B.18 Power spectrum SNR, extended source,  $m_\nu = 3$ ,  $r_o = 12$  cm. FSR = a) 50% b) 60% c) 70% d) 80%



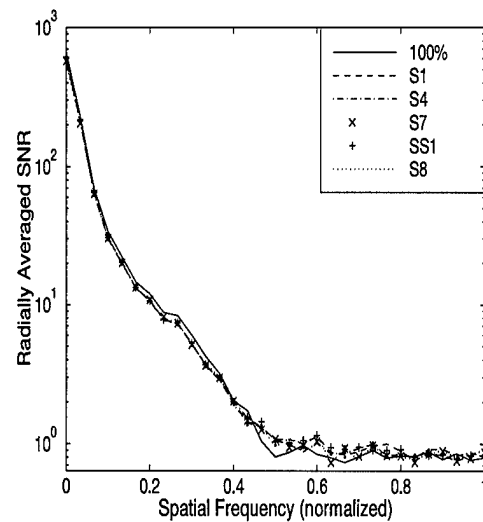
(a)



(b)

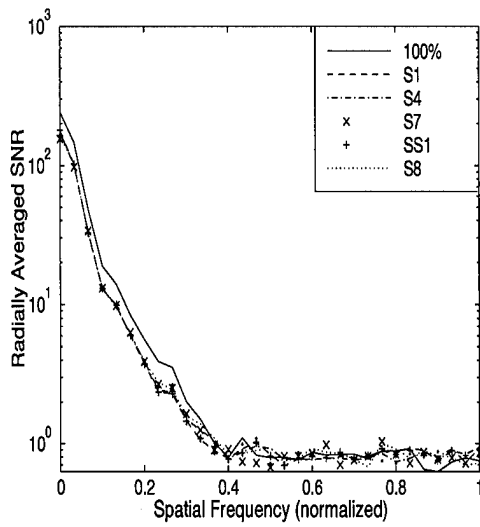


(c)

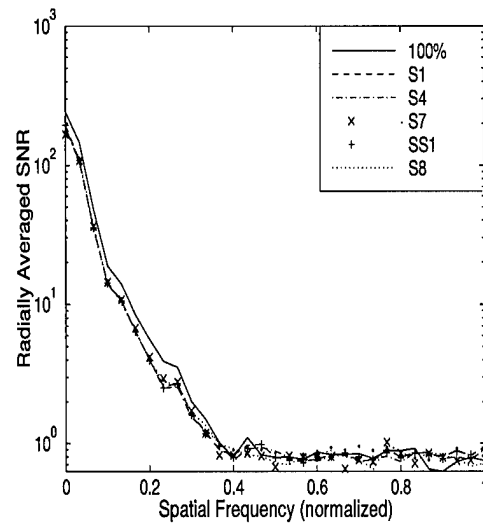


(d)

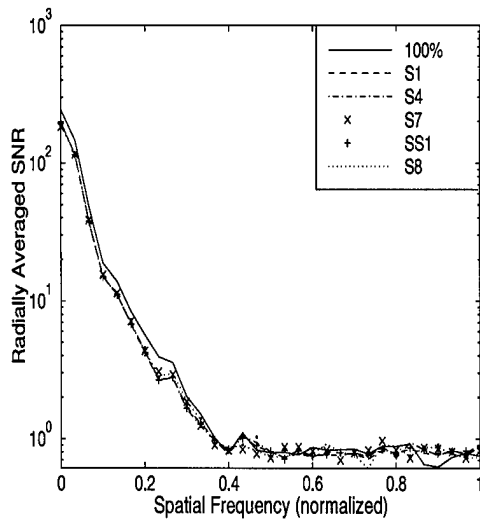
Figure B.19 Power spectrum SNR, extended source,  $m_\nu = 5$ ,  $r_o = 12$  cm. FSR = a) 50% b) 60% c) 70% d) 80%



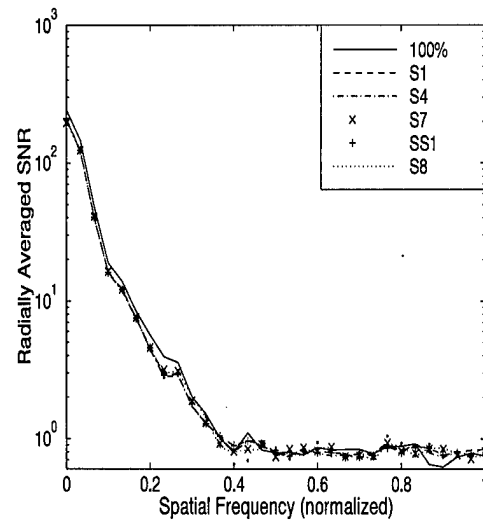
(a)



(b)

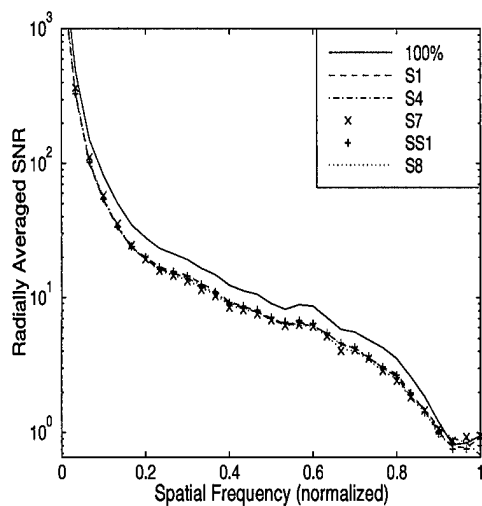


(c)

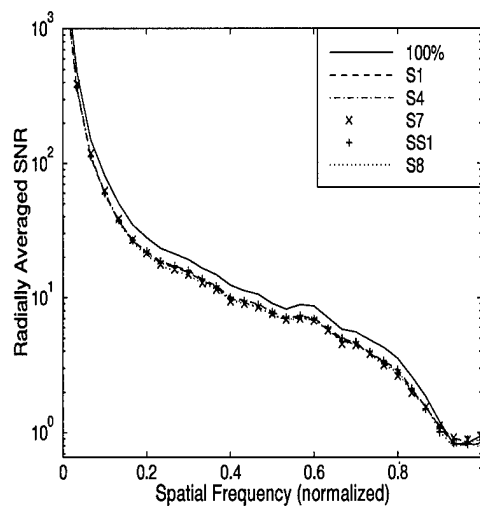


(d)

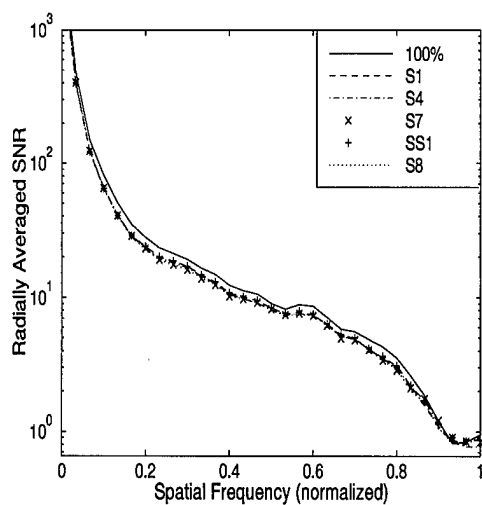
Figure B.20 Power spectrum SNR, extended source,  $m_\nu = 7$ ,  $r_o = 12$  cm. FSR = a) 50% b) 60% c) 70% d) 80%



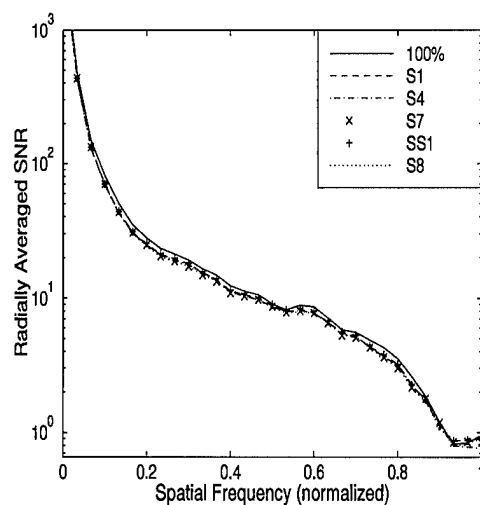
(a)



(b)

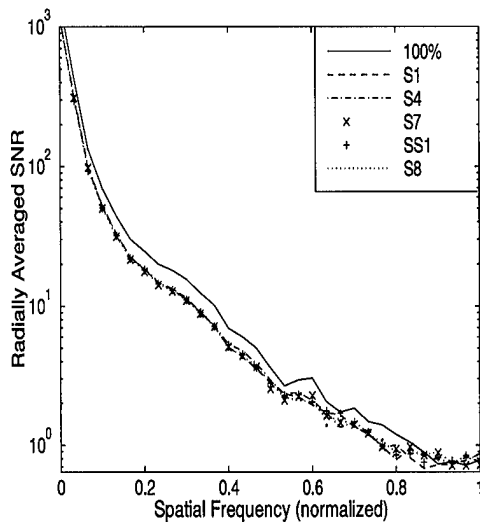


(c)

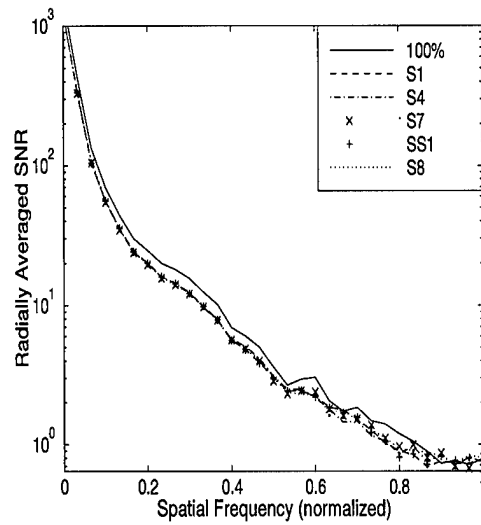


(d)

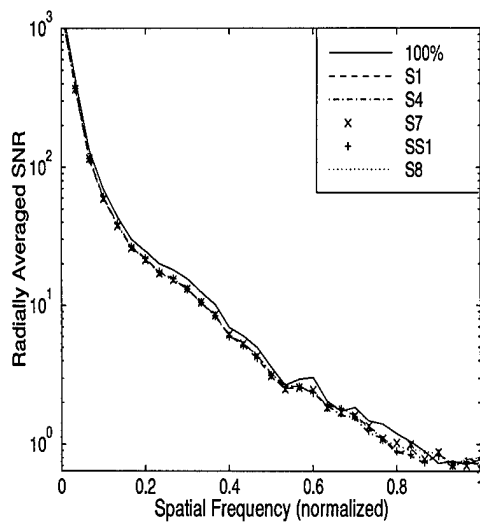
Figure B.21 Power spectrum SNR, extended source,  $m_\nu = 1$ ,  $r_o = 17$  cm. FSR = a) 50% b) 60% c) 70% d) 80%



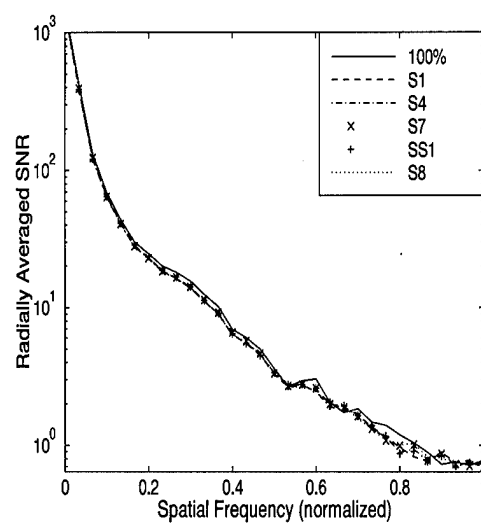
(a)



(b)

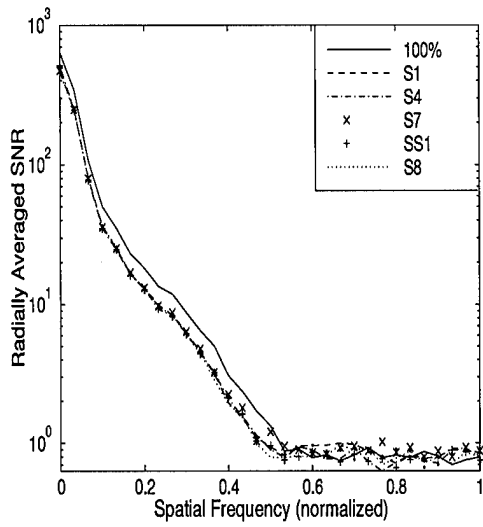


(c)

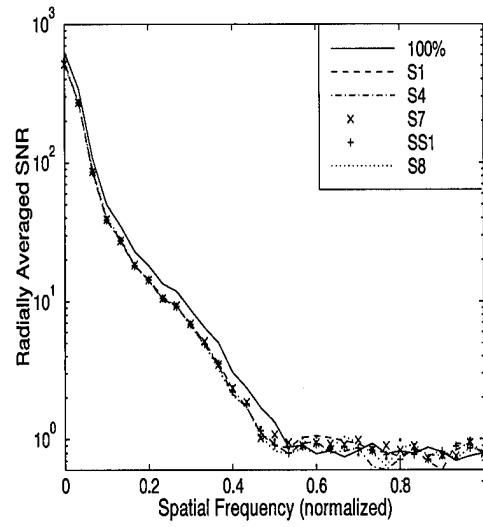


(d)

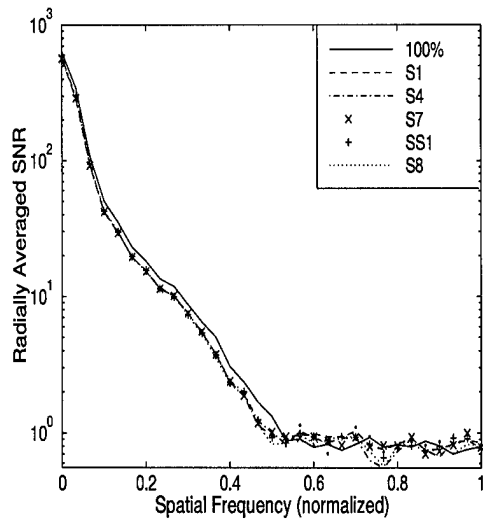
Figure B.22 Power spectrum SNR, extended source,  $m_\nu = 3$ ,  $r_o = 17$  cm. FSR = a) 50% b) 60% c) 70% d) 80%



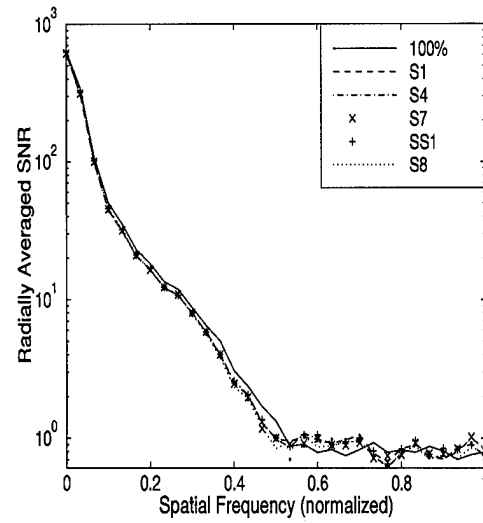
(a)



(b)

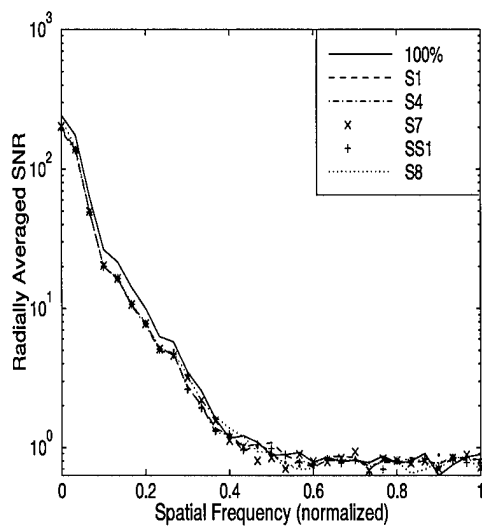


(c)

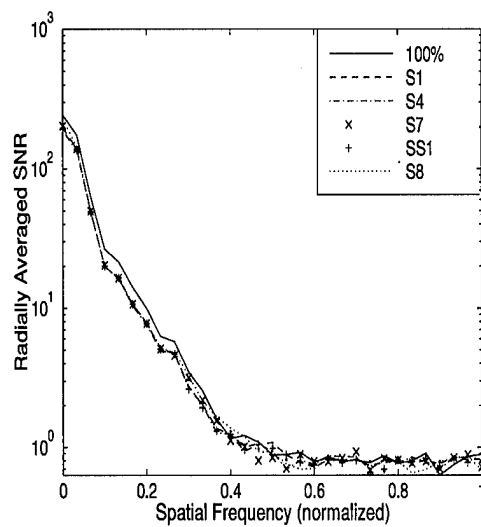


(d)

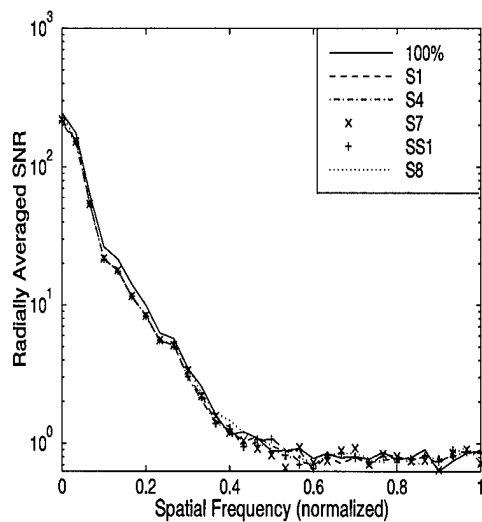
Figure B.23 Power spectrum SNR, extended source,  $m_\nu = 5$ ,  $r_o = 17$  cm. FSR = a) 50% b) 60% c) 70% d) 80%



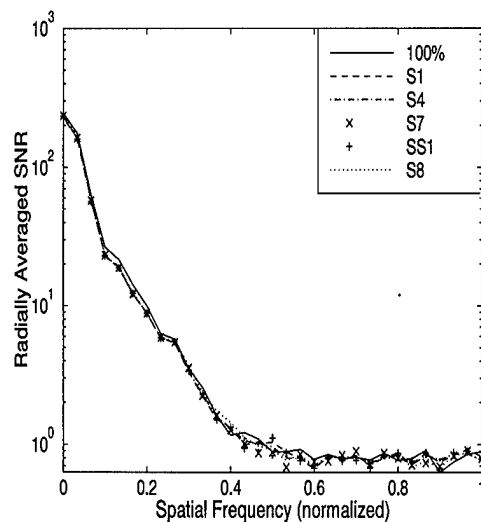
(a)



(b)



(c)

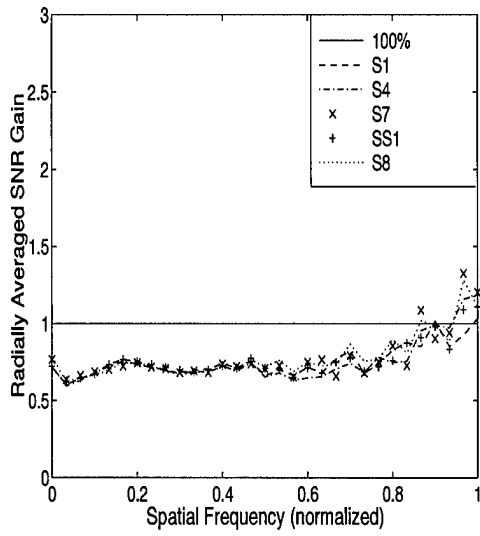


(d)

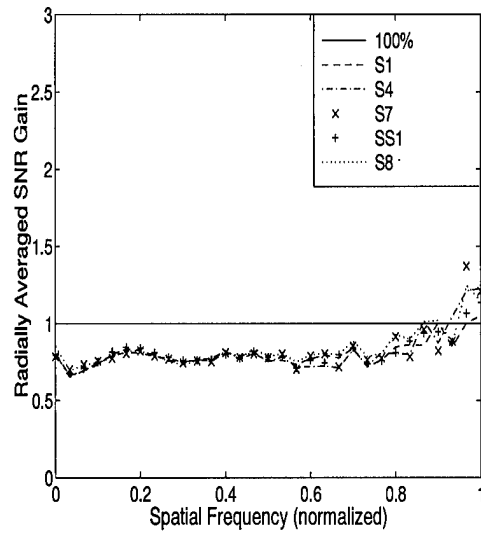
Figure B.24 Power spectrum SNR, extended source,  $m_\nu = 7$ ,  $r_o = 17$  cm. FSR = a) 50% b) 60% c) 70% d) 80%

### *B.3 Extended Source Power Spectrum Gain Plots*

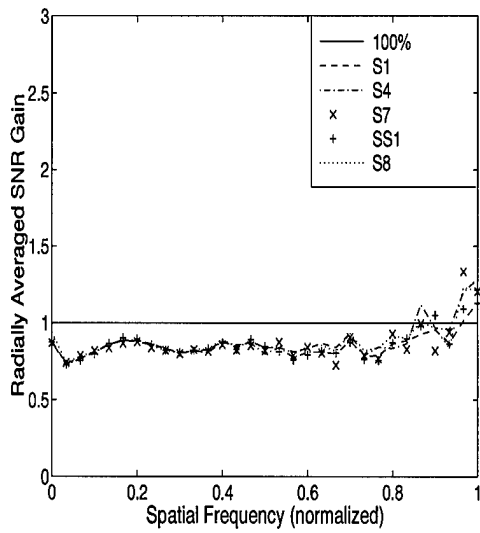
This section contains the power spectrum SNR gain plots for the point source experiment. Gain is defined as the ratio of the power spectrum achieved by using frame selection to that without frame selection. On each page, the four FSR strategies are presented, containing the results of the five metrics tested. A given set of visual parameters,  $r_o$  and  $m_\nu$ , are identified below.



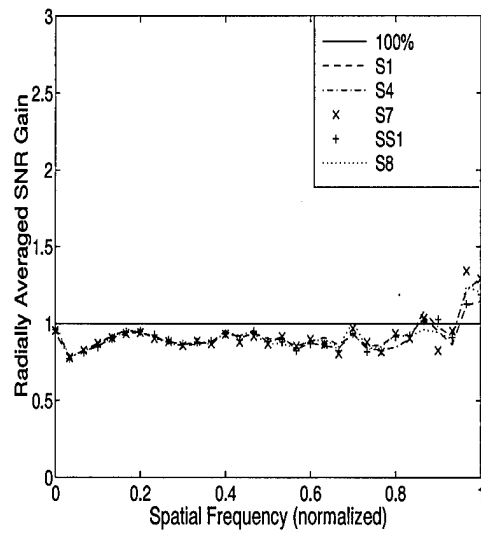
(a)



(b)

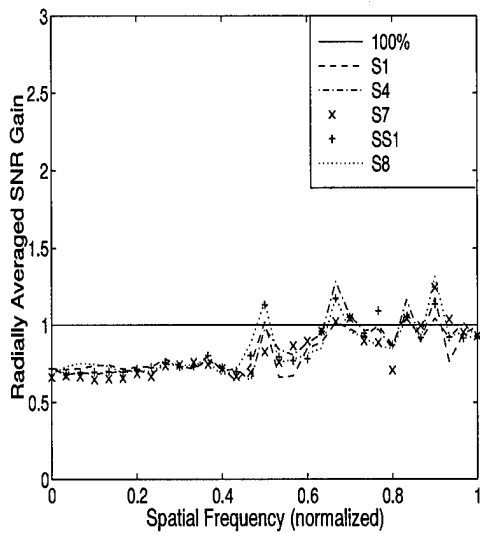


(c)

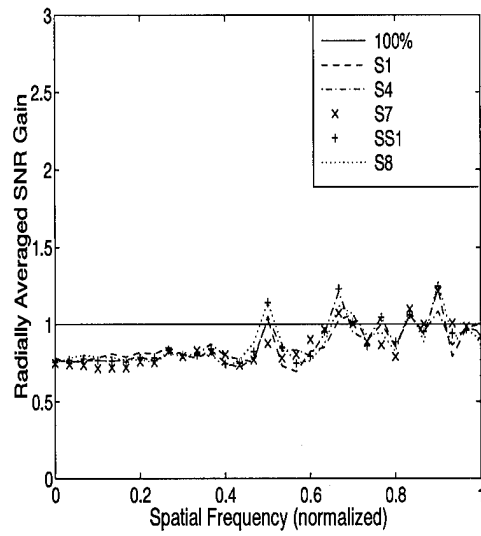


(d)

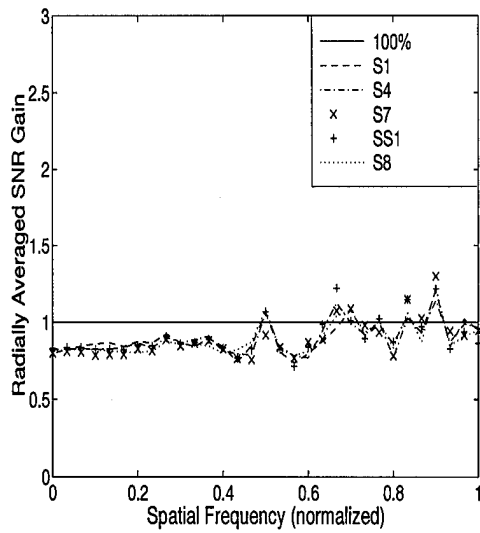
Figure B.25 Power spectrum gain, extended source,  $m_v = 1$ ,  $r_0 = 7$  cm. FSR = a) 50% b) 60% c) 70% d) 80%



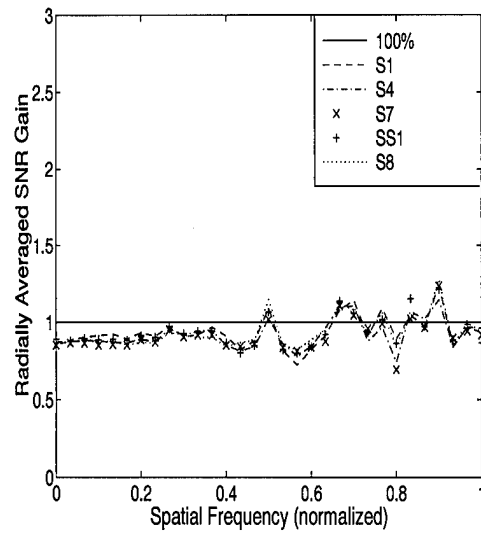
(a)



(b)

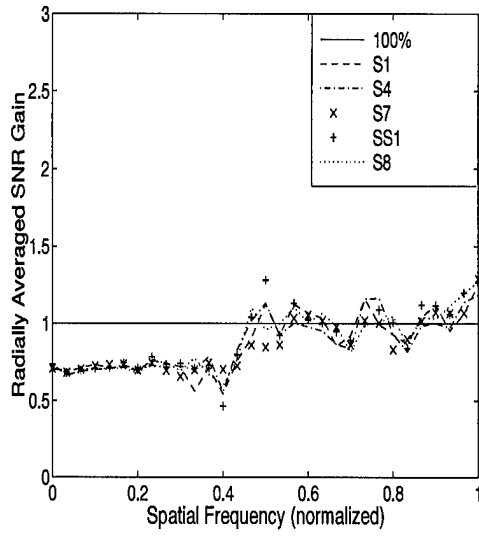


(c)

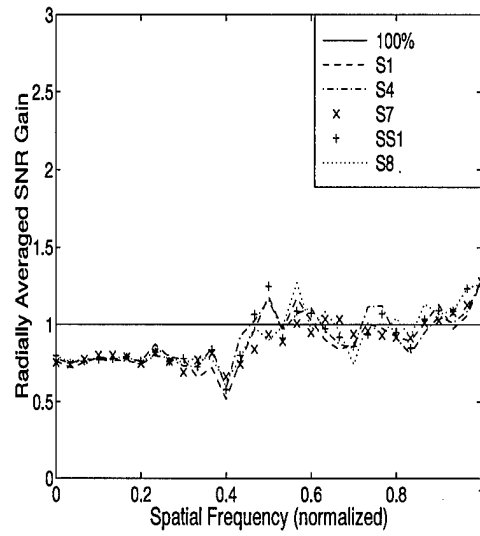


(d)

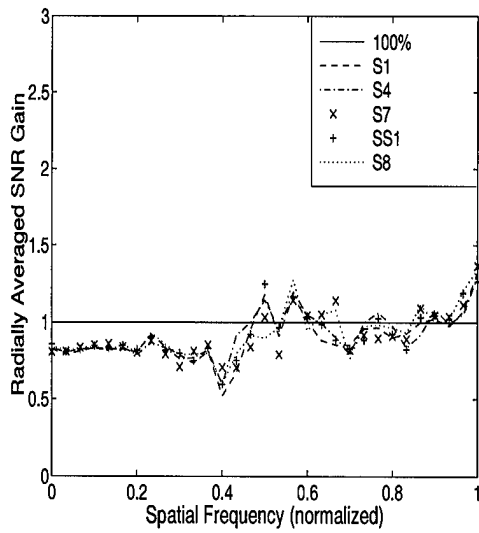
Figure B.26 Power spectrum gain, extended source,  $m_v = 3$ ,  $r_0 = 7$  cm. FSR = a) 50% b) 60% c) 70% d) 80%



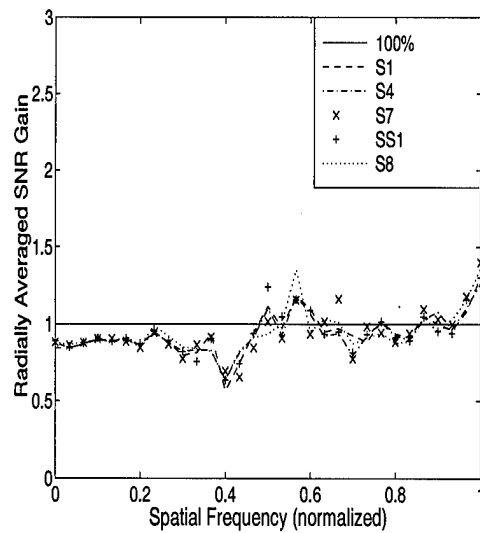
(a)



(b)

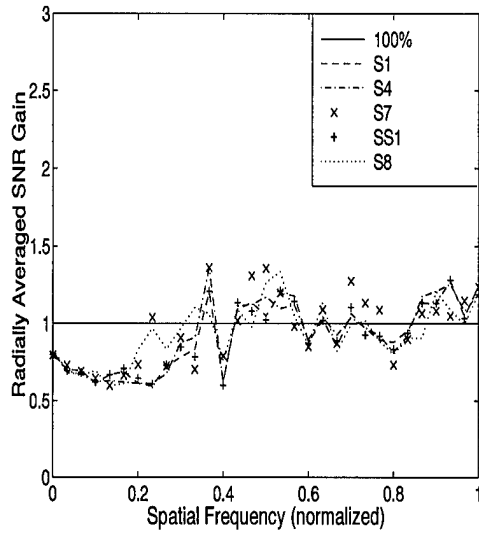


(c)

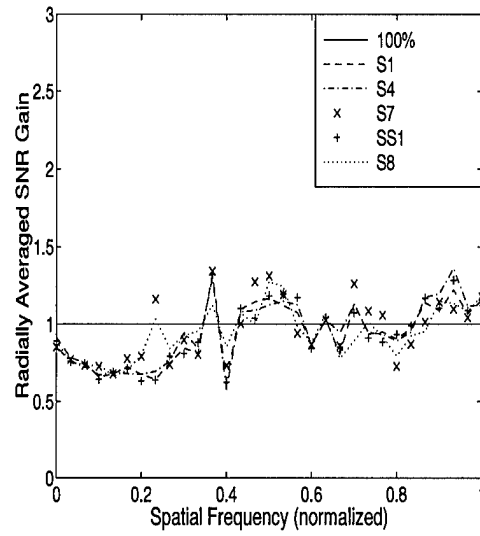


(d)

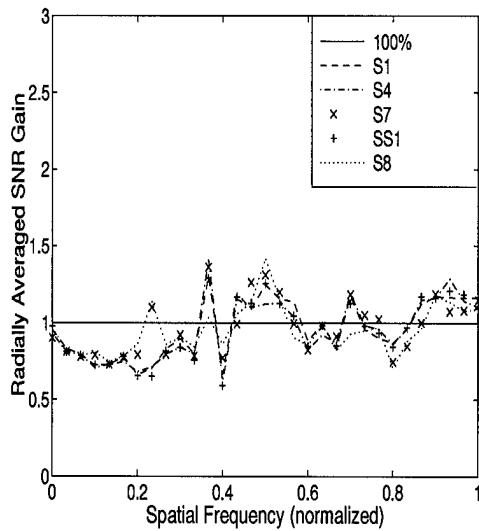
Figure B.27 Power spectrum gain, extended source,  $m_v = 5$ ,  $r_0 = 7$  cm. FSR = a) 50% b) 60% c) 70% d) 80%



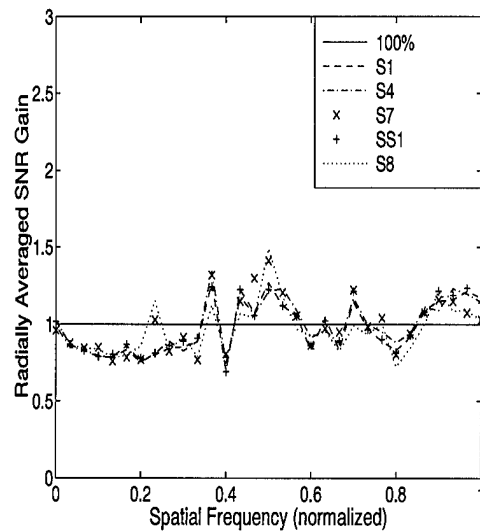
(a)



(b)

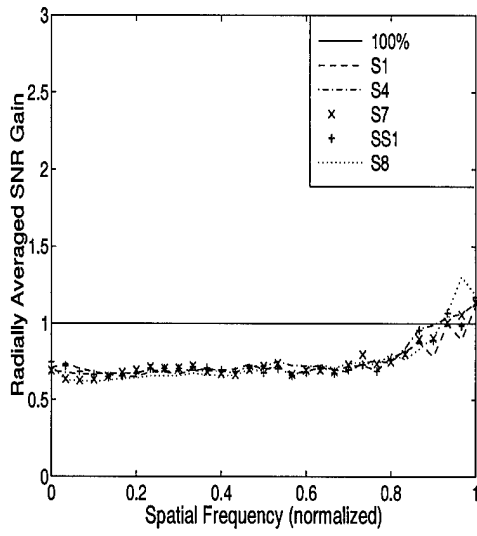


(c)

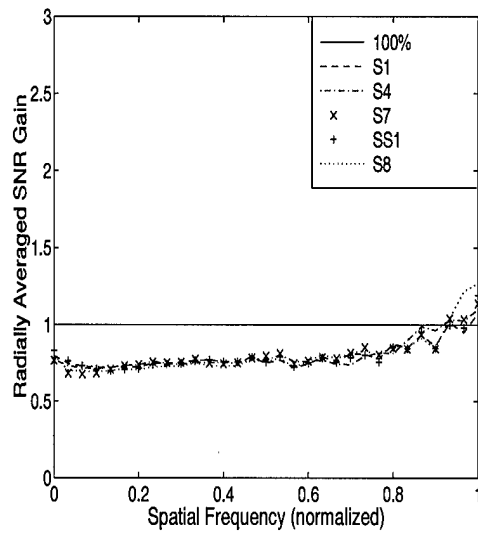


(d)

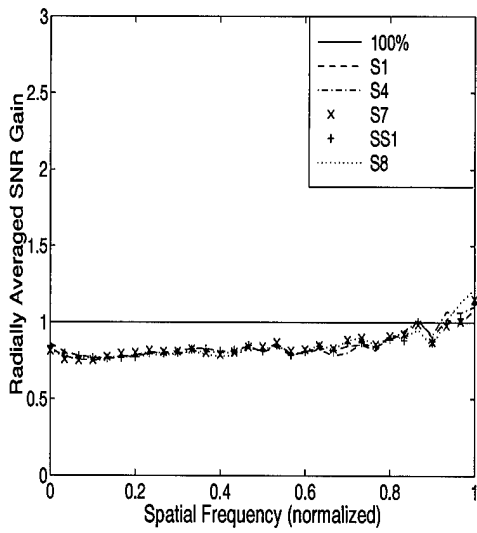
Figure B.28 Power spectrum gain, extended source,  $m_v = 7$ ,  $r_0 = 7$  cm. FSR = a) 50% b) 60% c) 70% d) 80%



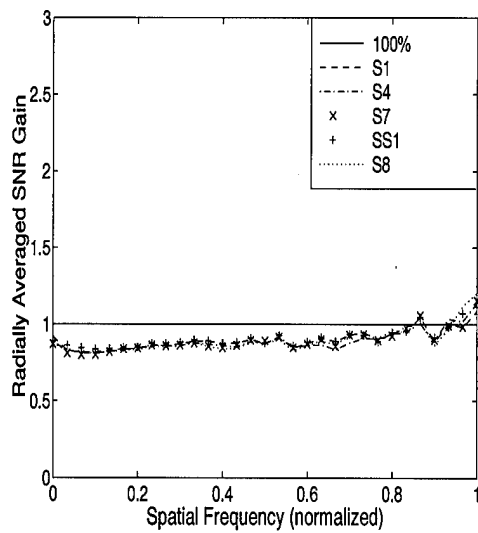
(a)



(b)

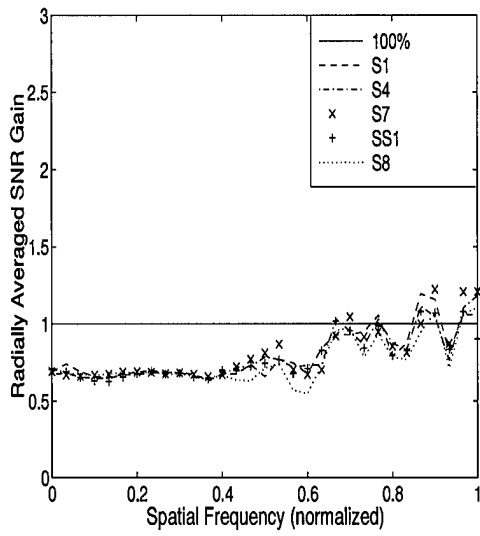


(c)

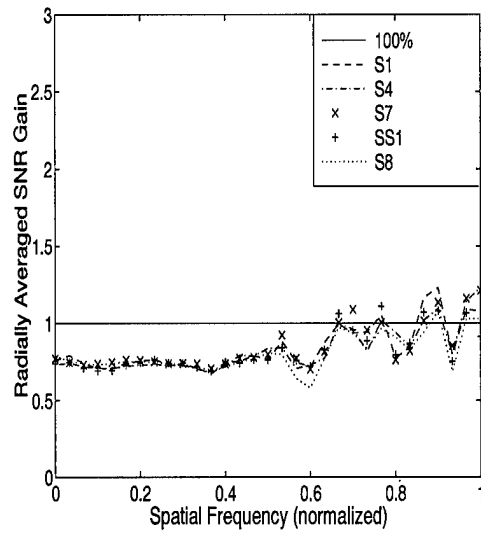


(d)

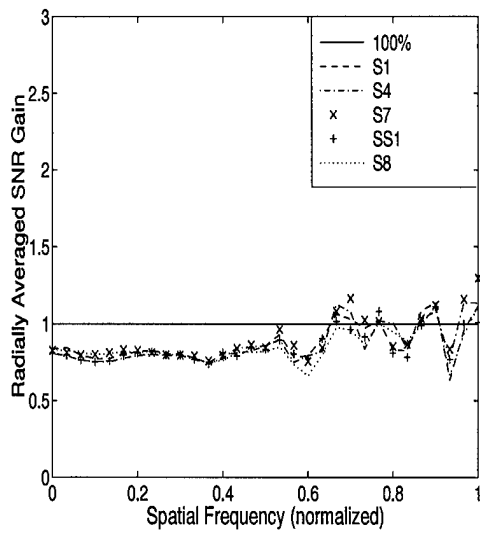
Figure B.29 Power spectrum gain, extended source,  $m_v = 1$ ,  $r_0 = 12$  cm. FSR =  
a) 50% b) 60% c) 70% d) 80%



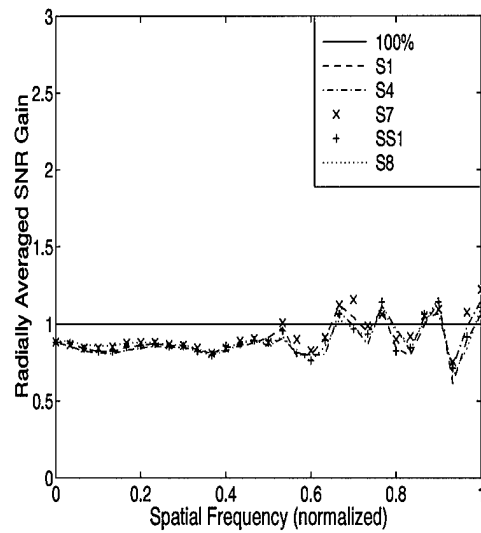
(a)



(b)

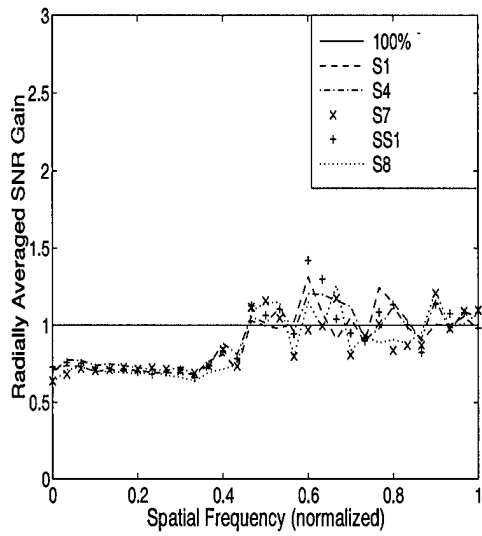


(c)

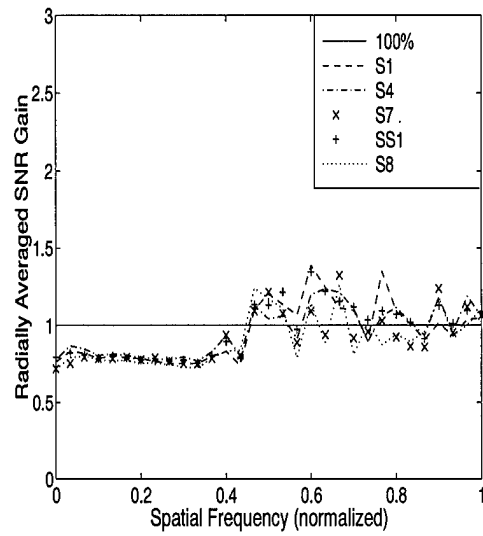


(d)

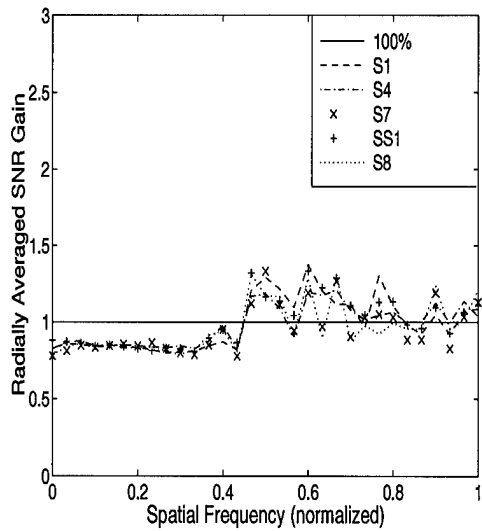
Figure B.30 Power spectrum gain, extended source,  $m_v = 3$ ,  $r_0 = 12$  cm. FSR = a) 50% b) 60% c) 70% d) 80%



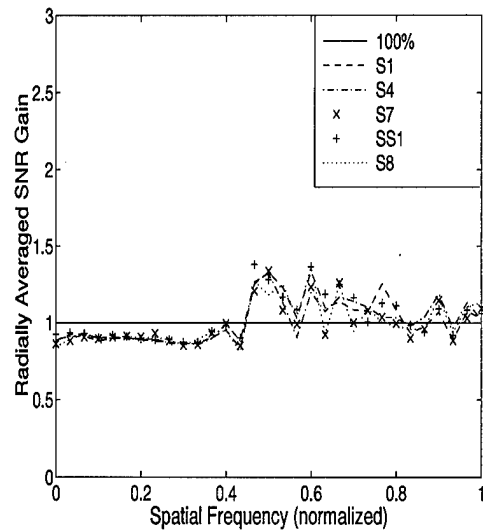
(a)



(b)

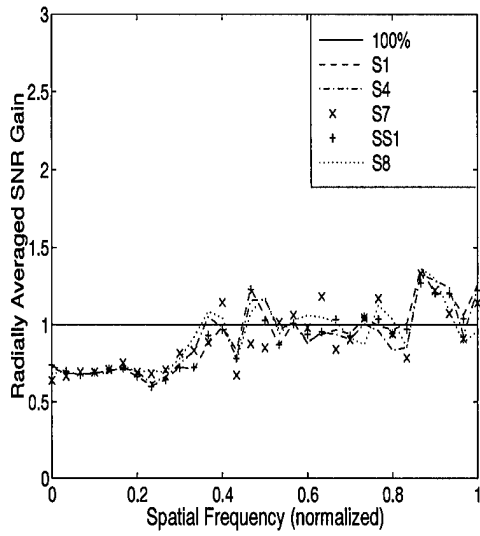


(c)

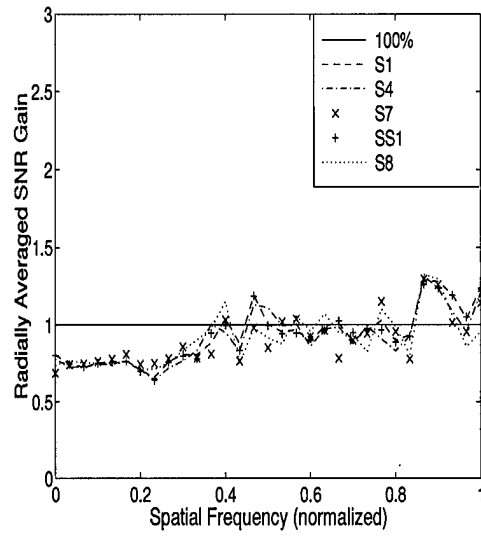


(d)

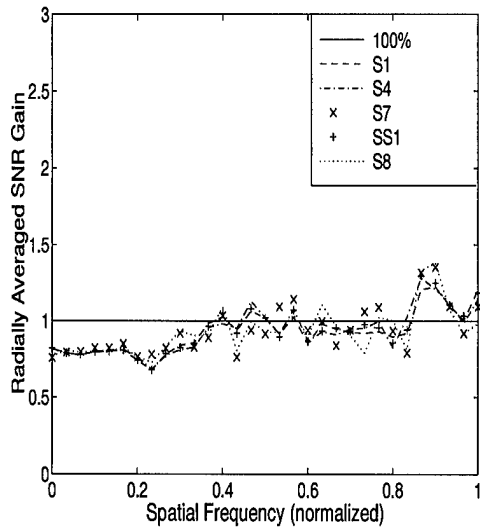
Figure B.31 Power spectrum gain, extended source,  $m_v = 5$ ,  $r_0 = 12$  cm. FSR = a) 50% b) 60% c) 70% d) 80%



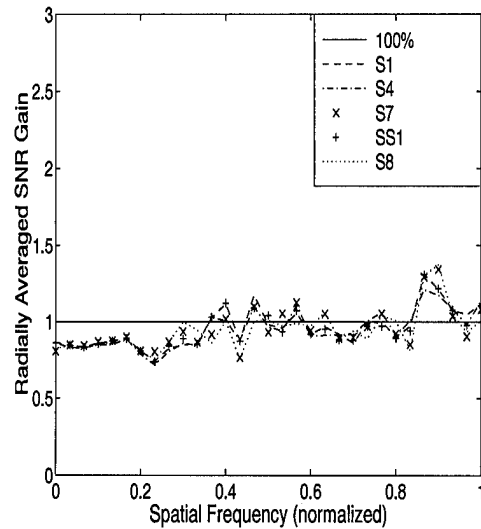
(a)



(b)

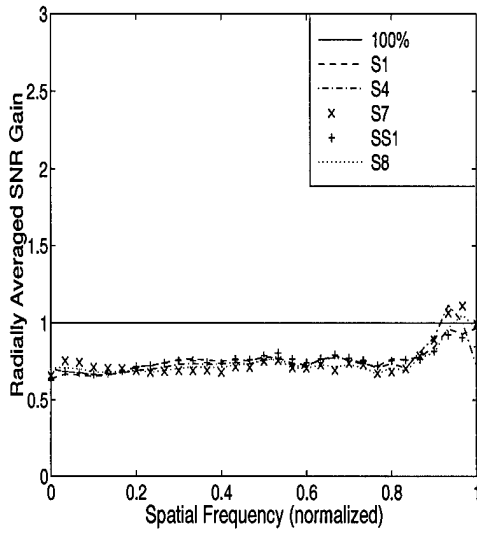


(c)

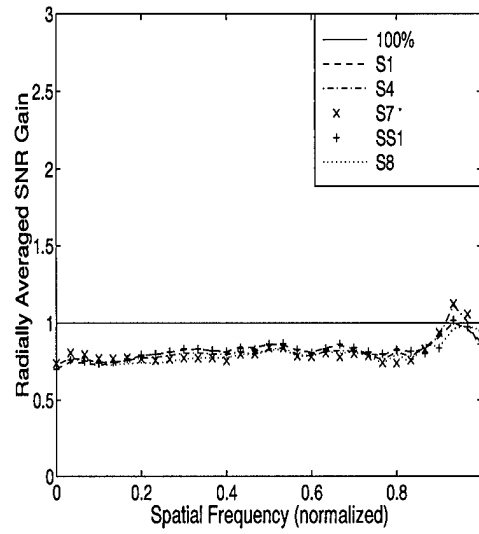


(d)

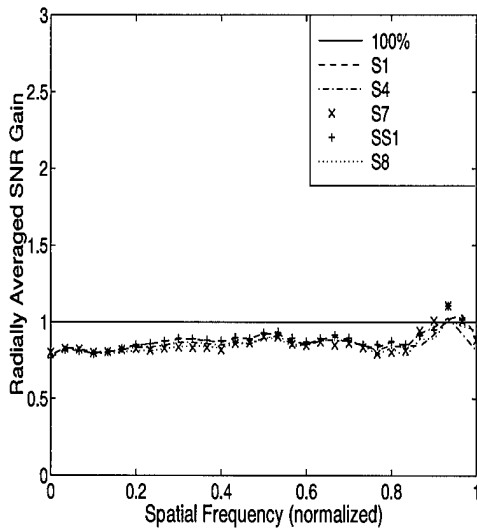
Figure B.32 Power spectrum gain, extended source,  $m_v = 7$ ,  $r_0 = 12$  cm. FSR = a) 50% b) 60% c) 70% d) 80%



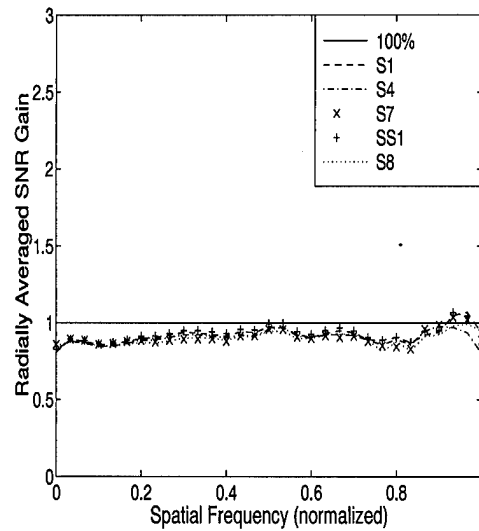
(a)



(b)

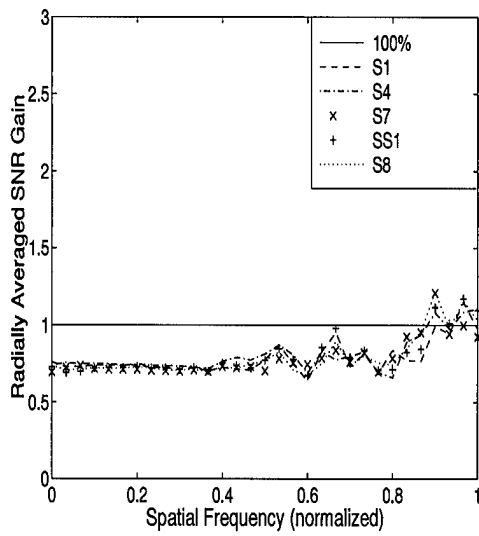


(c)

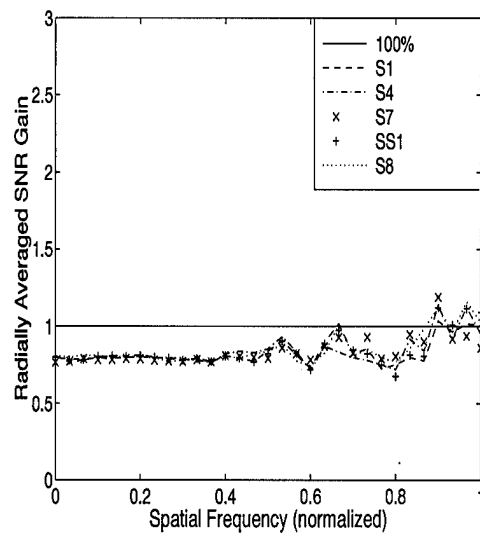


(d)

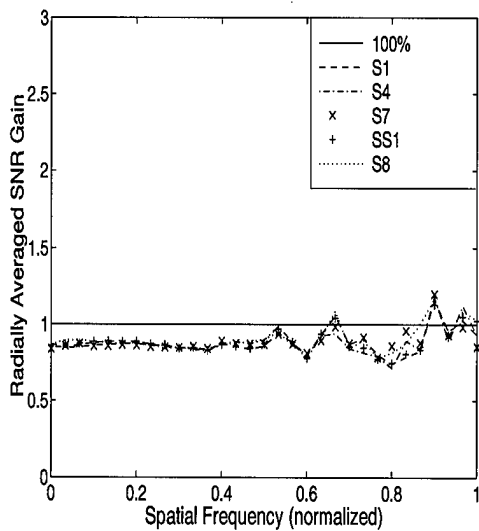
Figure B.33 Power spectrum gain, extended source,  $m_v = 1$ ,  $r_0 = 17$  cm. FSR = a) 50% b) 60% c) 70% d) 80%



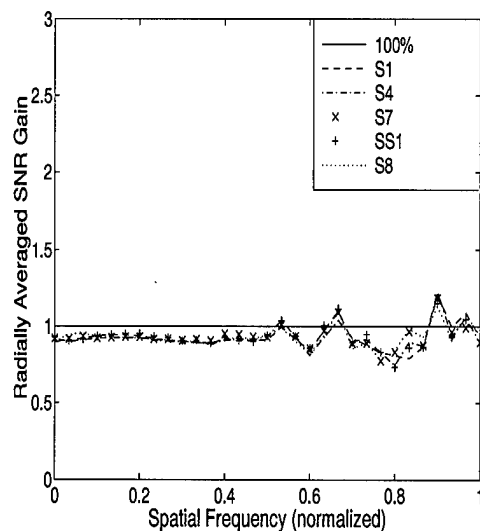
(a)



(b)

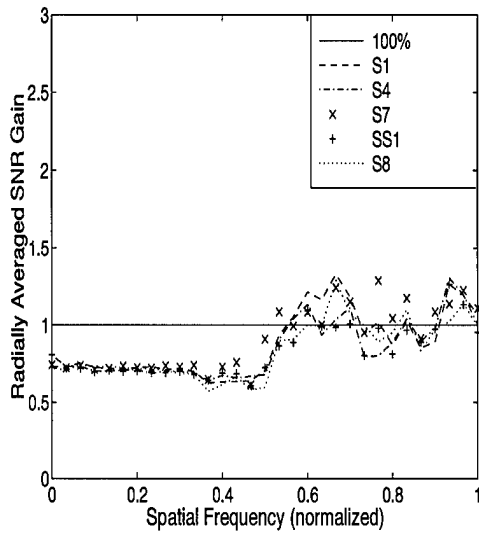


(c)

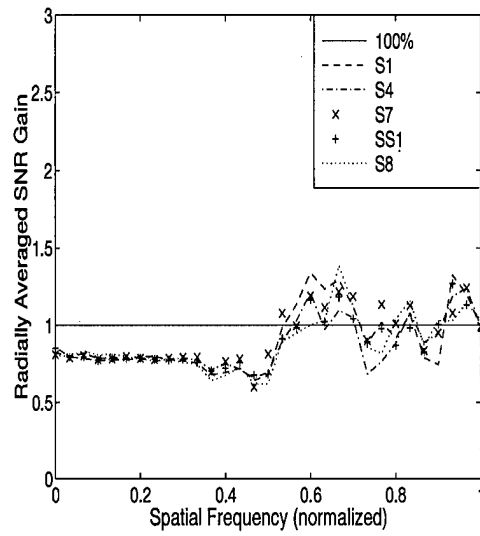


(d)

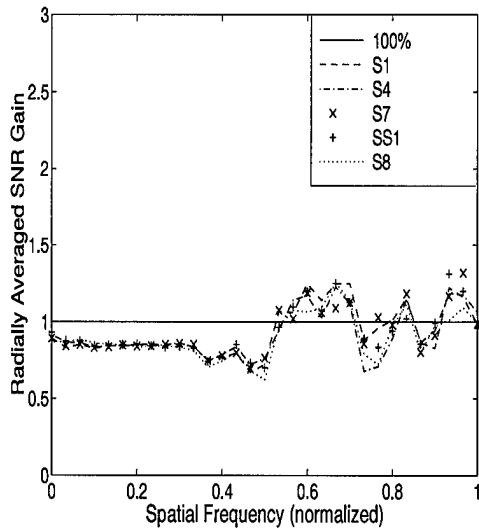
Figure B.34 Power spectrum gain, extended source,  $m_v = 3$ ,  $r_0 = 17$  cm. FSR =  
a) 50% b) 60% c) 70% d) 80%



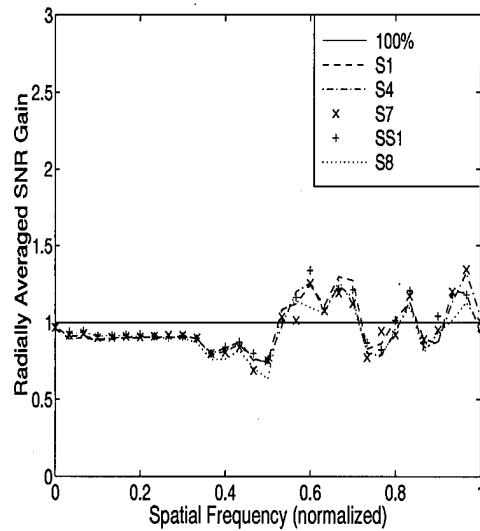
(a)



(b)

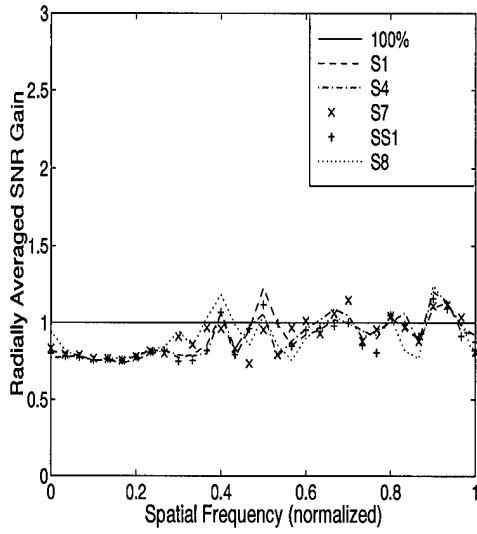


(c)

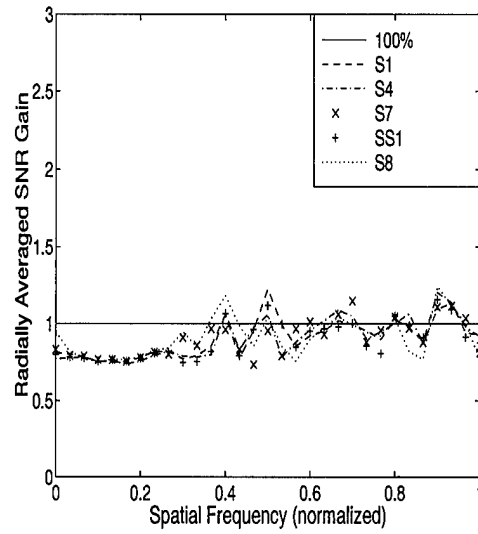


(d)

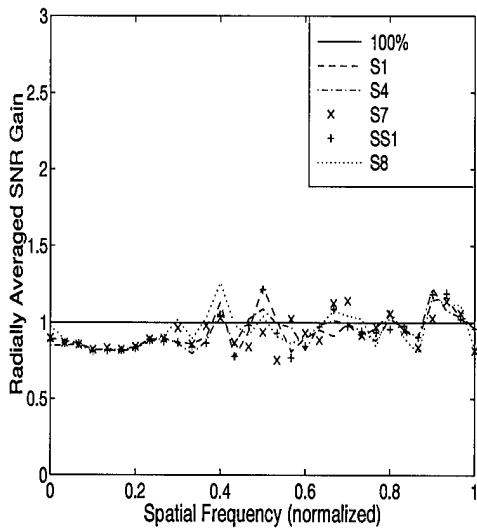
Figure B.35 Power spectrum gain, extended source,  $m_v = 5$ ,  $r_0 = 17$  cm. FSR =  
a) 50% b) 60% c) 70% d) 80%



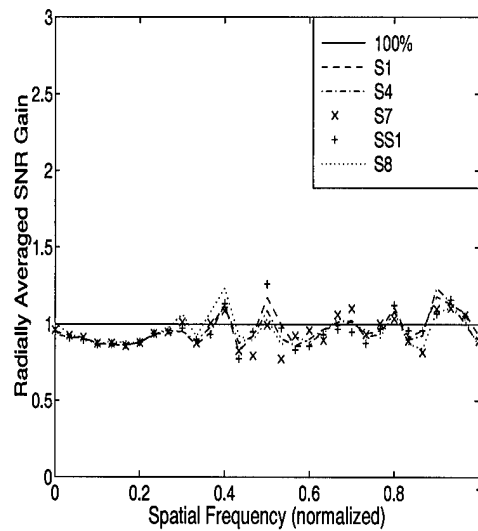
(a)



(b)



(c)



(d)

Figure B.36 Power spectrum gain, extended source,  $m_v = 7$ ,  $r_0 = 17$  cm. FSR = a) 50% b) 60% c) 70% d) 80%

#### B.4 Extended Source Comparative Phase Error Difference Plots

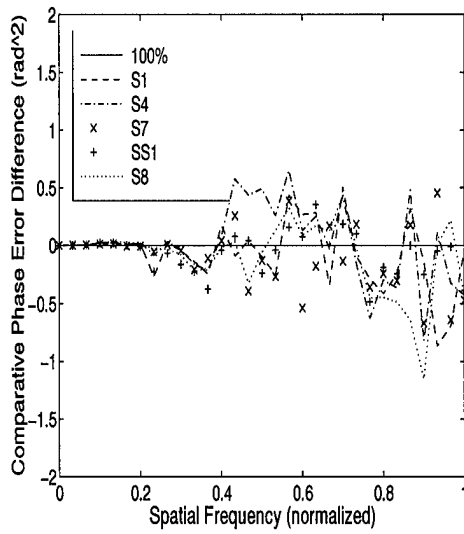
This section contains the phase error difference plots for the extended source experiment. Phase error difference is defined as the difference in the phase errors between the cases using frame selection to that without frame selection.

The relative phase error performance of a case with frame selection is compared to that without by

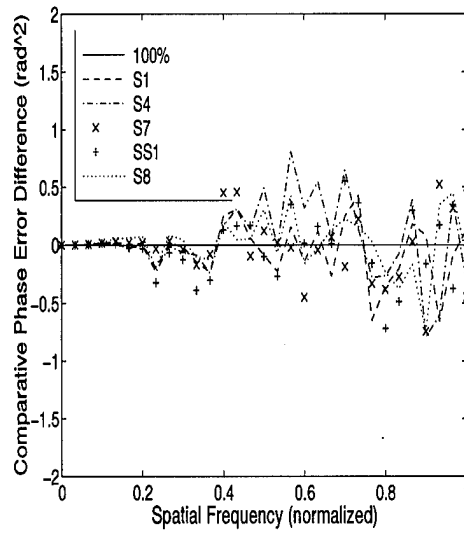
$$\phi_{\Delta}(\vec{f}) = \phi_{\epsilon}(\vec{f})_{100\%}^2 - \phi_{\epsilon}(\vec{f})_{FS}^2, \quad (\text{B.1})$$

where  $\phi_{\epsilon}(\vec{f})_{100\%}$  represents the phase error of the 100% case, and  $\phi_{\epsilon}(\vec{f})_{FS}$  represents a frame selected case. Areas in the spectrum where performance is improved as a result of frame selection, will have positive  $\phi_{\Delta}$  values. Conversely, where the performance declines as a result of frame selection,  $\phi_{\Delta}$  values are negative.

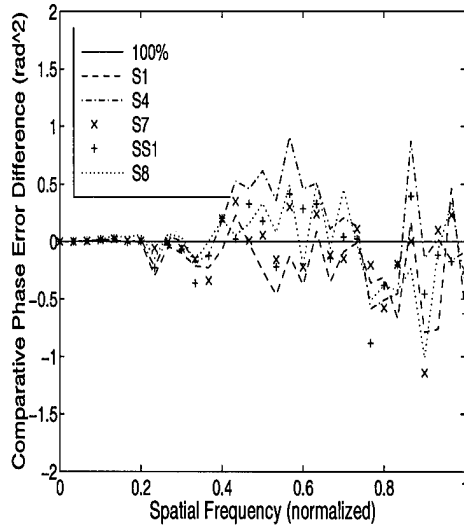
On each page, the four FSR strategies are presented, containing the results of the five metrics tested. A given set of visual parameters,  $r_o$  and  $m_{\nu}$ , are identified below.



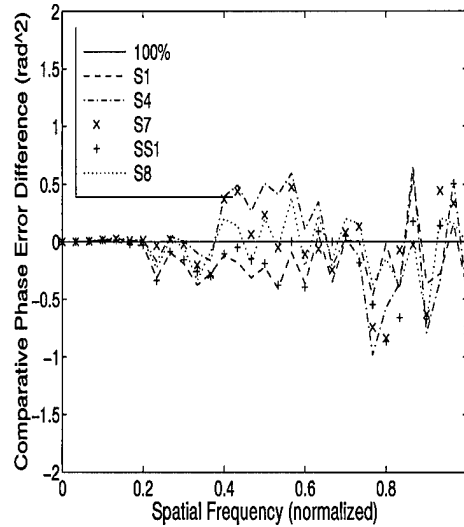
(a)



(b)

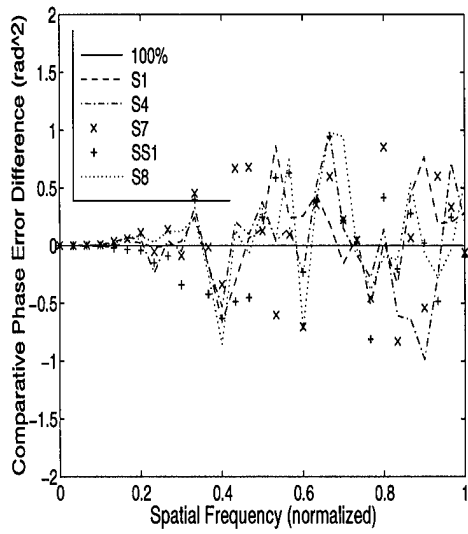


(c)

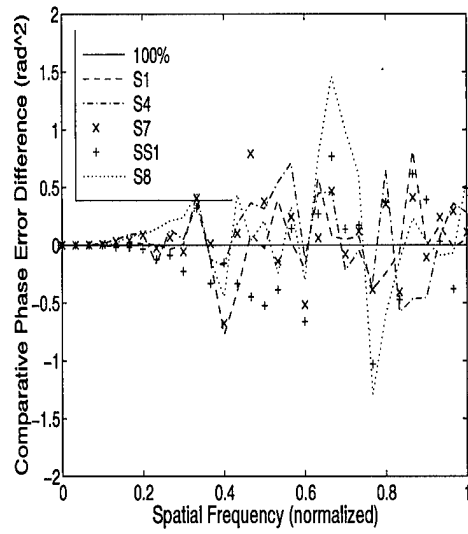


(d)

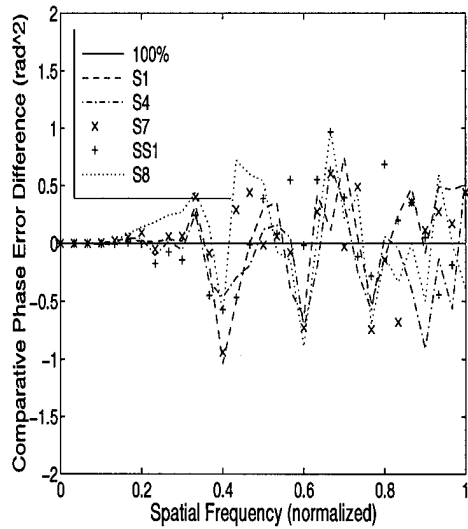
Figure B.37 Comparative phase error difference, extended source,  $m_\nu = 1$ ,  $r_o = 7$  cm. FSR = a) 50% b) 60% c) 70% d) 80%



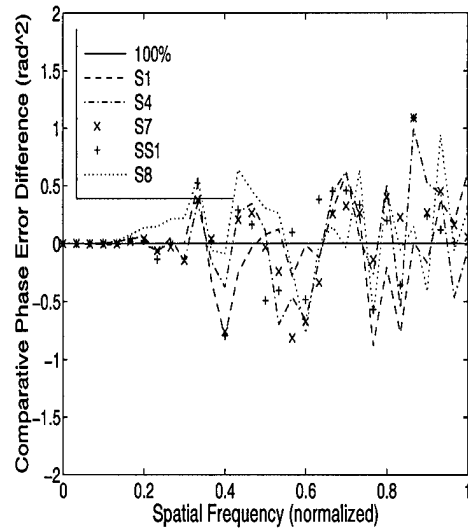
(a)



(b)

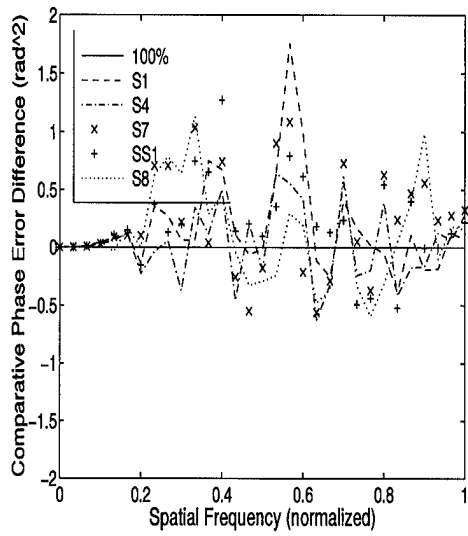


(c)

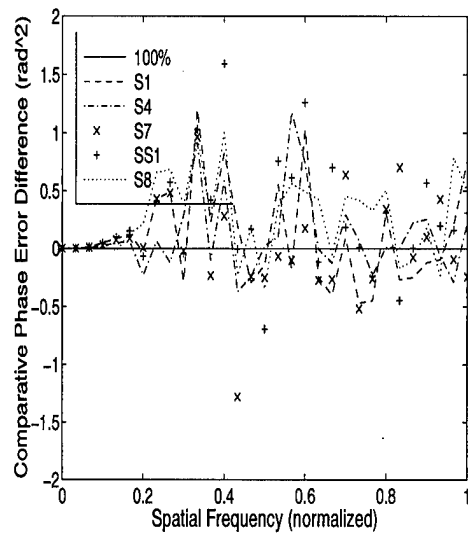


(d)

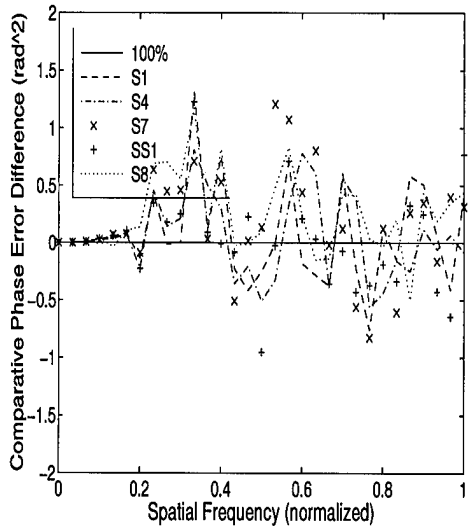
Figure B.38 Comparative phase error difference, extended source,  $m_v = 3$ ,  $r_o = 7$  cm. FSR = a) 50% b) 60% c) 70% d) 80%



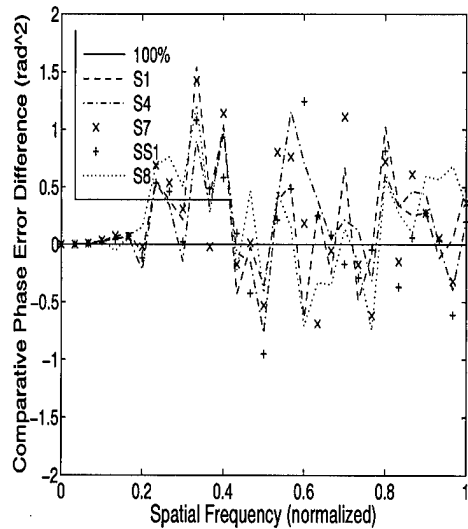
(a)



(b)

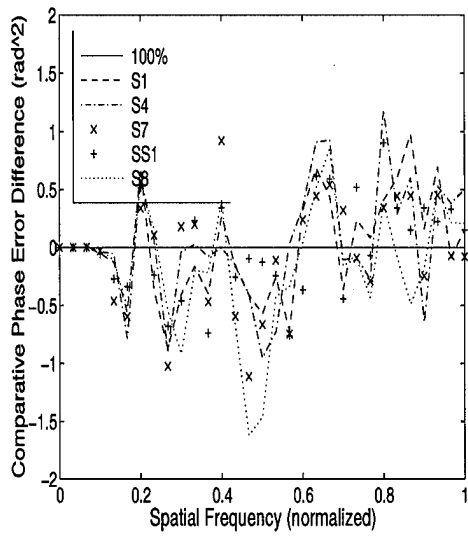


(c)

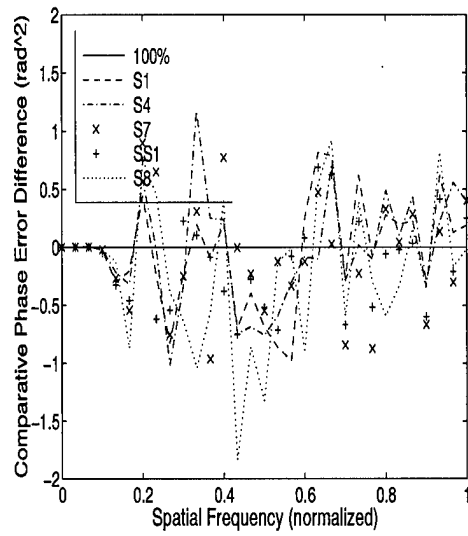


(d)

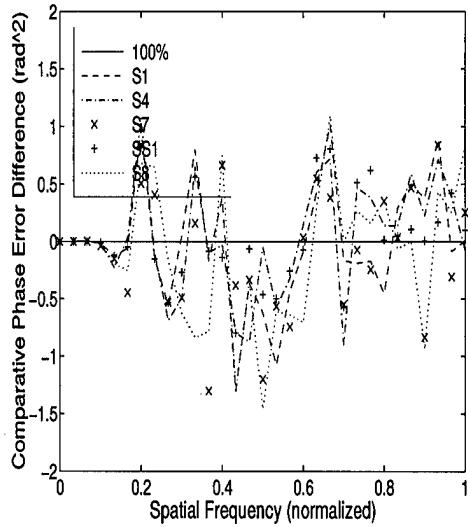
Figure B.39 Comparative phase error difference, extended source,  $m_\nu = 5$ ,  $r_o = 7$  cm. FSR = a) 50% b) 60% c) 70% d) 80%



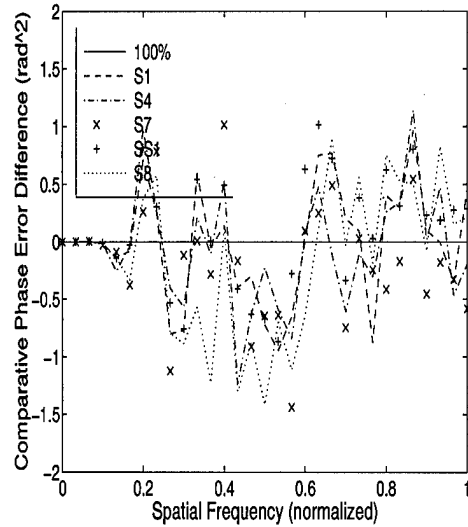
(a)



(b)

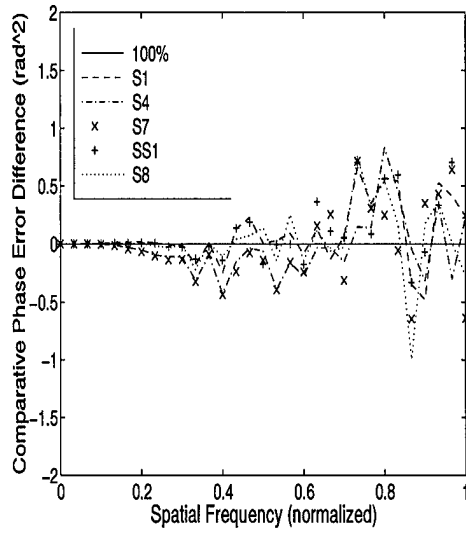


(c)

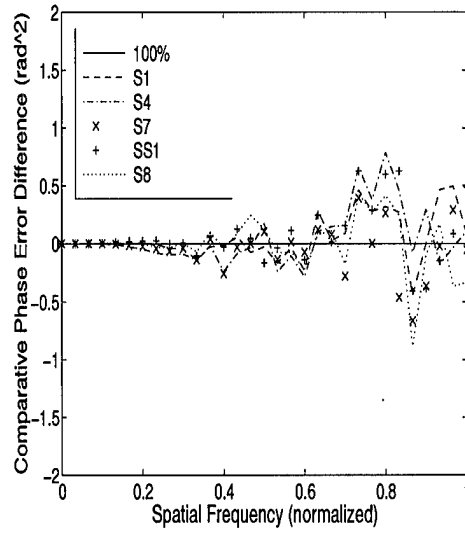


(d)

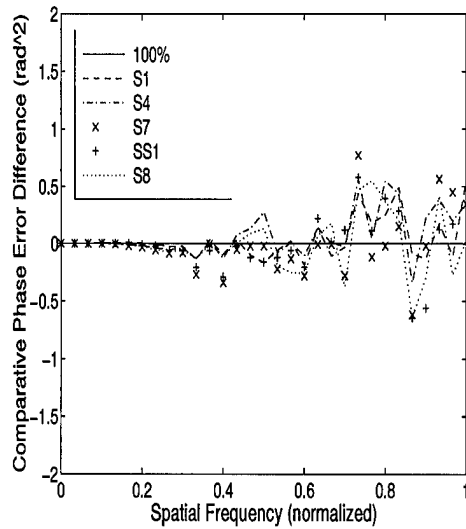
Figure B.40 Comparative phase error difference, extended source,  $m_\nu = 7$ ,  $r_o = 7$  cm. FSR = a) 50% b) 60% c) 70% d) 80%



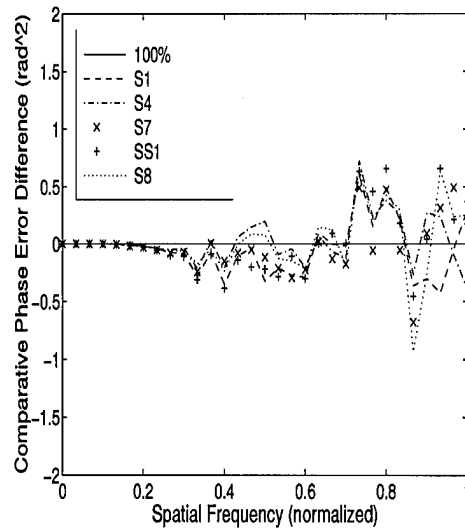
(a)



(b)

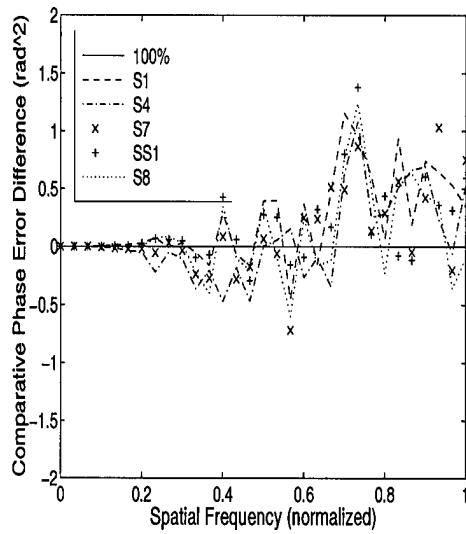


(c)

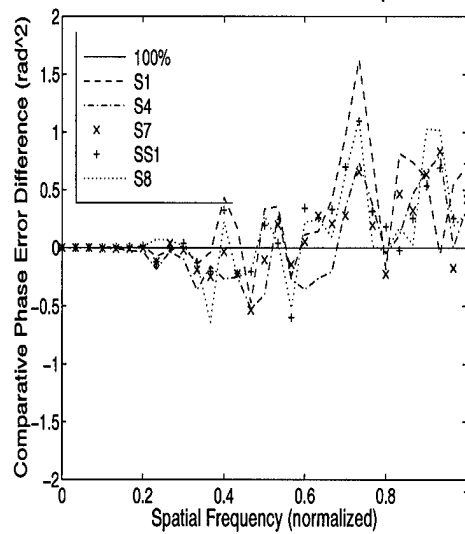


(d)

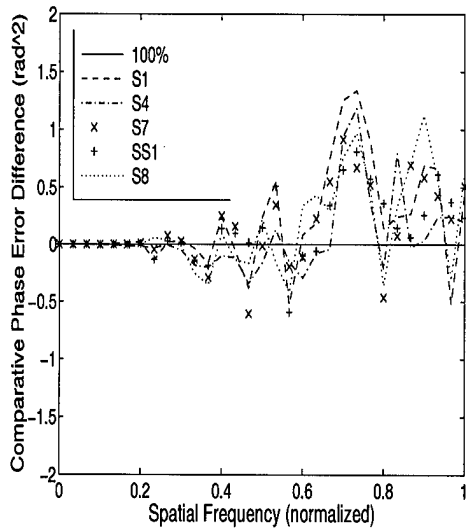
Figure B.41 Comparative phase error difference, extended source,  $m_v = 1$ ,  $r_o = 12$  cm. FSR = a) 50% b) 60% c) 70% d) 80%



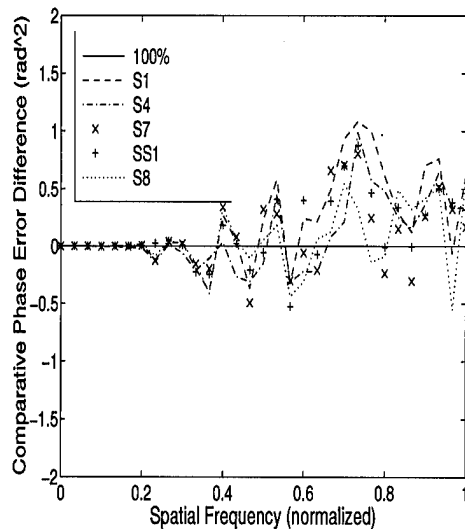
(a)



(b)

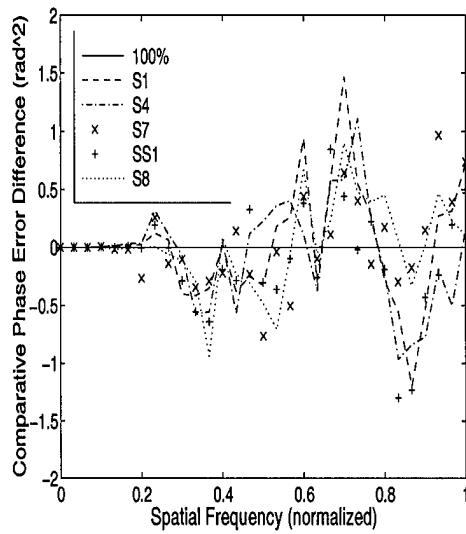


(c)

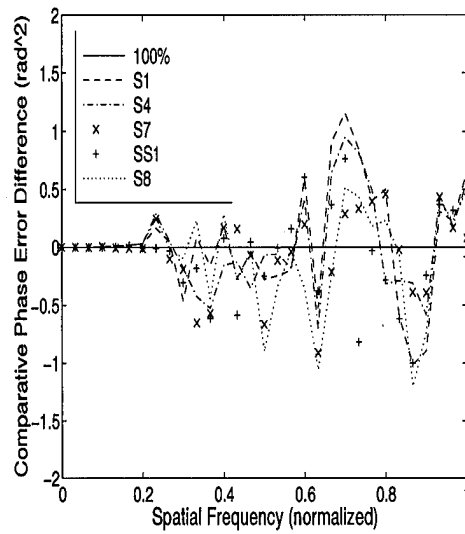


(d)

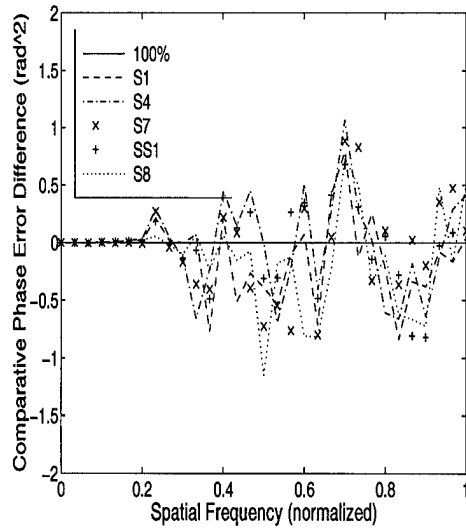
Figure B.42 Comparative phase error difference, extended source,  $m_\nu = 3$ ,  $r_o = 12$  cm. FSR = a) 50% b) 60% c) 70% d) 80%



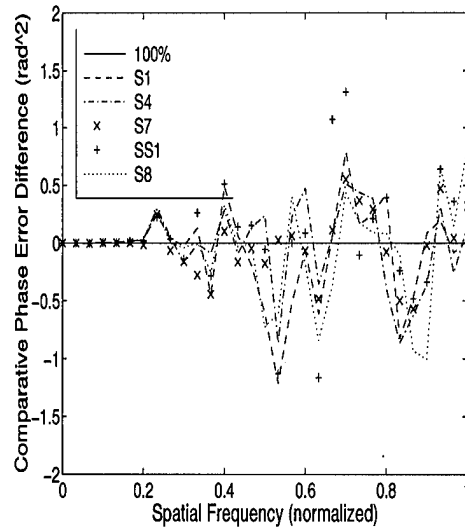
(a)



(b)

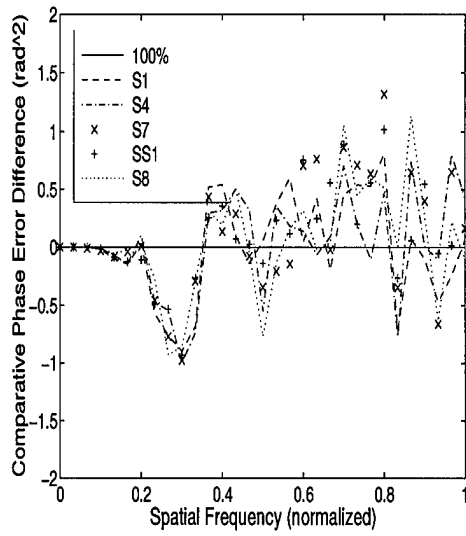


(c)

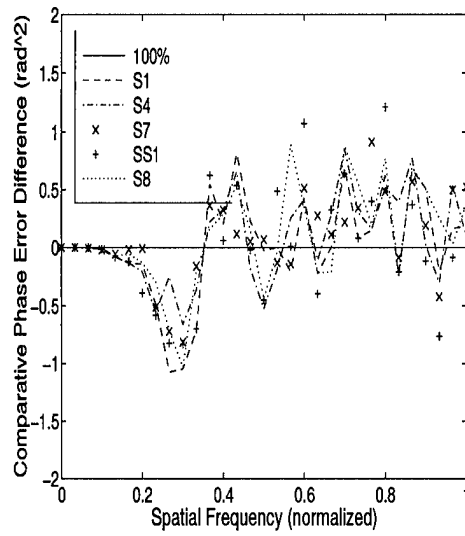


(d)

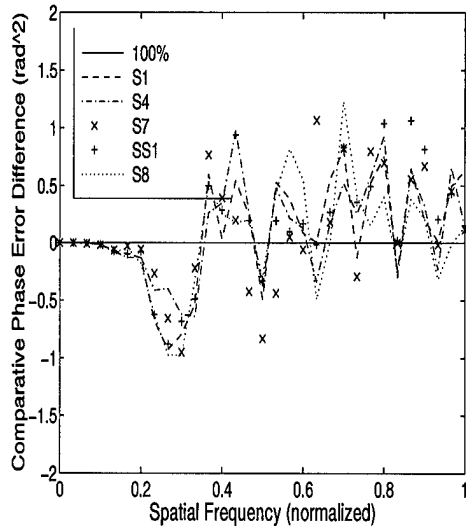
Figure B.43 Comparative phase error difference, extended source,  $m_\nu = 5$ ,  $r_o = 12$  cm. FSR = a) 50% b) 60% c) 70% d) 80%



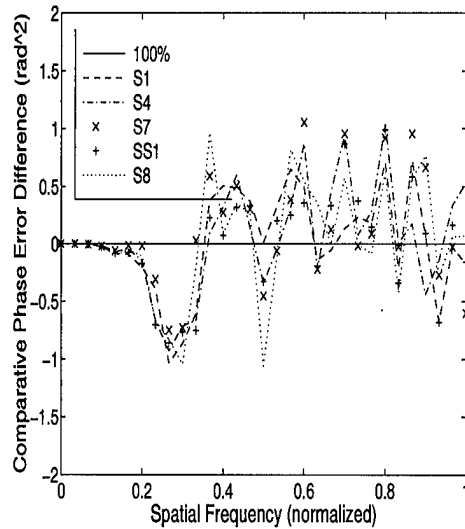
(a)



(b)

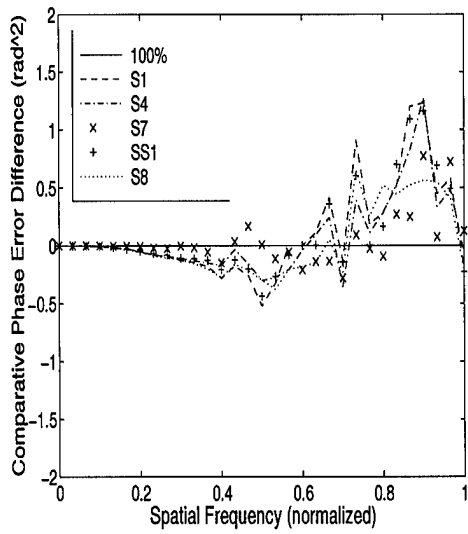


(c)

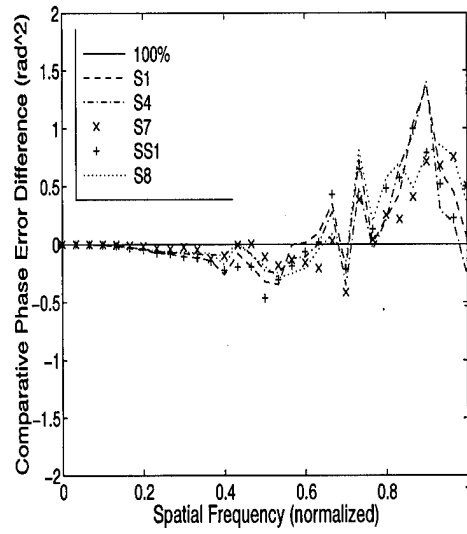


(d)

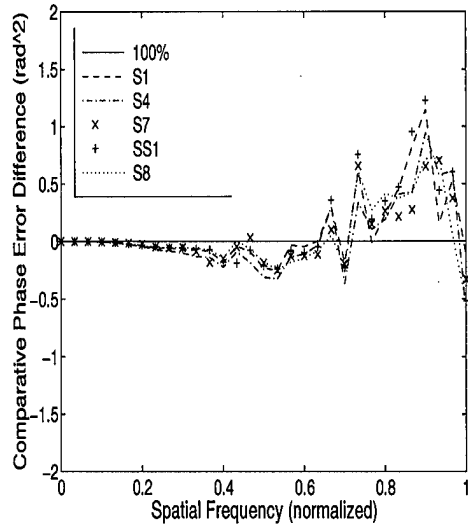
Figure B.44 Comparative phase error difference, extended source,  $m_\nu = 7$ ,  $r_o = 12$  cm. FSR = a) 50% b) 60% c) 70% d) 80%



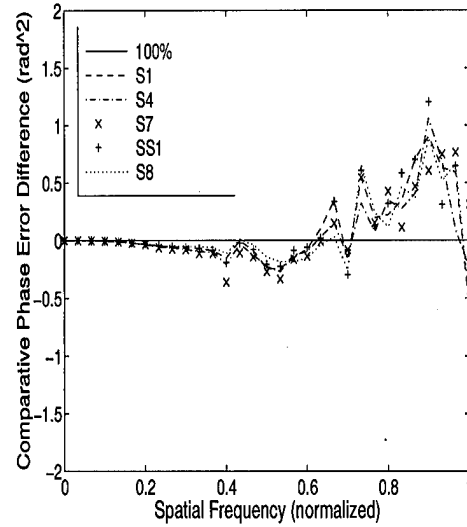
(a)



(b)

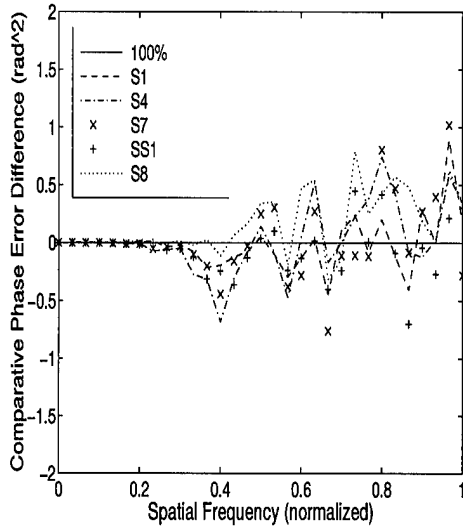


(c)

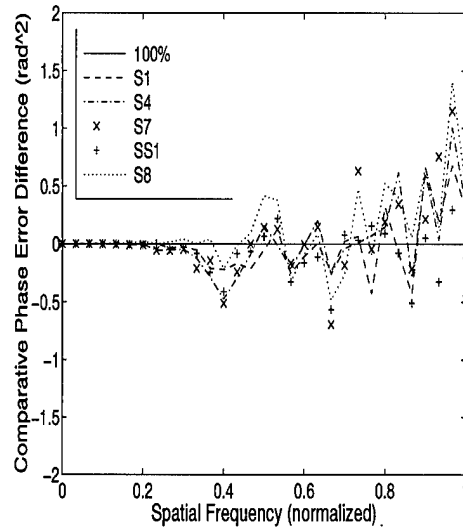


(d)

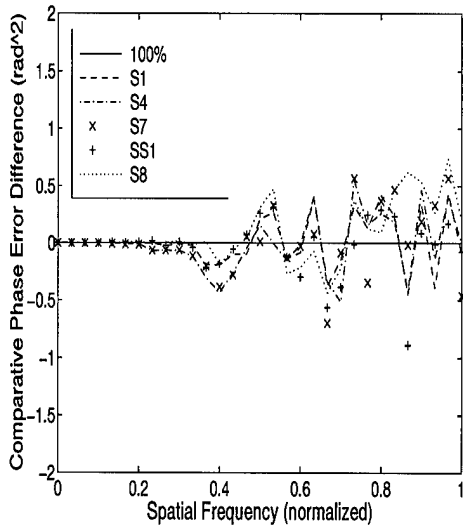
Figure B.45 Comparative phase error difference, extended source,  $m_v = 1$ ,  $r_o = 17$  cm. FSR = a) 50% b) 60% c) 70% d) 80%



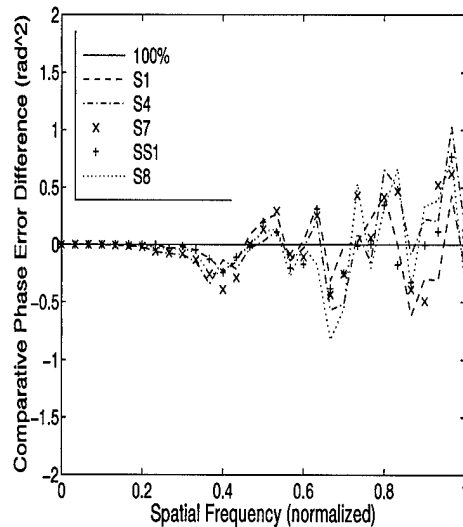
(a)



(b)

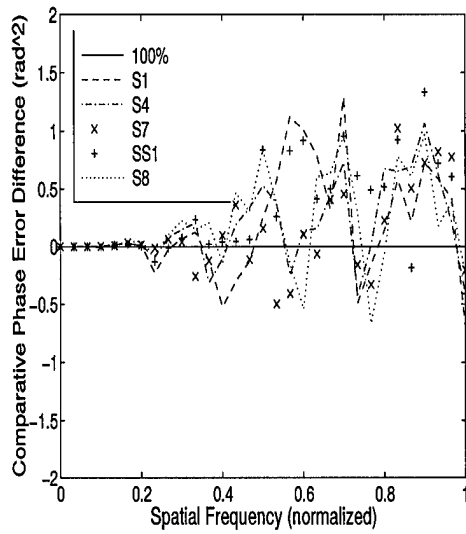


(c)

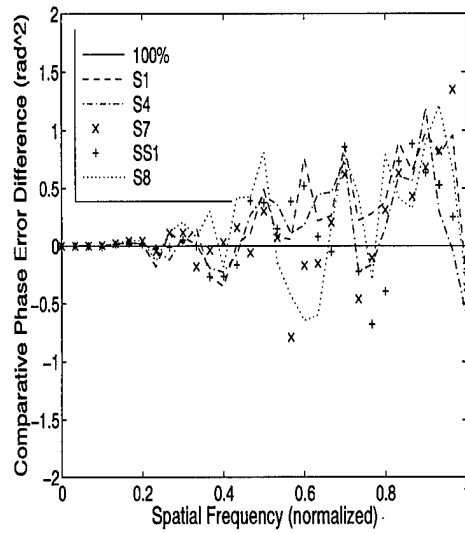


(d)

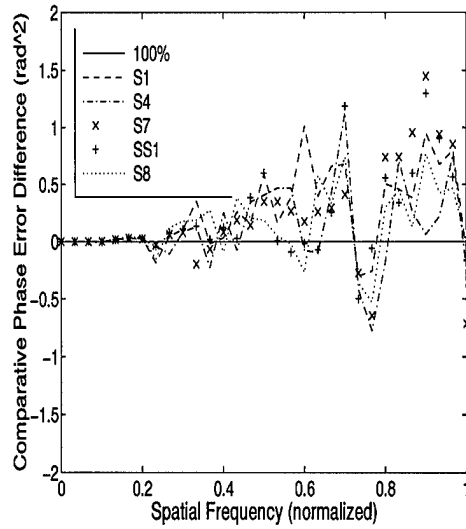
Figure B.46 Comparative phase error difference, extended source,  $m_\nu = 3$ ,  $r_o = 17$  cm. FSR = a) 50% b) 60% c) 70% d) 80%



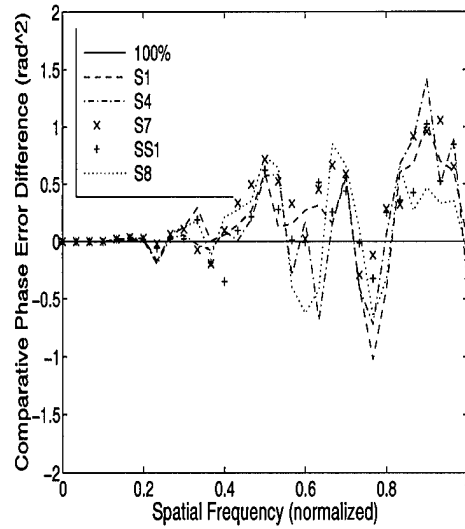
(a)



(b)

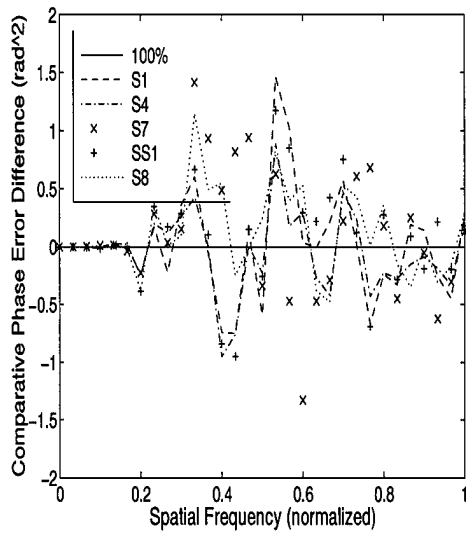


(c)

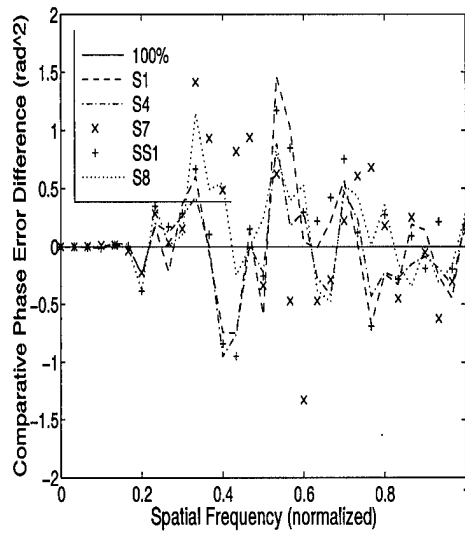


(d)

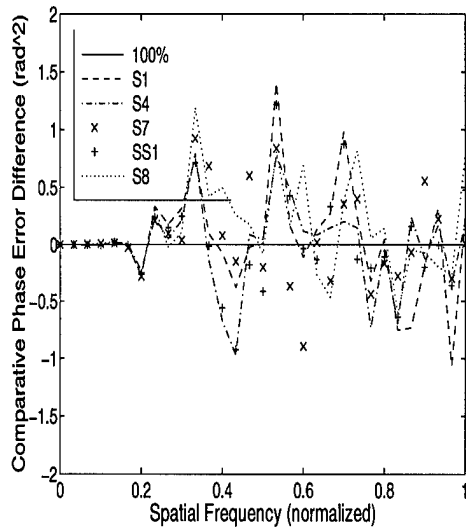
Figure B.47 Comparative phase error difference, extended source,  $m_\nu = 5$ ,  $r_o = 17$  cm. FSR = a) 50% b) 60% c) 70% d) 80%



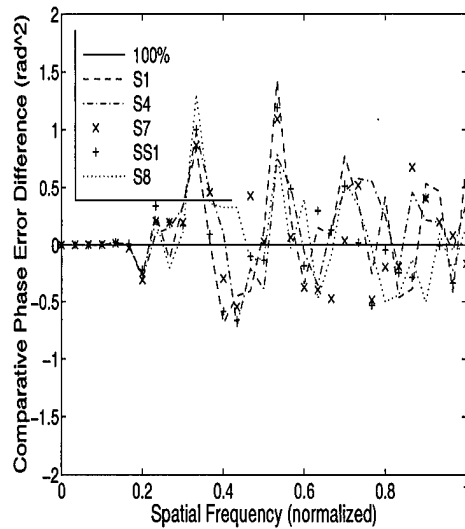
(a)



(b)



(c)



(d)

Figure B.48 Comparative phase error difference, extended source,  $m_\nu = 7$ ,  $r_o = 17$  cm. FSR = a) 50% b) 60% c) 70% d) 80%

## Bibliography

1. Ayers, G. R. and others. "Knox-thompson and triple correlation imaging through atmospheric turbulence," *Journal of Optical Society of America*, 5:963-985 (1988).
2. Boyd, R. W. *Radiometry and Detection of Optical Radiation*. John Wiley and Sons, New York, 1983.
3. Dainty, J. C. and A. H. Greenaway. "Estimation of spatial power spectra in speckle interferometry," *J. Opt. Soc. Am.*, 5:786-790 (1979).
4. Devany, M. N. R. M. Redfern E. B. Ramirez R. G. Renasco P. O'Kane and F. Rosa. "Real-Time Image Sharpening." *Diffraction-Limited Imaging with Very Large Telescopes* edited by D. M. Alloin and J. M. Mariotti, 369-378, Kluwer Academic Publishers, 1989.
5. Ford, Capt Steve. *Frame Selection Performance Limits For Statistical Image Reconstruction of Adaptive Optics Compensated Images*. MS thesis, AFIT/GEO/ENP/94D-03, Graduate School of Engineering, Air Force Institute of Technology (AETC), Wright-Patterson AFB OH, December 1994 (AD-AAL5467).
6. Fried, D. L. "Probability of getting a lucky short-exposure image through turbulence," *J. Opt. Soc. Am.*, 68:1651-1658 (1978).
7. Fuensalida, J. J. F. Rosa and F. J. Fuentes. "Applications of image sharpening techniques," *Astronomy and Astrophysics*, 191:L13-L15 (1988).
8. Gonzalez, R. C. and R. E. Woods. *Digital Image Processing*. Addison-Wesley Publishing Company, Reading, MA, 1992.
9. Goodman, Joseph W. *Introduction to Fourier optics*. McGraw-Hill, Inc., New York, 1988.
10. Gray, Terry M. VMAG computer printout, July 1995. Air Force Institute of Technology (AETC).
11. Holst, Gerald C. *Digital Image Processing*. JCD Publishing, Winterpark, FL, 1995.
12. Lawrence, T. W. and others. "Speckle imaging of satellites at the u.s. air force maui optical station," *Applied Optics*, 31:6307-6321 (1992).
13. Lohman, A. W. G. Weigelt and B. Wirnitzer. "Speckle masking in astronomy: triple correlation theory and applications," *Applied Optics*, 22(4):4028-4037 (December 1983).
14. Matson, C. L. "Weighted-least-squares phase reconstruction from the bispectrum -A," *Journal of Optical Society of America*, 8:1905-1913 (1991).

15. Meng, J. and others. "Triple-correlation subplane reconstruction of photon-address images," *Journal of Optical Society of America-A*, 7:1243-1250 (1990).
16. Muller, R. A. and A. Buffington. "Real-time correction of atmospherically degraded telescope images through image sharpening," *J. Opt. Soc. Am.*, 64:1200-1210 (September 1974).
17. Newton, Sir Isaac. "Optics." *Great Books of the Western World 34*, edited by R. M. Hutchins, Chicago: Encyclopedia of Britannica, 1952.
18. Nieto, J. L. A. Llebaria and S. di Serego Alighieri. "Photon-counting detectors in time-resolved imaging mode: image recentering and selection algorithms," *Astronomy and Astrophysics*, 178:301-306 (1987).
19. Northcott, M. J. and others. "Algorithms for image reconstruction from photon-limited data using the triple correlation," *Journal of Optical Society of America -A*, 5:986-992 (1988).
20. Roggemann, M. C. and J. A. Meinhardt. "Image reconstruction by means of wave-front sensor measurements in closed-loop adaptive-optics systems," *Journal of the Optical Society of America*, 10(9):1996-2007 (September 1993).
21. Roggemann, M. C. D. W. Tyler and M. F. Bilmont. "Linear Reconstruction of Compensated Images: Theory and Experimental Results," *Applied Optics*, 31:7429-7441 (December 1992).
22. Roggemann, Michael C. FY95 AFIT research proposal, October 1994. Air Force Institute of Technology (AETC).
23. Roggemann, Michael C. and others. "Image-spectrum signal-to-noise-ratio improvements by statistical frame selection for adaptive-optics imaging through atmospheric turbulence," *Optical Engineering*, 33:3254-3264 (October 1994).
24. Roggemann, Michael C. and Byron M. Welsh. *Imaging through turbulence*. CRC Press, Boca Raton, Fl, 1996.
25. Stoudt, Capt Craig A. *Improved Quality of Reconstructed Images Through Sifting of Data in Statistical Image Reconstruction*. MS thesis, AFIT/GEO/ENP/93D-03, Graduate School of Engineering, Air Force Institute of Technology (AETC), Wright-Patterson AFB OH, December 1993 (AD-AAK7871).
26. Thompson, K. T. and B. J. Thomson. "Recovery of images from atmospherically degraded short exposure images," *Astrophysics Journal*, 193:L45-L48 (1974).
27. Welsh, B. M. and C. S. Gardner. "Performance analysis of adaptive-optics systems using laser guide stars and slope sensors," *Journal of the Optical Society of America*, 6(12):1913-1923 (December 1989).

## *Vita*

Capt Harpold was born in Norfolk County England to US Air Force parents on May 11th, 1960. In 1978 she graduated from Stevens High School in Rapid City, South Dakota, and then in 1980 she enlisted in the Air Force as an Avionics Instrumentations Systems Specialist. Her tours of duty include Ellsworth AFB, SD, where she practiced her skill on B-52 bombers, KC-135 tankers and UH-1 helicopters, and Dover AFB DE where she worked on C-5, C-141 and C-130 cargo aircraft. In 1989, Tsgt Harpold earned her Bachelor of Science Degree in Physics with honors, from Arizona State University, under the Airman Education and Commissioning Program. Next, she earned her commission through the Officer Training School in September of 1989. From there, she was assigned to the Office of Aerospace Studies at Kirtland AFB, New Mexico, where she served as a scientific operational researcher in space physics. In May of 1994, Captain Harpold was reassigned to the Air Force Institute of Technology to pursue a Master of Science degree in Physics. In January of 1995 Captain Harpold reports to the Wright Laboratory at Wright-Patterson Air Force Base, Ohio, where she will serve as a laser physicist.

Permanent address: 2968 Lantz Rd  
Beavercreek, Ohio 45434

# REPORT DOCUMENTATION PAGE

Form Approved  
OMB No. 0704-0188

Public reporting burden for this collection of information is estimated to average 1 hour per response, including the time for reviewing instructions, searching existing data sources, gathering and maintaining the data needed, and completing and reviewing the collection of information. Send comments regarding this burden estimate or any other aspect of this collection of information, including suggestions for reducing this burden, to Washington Headquarters Services, Directorate for Information Operations and Reports, 1215 Jefferson Davis Highway, Suite 1204, Arlington, VA 22202-4302, and to the Office of Management and Budget, Paperwork Reduction Project (0704-0188), Washington, DC 20503.

<b>1. AGENCY USE ONLY (Leave blank)</b>		<b>2. REPORT DATE</b> December 1995	<b>3. REPORT TYPE AND DATES COVERED</b> Master's Thesis	
<b>4. TITLE AND SUBTITLE</b> THE ROLE OF FRAME SELECTION AND BISPECTRUM PHASE RECONSTRUCTION FOR SPECKEL IMAGING THROUGH ATMOSPHERIC TURBULENCE			<b>5. FUNDING NUMBERS</b>	
<b>6. AUTHOR(S)</b> Elizabeth A. Harpold				
<b>7. PERFORMING ORGANIZATION NAME(S) AND ADDRESS(ES)</b> Air Force Institute of Technology, WPAFB OH 45433-6583			<b>8. PERFORMING ORGANIZATION REPORT NUMBER</b> AFIT/GAP/ENP/95D-07	
<b>9. SPONSORING / MONITORING AGENCY NAME(S) AND ADDRESS(ES)</b> Capt Bruce Stribling PL/OL-YY 535 Lipoa Pkwy, Suite 200 Kihei, HI 96753			<b>10. SPONSORING / MONITORING AGENCY REPORT NUMBER</b>	
<b>11. SUPPLEMENTARY NOTES</b>				
<b>12a. DISTRIBUTION / AVAILABILITY STATEMENT</b> Distribution Unlimited			<b>12b. DISTRIBUTION CODE</b>	
<b>13. ABSTRACT (Maximum 200 words)</b> Frame selection using quality sharpness metrics have been shown in previous AFIT theses, to be effective in improving the final product of images obtained using adaptive optics. This thesis extends this idea to <i>uncompensated</i> speckle image data. Speckle image reconstruction is simulated with and without frame selection. Speckle images require the processing of hundreds of data frames. Frame selection is a method of reducing the amount of data required to reconstruct the image. A collection of short exposure image data frames of a single object are sorted based on sharpness metrics. Only the highest quality frames are retained and processed for the final image. The phase spectrum is reconstructed using the bispectrum technique. The benefits of frame selection for point (star) sources and extended (satellite) sources are examined by comparing composite image data with and without frame selection. The resulting power spectrum is evaluated through the SNR gain measurements, and the resulting phase spectrum is evaluated by measuring the phase error between the composite image and the object. In both cases, the results show that frame selection does not improve the power or the phase spectrums. For point sources, results show frame selection causes slight decrease in performance. For extended sources, the change in performance is insignificant. However, frame selection does offer a means for data reduction without significantly reducing performance in a wide variety of target brightness levels and atmospheric turbulence conditions.				
<b>14. SUBJECT TERMS</b> Frame Selection, Speckle Interferometry, Image Processing, Bispectrum, Phase Reconstruction			<b>15. NUMBER OF PAGES</b> 189	
			<b>16. PRICE CODE</b>	
<b>17. SECURITY CLASSIFICATION OF REPORT</b> UNCLASSIFIED	<b>18. SECURITY CLASSIFICATION OF THIS PAGE</b> UNCLASSIFIED	<b>19. SECURITY CLASSIFICATION OF ABSTRACT</b> UNCLASSIFIED	<b>20. LIMITATION OF ABSTRACT</b> UL	

## GENERAL INSTRUCTIONS FOR COMPLETING SF 298

The Report Documentation Page (RDP) is used in announcing and cataloging reports. It is important that this information be consistent with the rest of the report, particularly the cover and title page. Instructions for filling in each block of the form follow. It is important to *stay within the lines* to meet *optical scanning requirements*.

**Block 1. Agency Use Only (Leave blank).**

**Block 2. Report Date.** Full publication date including day, month, and year, if available (e.g. 1 Jan 88). Must cite at least the year.

**Block 3. Type of Report and Dates Covered.** State whether report is interim, final, etc. If applicable, enter inclusive report dates (e.g. 10 Jun 87 - 30 Jun 88).

**Block 4. Title and Subtitle.** A title is taken from the part of the report that provides the most meaningful and complete information. When a report is prepared in more than one volume, repeat the primary title, add volume number, and include subtitle for the specific volume. On classified documents enter the title classification in parentheses.

**Block 5. Funding Numbers.** To include contract and grant numbers; may include program element number(s), project number(s), task number(s), and work unit number(s). Use the following labels:

<b>C</b> - Contract	<b>PR</b> - Project
<b>G</b> - Grant	<b>TA</b> - Task
<b>PE</b> - Program Element	<b>WU</b> - Work Unit Accession No.

**Block 6. Author(s).** Name(s) of person(s) responsible for writing the report, performing the research, or credited with the content of the report. If editor or compiler, this should follow the name(s).

**Block 7. Performing Organization Name(s) and Address(es).** Self-explanatory.

**Block 8. Performing Organization Report Number.** Enter the unique alphanumeric report number(s) assigned by the organization performing the report.

**Block 9. Sponsoring/Monitoring Agency Name(s) and Address(es).** Self-explanatory.

**Block 10. Sponsoring/Monitoring Agency Report Number.** (If known)

**Block 11. Supplementary Notes.** Enter information not included elsewhere such as: Prepared in cooperation with...; Trans. of...; To be published in... When a report is revised, include a statement whether the new report supersedes or supplements the older report.

**Block 12a. Distribution/Availability Statement.** Denotes public availability or limitations. Cite any availability to the public. Enter additional limitations or special markings in all capitals (e.g. NOFORN, REL, ITAR).

**DOD** - See DoDD 5230.24, "Distribution Statements on Technical Documents."

**DOE** - See authorities.

**NASA** - See Handbook NHB 2200.2.

**NTIS** - Leave blank.

**Block 12b. Distribution Code.**

**DOD** - Leave blank.

**DOE** - Enter DOE distribution categories from the Standard Distribution for Unclassified Scientific and Technical Reports.

**NASA** - Leave blank.

**NTIS** - Leave blank.

**Block 13. Abstract.** Include a brief (*Maximum 200 words*) factual summary of the most significant information contained in the report.

**Block 14. Subject Terms.** Keywords or phrases identifying major subjects in the report.

**Block 15. Number of Pages.** Enter the total number of pages.

**Block 16. Price Code.** Enter appropriate price code (*NTIS only*).

**Blocks 17. - 19. Security Classifications.** Self-explanatory. Enter U.S. Security Classification in accordance with U.S. Security Regulations (i.e., UNCLASSIFIED). If form contains classified information, stamp classification on the top and bottom of the page.

**Block 20. Limitation of Abstract.** This block must be completed to assign a limitation to the abstract. Enter either UL (unlimited) or SAR (same as report). An entry in this block is necessary if the abstract is to be limited. If blank, the abstract is assumed to be unlimited.